### Learning Imaging

Series Editors: R. Ribes · A. Luna · P.R. Ros

Joan C. Vilanova · Antonio Luna Pablo R. Ros (Editors)

## Learning Genitourinary and Pelvic Imaging



JOAN C. VILANOVA Clinica Girona Dept. Magnetic Resonance Lorenzana 36 17002 Gerona Spain kvilanova@comg.cat

Antonio Luna Clinica Las Nieves Sercosa Carmelo Torres 2 23007 Jaén Spain aluna70@sercosa.com PABLO R. Ros Case Western Reserve University Dept. Radiology Bolwell B124 Euclid Ave. 11100 44106 Cleveland Ohio USA pablo.ros@uhhospitals.org

ISBN: 978-3-642-23531-3 e-ISBN: 978-3-642-23532-0

DOI: 10.1007/978-3-642-23532-0

Springer Heidelberg Dordrecht London New York

Library of Congress Control Number: 2011940863

© Springer-Verlag Berlin Heidelberg 2012

This work is subject to copyright. All rights are reserved, whether the whole or part of the material is concerned, specifically the rights of translation, reprinting, reuse of illustrations, recitation, broadcasting, reproduction on microfilms or in any other way, and storage in data banks. Duplication of this publication or parts thereof is permitted only under the provisions of the German Copyright Law of September 9, 1965, in its current version, and permission for use must always be obtained from Springer-Verlag. Violations are liable for prosecution under the German Copyright Law.

The use of general descriptive names, registered names, trademarks, etc. in this publication does not imply, even in the absence of a specific statement, that such names are exempt from the relevant protective laws and regulations and therefore free for general use.

Product liability: The publishers cannot guarantee the accuracy of any information about dosage and application contained in this book. In every individual case the user must check such information by consulting the relevant literature.

Printed on acid-free paper

9 8 7 6 5 4 3 2 1

Springer is part of Springer Science+Business Media (www.springer.com)

### Contents

### 1 Kidney

CARLOS NICOL	au, Carmen Sebastià, and Blanca Paño Brufau	1
Case 1	Bilateral Renal Artery Fibromuscular Dysplasia	2
Case 2	Active Multifocal Bleeding of the Renal Capsular Branches	
	Secondary to Subcapsular Hematoma	4
Case 3	Pyelonephritis	6
Case 4	Peritoneal Seeding of Xanthogranulomatous	
	Pyelonephritis	8
Case 5	Multiple Angiomyolipomas	10
Case 6	Renal Lymphoma	12
Case 7	Renal Fusion Anomaly: Horseshoe Kidney	14
Case 8	Renal Complex Cyst	16
Case 9	Clear Cell Renal Cell Carcinoma	18
Case 10	Papillary Renal Cell Carcinoma	20
Further <b>R</b>	Reading	22

### 2 Adrenal

RAFAEL SALVADOR IZQUIERDO, BLANCA PAÑO BRUFAU,

and Rafael O	liveira Cafaia	23
Case 1	Adrenal Hemorrhage	24
Case 2	Lipid-Rich Adenoma	26
Case 3	Lipid-Poor Adenoma	28
Case 4	Myelolipoma	30
Case 5	Adrenal Ganglioneuroma	32
Case 6	Pheochromocytoma	34
Case 7	Adrenal Metastases	36
Case 8	Adrenocortical Carcinoma	38
Case 9	Lymphoma	40
Case 10	Adrenocorticotropin-Independent Macronodular	
	Adrenal Hyperplasia	42
Further I	Reading	44

### 3 Urinary Bladder, Collecting System, and Urethra

CARMEN SEBAS	STIÀ, LAURA BUÑESCH, AND CARLOS NICOLAU	45
Case 1	Urothelial Carcinoma of the Renal Pelvis	46
Case 2	Urogenital Tuberculosis	48
Case 3	Ureteropelvic Junction Obstruction	50
Case 4	Uric Acid Urolithiasis	52
Case 5	Bladder Leiomyoma	54

VI Contents
-------------

Case 6	Urachal Tumor	56
Case 7	Extraperitoneal Bladder Rupture	58
Case 8	Bladder Cancer	60
Case 9	Complicated Urethritis	62
Case 10	Urethral Cancer	64
Further Reading		66

### 4 Prostate and Seminal Vesicles

JOAN C. VILAN	ova, Roberto García-Figueiras, Maria Boada,	
and Joaquim	Barceló	67
Case 1	Vesiculitis	68
Case 2	Utricle Cyst	70
Case 3	Seminal Vesicle Cyst with Renal Agenesis	72
Case 4	Chronic Prostatitis	74
Case 5	Benign Prostatic Hypertrophy	76
Case 6	Seminal Vesicles Infiltration	78
Case 7	Central Gland Prostate Cancer	80
Case 8	Bilateral Peripheral Prostate Cancer	82
Case 9	Local Recurrence After Radical Prostatectomy	84
Case 10	Local Recurrence After Brachytherapy	88
Further	Reading	90

### 5 Scrotum

Sandra Balea	to, Gabriel C. Fernández, and Joan C. Vilanova	93
Case 1	Testicular Adrenal Rest Tissues	94
Case 2	Giant Intratesticular Cyst	96
Case 3	Scrotal Trauma: Testicular Rupture	98
Case 4	Segmental Testicular Infarction	100
Case 5	Spermatic Cord Torsion	102
Case 6	Torsion of the Appendix Testis	104
Case 7	Cystic Transformation of the Rete Testis	106
Case 8	Fibrous Pseudotumor of the Testis	108
Case 9	Seminoma	110
Case 10	Leydig Cell Tumor of the Testis	112
Further <b>R</b>	Reading	114

### **6 Obstetrics**

Marcelo Potolicchio, Antonio Luna, and Joan C. Vilanova		115
Case 1	Pulmonary Cystic Adenomatosis	116
Case 2	Arthrogryposis	120
Case 3	Harelip	122
Case 4	Fetal Myelomeningocele	124
Case 5	Fetal Renal Polycystosis	126
Case 6	Down Syndrome	128
Case 7	Edward's Syndrome	130
Case 8	Fallot's Tetralogy	134

Case 9	Case 9 Congenital Spondyloepimetaphyseal Dysplasia (SEDC),	
	Strudwick Type	136
Case 10	Fetal Lissencephaly	138
Further Reading		140

### 7 Uterus

Teodoro Martín Noguerol, Antonio Luna

and Joa	n C. Vi	LANOVA	141
Ca	se 1	Bicornuate uterus	142
Ca	ise 2	Rokitanski Syndrome	144
Ca	ise 3	Uterine Leiomyomas	146
Ca	se 4	Endometrial Polyp	148
Ca	ise 5	Adenomyosis	150
Ca	ise 6	Endometrial Cancer	152
Ca	ise 7	Recurrent Endometrial Cancer	154
Ca	ise 8	Imaging Follow-Up of Embolized Uterine Fibroid	156
Ca	ise 9	Hydatiform Mole	158
Ca	se 10	Uterine Sarcoma	160
Fu	rther R	Reading	162

### 8 Cervix and Vagina

MARIANO VOLP	acchio, Joan C. Vilanova, and Antonio Luna	165
Case 1	Incidental Cervical Cancer	166
Case 2	MR Staging of Cervical Cancer	168
Case 3	Bicornuate Bicollis Uterus	170
Case 4	Nabothian Cysts	172
Case 5	Adenoma Malignum	174
Case 6	Bartholin Gland Cyst	176
Case 7	Endometriosis	178
Case 8	Aginal Prolapse	180
Case 9	Vaginal Cancer	182
Case 10	Vesicovaginal Fistula	184
Further <b>R</b>	eading	186

### 9 Adnexa

GUADALUPE GA	ARRIDO, IGNACIO ALVAREZ REY, AND JOAN C. VILANOVA	187
Case 1	Borderline Mucinous Ovarian Tumor	188
Case 2	Ovarian Torsion	190
Case 3	Ovarian Mature Cystic Teratoma	192
Case 4	Pelvic Congestion Syndrome	194
Case 5	Pelvic Inflammatory Disease and Fitz-Hugh-Curtis	
	Syndrome	196
Case 6	Bilateral Hydrosalpinx	198
Case 7	Virchow's Node as First Manifestation of Bilateral	
	Ovarian Serous Carcinoma	200
Case 8	Ovarian Endometriosis and Hematosalpinx	202

Case 9	Hemorrhagic Corpus Luteum Cyst	204
Case 10	Fallopian Tube Metastases in Endometrial Carcinoma	206
Further Reading		

### 10 Retroperitoneum

Roberto Garc	cía Figueiras, María Pérez Alarcón,		
AND IRIA COUTO RODRÍGUEZ			
Case 1	Retroperitoneal Hemorrhage	210	
Case 2	Iliopsoas Abscess	212	
Case 3	Retroperitoneal Fibrosis	214	
Case 4	Erdheim-Chester Disease	216	
Case 5	Liposarcoma	218	
Case 6	Leiomyosarcoma	220	
Case 7	Ganglioneuroma	222	
Case 8	Paraganglioma	224	
Case 9	Lymphoma	226	
Case 10	Retroperitoneal Soft Tissue Metastases	228	
Further Reading 23			

### Contributors

IGNACIO ALVAREZ REY Servicio de Radiodiagnóstico Xanit Hospital Internacional Benalmádena Málaga Spain

JOAQUIM BARCELÓ Department of Radiology Clínica Girona-Hospital Sta. Caterina University of Girona Girona Spain

SANDRA BALEATO Department of Radiology CHUS Complexo Hositalario Universitario de Santiago Coruña Spain

MARIA BOADA Department of Radiology Clínica Girona Girona Spain

LAURA BUÑESCH Department of Radiodiagnostic Imaging Center Hospital Clínic Barcelona Spain IRIA COUTO RODRÍGUEZ Department of Radiology Complexo Hospitalario Universitario de Santiago de Compostela Santiago de Compostela Spain

GABRIEL C FERNÁNDEZ Department of Radiology HNSS (Hospital Nuestra Señora de Sonsoles) Ávila Spain

ROBERTO GARCÍA-FIGUEIRAS Department of Radiology Complexo Hospitalario Universitario de Santiago de Compostela Santiago de Compostela Spain

GUADALUPE GARRIDO Diagnostic Imaging Department Hospital Clínico Málaga Spain

Antonio Luna Clinica Las Nieves Sercosa Jaén Spain

Teodoro Martín Noguerol Clinica Las Nieves, Sercosa Jaén Spain CARLOS NICOLAU Department of Radiodiagnostic Imaging Center Hospital Clínic Barcelona Spain

RAFAEL OLIVEIRA CAFAIA Radiology Department Hospital Clínic Barcelona Spain

BLANCA PAÑO BRUFAU Radiology Department Hospital Clínic Barcelona Spain

MARÍA PÉREZ ALARCÓN Department of Radiology Complexo Hospitalario Universitario de Santiago de Compostela Santiago de Compostela Spain

Marcelo Potolicchio Ultrasound Unit DADISA Cádiz Spain RAFAEL SALVADOR IZQUIERDO Radiology Department Hospital Clínic Barcelona Spain

CARMEN SEBASTIÀ Department of Radiodiagnostic Imaging Center Hospital Clínic Barcelona Spain

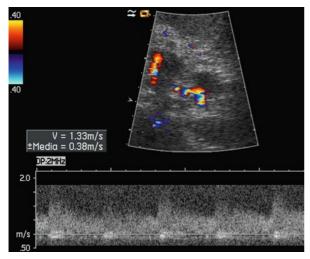
JOAN C. VILANOVA Department of Radiology Clínica Girona-Hospital Sta. Caterina Gerona Spain

MARIANO VOLPACCHIO Centro diagnóstico Rossi Buenos Aires Argentina Carlos Nicolau, Carmen Sebastià, and Blanca Paño Brufau

### Contents

Case 1	Bilateral Renal Artery Fibromuscular Dysplasia	2
Case 2	Active Multifocal Bleeding of the Renal Capsular Branches Secondary to Subcapsular Hematoma	4
Case 3	Pyelonephritis	6
Case 4	Peritoneal Seeding of Xanthogranulomatous Pyelonephritis	8
Case 5	Multiple Angiomyolipomas	10
Case 6	Renal Lymphoma	12
Case 7	Renal Fusion Anomaly: Horseshoe Kidney	14
Case 8	Renal Complex Cyst	16
Case 9	Clear Cell Renal Cell Carcinoma	18
Case 10	Papillary Renal Cell Carcinoma	20

### Case 1 Bilateral Renal Artery Fibromuscular Dysplasia





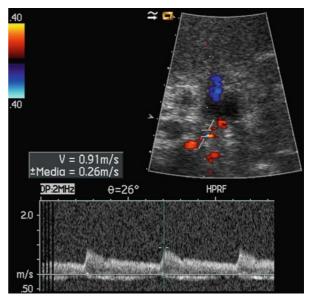


Fig. 1.2



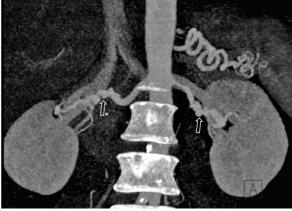




Fig. 1.3

A 54-year-old man presented to the emergency room with a hypertensive crisis and was successfully treated with antihypertensive treatment. A renal artery Doppler ultrasound was performed as part of the evaluation of the hypertension.

#### Comments

Fibromuscular dysplasia (FMD) is a non-atherosclerotic, non-inflammatory vascular disease that affects medium- and large-sized arteries, most commonly the renal and internal carotid arteries, but has been described in almost every arterial bed in the body. Clinical presentation may vary from an asymptomatic condition to a multisystem disease that mimics necrotizing vasculitis. It is known to be the second major cause of renovascular hypertension, atherosclerosis being the leading cause. Renovascular FMD tends to affect young women with no cardiovascular risk factors. Asymptomatic FMD is a finding that appears in 2-6% of multi-detector computed tomography (MDCT) scans of living renal donors, who are considered a sample of healthy people. In two-thirds of symptomatic patients, renal artery FMD is bilateral. Little is known about the long-term progression of asymptomatic FMD that is discovered incidentally. Duplex ultrasound imaging can accurately detect elevated blood-flow velocities in the middle to distal portion of the main renal arteries or segmental arteries. If the areas of stenosis are hemodynamically significant, a parvus-tardus waveform is seen on Doppler ultrasound in the intrarenal arteries. CT findings of FMD are very characteristic and show a "string-of-beads" or beaded appearance or focal stenosis or aneurysms usually in the mid- or distal main renal artery and the segmental renal arteries. If MDCT findings of FMD are clear, we can accurately diagnose the condition with this technique. In case of doubt, an angiography is mandatory.

Because of its better spatial resolution and the subtle findings of FMD, MDCT is preferred over MR for diagnosis. It is not difficult to differentiate FMD from renal artery atherosclerosis since the latter occurs at the origin or proximal artery in older patients with typical cardiovascular risk factors. If the medical treatment fails, percutaneous transluminal angioplasty or surgical revascularization are the primary therapeutic options.

Doppler ultrasound of the right artery shows increased flow of the distal right main renal artery (1.3 m/seg) compared to the proximal right main renal artery (0.9 m/seg) (Figs. 1.1 and 1.2). Doppler ultrasound shows decreased initial acceleration in intrarenal arteries consistent with the parvus-tardus waveform (not shown). Due to the suspicious findings of right main renal artery stenosis on Doppler ultrasound examination, an angio-CT was performed. Thin-MIP reformatted images in axial and coronal views (Figs. 1.3 and 1.4) show typical beading of the middle to distal portion of both renal arteries ("string of beads" appearance), suggestive of renal artery FMD (arrows). Note that the proximal renal arteries are not affected.

#### **Imaging Findings**

### Case 2

### Active Multifocal Bleeding of the Renal Capsular Branches Secondary to Subcapsular Hematoma

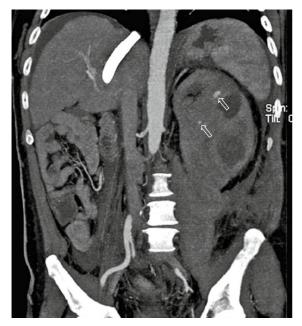


Fig. 1.5



Fig. 1.6

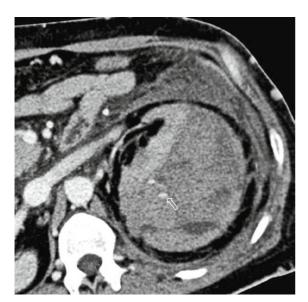


Fig. 1.7





A 48-year-old man with antiphospholipid syndrome and Budd-Chiari syndrome was admitted to the hospital for a renal biopsy to diagnose the sudden impairment of renal function. No complications appeared during the left renal biopsy and the patient was discharged the following day. Fifteen days after the biopsy and coinciding with the day the patient restarted the anticoagulant therapy, he complained of left flank pain and went to the emergency room. Laboratory tests showed a severely low red blood cell count. CT and angiography showed multifocal active bleeding on the renal surface from a subcapsular hematoma. Multiple partial embolizations of the left kidney were successfully performed and the patient was discharged 10 days later with a renal function of 30%.

Multifocal bleeding from ruptured capsular branches is an extremely rare condition; only two cases have been reported in the English literature. This condition usually appears after aggressive procedures on the kidneys (nephrostomy, stent placement or biopsy), with increased frequency in atrophic kidneys or in patients on anticoagulant therapy. It is believed that this traumatic procedure leads to subcapsular hematoma formation that causes rupture of the capsular arteries with multiple focal active bleeding. CT depicts a non-enhanced hyperdense subcapsular collection that compresses the kidney with multiple small focus of active bleeding inside the hematoma. Angiography shows multiple areas of perirenal arterial extravasation or pseudoaneurysms formation. Differential diagnosis with aneurysms secondary to vasculitis is required. These aneurysms occur in the intrarenal arterial branches whereas capsular pseudoaneurysms occur on the renal surface. The treatment of choice is angiographic embolization or nephrectomy. Usually an important loss of renal function appears after embolization secondary to the multiple bleeding sites.

# Arterial enhanced coronal and axial CT scans (Figs. 1.5–1.7) show compressed kidney by a severe subcapsular hematoma. Multiple small foci of active arterial bleeding are seen inside the hematoma near the kidney surface (arrows in Figs. 1.6 and 1.7). Selective angiography of the left renal artery demonstrates multiple small pseudoaneurysms in the kidney surface consistent with active bleeding of the capsular arteries (Fig. 1.8).

#### Comments

### **Imaging Findings**

### Case 3 Pyelonephritis Comments

A 55-year-old diabetic woman presents with a 7-day history of bilateral flank pain, fever of 39°C, nausea and vomiting.

In adults, diagnosis of urinary tract infection is typically based on characteristic clinical features and abnormal laboratory values.

Imaging should, in general, be reserved for those patients in whom conventional treatment has failed.

### Ultrasonography (US)

It is important to be aware of the US findings because sometimes they are subtle. US is limited in the identification of perinephric extension of infection, and in the visualization of small microabscesses.











Fig. 1.11



Fig. 1.12

7

Doppler evaluation typically demonstrates decreased perfusion in the affected parenchyma. Power Doppler is superior to color Doppler in defining the extent of hypoperfusion. However, Doppler evaluation is limited in the detection of low flow and flow in small vessels.

The advent of US contrast agents improves sensitivity of US in defining the extent of hypoperfusion.

CT is the modality of choice for evaluating acute pyelonephritis. According to the Society of Uroradiology, all regions of hypoattenuating parenchyma on CT should be considered acute pyelonephritis and the disease should be described in terms of uni/bilateral, focal/ diffuse, focal swelling/no-focal swelling or renal enlargement/no-renal enlargement.

A reasonable renal infection CT protocol should include precontrast followed by postcontrast imaging at nephrographic phase, and include the excretory phase only if urinary obstruction is suspected.

Unenhanced CT can detect obstruction, calculi, gas formation, hemorrhage, parenchymal calcifications, renal enlargement and inflammatory. Perinephric stranding alone should be interpreted with caution as even in presence of acute symptomatology, it may relate to previous infection, trauma or vascular disease.

At excretory phase, soft tissue filling defects in the collecting system may be present corresponding to blood clots, inflammatory debris or sloughed tissue from papillary necrosis.

Typical features at US/CT include:

- 1. Focal or global enlargement of the kidney, sometimes with a mass-like appearance.
- 2. Ill-defined, wedged-shaped area of hypoechoic/decreased attenuation radiating from the papilla to the cortical surface. Differential diagnosis includes areas of focal infarction, tumors or scarring.
- 3. At CT, striated nephrogram, seen as linear bands of alternating hyper and hypoattenuation orientated parallel to the axes of the tubules and collecting ducts. Striations are not pathognomonic of acute pyelonephritis.
- 4. Loss of corticomedullary differentiation at US.
- 5. Obliteration of the renal sinus and perinephric fat planes, stranding, thickening of Gerota's fascia at CT.
- 6. Thickening of the pelvicalyceal wall.
- 7. Microabscesses are identified as hypoechoic mass that lacks internal flow on color Doppler images at US, or non-enhancing fluid collections within abnormal areas of parenchyma that may have an enhancing rim. Abscess cavities may be large and require drainage in some cases.
- 8. Hydronephrosis/pyonephrosis.

US (Fig. 1.9) image shows right global enlarged kidney with several cortical hypoechoic round areas with ill-defined margins (open arrows). Power Doppler US evaluation (Fig. 1.10) and especially contrast-enhanced US (Fig. 1.11) improve the sensitivity to parenchyma abnormalities and demonstrate decreased perfusion in the affected parenchyma (arrows). CT in nephrographic phase (Fig. 1.12) shows bilateral renal enlargement, striated nephrogram (arrows) and peripheral fat stranding (open arrowhead). Ill-defined, non-enhancing fluid collections (microabscesses) within abnormal areas of parenchyma radiating from the papilla (arrowheads) are seen.

### Computed Tomography (CT)

### Radiological Findings

### Case 4 Peritoneal Seeding of Xanthogranulomatous Pyelonephritis



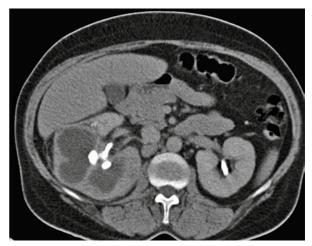


Fig. 1.14

Fig. 1.13



Fig. 1.15



Fig. 1.16

A 57-year-old woman was admitted to the emergency room complaining of fever and lumbar pain. Laboratory tests showed infection parameters. Abdominal ultrasound (US) and computed tomography (CT) were performed. Laparoscopic right nephrectomy was done; during surgery right kidney and peritoneum were accidentally opened. Five days later, the patient had no complications and was discharged. Six months later, he complained of pelvic pain with no other symptoms, and transvaginal US and CT were performed.

#### Comments

Xanthogranulomatous pyelonephritis (XP) is an uncommon reaction of the kidney to chronic infection in the setting of chronic obstruction. Diabetes mellitus is seen in 10% of these patients. The most common organisms involved are P. mirabilis and E. coli. Renal parenchyma is replaced by granulation tissue containing lipid-laden macrophages. Most cases occur in association with a renal pelvic calculus; hydronephrosis is thought to be a contributing factor. Symptoms are often non-specific. Although US is useful in the diagnosis of this condition, CT is the imaging technique of choice. US demonstrates an enlarged kidney with cystic areas corresponding to enlarged calyces. Characteristic CT findings include a non-functioning enlarged kidney with a staghorn calculus within a contracted renal pelvis. Expansion of calyces, parenchymal atrophy and inflammatory changes in perinephric fat are also strongly suggestive of XP. Calyces are filled with hypodense inflammatory infiltrate; these hypoattenuating calyces, with lipid content, often show around zero or negative HU values. Psoas abscess and fistula formation are the typical patterns of disease progression. Nephrectomy is the treatment of choice; percutaneous nephrostomy is not indicated. Accidental intraperitoneal seeding during surgery, as for our case, has not been previously described in the literature. Focal XP must be differentiated from other causes of hydronephrosis including obstructing urothelial carcinoma, and cystic masses such as cystic renal cell carcinoma and multilocular cystic nephroma.

### **Imaging Findings**

Contrast-enhanced coronal and axial CT images demonstrate a non-functioning enlarged right kidney with staghorn calculi, dilated calyces and renal atrophy (Figs. 1.13 and 1.14). Contrast-enhanced axial and coronal CT scans, 6 months after surgery, demonstrate enhancing masses with hypodense center and calcifications in the omentum (Fig. 1.15) and between the uterus and bladder (Fig. 1.16). Surgery demonstrated granulomatous tissue containing lipid-laden macrophages consistent with intraperitoneal seeding of XP.

Case 5 Multiple Angiomyolipomas A 44-year-old woman with tuberous sclerosis presented to the emergency room with sudden right flank pain, hypotension and skin pallor.





Fig. 1.18

Fig. 1.17

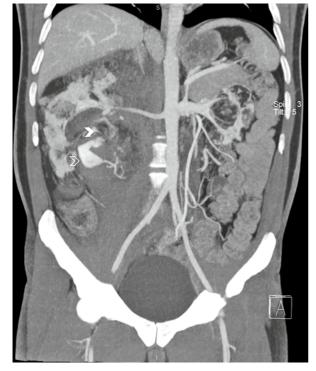






Fig. 1.20

#### Comments

Angiomyolipomas are hamartomas containing varying proportions of fat, smooth muscle and thick-walled blood vessels. Epidemiologically, angiomyolipoma (AML) is seen in two distinct clinical settings. Approximately 80% of AMLs occur in middle-aged adults, with a significant female predisposition. In this population, the lesions are usually small, solitary and asymptomatic. The remaining 20% of patients with AML have tuberous sclerosis. Renal AMLs are present in approximately 80% of patients with tuberous sclerosis. AMLs in these patients are usually multiple, bilateral tumors that usually reach a large size and are often symptomatic (pain, gross hematuria, anemia, etc.). Tumors >4 cm carry an increased risk for potentially life-threatening hemorrhage (Wünderlich syndrome), which has been reported in up to 10% of these patients.

A reliable diagnosis of AML can be made based on imaging features when fat is demonstrated within a renal mass. At least 90% of AMLs contain fat that is detectable with thinsection CT or MRI. The detection of fat within a mass that arises in the kidney is considered diagnosis of AML. Other features supporting the diagnosis of AML include the presence of enlarged or aneurysmal vessels within the tumor. Isolated cases of RCC, Wilm's tumor or oncocytoma with intratumoral fat have been reported. Liposarcomas arising from the renal capsule are uncommon and may contain mature fat. Liposarcomas are rare tumors that usually occur in older patients, and are generally large at the time of diagnosis and centered in the perinephric space. These tumors displace or compress the kidney and are hypovascular without enlarged internal vessels or aneurysms.

At sonography, an AML is characteristically more echogenic than the surrounding renal parenchyma and shows an acoustic shadowing. However, this feature is also seen in 32% of small renal cell carcinoma (<3 cm in diameter). Therefore, sonography does not allow a diagnosis with the degree of confidence achieved by CT. When a small amount of fat is suspected in a renal mass, an unenhanced CT examination with thin sections and, if necessary, a pixel analysis (<-10 UH) is the most sensitive test to confirm diagnosis.

At MRI imaging, the most reliable demonstration of macroscopic fat within an AML can be achieved by comparing the appearance of the tumor on T1-weighted images with fatsaturation sequences. AMLs with a predominant fatty component are isointense relative to fat in all MRI sequences. Macroscopic fat appears bright on T1-weighted images, and the signal visible decreases with fat saturation. The use of in-phase and opposed-phase imaging is also helpful in the diagnosis of very small lesions of AML. In predominantly fatty AMLs, a characteristic India ink artifact is seen at the interface between the fat-containing mass and the normal renal parenchyma on opposed-phase, whereas the central portions of the lesion do not demonstrate changes in signal intensity in comparison with the in-phase images.

### Imaging Findings

compatible with AML (open arrows). Right anterior perirenal and pararenal hyperdense (36 UH) collection is suggestive of hematoma (arrow). Axial nephrographic-phase CT scan (1 mm) shows (Fig. 1.18) arterial pseudoaneurysm (open arrowhead) arising from the inferior polar branch of the right kidney with contrast extravasation (solid arrow head). Coronal MIP reconstructions (Fig. 1.19) and angiographic images (Fig. 1.20) show similar findings. The pseudoaneurysm was successfully embolized.

Axial unenhanced CT (Fig. 1.17) shows multiple bilateral lesions that contain fat, being

### Case 6 Renal Lymphoma Comments

A 69-year-old patient presented with left flank pain and fever of 2 months of duration.

Renal involvement by lymphoma may be due to hematogenous dissemination or contiguous extension of retroperitoneal disease. Renal lymphoma may also be seen in immunocompromised patients. Primary renal lymphoma that is isolated to the renal parenchyma with no systemic manifestations is uncommon (less than 1% of extranodal lymphoma).

Understanding of tumor growth and the mechanism of spread histologically is important to interpret the resulting patterns of involvement. Hematogenous involvement usually results in bilateral distribution of tumor foci within renal cortex.

Contrast-enhanced computed tomography in the nephrographic-phase imaging is the most sensitive for lesion detection. If the tumor is central and affects the hilar region or collecting system, excretory phase imaging is necessary.

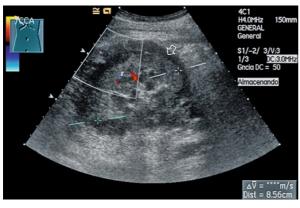








Fig. 1.23

Fig. 1.22





The suggestion of renal lymphoma is one of the few situations in which renal biopsy should be recommended, since the diagnosis of lymphoma determines medical therapy.

Renal lymphoma has a wide variety of CT appearances.

### 1. Multiple renal masses

Involvement is typically bilateral, but may also affect only one kidney. At contrastenhanced-CT the lesions enhance less than the normal renal tissue and appear as relatively homogeneous masses. The presence of retroperitoneal adenopathy is an additional clue of the diagnosis. In MR images, minimal heterogeneous enhancement is seen on early and delayed gadolinium-enhanced MR images. At US lesions appear typically hypoechoic and homogeneous. There are benign and malignant entities that mimic renal lymphoma including metastatic disease, acute pyelonephritis, renal infarcts, abscesses and multiple synchronous renal cell carcinomas.

### 2. Direct extension from retroperitoneal adenopathy

The second most common presentation of renal lymphoma is as contiguous extension to the kidneys or perinephric space from large retroperitoneal masses (25–30% of cases). At CT, lymphomatous masses usually envelop the renal vasculature invading the renal hilum. However, the vasculature remains patent despite tumor encasement, a finding that is characteristic of lymphoma, and thrombosis is rare.

### 3. Solitary lesion

Renal lymphoma manifests as a solitary mass that grows primarily by expansion in 10–25% of patients. At contrast-enhanced-CT the masses are typically hypovascular and demonstrate minimal enhancement.

### 4. Perinephric disease

Isolated perinephric lymphoma is unusual (<10% of cases). The presence of a mass of perinephric soft tissue compressing the normal parenchyma without causing significant impairment of renal function strongly suggests the diagnosis although occurs infrequently.

CT in nephrographic phase is crucial for demonstrating a perirenal mass and accurate staging. At US, hypoechoic tissue of variable thickness is seen surrounding the kidney. The differential diagnoses include sarcoma arising from the renal capsule and metastases to the perinephric space, as well as benign entities such as perinephric hematoma, amyloidosis and retroperitoneal fibrosis.

US imaging (Fig. 1.21) shows hypoechoic tissue (open arrow) surrounding the left kidney. Axial CT image at nephrographic phase (Fig. 1.22) shows hypodense and homogeneous soft tissue mass (open arrow) surrounding the left kidney that enhance less than the normal renal tissue. The mass causes anterior displacement, and focal cortical infiltration of left kidney (arrowhead). The ipsilateral psoas muscle is also infiltrated (arrowhead). Small retroperitoneal lymph nodes were identified (arrowhead). Axial CT imaging at excretory phase (Fig. 1.23) shows that the mass affects collecting system produces hydronephrosis. Excretory phase image shows delayed uptake and elimination of contrast material. Axial delayed gadolinium-enhanced fat-suppressed T1-weighted sequence (Fig. 1.24) performed 1 month later shows bilateral perirenal masses (open arrows) with minimal heterogeneous enhancement that extend above the large retroperitoneal vessels (arrowhead) and infiltrate the pancreatic isthmus (arrowhead) and cortical parenchyma.

#### **Imaging Findings**

### Case 7 Renal Fusion Anomaly: Horseshoe Kidney



Fig. 1.25



Fig. 1.26









A 35-year-old woman with abdominal pain and microhematuria was referred to the Radiology Department. An US examination was performed.

#### Comments

Renal fusion anomalies, in which both kidneys are fused together, are uncommon. They result from partial failure of renal ascent during embryological development. In 90% of the cases, the fusion is at the lower poles of the kidneys. Horseshoe kidney is the most common renal fusion anomaly and is usually discovered incidentally during US examination performed for non-specific abdominal purposes. Poor visualization of the lower poles when exploring the renal fossa is suggestive of horseshoe kidney. The renal parenchyma can be followed with the transducer to the abdominal midline, where the lower poles are connected by a band of renal parenchyma crossing the midline. Horseshoe kidneys are frequently associated with rotational anomalies, particularly with incomplete rotation, and the pelvis of horseshoe kidney has a more anterior location. Horseshoe kidney is usually asymptomatic but can be accompanied by several complications such as stone disease, ureteropelvic junction obstruction, dilation due to reflux and urinary tract infections. In addition, horseshoe kidney is considered a risk factor for the development of renal and urologic malignancies. When a complication is detected in horseshoe kidneys, the treatment may differ from that of the normal kidney due to the abnormal location of horseshoe kidneys, posing a challenge for the urologists. Once a fused kidney is diagnosed, follow-up is recommended in order to detect these potential complications and prevent severe renal damage. US is usually the first-line technique to screen for the presence of complications. However, when a complication is present, especially in cases of stones, hydronephrosis or masses, a MDCT examination is recommended for treatment planning. For this purpose, post-processing techniques are helpful including multiplanar reformat (MPR), maximum intensity projection (MIP) or volume rendering (VR) 3D images. Those techniques provide very precise information of the vascular supply and the urinary tract of the fused kidneys.

### **Imaging Findings**

US image (Figs. 1.25 and 1.26), axial MDCT reconstruction image during nephrographic phase (Fig. 1.27) and coronal MDCT reconstruction image during excretory phase (Fig. 1.28) of both kidneys demonstrate midline fusion (open arrows). A kidney stone was detected (Fig. 1.26) in the left kidney (arrow). The band of renal parenchyma connecting both kidneys may be identified using US and MDCT. Coronal reconstruction on the excretory phase allows a better knowledge of the position and distribution of the excretory tract.





Fig. 1.29

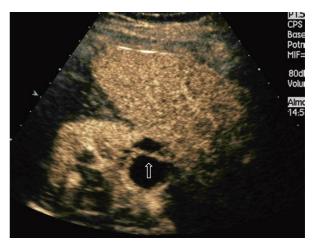
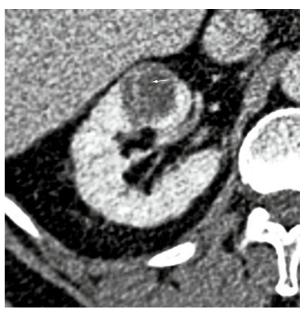


Fig. 1.30









A 66-year-old man presented with a past history of kidney stones and microhematuria. An US examination was performed and a cyst with thickened septum was detected.

Based on imaging findings, most renal cell carcinomas (RCC) are solid but as many as 10%

#### Comments

have some cystic component. When a renal complex cystic lesion is detected, the most important issue is to differentiate cystic RCC from benign complex cysts usually secondary to bleeding or infection. The evaluation of a complex cyst requires the intravenous injection of a contrast agent, and the detection of enhancement of solid components or an irregular thickened wall or septa are the most specific signs suggesting malignancy. This evaluation can be performed using CT, MR or contrast-enhanced US (CEUS). Complex cyst can be classified into five groups using the worldwide-accepted Bosniak classification that correlates the malignant potential of the cysts with several features such as the presence and number of septa, thickening of the wall and septa, presence of solid masses and nodular enhancement and determines the probability of malignancy depending on these features. Bosniak I and II have an estimated 0% probability of malignancy and are cysts with no septa or with few hairline-thin septa that may show minimal thin enhancement but no softtissue nodular enhancement. Bosniak IIf cysts, with an estimated 5% of malignancy, are renal cysts with multiple hairline-thin septa, smooth minimal thickening of the wall or septa, and absence of nodular enhancement. They are considered benign but need to remain stable at follow-up. Bosniak III cysts, with an estimated 50% probability of malignancy, may have thickened irregular wall or septa with enhancement after the administration of contrast agent but without enhancing solid masses. This category includes benign hemorrhagic or infected cysts, multilocular cystic nephromas and cystic RCC. Finally, Bosniak IV cysts, with an estimated 95-100% probability of malignancy, are clear malignant cystic masses with the presence of soft-tissue enhancing mass independent of the wall or septa. With respect to the management of complex cysts, there are three points to be considered: the first is that surgery is recommended in Bosniak III and IV cysts due to the high probability of malignancy. Second, when a follow-up is recommended (IIf group), at least a 3-year follow-up is necessary to assure that the lesion is benign due to the slow growth of some cystic RCCs. In addition, although the excellent correlation of complex cysts features with CEUS, CT and MR imaging, CEUS and MR imaging are more sensitive than CT to detect the microvascularization of the wall and septa with the advantage of absence of radiation.

Baseline US (Fig. 1.29) shows a cystic complex renal mass in the right kidney with presence of septa and thickened posterior wall. A CEUS examination was performed (Figs. 1.30 and 1.31) and demonstrated enhancement of the thickened wall and of the thickened septa (open arrow). The complex cyst was classified as Bosniak III. Nephrographic-phase CT scan (Fig. 1.32) also showed the enhancing septa (arrow). The patient was referred to surgery and the histologic analysis revealed a cystic RCC.

### **Imaging Findings**

### Case 9 Clear Cell Renal Cell Carcinoma

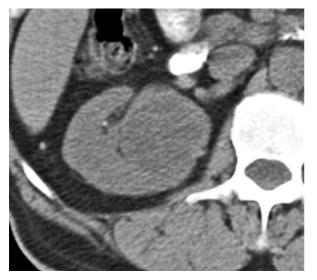




Fig. 1.34

Fig. 1.33



Fig. 1.35



Fig. 1.36

A solid renal mass was detected in the right kidney on abdominal US examination performed for right flank pain on a 68-year-old man.

When a solid renal mass is detected on US examination, additional MDCT or MR imaging-

### Comments

in few cases also biopsy- are recommended, because baseline US is not accurate enough to characterize renal lesions. Characterization is mainly based on some imaging features including the presence of fat, enhancement pattern and presence of extrarenal features of malignancy such as lymph nodes or metastases. If the presence of fat is ruled out, renal cell carcinoma (RCC) is the most probable diagnosis. MDCT is the main imaging technique for renal tumor characterization. CT protocol must include one unenhanced phase and three enhanced phases (corticomedullary, nephrographic and excretory phase). The unenhanced phase allows detection of calcifications and fat, as well as the assessment of enhancement when compared with the enhanced phases. Corticomedullary phase provides a useful angiographic image of the arterial and venous supply to the kidney, and the nephrographic phase is the optimal phase for the detection and characterization of renal masses. Finally, the excretory phase provides information about the involvement of the collecting system. MR imaging can also evaluate with similar accuracy the enhancing behavior. Regarding the enhancement pattern, most RCC and especially the most common subtype (clear cell RCC) typically show hypervascularity followed by washout. The enhancement pattern correlates with histological findings since the homogeneity or heterogeneity of the enhancement depends on the presence of hemorrhagic, necrotic or cystic areas. One major problem with imaging modalities is that they cannot differentiate adequately renal cancer from oncocytomas, which have a very similar enhancement pattern to that of clear cell RCC in all phases. The presence of a central scar is a characteristic feature of oncocytomas. However, this occurs in less than a half of the cases, therefore, most oncocytomas may resemble RCC. In addition, some RCCs have heterogeneous enhancement with necrotic or fibrotic areas that can mimic a central scar, thus the final diagnosis can be only obtained by histology. At this point, it has been suggested that Diffusion-weighted imaging could help in the differentiation between RCC and oncocytomas since malignant tumors have higher restriction to the molecular diffusion of water than benign tumors due to the increased cellularity of neoplastic tissues. In this sense, two recent studies (Taouli et al. Radiology 2009; Incy et al. Eur J Radiol 2011) have demonstrated lower ADC values in RCC than in oncocytomas.

### **Imaging Findings**

A 4-phase MDCT scan was indicated to characterize the lesion. A centrally located lesion with no intratumoral fat was identified on unenhanced phase (Fig. 1.33). The corticomedullary phase (not shown) and nephrographic phase demonstrated heterogeneous enhancement of the well-defined lesion with intracystic intratumoral areas (Fig. 1.34, open arrows) with washout and hypoattenuation in excretory phase (Fig. 1.35). Pathologic diagnosis obtained after nephrectomy was clear cell RCC, and the heterogeneity of the enhancement pattern correlated well with the presence of intratumoral cystic areas (Fig. 1.36).

### Case 10 Papillary Renal Cell Carcinoma



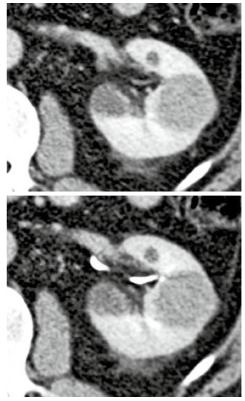


Fig. 1.38

Fig. 1.37



Fig. 1.39

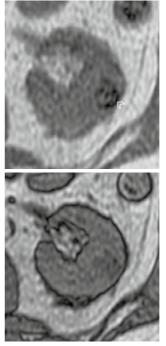


Fig. 1.40

A 54-year-old man was referred to the Radiology Department due to abdominal pain. An incidental solid renal mass was detected on US and an MR imaging was indicated to characterize it.

### In recent years, there has been an increase in the detection of renal cell carcinomas (RCC) due to the increasing use of imaging modalities for abdominal purposes. There are at least three major histological subtypes of RCC: clear cell RCC, accounting for 80% of the cases; papillary RCC, accounting for 10-15%; and chromophobe RCC accounting for 5%. Knowledge of the subtype before treatment is useful because survival and response to treatment are usually worse in clear cell RCC. Differentiation can be obtained using MDCT or MR imaging. The enhancement pattern is different depending on the RCC subtype. Clear cell RCCs enhance intensely and heterogeneously, in contrast to papillary and chromophobe RCCS that are hypovascular and enhance more homogeneously. In addition, clear cell RCC does not enhance more in the excretory phase than in the nephrographic phase, while some papillary RCCs may show continuous enhancement in the excretory phase. MR can provide additional information in the differentiation between clear cell carcinomas and non-clear (papillary and chromophobe) cell carcinomas. Clear cell RCCs usually have high signal on T2 and can have a drop of signal on opposite phase, reflecting the presence of intracellular fat. On the other hand, non-clear cell RCCs usually present with low signal on T2 with drop of signal on in phase sequences. In addition, using Diffusion-weighted imaging (DWI), clear cell and non-clear cell RCCs have different diffusion characteristics, with papillary RCC being the subtype with the lowest apparent diffusion coefficient (ADC) values. This fact can be justified by the high cellularity of the papillary RCC subtype. However, imaging modalities have serious difficulties in differentiating papillary RCCs from fat-poor angiomyolipoma, since very few angiomyolipomas show no fat using imaging modalities. The homogeneous and sometimes persistent enhancement pattern found in papillary RCC is also characteristic of fat-poor angiomyolipomas. Both tumors may show low signal on T1 and T2 MRI, with no drop of signal in opposite phase, and have low ADC values on DWI. However, very few studies with DWI of renal tumors have been performed, and further studies in larger patient populations are necessary to verify possible differences in the ADC values between papillary RCC and poor-fat angiomyolipomas.

### **Imaging Findings**

An incidental solid lesion was detected on baseline US (open arrow) (Fig. 1.37). An MDCT scan was indicated and a well-defined mass with homogeneous hypoattenuating enhancement in all the enhanced-phases was identified (Fig. 1.38, nephrographic and excretory phase) suggesting a non-clear RCC. No fat was detected inside the tumor. Typical features of non-clear RCC were also found on MRI with low signal on T2-weighted image (Fig. 1.39, arrow) and drop of signal on "in phase" sequence (Fig. 1.40, open arrowhead). Pathologic diagnosis obtained by laparoscopic partial nephrectomy was papillary RCC.

#### Comments

### **Further Reading**

### Books

- Dogra V (2004) Atlas of genitourinary radiology: the pathologic basis. Springer, Berlin/Heidelberg
- Guermazi A (2006) Imaging of kidney cancer. Springer, Heidelberg
- Hamm B (2008) Urogenital imaging. George Thieme Verlag, Stuttgart
- Quaia E (2010) Radiological imaging of the kidney. Springer, Heidelberg
- Zagoria RJ (2004) Genitourinary radiology: the requisites. Mosby, Philadelphia

### Web Links

http://www.auanet.org/content/guidelines-and-quality-care/ clinical-guidelines.cfm

http://emedicine.medscape.com/radiology

http://www.med-ed.virginia.edu/courses/rad/gu/index.html http://www.rsna.org/Education/archive/afip.cfm#genitourinary http://www.uroweb.org/guidelines/online-guidelines/

### Articles

- Axelrod DJ, Freeman H, Puvkin L, Guller J, Mitty HA (2004) Guide wire perforation leading to fatal perirenal hemorrhage from transcortical collaterals after renal artery stent placement. J Vasc Interv Radiol 15:985–987
- Aytekin C, Yildirim UM, Ozyer U, Hartman A, Boyvat F (2010) Emergency renal ablation for life-threatening hemorrhage from multiple capsular branches during renal artery bleeding. Cardiovasc Intervent Radiol 33:663–666
- Blondin D, Lanzman R, Schellhammer F et al (2010) Fibromuscular dysplasia in living renal donors: still a challenge to computed tomographic angiography. Eur J Radiol 75(1):67–71
- Browne RFJ, Zwrirewich C, Torreggiani WC (2004) Imaging of urinary tract infection in the adult. Eur Radiol 14:E168-E183
- Craig WD, Wagner BF, Travis MD (2008) From the archives of the AFIP. Pyelonephritis: radiologic pathologic review. Radiographics 28:255–276
- Correas JM, Claudon M, Tranquart F, Hélénon O (2006) The kidney: imaging with microbubble contrast agents. Ultrasound Q 22(1):53–66
- Demertzis J, Menias CO (2007) State of the art: imaging of renal infections. Emerg Radiol 14:13–22

- Dyer R, DiSantis DJ, McClennan BL (2008) Simplified imaging approach for evaluation of the solid renal mass in adults. Radiology 247(2):331-343
- Glodny B, Petersen J, Hofmann KJ, Schenk C, Herwig R, Trieb T, Koppelstaetter C, Steingruber I, Rehder P (2009) Kidney fusion anomalies revisited: clinical and radiological analysis of 209 cases of crossed fused ectopia and horseshoe kidney. BJU Int 103(2):224–235
- Israel GM, Bosniak MA (2008) Pitfalls in renal mass evaluation and how to avoid them. Radiographics 28(5):1325-1338
- Kawashima A, Sandler CM, Wasserman NF, LeRoy AJ, King BF Jr, Goldman SM (2004) Imaging of urethral disease: a pictorial review. Radiographics 24(Suppl 1):S195–S216
- Maturen KE, Nghiem HV, Caoili EM, Higgins EG, Wolf JS Jr, Wood DP Jr (2007) Renal mass core biopsy: accuracy and impact on clinical management. AJR Am J Roentgenol 188(2):563–570
- Mundy AR, Andrich DE (2011) Urethral strictures. BJU Int 107(1):6-26
- Nicolau C, Bunesch L, Sebastia C (2011) Renal complex cysts in adults: contrast-enhanced ultrasound. Abdom Imaging Jul 7 [Epub ahead of print]
- Sheth S, Ali S, Fishman E (2006) Imaging of renal lymphoma: patterns of disease with pathologic correlation. Radiographics 26:1151–1168
- Silverman SG, Mortele KJ, Tuncali K, Jinzaki M, Cibas ES (2007) Hyperattenuating renal masses: etiologies, pathogenesis and imaging evaluation. Radiographics 27:1131–1143
- Silverman SG, Israel GM, Herts BR, Richie JP (2008) Management of the incidental renal mass. Radiology 249(1):16-31
- Slovak DP, Olin JW (2004) Fibromuscular dysplasia. N Engl J Med 350:1862–1871
- Stunell H, Buckley O, Feeney J et al (2007) Imaging of acute pyelonephritis in the adult. Eur Radiol 17:180–1828
- Sun MR, Ngo L, Genega EM, Atkins MB, Finn ME, Rofsky NM, Pedrosa I (2009) Renal cell carcinoma: dynamic contrast-enhanced MR imaging for differentiation of tumor subtypes – correlation with pathologic findings. Radiology 250(3):793–802
- Taouli B, Thakur RK, Mannelli L, Babb JS, Kim S, Hecht EM, Lee VS, Israel GM (2009) Renal lesions: characterization with diffusion-weighted imaging versus contrast-enhanced MR imaging. Radiology 251(2):398–407
- Türkvatan A, Olçer T, Cumhur T (2009) Multidetector CT urography of renal fusion anomalies. Diagn Interv Radiol 15(2):127–134
- Urban BA, Fishman EK (2000) Renal lymphoma: CT patterns with emphasis on helical CT. Radiographics 20:197–212
- Yu NC, Raman SS, Patel M, Barbaric Z (2004) Fistulas of the genitourinary tract: a radiologic review. Radiographics 24(5):1331–1352

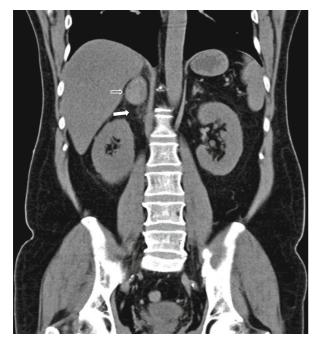
### Adrenal

### RAFAEL SALVADOR IZQUIERDO, BLANCA PAÑO BRUFAU, AND RAFAEL OLIVEIRA CAFAIA

### Contents

Case 1	Adrenal Hemorrhage	24
Case 2	Lipid-Rich Adenoma	26
Case 3	Lipid-Poor Adenoma	28
Case 4	Myelolipoma	30
Case 5	Adrenal Ganglioneuroma	32
Case 6	Pheochromocytoma	34
Case 7	Adrenal Metastases	36
Case 8	Adrenocortical Carcinoma	38
Case 9	Lymphoma	40
Case 10	Adrenocorticotropin-Independent Macronodular Adrenal Hyperplasia	42

Case 1 Adrenal Hemorrhage A 30-year-old patient who suffered a traffic accident presented to the emergency room with right upper quadrant pain.



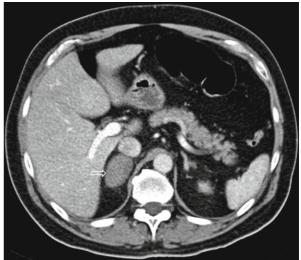
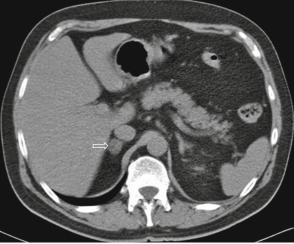


Fig. 2.2

Fig. 2.1



Fig. 2.3





#### Comments

The causes of adrenal hemorrhage can be classified as traumatic and nontraumatic. Direct trauma is the main cause of unilateral adrenal bleeding, more frequently right-sided. Adrenal hemorrhage is commonly associated with injuries of high severity. Right-sided hemorrhage is associated with liver, spleen, bilateral renal injuries, and pneumothorax; when hemorrhage involves the left adrenal, splenic, left kidney, and pneumothoracic injuries are the most common accompanying injuries. Periadrenal stranding is identified in most cases.

On the other hand, direct trauma is seldom the origin of bilateral adrenal hemorrhage. Nontraumatic hemorrhage of the gland in adults is uncommon and can be classified into four categories:

Stress (surgery, burns, sepsis, hypotension, etc.).

Hemorrhagic diathesis or coagulopathy (heparin-associated thrombocytopenia, antiphospolipid antibody syndrome, anticoagulation, use of steroids, etc.).

Underlying adrenal tumors (myelolipoma, pheochromocytoma, adrenocortical carcinoma). Idiopathic/spontaneous.

Potential causes of unilateral or bilateral hemorrhage are listed in Table 2.1

Table 2.1 Potential causes of unilateral or bilateral hemorrhage

Unilateral	Bilateral
Trauma/biopsy	Stress
Spontaneous (rule out tumor)	Hemorrhagic diathesis or coagulopathy
Tumor	Spontaneous

CT is the imaging modality of choice in patients with clinical suspicion of adrenal hemorrhage. Acute adrenal hemorrhage appears as enlarged adrenal gland with irregular margins but commonly retaining adreniform shape. However, sometimes the adrenal hemorrhage may present as an adrenal mass. At unenhanced CT, acute bleeding shows high attenuation (50–90 HU). No enhancement following IV contrast is observed. In doubtful cases, findings of decreased density and size at follow-up as well as the presence of calcifications may help confirm the diagnosis.

MR imaging is the most sensitive and specific modality for diagnosing adrenal hemorrhage. The appearance of adrenal hemorrhage on MRI depends on the progression of the bleeding. In the subacute phase, the hemorrhage shows high signal on T1-weighted sequences, secondary to the presence of methemoglobin. No postcontrast enhancement is observed in acute phase. During the chronic phase there is a ring of low signal on T2-weighted sequences, secondary to the presence of hemosiderin.

### **Imaging Findings**

in size. This lesion is hyperdense (49 HU) at unenhanced CT. Slight stranding of adjacent fat is observed (arrow). Axial enhanced CT at portal phase (Figs. 2.2 and 2.3) shows no significant enhancement of the right adrenal lesion following iv contrast (52 HU) (arrow). It is important to keep in mind that adrenal hemorrhage is commonly associated with other injuries, as in this case where it appears associated with a laceration of the liver dome (segment VII) (arrow). Axial unenhanced CT (Fig. 2.4) performed 6 months later shows that the lesion has decreased in size and is hypodense (arrow). Stranding is not observed in the adjacent fat.

Coronal/axial unenhanced CT (Figs. 2.1 and 2.2) shows right adrenal lesion (arrow) of 4 cm

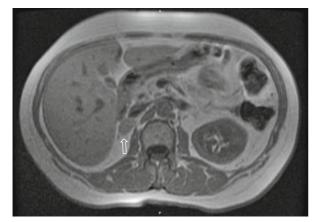


A 56-year-old female with a history of episodes of renal colic. An US was performed to detect urolithiasis, which showed an incidental finding of a right adrenal nodule.

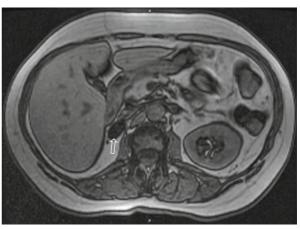




Fig. 2.6









# Comments

The adrenal adenomas are benign tumors of the adrenal cortex, commonly unilateral. The estimated prevalence in general population is approximately 6%, without significant differences between men and women. The prevalence of adrenal adenomas increases with increasing age. Approximately 85% are nonfunctioning and clinically inapparent, and 15% are functioning and may develop clinically apparent or subclinical hormone hyperproduction (frequently due to autonomous cortisol or aldosterone secretion, and less often due to sex hormone secretion). Therefore, all patients with an adrenal lesion should undergo a hormonal evaluation. On CT or MRI may present as small-sized homogeneous lesions (usually <4 cm in diameter) with smooth borders. Nevertheless, these are nonspecific characteristics, given that other malignant and benign adrenal lesions can present similar features.

In the presence of an incidentally discovered adrenal mass in patients not known to have cancer, the initial diagnostic hypothesis may be that of an adenoma. However, metastasis, lymphoma, carcinoma, pheochromocytoma, hemorrhage, adrenal hyperplasia, infectious diseases (tuberculosis, histoplasmosis, blastomicosis), neuroblastoma, ganglioneuroma, hemangioma, and hemangiosarcoma should be included in the differential diagnosis.

Seventy percent of adrenal adenomas have a high intracellular fat content (lipid-rich adenomas), detection of which is the cornerstone of establishing diagnosis with a high confidence. Nonenhanced CT is the mainstay of image diagnosis of lipid-rich adrenal adenomas due to its high sensitivity and specificity, low cost, and easy interpretation. An attenuation value  $\leq 10$  HU (Hounsfield units) is diagnostic of adrenal adenoma. If an incidental adrenal mass is detected on routine contrast-enhanced CT acquired in the dual-energy mode, it is possible to suppress the iodine signal, thus allowing density measurements of adrenal lesions on virtual nonenhanced imaging.

Chemical shift MRI is another technique that has a high diagnostic accuracy in the characterization of lipid-rich adenomas. It consists in acquiring T1-weighted gradientecho in-phase and opposed-phase sequences. The signal intensity loss in the lesion on opposed-phase images relative to the spleen (visual comparison) is indicative of the presence of intracytoplasmatic lipids.

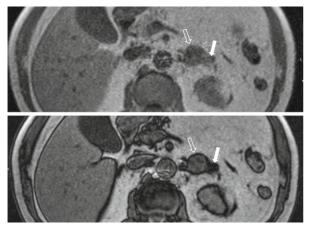
US (Fig. 2.5) demonstrates the presence of a well-delineated nodule in the right adrenal area (open arrow).

A nonenhanced CT (Fig. 2.6) is performed and shows a homogeneous low attenuation (3 HU) right adrenal nodule of 2.7 cm with smooth borders (open arrow). Based on these features, especially the low attenuation values, a diagnosis of lipid-rich adenoma can be established.

A MRI is also performed with T1-weighted gradient-echo in-phase (Fig. 2.7) and opposed-phase (Fig. 2.8) sequences. There is an evident signal intensity loss in the adrenal nodule (open arrows) on opposed-phase with regard to the in-phase images, which is indicative of the presence of intracytoplasmatic lipids and therefore is diagnostic of adenoma.

Case 3 Lipid-Poor Adenoma Comments A 67-year-old female who undergoes a lumbar spine MRI due to history of chronic low back pain, which showed an incidental finding of a left adrenal nodule. An abdominal MRI was performed, followed by a three-phase adrenal CT, as part of the diagnostic workup.

Approximately 30% of adrenal adenomas have a low intracellular fat content (lipid-poor adenomas). They have an unenhanced CT attenuation greater than 10 UH and therefore cannot be reliably differentiated from other adrenal lesions with this technique. Although some



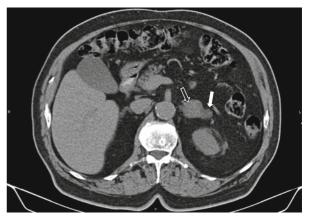
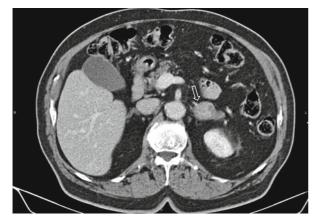
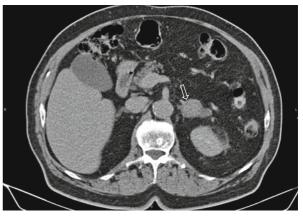


Fig. 2.9

Fig. 2.10









morphological features (small size, homogeneity, smooth contour) are suggestive of its benignity, other benign and malignant adrenal lesions can have similar features. The differential diagnosis must be established mainly with metastasis, carcinoma, pheochromocytoma, and lymphoma, which are lesions that could have an important impact on prognosis of patients. The clinical and biochemical parameters, as well as the previous history play an important role in the characterization of adrenal lesions with CT attenuation values greater than 10 HU at nonenhanced CT. Diagnosis of lipid-poor adenomas is a challenging task for radiologists. Chemical shift MRI technique is a useful technique for study of adrenal lesions with nonenhanced attenuation of 10–30 HU. It can be explained by the fact that, despite their high unenhanced CT attenuation, they have sufficient lipid content to allow their characterization. The signal intensity loss in the lesion on opposed-phase images relative to the spleen is indicative of the presence of intracytoplasmatic lipids and therefore is diagnostic of adenoma.

The dedicated adrenal CT protocol consists of an initial nonenhanced CT followed by enhanced CT at 60 s and 15 min after initiating the intravenous injection of the contrast material. It will permit calculation of absolute washout (or relative washout if nonenhanced CT images were not acquired initially):

Absolute Washout = (AC 60 sec - AC 15 min)/(AC 60 sec - AC nonenhanced) x 100

Relative Washout =  $(AC 60 \text{ sec} - AC 15 \text{ min})/(AC 60 \text{ sec}) \times 100$ 

\*AC = attenuation coefficient (HU)

Absolute washout values  $\geq 60\%$  (or relative washout values  $\geq 40\%$ ) has demonstrated high accuracy in diagnosis of adrenal adenoma, independently of its lipid content.

18F-FDG PET/CT has high sensitivity but lower specificity to differentiate between benign and malignant adrenal lesions, with a 5% false-positive rate.

A small percentage of these lesions will remain indeterminate despite the use of all available noninvasive diagnostic imaging techniques. Depending on patient's characteristics, imaging features as well as the level of suspicion, adrenalectomy, fine needle aspiration, or expectant management with serial biochemical and imaging follow-up should be recommended.

# **Imaging Findings**

An MRI with T1-weighted gradient-echo in-phase (Fig. 2.9a) and opposed-phase (Fig. 2.9b) sequences is performed. There is a 2.8 cm left adrenal nodule (open arrows) which does not show significant signal intensity loss on opposed-phase with regard to the in-phase images.

A three-phase abdominal CT with specific adrenal protocol is then performed, and demonstrates a well-delimited homogeneous left adrenal nodule (open arrows) with non-enhanced (Fig. 2.10) attenuation values of 24 HU. The enhanced images acquired at 60 s (Fig. 2.11) and 15 min (Fig. 2.12) show attenuation values of 86 and 44 HU, respectively. The absolute washout value is  $\geq$ 60% and therefore is diagnostic of lipid-poor adenoma.

A small left adrenal nodule can also be seen on CT and MRI (arrows). It has low attenuation values (-6 HU) on nonenhanced CT (Fig. 2.10) and shows signal intensity loss on opposed phase (Fig. 2.9), compatible with a lipid-rich adenoma.







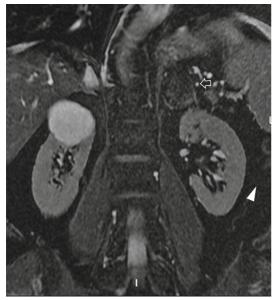






Fig. 2.14

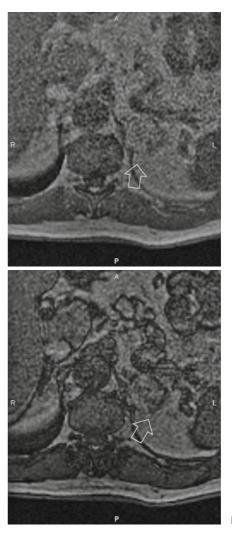


Fig. 2.16

A 61-year-old man, a heavy smoker, with an incidental adrenal finding on a chest CT scan. Follow-up of the adrenal lesion was performed with MR.

# Myelolipomas are rare benign nonfunctioning adrenal tumors present in 0.08-0.2% of autopsies. They are composed of a variable proportion of mature fat and bone marrow elements. There is no sexual predominance and, although typically unilateral, they can be multiple and bilateral. Punctate calcifications can be seen in 20% of cases. Myelolipoma is generally asymptomatic and usually detected as an incidental finding in cross-sectional imaging performed for other purposes. Rarely, patients may present with acute flank pain or hypovolemic shock secondary to spontaneous bleeding.

As with renal angiomyolipomas, confident diagnosis is achieved detecting the presence of fat in an adrenal mass. The suprarenal localization determines the differentiation with angiomyolipomas, and this is where multiplanar images of reconstructed multidetector CT or sagittal and coronal MRI sequences are most helpful.

On CT, fatty areas have attenuation values below -30 HU. Areas of bone marrow elements present as soft tissue densities within the lesion. The margins are well defined except when bleeding extends the lesion into the adjacent fat.

The fatty elements of myelolipomas behave as the retroperitoneal fat in the different MRI sequences, typically hyperintense in T1WI. Fat-suppressed images show signal intensity loss in fatty areas. No chemical-shift should be expected because fat in these lesions in the form of adipose tissue is not related to intracellular lipids as opposed to adrenal adenomas. Bone marrow elements have no characteristic signal intensity and may appear variable depending on its composition. Areas of hemorrhage vary its signal intensity depending on the time passed since bleeding.

Myelolipomas have no malignant potential. The clinical relevance of these lesions lies in the increased spontaneous bleeding risk with size, especially when larger than 10 cm.

# **Imaging Findings**

Comments

# Nonenhanced axial CT (Fig. 2.13) demonstrates the presence of a predominantly fat nodular lesion in the left adrenal gland (open arrow). The lesion has a punctate peripheral calcification (arrow). Figure 2.14: T2-weighted axial image at the same level as Fig. 2.13 shows internal signal intensity similar to the surrounding fat (open head arrow). T2-weigted coronal fat-suppressed MR image (Fig. 2.15) shows signal intensity drop of the fatty tissue from the lesion (open arrow), similar to the surrounding retroperitoneal fat (head arrow) compared to Fig. 2.12. In-phase (a) and out of phase (b) axial T1-weighted MR images (Fig. 2.16) depict no drop of signal in the fatty tissue of the angiomyolipoma as opposed to adenomas.

# Case 5 Adrenal Ganglioneuroma



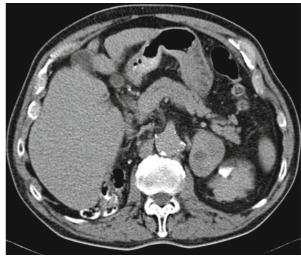
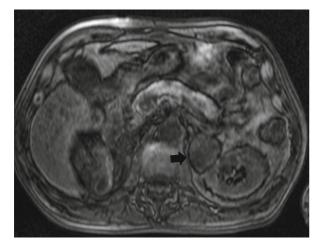
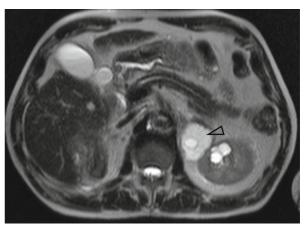


Fig. 2.17

Fig. 2.18









Imaging workup of a 71-year-old male with recurrent bladder tumor. No previous abdominal scan had been performed.

# Ganglioneuromas are uncommon neurogenic slow-growing tumors that may arise from any of the paravertebral sympathetic ganglia, occasionally from the adrenal medulla. Unlike ganglioblastomas and neuroblastomas – also neurogenic tumors derived from the sympathetic neurons of the neural crest – ganglioneuromas lack malignant potential and are therefore considered benign.

They are usually found in the posterior mediastinum or in the retroperitoneum, and 15–30% are adrenal.

A low percentage of cases are symptomatic due to catecholamine secretion or present as unspecific abdominal pain or palpable mass. Asymptomatic ganglioneuromas account for about half of the cases and are discovered incidentally in young adults with no sex predilection.

Adrenal ganglioneuromas appear on CT as a well-defined solid homogeneous mass. Size at diagnosis is generally over 5 cm. On nonenhanced CT they usually have low attenuation values and demonstrate a low or moderate enhancement after contrast administration. Calcifications can be present in approximately half of the cases.

On MR, they have low signal intensity on T1-weighted sequences and heterogeneous high signal intensity on T2-weighted sequences. Slow and late progressive enhancement can be seen with contrast, especially on delayed images.

A typical whorled appearance has been described for ganglioneuromas.

Ganglioneuroblastomas are similar tumors that unlike ganglioneuromas have immature tissue that is malignant or has malignant potential. They are less frequent and appear in childhood. The adrenal gland is the most common site of origin. They may present with abdominal pain and distension. As aggressive tumors, they may have irregular contours and invasion of adjacent organs but there are no typical imaging features on CT. Signal intensity on MR of ganglioneuroblastomas and neuroblastomas is similar to that of ganglioneuromas. Dynamic MR helps in the differential diagnosis as the formers have increased early enhancement unlike ganglioneuromas.

Final diagnosis is histological after surgical resection that is generally indicated because they are usually nonfunctional adrenal masses with size greater than 5 cm. Prognosis of completely resected mature adrenal ganglioneuromas is excellent.

# **Imaging Findings**

Arterial phase axial CECT (contrast enhanced) (Fig. 2.17) shows a homogeneous hypodense well-circumscribed left adrenal mass (open arrow). There is no enhancement in arterial phase. No calcifications are present in this case. Axial CECT on delayed phase (Fig. 2.18) demonstrates delayed enhancement, as compared to Fig. 2.17. Diffuse low signal intensity can be seen on precontrast axial T1-weighted image with fat saturation (Fig. 2.19, solid arrow). Delayed diffuse enhancement similar to CT was seen on postcontrast images (not shown). Axial T2-weighted image (Fig. 2.20) shows hyperintense signal intensity of the lesion (open head arrow).

### **Comments**

Case 6 Pheochromocytoma



Fig. 2.21

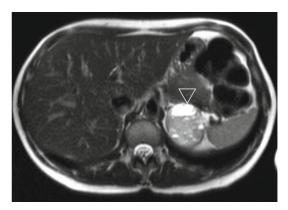


Fig. 2.22

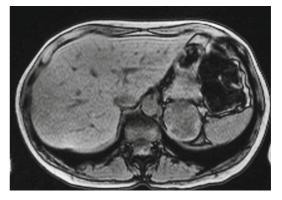
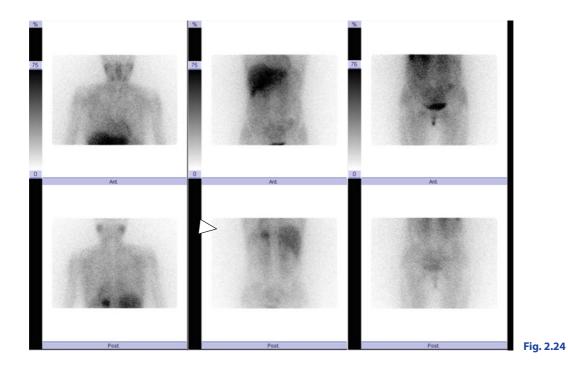


Fig. 2.23



A 38-year-old patient presented with a 3-year history of palpitations, sweating, hand tremor, and fatigue.

# Pheochromocytoma is a neuroendocrine tumor of the adrenal medulla that secretes catecholamines. These tumors are typically unilateral and benign, but may be bilateral and malignant in 10% of cases. Approximately 10% of pheochromocytomas are extraadrenal and are then called paragangliomas. The clinical diagnosis is suspected in a young patient with hypertension; however, it is important to know that phechromocytomas are the cause of hypertension in less than 1% of hypertensive patients. Laboratory tests for the evaluation of suspected pheochromocytoma include plasma catecholamine levels, 24-h urine vanilmandelic acid, and metanephrine levels (the sensitivity of these tests is >99% and specificity is 89%).

CT is the imaging modality of choice to confirm the diagnosis when clinical and laboratory tests suggest pheochromocytoma. Small pheochromocytomas usually appear as oval and well-defined lesions. Large lesions (>4–5 cm) are more likely to contain areas of necrosis or hemorrhage, as they are hypervascular tumors. Generally, pheochromocytomas contain no fat. However, in a small percentage of cases pheochromocytomas may have enough intracellular lipid content to present attenuation values <10 UH, which would make them indistinguishable from adenomas. Values of absolute washout and relative washout are similar to those of metastasis (<60% and <40%, respectively). Moreover, attenuation values in the portal phase tend to be higher than those of adenomas (up to 110-120 HU), although there is overlap. Heterogeneous enhancement of larger lesions is often observed making these pheochromocytomas indistinguishable from other adrenal lesions; therefore, biochemical correlation is required for diagnosis. In the clinical practice contrast administration is often avoided in case of high suspicion of pheochromocytoma as it might cause hypertensive crisis.

T2-weighted MRI sequences are more specific than CT because of the hyperintensity resulting from the presence of a cystic component. These tumors also manifest with moderate signal intensity on T2-weighted images. Pheochromocytomas rarely lose signal in out-of-phase (except for the rare cases of microscopic fat). After gadolinium administration, pheochromocytoma shows a marked and persistent enhancement.

# **Imaging Findings**

Coronal contrast enhanced CT arterial phase (Fig. 2.21) shows a left solid hypervascular adrenal mass with well-defined margins (open arrow) and small hypodense areas suggestive of areas of cystic change (arrow). The lesion does not contain fat or calcification. An MRI was also performed. Axial T2-weighted MRI sequences (Fig. 2.22) show a heterogeneous mass with areas of hyperintensity (open arrowhead) resulting from cystic component. No signal loss in out-of-phase sequences was seen (Fig. 2.23).I-131 MIBG scintigraphy (Fig. 2.24) demonstrates focal deposition of radiotracer in left suprarenal location (posterior) (open arrow), with no activity in other areas studied.

### **Comments**



A 77-year-old patient presented with a 5-year history of anorexia and weight loss. An abdominal CT study was performed.





Fig. 2.25

Fig. 2.26







Fig. 2.28

# Comments

Metastases are the most common malignant lesion involving the adrenal gland. Primary tumors that most often metastasize to the adrenal glands are the lung (40%), breast (20%), gastrointestinal tract, renal cell carcinoma, thyroid, and melanoma. Although adrenal metastases are frequent, we need to take into consideration that 50% of adrenal masses in oncologic patients are benign (mostly nonfunctioning adenomas). However, adrenal metastases in the absence of a known primary tumor (true incidentalomas) are rare. A rapid growth in 4–6 months, reduction in size following chemotherapy, or the appearance of new lesions is very suggestive of metastases. Metastases are usually bilateral but may also be unilateral.

It is important to emphasize that adrenal metastases have no characteristic imaging features. Larger lesions at CT imaging are accompanied by data that suggest malignancy such as ill-defined and nodular margins, heterogeneous attenuation, and a ring of enhancement or local invasion. They can also develop central necrosis. Calcifications are rare. The presence of concomitant metastases in other organs is unusual. Small metastases may resemble adenomas. Metastases show an absolute percentage enhancement washout of less than 60% and a relative percentage enhancement washout of less than 40%.

At MR imaging, adrenal metastases exhibit low signal intensity on T1-weighted images and high signal intensity on T2-weighted images, with progressive enhancement after administration of contrast material. The most important diagnostic feature is the lack of signal loss on out-of-phase images (in comparison with adrenal adenomas).

18F-FDG PET/CT has a sensitivity of 97% and a specificity of 91% for differentiating between benign and malignant lesions, and the qualitative analysis (visual comparison between the adrenal mass uptake and liver uptake) has better accuracy compared to the quantitative analysis. PET is a highly accurate technique to differentiate between malignant and benign adrenal disease for lesions >1 cm, especially in the setting of cancer patients, other imaging studies being usually unnecessary in this subgroup of patients. However, this technique has limitations: 9% rate of false positive, due to a variety of benign causes, and a 3% rate of false negatives due to hemorrhagic or necrotic metastases, small size (<10 mm), or derived from tumors of low metabolism (bronchioloalveolar carcinoma and carcinoid tumors). PET/CT is also a high-cost technique and of limited availability.

In those lesions that grow gradually, fine needle aspiration (FNA) can be used before deciding for surgery. In cancer patients with a high suspicion of metastatic disease, FNA is particularly indicated when the definite diagnosis may involve a change in the therapeutic management.

Coronal enhanced CT scans at nephrographic and excretory phase (Figs. 2.25 and 2.26) show left adrenal mass (open arrows) of 9 cm in size, with heterogeneous enhancement, irregular margins, and central necrosis (arrows). In addition, a small satellite lesion of 1 cm cranial to the mass is observed (open arrowheads). Moreover, a lytic lesion with soft tissue component in the right sacroiliac region is observed (arrowheads). Axial enhanced CT at nephrographic phase (Fig. 2.27) shows in the middle third of the right kidney an enhancing lesion measuring 3 cm suggestive of renal cell carcinoma (star). Axial contrast-enhanced CT image (Fig. 2.28), obtained with lung window settings, shows four round and small nodular lesions of diferent sizes in lower lobes, suggestive of metastasis (small arrows).

Case 8 Adrenocortical Carcinoma A 67-year-old male presented with an 18-month history of progressive right-sided flank pain/discomfort with weight loss, asthenia, and anorexia. A large mass was palpable in the right upper quadrant of the abdomen on physical examination. Biochemical and endocrine evaluation showed normal adrenal function.



Fig. 2.29



Fig. 2.30









# Comments

Adrenocortical carcinomas (ACC) are rare malignant tumors arising from the cortex of adrenal gland with an annual incidence of 0.5–2 patients/million population. Approximately 50% are functional, and Cushing's syndrome is the most frequent presentation. Up to 5% of all incidentally found adrenal masses are ACC, and its prevalence is related to the size (2% of tumors  $\leq$ 4 cm, 6% of tumors  $\geq$ 4 cm and  $\leq$ 6 cm, and 25% of tumors larger than 6 cm). Large-sized lesions have also worse prognosis, with a 5-year survival rate of less than 50%. At the time of diagnosis, 20–50% of patients have metastasis.

ACC presents characteristically as large heterogeneous masses in the suprarenal region, frequently displacing adjacent organs, with irregular, nodular, and poorly defined margins. Heterogeneous enhancement after intravenous administration of contrast material, mainly peripheral, is characteristic. On MRI, there may be an inhomogeneous predominantly low signal intensity on T1WI and high signal intensity on T2WI; and on CT, may show low attenuation areas with foci of high attenuation that correlate with necrosis and hemorrhage. Calcifications may be found in 20–30% of cases. The presence of these features as well as local invasion, distant metastasis, and lymphadenopathies are suggestive of ACC. In some cases, there may be tumor extension into the inferior vena cava via the adrenal veins, the identification of which is crucial for surgical planning.

Nevertheless, lesions <5 cm may be homogeneous, with smooth and well-delineated borders, without invasion of adjacent structures. Therefore, adenoma and small-sized metastases must be included in the differential diagnosis.

On chemical shift MRI, ACC do not exhibit signal loss on opposed-phase images because they generally do not contain intracellular fat.

ACC are fast-growing tumors and it is unusual that untreated malignant lesions do not increase in size over a period of 6 months. Therefore, the stability of tumor size on imaging follow-up may exclude the diagnosis of ACC.

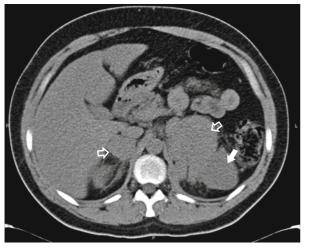
The definitive diagnosis is usually established by histology and immunohistology (core needle biopsy or excisional surgery).

A multiphasic abdominal MDCT is performed. Late arterial phase axial CT through the upper abdomen (Fig. 2.29) and oblique coronal MPR image from portal venous phase CT (Fig. 2.30) show a large hypervascularized right flank/upper quadrant abdominal mass which presents heterogeneous enhancement after intravenous administration of contrast material, mainly peripheral (open arrows), as well as a central area of necrosis (asterisks). The mass displaces the right kidney inferiorly and compresses the liver and inferior cava vein (arrow). There is a thin hypodense cleavage plane (open arrowheads) between the tumor and the liver, inferior cava vein and kidney, which excludes direct tumor invasion. Calcifications can be seen inside the tumor (arrowhead).

Oblique coronal thick-slice MIP image (Fig. 2.31) shows marked hypervascularization with thick neoformated arterial vessels (open arrows).

Coronal thin-slice MIP image (Fig. 2.32) shows compression of the inferior vena cava which is permeable (open arrows).





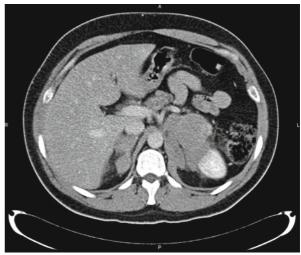


Fig. 2.33

Fig. 2.34



Fig. 2.35

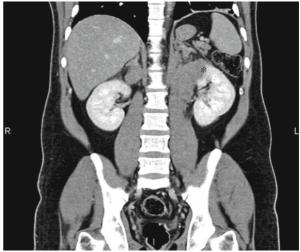


Fig. 2.36

A 31-year-old man with AIDS is evaluated for abdominal pain. A renal mass is seen on ultrasound and further characterization is performed with abdominal CT.

# Lymphomas are lymphoproliferative malignancies that are classified into Hodgkin and non-Hodgkin; the latter includes more than 30 types. Extranodal lymphoma refers to involvement of organs and tissues other than lymph nodes, thymus or, in non-Hodgkin lymphoma, also the spleen. Extranodal lymphoma is more common in non-Hodgkin lymphomas and in patients with recurrent disease or immunodeficiency-related diseases such as AIDS.

Although lymphoma of the adrenal gland is uncommon, in 4% of patients with non-Hodgkin lymphoma there is adrenal involvement. Primary adrenal lymphoma is extremely rare and most of adrenal lymphomas are secondary to extraadrenal non-Hodgkin lymphomas usually associated with retroperitoneal adenopathy. Diffuse B-cell type is the most common type of primary adrenal lymphoma.

They may replace normal gland and although they are usually clinically silent, they may present with adrenal insufficiency symptoms (Addison disease), especially when bilateral. Up to 50% of cases are bilateral, a percentage that rises to 70% in primary adrenal lymphomas.

On NECT, lymphomas normally appear as a big soft tissue mass, mainly hypodense with preserved adrenal shape. When large, they may appear heterogeneous or as a complex cystic mass due to central necrosis. Smaller lesions tend to be homogeneous and are difficult to differentiate from lipid-poor adenomas. Contrast enhancement is moderate being less than the renal cortex. Calcification is rare in the absence of treatment.

On MR, adrenal lymphomas have low signal intensity on T1-weighted images and a typical heterogeneous signal on T2 WI.

On US lymphomas appear as homogeneously hypoechoic lesions with echogenic areas within the mass.

The presence of concomitant multiple big retroperitoneal lymphadenopathy or ipsilateral renal involvement suggests diagnosis of adrenal lymphoma.

# Axial nonenhanced CT (Fig. 2.33) shows bilateral adrenal masses (open arrows). The left adrenal contacts widely with the upper pole of the kidney (solid arrow). On CECT (Fig. 2.34), mild homogeneous enhancement is seen in the adrenal masses, lower than kidney enhancement. Coronal CECT (Fig. 2.35) depicts associated retroperitoneal interaortocaval lymphadenopathy (open head arrow). The adrenal mass reached and encased the renal artery without infiltration (solid head arrow). On CECT (Fig. 2.36), the retroperitoneal adrenal mass infiltrates the left upper pole of the kidney (asterisk).

# **Comments**

Case 10 Adrenocorticotropin-Independent Macronodular Adrenal Hyperplasia A 53-year-old male was admitted to the emergency room and was diagnosed of a type B thoracic aorta dissection on the CT examination with bilateral adrenal nodules. Subsequent hormonal study showed increased cortisol in urine and low adrenocorticotropin (ACTH).



Fig. 2.37



Fig. 2.38

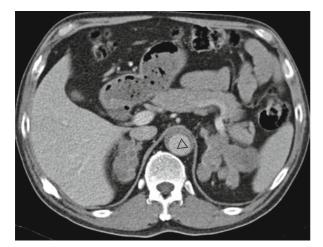


Fig. 2.39

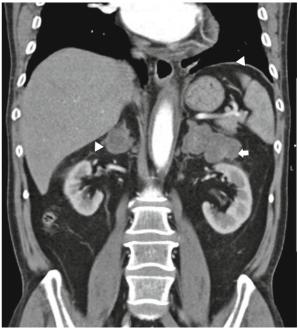


Fig. 2.40

## Comments

The most common cause of Cushing's syndrome is iatrogenic. Endogenous Cushing's syndrome is divided into ACTH-dependent and ACTH-independent forms. The latter is less common (around 20%) and always caused by primary adrenal disease.

ACTH-independent macronodular adrenal hyperplasia (AIMAH) is one of the causes of ACTH-independent Cushing's syndrome. Other causes include adrenal neoplasms (functional adenoma or carcinoma) that account for 95% of the cases, and primary pigmented nodular adrenocortical disease (PPNAD).

The pathogenesis of this disease still remains unclear and several hypotheses are under debate, including autonomous hypersecretion after chronic ACTH stimulation or secretion in response to other stimulating hormones other than ACTH.

AIMAH occurs in patients with a mean age older than those with ACTH-independent functional adenomas – around the fourth decade of life – and has a slight male predilection. Although a few familial cases have been reported, AIMAH is generally sporadic. Symptoms associated with this condition are hypertension, weight gain, and glucose intolerance or diabetes mellitus.

Normal adrenal glands have an inverted V or Y shape on axial CT imaging and normal limb thickness is <5 mm. Adrenal hyperplasia is defined by histopathological examination; however, large lesions may be characterized by imaging techniques. ACTH-dependent Cushing's syndrome adrenal hyperplasia appears as diffuse bilateral enlargement or nodular hyperplasia (micro or macronodular) with nodules generally <2 cm. PPNAD is usually seen as micronodular hyperplasia.

CT appearance of AIMAH is quite unique, showing massive bilateral adrenal hyperplasia with multiple nodules in the limbs that range from 1 to 5.5 cm, being larger than those of other diseases. Nodules, as in lipid-rich adenomas, are hypodense on unenhanced CT images. As CT imaging is characteristic, MR is not mandatory but can still be useful. On T1-weighted MRI sequences, nodules are seen as hypointense in relation to liver, slightly hyperintense on T2-weighted images and with a drop of signal on out-of-phase images. I-131-labeled adrenal scintigraphy shows increased bilateral uptake.

The nodules in PPNAD are hypointense on T2-weighted images, and nodules of hyperplasia on ACTH-dependent Cushing's syndrome tend to be isointense.

The treatment of choice is bilateral adrenalectomy that may be performed by laparoscopy.

### **Imaging Findings**

Nonenhanced axial CT image (Fig. 2.37) shows bilateral adrenal hyperplasia (open arrows) seen as multiple nodules, some >2 mm, along the adrenal limbs. Lipid-rich nodules are seen as hypodense nodules. Contrast-enhanced CT scan in arterial phase (Fig. 2.38) shows the aortic dissection (solid arrow). Mild enhancement, more evident at the periphery of the nodules is depicted (open arrow). Contrast-enhanced CT scan in venous phase (Fig. 2.39) depicts better the peripheral enhancement of the nodules. Coronal image (Fig. 2.40) demonstrates the characteristic macronodular hyperplasia of AIMAH (solid arrowhead).

# **Further Reading**

# Books

- Federle MP (2008) Expertddx: abdomen. Lippincott Williams & Wilkins, Salt Lake City
- Federle MP, Jeffrey JRB, Woodward PJ (2010) Diagnostic imaging:abdomen. Amirsys, Salt Lake City
- Lee JKT (2006) Computed body tomography with MRI correlation. Lippincott Williams & Wilkins, Philadelphia
- Ros PR, Mortele KJ (2007) CT and MRI of the abdomen and pelvis: a teaching file. Wolters Kluwer/Lippincott Williams & Wilkins, Philadelphia
- Zagoria RJ (2006) Genitourinary radiology: the requisites. Mosby, Philadelphia

# Webpages

http://www.annals.org

http://edips-download.myesr.org/

http://posterng.netkey.at/esr/online\_viewing/index. php?module=view\_search&task=search&searchFulltext=ad renal

http://www.rsna.org/Education/

www.uroweb.org

# Articles

- Blake MA, Cronin CG, Boland GW (2010a) Adrenal imaging. AJR Am J Roentgenol 194(6):1450–1460
- Blake MA, Prakash P, Cronin CG (2010b) PET/CT for adrenal assessment. AJR Am J Roentgenol 195(2):W91-W95
- Boland GW (2010) Adrenal imaging: why, when, what, and how? Part 1. Why and when to image? AJR Am J Roentgenol 195(6):W377-W381
- Boland GW, Blake MA, Hahn PF, Mayo-Smith WW (2008) Incidental adrenal lesions: principles, techniques, and algorithms for imaging characterization. Radiology 249(3):756–775
- Boland GW (2011a) Adrenal imaging: from Addison to algorithms. Radiol Clin North Am 49(3):511–528
- Boland GW (2011b) Adrenal imaging: why, when, what, and how? Part 2. What technique? AJR Am J Roentgenol 196(1): W1-W5
- Boland GW (2011c) Adrenal imaging: why, when, what, and how? Part 3. The algorithmic approach to definitive characterization of the adrenal incidentaloma. AJR Am J Roentgenol 196(2):W109–W111
- Boland GW, Dwamena BA, Jagtiani Sangwaiya M, Goehler AG, Blake MA, Hahn PF et al (2011) Characterization of adrenal masses by using FDG PET: a systematic review and metaanalysis of diagnostic test performance. Radiology 259(1): 117–126

- Caoili EM, Korobkin M, Francis IR, Cohan RH, Platt JF, Dunnick NR et al (2002) Adrenal masses: characterization with combined unenhanced and delayed enhanced CT. Radiology 222(3):629–633
- Elsayes KM, Mukundan G, Narra VR, Lewis JS Jr, Shirkhoda A, Farooki A et al (2004) Adrenal masses: mr imaging features with pathologic correlation. Radiographics 24(Suppl 1):S73–S86
- Guo YK, Yang ZG, Li Y, Deng YP, Ma ES, Min PQ et al (2007) Uncommon adrenal masses: CT and MRI features with histopathologic correlation. Eur J Radiol 62(3):359–370
- Johnson PT, Horton KM, Fishman EK (2009) Adrenal imaging with MDCT: nonneoplastic disease. AJR Am J Roentgenol 193(4):1128–1135
- Kenney PJ, Wagner BJ, Rao P, Heffess CS (1998) Myelolipoma: CT and pathologic features. Radiology 208(1):87–95
- Leite NP, Kased N, Hanna RF, Brown MA, Pereira JM, Cunha R et al (2007) Cross-sectional imaging of extranodal involvement in abdominopelvic lymphoproliferative malignancies. Radiographics 27(6):1613–1634
- Miller JC, Blake MA, Boland GW, Copeland PM, Thrall JH, Lee SI (2009a) Adrenal masses. J Am Coll Radiol 6(3):206–211
- Miller JC, Blake MA, Boland GW (2009b) Definitive characterisation of adrenal lesions. BMJ 338:a3092
- Miller FH, Wang Y, McCarthy RJ, Yaghmai V, Merrick L, Larson A et al (2010) Utility of diffusion-weighted MRI in characterization of adrenal lesions. AJR Am J Roentgenol 194(2): W179-W185
- NIH State-of-the-Science Statement on management of the clinically inapparent adrenal mass ("incidentaloma"). (2002) NIH Consens State Sci Statements. 19(2) 1–23.
- Pena CS, Boland GW, Hahn PF, Lee MJ, Mueller PR (2000) Characterization of indeterminate (lipid-poor) adrenal masses: use of washout characteristics at contrast-enhanced CT. Radiology 217(3):798-802
- Rockall AG, Babar SA, Sohaib SA, Isidori AM, Diaz-Cano S, Monson JP et al (2004) CT and MR imaging of the adrenal glands in ACTH-independent Cushing syndrome. Radiographics 24(2): 435-452
- Sahdev A, Reznek RH, Evanson J, Grossman AB (2007) Imaging in Cushing's syndrome. Arq Bras Endocrinol Metabol 51(8): 1319–1328
- Song JH, Mayo-Smith WW (2011) Incidentally discovered adrenal mass. Radiol Clin North Am 49(2):361–368
- Terzolo M, Stigliano A, Chiodini I, Loli P, Furlani L, Arnaldi G et al (2011) AME position statement on adrenal incidentaloma. Eur J Endocrinol 164(6):851–870
- Verma A, Mohan S, Gupta A (2008) ACTH-independent macronodular adrenal hyperplasia: imaging findings of a rare condition: a case report. Abdom Imaging 33(2):225–229
- Wong KK, Arabi M, Bou-Assaly W, Marzola MC, Rubello D, Gross MD (2011) Evaluation of incidentally discovered adrenal masses with PET and PET/CT. Eur J Radiol Feb 3. [Epub ahead of print]

# Urinary Bladder, Collecting System, and Urethra 3

Carmen Sebastià, Laura Buñesch, and Carlos Nicolau

# Contents

Case 1	Urothelial Carcinoma of the Renal Pelvis	46
Case 2	Urogenital Tuberculosis	48
Case 3	Ureteropelvic Junction Obstruction	50
Case 4	Uric Acid Urolithiasis	52
Case 5	Bladder Leiomyoma	54
Case 6	Urachal Tumor	56
Case 7	Extraperitoneal Bladder Rupture	58
Case 8	Bladder Cancer	60
Case 9	Complicated Urethritis	62
Case 10	Urethral Cancer	64

# Case 1 Urothelial Carcinoma of the Renal Pelvis



Fig. 3.1







Fig. 3.2

A 51-year-old woman heavy smoker presented with macroscopic hematuria. A CT-urography and cystoscopy were performed. A mass in the right renal pelvis was found and a nephroureterectomy was performed.

Urothelial carcinoma of the upper urinary tract is relatively uncommon. Excretory urography (EU) detection rates for this condition range from only 50% to 60%. CT urography demonstrates a high sensitivity (94–96%) for detecting upper tract uroepithelial malignancies. Two different CT patterns of urothelial carcinomas have been described: pelvicalyceal and ureteral masses and pelvicalyceal and ureteral wall thickening.

Pelvicalyceal and ureteral carcinomas present as a soft tissue mass in unenhanced CT that enhance after IV contrast administration and have irregular internal margin, as in the present case. Differential diagnosis with blood clots, papillae, and fungus ball is required because these masses do not enhance after intravenous contrast administration. Differential diagnosis with benign enhancing masses can only be done by biopsy (nephrogenic adenoma, fibroepithelial polyp, malacoplakia, and inflammatory pseudotumor).

Pelvicalyceal and ureteral wall thickening can have either benign or malignant appearances according to the signs described in the recent literature:

- Pelvicalyceal and ureteral stenosis with low density, smooth, and long mural thickening are suspicious of benign cause. Edema, inflammation, infection, and fibrosis can present with these features.
- Pelvicalyceal or ureteral soft-tissue density, short and irregular internal mural thickening are suspicious of malignancy, mainly urothelial carcinoma.

Unenhanced axial CT scan (Fig. 3.1) shows a soft-tissue density mass in the renal pelvis (*open arrow*). Contrast-enhanced axial CT (Fig. 3.2) depicts enhancement of this mass (30 HU). CT in the excretory phase (CT urography) (Fig. 3.3) demonstrates an anterior mural pelvic mass with internal irregular margin (*arrows*). Pathologic specimen depicted a low-grade papillary urothelial carcinoma of the right renal pelvis.

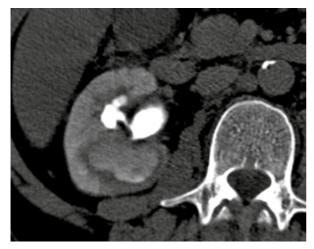
# **Comments**

# Case 2 Urogenital Tuberculosis

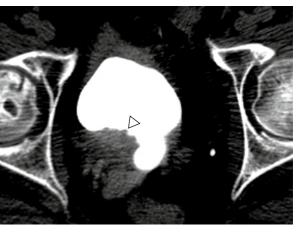




Fig. 3.4









A 43-year-old man with AIDS receiving antiretroviral therapy presented to the hospital with a 3-month history of fever, right lumbar pain, and dysuria. Urine culture was positive for *Mycobacterium tuberculosis*. An abdominal CT was performed.

# Comments

Urinary tract tuberculosis (tbc) occurs in 8-15% of patients with pulmonary tuberculosis. It has an insidious onset with urinary symptoms developing in advanced disease. AIDS infection increases the risk of bacillemia and extrapulmonary tuberculosis. In fact, twothirds of patients with urogenital tuberculosis had concomitant AIDS. Sterile leukocyturia and hematuria are suggestive of urogenital tuberculosis. When tuberculosis bacilli reach the kidney, granulomas form and remain indolent for many years; these kidney granulomas are depicted as renal abscess or masses. If reactivation occurs the infection spreads into the medulla, involving the papillae and the collecting system. Renal tuberculosis manifests by a dilated calyx and attenuated papillae; infundibular stricture formation may result in focal nonexcretion ("phantom calyx" formation). Calcification is present in a large number of cases presenting as thin rims surrounding cavities or diffuse uniformly radiodense cavities called autohephrectomy in late-stage disease. Ureteral smooth long thickening and mural bladder thickening with perivesical fat stranding can be seen in the acute phase that turns into ureteral stenosis and reduction of bladder capacity and pyeloureteral reflux if the process chronifies. The findings of multiple stenoses of the collecting system or simultaneous involvement of kidneys and bladder are highly suggestive of tbc. Differential diagnosis with other systemic bacterial infections and AIDS-related lymphoma must be done. In cases of relapse and medical resistance nephrectomy is recommended.

CT images depict persistent parenchymal contrast enhancement and dilated calyx secondary to infundibular stenosis (Figs. 3.4 and 3.5, *open arrow*) and diffuse ureteral low enhancement and smooth mural thickening consistent with acute infection (Fig. 3.6, *arrows*). Ureteral meatus edema and bladder wall thickening is also seen (Figs. 3.6 and 3.7, *open arrowheads*). All these signs are very specific of acute tuberculosis infection.

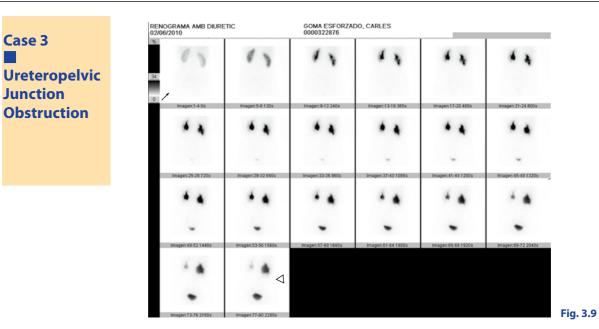
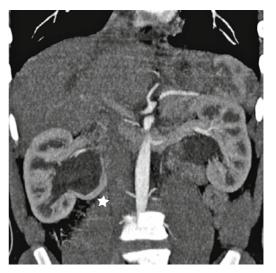




Fig. 3.8



Fig. 3.10





A 13-year-old boy presented with right lumbar pain. An ultrasound examination was initially performed.

Ureteropelvic junction obstruction (UPJO) is defined as an impairment of the flow of urine from the renal pelvis into the proximal ureter. Primary UPJO occurs in the absence of a history of infection, stones, surgery, or ischemia (which are the main causes of secondary UPJO). Various intrinsic and extrinsic conditions have been proposed as causes of primary UPJO, the most commonly accepted being the presence of an aperistaltic segment of the ureter or the pelvis and true congenital ureteral strictures (intrinsic), and fixed angulations, bands of tissue, high insertion of the ureter on the renal pelvis, and crossing vessels (extrinsic).

The finding of a dilated renal pelvis with a ureter of normal diameter is the key for the diagnosis on imaging examinations. Differential diagnosis must be made with nonobstructive extrarenal pelvis, which shows a less abrupt transition between the dilated pelvis and the ureter.

Imaging evaluation of UPJO must include the determination of the degree of renal obstruction, the assessment of renal function, the identification of the cause of the problem, and the description of renal and perirenal anatomic variants that can influence the surgical technique. The presence of crossing vessels as cause of the stenosis is also an independent factor that worsens the prognosis.

Crossing vessels are arteries or veins that cross the ureteropelvic junction area and may cause UPJO. Imaging studies can suggest the causative role of a determined vessel, depending on its precise anatomic relationship with the ureteropelvic junction, and its site of origin (origins close to the aorta are more frequently associated with UPJO).

Computed tomography (CT), magnetic resonance (MR), contrast-enhanced color Doppler imaging (CE-CDI), digital substraction angiography (DSA), and endoluminal ultrasound have been proposed as methods for the detection of crossing vessels.

CT examinations must be performed on a multidetector CT scanner since it offers isotropic or near isotropic row datasets that provide optimal imaging of the renal hilar anatomy. Most UPJO CT protocols include arterial and venous (nephrographic) phase contrast-enhanced imaging that demonstrate arterial anatomy and asymmetries in cortical perfusion, as well as venous anatomy and asymmetries in tubular excretion, respectively.

Multiplanar reformats (MPR) are mandatory for the adequate evaluation of anatomical relationships.

# **Imaging Findings**

Figure 3.8: Longitudinal ultrasound scan of the kidney shows moderate pelvicaliceal dilation of extrarenal predominance (*open arrow*). Figure 3.9: Sequential images of 99mTC-MAG3 scintigraphy show mild delayed enhancement of the right kidney (*arrow*) and pelvic obstruction (*open arrowhead*). Figure 3.10: Curved MPR of arterial phase contrast-enhanced CT shows an inferior accessory artery (*arrowhead*) running anterior to the dilated pelvis (*open arrow*). Note also the symmetry in renal perfusion. Figure 3.11: Curved MPR of venous phase contrast-enhanced CT scan shows an inferior accessory vein (asterisk) running parallel to the accessory artery.

### **Comments**

# Case 4 Uric Acid Urolithiasis



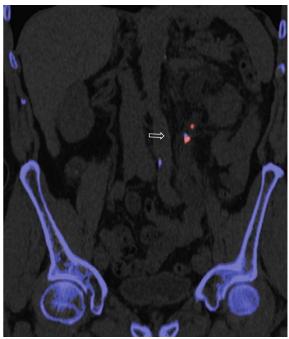
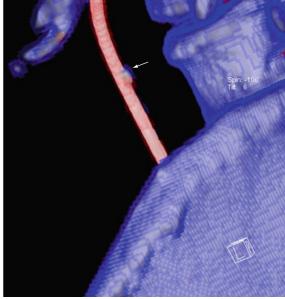


Fig. 3.12

Fig. 3.13









A 75-year-old man complained of noncomplicated nephritic colic for 15 days. No lithiasis was visible on the abdominal X-ray. Dual-energy multidetector CT (MDCT) was performed. Dilatation of left upper urinary tract due to uric acid lithiasis was diagnosed. A control Dual-energy MDCT was repeated after completion of alkaline treatment.

### Comments

The prevalence of urinary calculus disease has risen over the past few decades. The main determinants in the clinical care of patients with urolithiasis are the location, size, and chemical composition of calculi, as well as the presence of anatomic and functional anomalies in the upper urinary tract. MDCT has a high diagnostic accuracy in the detection of urolithiasis approaching 100%. Dual-energy CT technology provides improved diagnostic characterization of materials. One of the most important applications of dual-energy CT is the differentiation between uric acid versus nonuric acid lithiasis. More advanced spectral dual-energy CT postprocessing techniques would be used in the future to characterize at least five different stone compositions. On the basis of treatment, urinary stones can be classified into three main groups:

- Uric acid stones, which can be treated medically (alkaline treatment).
- Stones that can be easily fragmented by extracorporeal shock-wave lithotripsy (ESWL) struvite, calcium oxalate dihydrate, and carbapatite
- Stones resistant to ESWL, requiring endourological management cystine, calcium oxalate monohydrate, and brushite

# **Imaging Findings**

Unenhanced axial CT image shows dilatation of left renal pelvis (Fig. 3.12). Dual energy-CT postprocessed images demonstrate two lithiasis characterization with mostly uric acid composition. Uric acid lithiasis are represented in pink (note a small nonuric acid part in the big lower stone represented in blue) (Fig. 3.13, *openarrow*). Axial unenhanced CT and postprocessed VR images after alkaline treatment demonstrate a small nonuric acid ureteral stone that has not responded to alkaline treatment (Figs. 3.14 and 3.15, *arrows*). Note the left ureteral catheter.

# Case 5 Bladder Leiomyoma

# Comments

A 52-year-old man with constitutional syndrome presented with a juxtavesical nodule incidentally identified on abdominal computed tomography (CT) performed as part of the diagnostic workup.

Leiomyomas are noninfiltrative smooth muscle tumors with no mitotic activity, cellular atypia, or necrosis. The typical location of these benign mesenchymal neoplasms is the uterus (they can be found in 20–30% of women older than 35 years), but they may arise in almost any anatomic site. Their most frequent location in the urinary system is the renal capsule. Bladder leiomyomas are uncommon (only 0.4% of all bladder tumors) but they represent the most frequent benign soft tissue vesical neoplasm.

Typical leiomyomas are well-defined and homogeneous solid nodules ranging from a few millimetres to as much as 30 cm in size. On magnetic resonance (MR)







Fig. 3.17

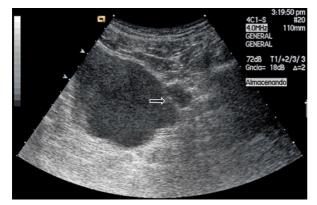




Fig. 3.18

Fig. 3.19

examinations, they show an intermediate signal intensity on T1-weighted images and a characteristic and highly specific low signal intensity on T2-weighted images. Degenerated leiomyomas may be markedly heterogeneous, with cystic areas or calcifications.

Bladder leiomyomas are usually small. They arise in the submucosa, but may show an intravesical, intramural, or extravesical growth. Intramural and extravesical leiomyomas are usually asymptomatic and found, as in the case presented here, incidentally. Intravesical leiomyomas may cause hematuria or irritative urinary symptoms, or even outflow obstruction when they are large or pedunculated.

Intravesical leiomyomas must be preoperatively distinguished from urothelial carcinomas to prevent unnecessary radical surgery. At radiological examinations, their smooth surface and the visualization of an intact mucosal layer help in the differentiation (carcinomas typically show a much more irregular surface and arise in the mucosa). On cystoscopy, a preserved mucosa is found.

Localized neurofibromas, paragangliomas, hemangiomas, lymphomas, or even nonneoplastic lesions like bladder endometriosis may be difficult to distinguish from bladder intramural leiomyomas on ultrasound or on computed tomography. Paragangliomas and hemangiomas typically show a higher contrast uptake and paragangliomas might present a highly specific ring calcification around their circumference. Primary vesical lymphomas are extremely rare, extravesical findings usually suggest the diagnosis in secondary lesions. Extravesical leiomyomas must be differentiated from nonvesical lesions, mainly adnexal nodules, or even lymphadenopathies.

MR characteristic features of typical leiomyomas usually suggest the correct diagnosis, but a histopathologic analysis is necessary for confirmation, especially because leiomyosarcomas and degenerated leiomyomas might have a similar appearance on MR images. The transurethral approach is best in intravesical lesions. It is mandatory to have a good evidence of the location of the nodule during the process, since leiomyoma biopsy samples may be identical to muscle samples of the bladder wall. A laparoscopic, or in some cases even percutaneous, approach is recommended when the nodule cannot be correctly depicted on cystoscopy (extravesical and some intramural nodules).

Treatment has traditionally involved resection, with the surgical approach depending on tumor size and location at the bladder wall. As no malignant transformation has been described in partially resected nodules and the accuracy of the histopathologic analysis is extremely high, a new acceptable approach is the conservative management in small asymptomatic lesions.

# **Imaging Findings**

Figure 3.16: Axial contrast-enhanced CT scan shows a well-circumscribed and homogeneous nodule at the left lateral wall of the bladder (*open arrow*). Figure 3.17: The same lesion is shown on this coronal contrast-enhanced CT scan (*open arrow*). Multiplanar reformats help define the relationship between the lesion and the bladder wall or extravesical structures. Figure 3.18: Ultrasound scan of the same nodule (*open arrow*). The preserved mucosa can be better identified with this technique. Figure 3.19: Enhanced ultrasound 31 s after the injection of the contrast agent shows homogeneous enhancement of the lesion (*open arrow*).

A 39-year-old woman presented with a 4-month history of gross hematuria.

# Case 6 Urachal Tumor

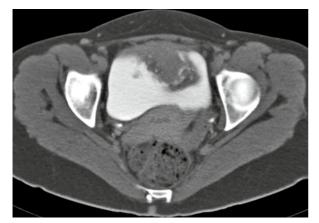
**Comments** 

The urachus, also called median umbilical ligament, is a midline tubular structure that extends from the anterior bladder dome to the umbilicus, lying between the transverse fascia and the parietal peritoneum, in the preperitoneal perivesical space (the extraperitoneal space of Retzius). It is a vestigial remnant of the embryonic precursor of the bladder that in most fetuses involutes to a fibrous band before birth. In some subjects, however, the thin duct remains completely or partially patent.

Malignant urachal neoplasms usually arise from patent remnants in the juxtavesical portion of the urachus (90%) and grow cranially toward the umbilicus and caudally through the bladder wall. Even though the urachus is, like the bladder, lined by transitional epithelium, the majority of urachal carcinomas are adenocarcinomas (90%), probably representing a malignant transformation of columnar metaplasia. Urachal adenocarcinomas account for less than 0.5% of all bladder malignant neoplasms.



Fig. 3.20



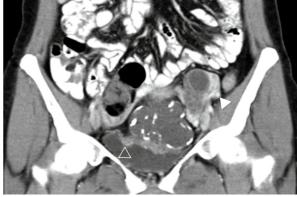


Fig. 3.21

Fig. 3.22

Urachal tumors tend to be clinically silent because of their extraperitoneal growth. Patients usually present when the bladder dome has already been infiltrated, commonly with hematuria, and sometimes with irritative bladder symptoms. The late presentation of symptoms leads to advanced disease at diagnosis and poor prognosis.

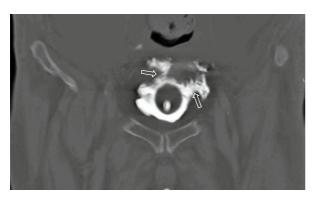
Up to 75% of urachal adenocarcinomas produce mucin. This explains the complex cystic and solid appearance of most of them on computarized tomography (CT) and magnetic resonance (MR). There may be discrepancy between CT and ultrasonography (US) appearances because cystic areas within the tumor containing low-density mucin, sometimes show high echogenicity. As mucinous adenocarcinomas elsewhere, urachal tumors may contain psammomatous calcifications that can be easily depicted on CT and US images (50–70% of cases). Coronal and sagittal reformats/sequences are especially useful to identify the characteristic location of the mass and to evaluate the macroscopic infiltration of the bladder dome, which can be difficult to depict on axial images.

The finding of a midline mass anterosuperior to the bladder dome, with cystic areas and calcification, is highly suggestive of urachal adenocarcinoma. The infection of an urachal remnant may be difficult to distinguish from carcinoma; calcification, mural nodularity, and clinical context usually lead to the correct diagnosis, and a percutaneous needle biopsy can be performed in doubtful cases. Squamous cell carcinomas of the bladder may show a significant extravesical growth, but the characteristic location and growth of urachal tumors in the Retzius space is usually enough for differentiating both neoplasms. Bladder adenocarcinoma might be histologically identical to urachal carcinoma, again extravesical growth of urachal tumors is the best clue for the diagnosis. Differentiation between a vesical and urachal origin of the tumor is important as a complete resection of the duct is recommended for the latter.

Urachal tumors usually have a highly invasive behavior; it is thus difficult for imaging techniques to accurately depict the microscopic extension of the neoplasms to the bladder wall or surrounding fat. A significant number of patients present with local invasion or metastatic disease. This fact makes a chest and abdominal CT in the preoperative workup advisable. Spread into pelvic lymph nodes is common; the organs most frequently infiltrated in distal extension are the omentum, lung, liver, and bone.

Figure 3.20: Axial contrast-enhanced CT scan at a level immediately cranial to the bladder dome shows a ventral midline mass (*open arrow*), predominantly cystic, with multiple calcifications and parietal nodules. Note the displacement of the anterior parietal peritoneum suggesting a preperitoneal location (*arrow*). Figure 3.21: Excretory-phase axial CT image at the level of the bladder dome suggests vesical invasion. The exact extent of the infiltration is difficult to define due to volume averaging effect. Figure 3.22: Coronal images allow a better depiction of the parietal infiltration of the bladder (*open arrowhead*). Note the high density of the vesical component of the tumor, in contrast with the cystic attenuation of the extravesical component. The left normal ovary can be identified (*arrowhead*).

# Case 7 Extraperitoneal Bladder Rupture





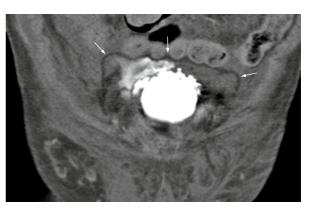


Fig. 3.24



Fig. 3.25





A 76-year-old man complained of severe pelvic pain after Transurethral resection for bladder tumor. On suspicion of bladder rupture, a CT-cystography was performed.

# Bladder rupture is an uncommon injury, occurring in 10% of patients with pelvic fractures. However, 83% of patients with bladder rupture have a pelvic fracture. Bladder injuries can be categorized into several types: contusion, extraperitoneal rupture with leakage of urine limited to the perivesical space, or intraperitoneal rupture, in which the peritoneal surface has been disrupted, with concomitant urinary extravasation. Extraperitoneal bladder rupture is more common, with an 80–90% frequency rate; combined rupture occurs in 12% of cases. The most common signs and symptoms are gross hematuria (82%) and abdominal tenderness (62%). CT-cystography has replaced retrograde cystography for bladder rupture diagnosis in most trauma centers with a sensitivity and specificity of 100%. Adequate distension of the urinary bladder is crucial to demonstrate perforation and this is achieved by instillation of at least 350 mL of dilute (4–5%) contrast medium. The coronal plane is extremely useful for detection of bladder rupture and images in this plane are particularly appealing to surgeons because the orientation of structures is analogous to that encountered during an exploratory laparotomy. Contusion and extraperitoneal rupture can be managed

Figures 3.23 and 3.24: Coronal CT cystograms show two sites of bladder rupture, at the right and left lateral walls (*open arrows*), into the extraperitoneal pelvic space. Note the peritoneal pelvic reflections (*arrows*). Coronal and axial CT images (Figs. 3.25 and 3.26) demonstrate bilateral extension of the urinoma into the infrarenal and perirenal spaces.

safely by catheter drainage alone. Intraperitoneal rupture should always be managed by surgical exploration. All bladder perforations resulting from penetrating trauma should

undergo emergency exploration and repair.

# Comments

# Case 8 Bladder Cancer



Fig. 3.27



Fig. 3.28

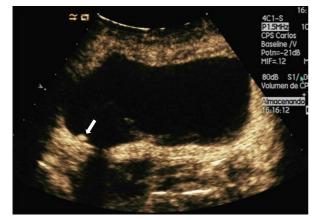


Fig. 3.29



Fig. 3.30

A 56-year-old man with a history of recurrent noninvasive bladder cancer presented to the Emergency Department with acute hematuria. An emergency cystoscopy was indicated but the results were nonconclusive due to the presence of intravesical blood clots that hampered proper visualization of the bladder walls. Thus, an ultrasound (US) study was required.

### Comments

Bladder cancer is one of the most common causes of acute hematuria of the low urinary tract. The current diagnostic standard method is cystourethroscopy, but it has significant limitations: it is invasive, expensive, and uncomfortable for the patients. In addition, cystourethroscopy misses a significant number of tumors during the acute period because of poor visualization of the bladder wall due to acute bleeding and presence of intravesical blood clots. On the other hand, transabdominal US is a noninvasive, inexpensive, and comfortable imaging technique frequently used to rule out the presence of bladder cancer. Bladder tumors <0.5 cm in size and those located in the bladder neck or in the dome are difficult to detect. In spite of its poor sensitivity to detect small bladder tumors, transabdominal US is the first-line imaging modality in patients with acute hematuria in many centers since it may detect urolithiasis or dilation of the urinary tract secondary to urolithiasis, and it has a very high positive predictive value for the detection of bladder cancer. Thus, if a bladder tumor is identified by US, the patient may be referred directly for transurethral resection of the bladder avoiding the necessity of more expensive imaging techniques to achieve a diagnosis. A recent additional tool is the administration of an intravenous contrast agent to improve US evaluation of the bladder. This modality allows real-time evaluation of the microvascularization of the bladder wall and of possible tumors. Contrast-enhanced US is especially helpful in the differentiation between blood clots within the bladder and bladder cancer in patients with acute hematuria. The differential diagnosis can be challenging using conventional US because the features of blood clots can mimic tumors if the clots adhere to the bladder wall or occupy most of the bladder lumen. In these cases, the use of a contrast agent allows the detection of tumor neovascularization that is one of the keys to diagnose bladder cancer using imaging modalities. On the contrary, bladder clots do not show enhancement because of their lack of vascularity.

# **Imaging Findings**

Baseline US study of the bladder (Figs. 3.27 and 3.28) reveal diffuse thickening of the posterior bladder wall with the presence of an intravesical mass compatible with a bladder clot (*open arrows*). However, this lesion could not be differentiated from bladder cancer because it was partially adhered to the thickened posterior bladder wall. The administration of a US contrast agent (Figs. 3.29 and 3.30) helped to confirm that the majority of the mass did not show enhancement, thus, corresponding to a blood clot. However, a small hypervascular lesion (*arrow*) compatible with bladder cancer was detected at the posterolateral right aspect of the bladder wall. Both findings were confirmed by cystoscopy and histology of the mass obtained by resection.

# Case 9 Complicated Urethritis



Fig. 3.31



Fig. 3.32

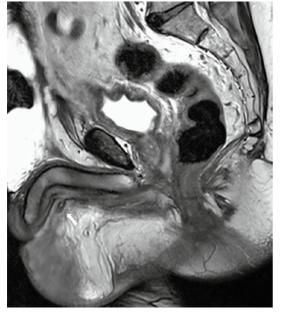


Fig. 3.33





**Comments** 

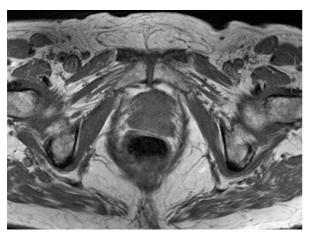
A 34-year-old man with a history of recurrent urethritis was referred to our Department complaining of penile-scrotal swelling immediately after urination accompanied by fever and local pain.

#### Urethral infection usually secondary to Neisseria gonorrhoeae is one of the most common causes of urethral disease in men. The acute infection usually affects the anterior urethra and, if not treated correctly, the infection may progress to the posterior urethra, prostate, seminal vesicles, and epididymis. Imaging modalities are indicated only when treatment has not been effective. The imaging techniques most commonly used to evaluate the ure thra are ultrasonography (US) and conventional fluoroscopic ure thrography (retrograde urethrography and voiding cystourethrography) because of their cost and availability. In complicated urethritis, imaging findings include the presence of irregularity of the urethral lumen and urethral strictures. These strictures are usually located in the anterior urethra and especially in the bulbar segment due to its anatomical position, but they can be multiple and also affect the posterior urethra. In severe cases, the presence of periurethral abscesses and fistulas that connect the urethra with periurethral soft tissues and neighboring organs are common. When periurethral extension is suspected, further imaging studies such as CT-urography and MR imaging are recommended due to the limitations of urethrography in the evaluation of periurethral tissues. Both CT-urography and MR imaging have multiplanar capability and high spatial resolution, and have demonstrated better accuracy than conventional urethrography in the characterization of urethral strictures and periurethral involvement. However, MR imaging has the advantage of absence of ionizing radiation. T2-weighted images and contrast-enhanced sequences are very useful to evaluate the inflammatory changes around the urethra, the presence of periurethral abscesses and fistulas, and the extension of the disease. Thickening of the urethra with diffuse periurethral intermediate signal intensity on T2-weighted images that enhances after the administration of Gadolinium is usually seen. In some cases, periurethral abscesses can be detected as well-defined collections with peripheral rim-like enhancement. In addition, periurethral fistulous tracts can be found connecting the urethra to the perineum or other organs including the vagina and rectum. Other common causes of periurethral fistulas are penile trauma, pelvic surgery, and unsuccessful attempt at bladder catheterization. These fistulas can also benefit from the evaluation with CT-urography or MR imaging.

#### **Imaging Findings**

Retrograde urethrography (Fig. 3.31) demonstrates a curvilinear collection of contrast material (*open arrow*) that extended from the penile urethra, a finding that is compatible with a urethral fistula. Voiding cystouretrography (Fig. 3.32) confirms the penile urethral fistula. Sagittal T2-weighted MR image of the pelvis (Fig. 3.33) reveals diffuse thickening of the urethra and periurethral tissues with a fistulous tract (*arrow*). Contrast-enhanced axial T1-weighted MR image (Fig. 3.34) shows inflammatory periurethral infiltration with loss of surrounding fat planes and a left fistulous tract (*arrow*) from the urethra to periurethral soft tissues.

Case 10 Urethral Cancer



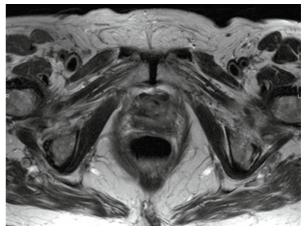
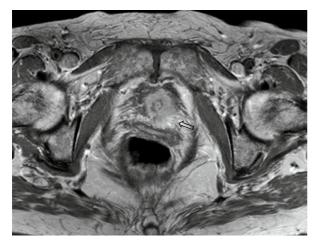
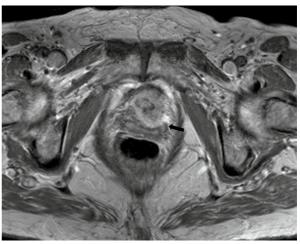


Fig. 3.35

Fig. 3.36









A 74-year-old woman was referred to the Radiology Department with a suspected urethral mass after clinical examination due to the presence of dysuria and hematuria.

#### Comments

Urethral cancer is rare, accounting for 1% of urological tumors and is much more common in women than in men. Squamous cell carcinoma is the most common type of urethral cancer and may appear as a lobulated, exophytic, or infiltrating mass. Metastatic urethral involvement is much more frequent, especially occurring by continuous dissemination from malignancies in adjacent organs such as the vagina, cervix, bladder, or anus. The diagnosis of urethral cancer is performed by urethroscopy and the major role of imaging modalities is local staging. Urethral carcinoma can spread directly to adjacent structures or metastasize to regional lymph nodes. CT and US have been described as useful for local staging but both have limitations to differentiate the urethra from adjacent structures. MR imaging with its superior soft tissue resolution is the recommended imaging modality for local staging of primary and secondary involvement of the urethra. The administration of contrast agent is considered the best method to evaluate the urethra and periurethral tissues. Endorectal or endovaginal coils provide higher spatial resolution but they are uncomfortable and not widely used. MR imaging is helpful in evaluating the size, location, and local extension of urethral tumors. Urethral cancer appears as intermediate/high signal mass on T2-weighted images disrupting the "target-like" zonal anatomy of the urethra and shows enhancement after the administration of contrast agent. In addition, diffusionweighted imaging is useful, especially in patients with contraindication to contrast agents, because urethral cancer and metastases usually show restriction to water diffusion. The extraurethral spread of the process is a very important factor for prognosis and treatment planning and can be well identified using MR imaging. MR imaging is particularly useful in cases of suspected fistula because it can depict the fistulous tract. Moreover, MR allows the detection of enlarged inguinal and pelvic lymph nodes.

#### **Imaging Findings**

Axial T1-weighted image (Fig. 3.35) shows enlargement of the urethra without well-defined masses. Axial T2-weighted image (Fig. 3.36) shows an inhomogeneous soft-tissue mass of the left distal urethra with ill-defined posterior borders. Contrast-enhanced axial T1-weighted image at two different levels of the urethra (Figs. 3.37 and 3.38) reveal a well-defined enhancing tumor (*arrowheads*) expanding the urethra and invading the anterior wall of the vagina (*arrow*).

#### **Further Reading**

#### Books

- Hricak H, Husband J, Panicek DM (2007) Oncologic imaging: essentials of reporting common cancers. Saunders, Philadelphia
- Lee JKT (2006) Computed body tomography with MRI correlation. Lippincott Williams & Wilkins, Philadelphia
- Patel U (2010) Imaging and urodynamics of the lower urinary tract. Springer, London
- Ros PR, Mortele KJ (2007) CT and MRI of the abdomen and pelvis: a teaching file. Wolters Kluwer/Lippincott Williams & Wilkins, Philadelphia
- Zagoria RJ (2006) Genitourinary radiology: the requisites. Mosby, Philadelphia

#### Web Links

http://edips-download.myesr.org/

http://emedicine.medscape.com/radiology www.esur.org http://www.rsna.org/Education/ http://www.uroweb.org/guidelines/online-guidelines/

#### Articles

- Boli DT, Patti NA, Paulson EK, Merkle EM, Simmons WN, Pierre SA, Preminger GM (2009) Renal stone assessment with dualenergy MDCT and advanced postprocessing techniques: improved characterization of renal stone composition –pilot study. Radiology 250(3):813–820
- Braun P, Guilabert JP, Kazmi F (2007) Multidetector computed tomography arteriography in the preoperative assessment of patients with ureteropelvic junction obstruction. Eur J Radiol 61:170–175
- Chan DPN, Abujudeh HH, Cushing GL, Novelline RA (2006) CT cystography with multiplanar reformation for suspected bladder rupture: experience in 234 cases. AJR Am J Roentgenol 187:1296–1302
- Chaudhari VV, Patel MK, Douek M, Raman SS (2010) MR imaging and US of female urethral and periurethral disease. Radiographics 30(7):1857–1874
- Craig WD, Wagner BJ, Travis MD (2008) Pyelonephritis: radiologic-pathologic review. Radiographics 28:255–276
- El-Ghar MA, Osman Y, Elbaz E, Refiae H, El-Diasty T (2010) MR urethrogram versus combined retrograde urethrogram and sonourethrography in diagnosis of urethral stricture. Eur J Radiol 74(3):e193–e198, Epub 2009 Jul 15
- Fasih N, Prasad Shanbhogue AK, Macdonald DB, Fraser-Hill MA, Papadatos D, Kielar AZ et al (2008) Leiomyomas beyond the uterus: unusual locations, rare manifestations. Radiographics 28:1931–1948
- Figueiredo AA, Lucon AM, Arvellos An et al (2010) A better understanding of urogenital tuberculosis, pathophysiology based on radiologic findings. Eur J Radiol 76:246–257

- Figueiredo AA, Lucon AM, Ikejiri DS, Falci R, Srougi M (2008) Urogenital tuberculosis in a patient with AIDS: an unusual presentation. Nat Clin Pract Urol 5:456–460
- Grenier N, Quaia E, Prasad PV, Juillard L (2011) Radiology imaging of renal structure and function by computed tomography, magnetic resonance imaging, and ultrasound. Semin Nucl Med 41(1):45–60
- Kawashima A, Sandler CM, Wasserman NF, LeRoy AJ, King BF Jr, Goldman SM (2004) Imaging of urethral disease: a pictorial review. Radiographics 24(Suppl 1):S195–S216
- Kim B, Kawashima A, LeRoy AJ (2007) Imaging of the male urethra. Semin Ultrasound CT MR 28(4):258–273
- Lawer LP, Jarret TW, Corl FM, Fishman EK (2005) Adult ureteropelvic junction obstruction: insights with three-dimensional multi-detector row CT. Radiographics 25:121–134
- Mitterberger M, Pinggera GM, Neururer R, Peschel R, Colleselli D, Aigner F et al (2008) Comparison of contrast-enhanced color Doppler imaging, computed tomography, and magnetic resonance imaging for the detection of crossing vessels in patients with ureteropelvic junction obstruction. Eur Urol 53:1254–1262
- Nicolau C, Bunesch L, Sebastia C, Salvador R (2010) Diagnosis of bladder cancer: contrast-enhanced ultrasound. Abdom Imaging 35(4):494–503, Epub 2009 May 21
- Sung DJ, Kim YH, Cho SB, Oh YW, Lee NJ, Kim JH, Chung KB, du Moon G, Kim JJ (2006) Obliterative urethral stricture: MR urethrography versus conventional retrograde urethrography with voiding cystourethrography. Radiology 240(3):842–848
- Thali-Schwab CM, Woodward PJ, Wagner BJ (2005) Computed tomographic appearance of urachal adenocarcinomas: review of 25 cases. Eur Radiol 15:79–84
- Van der Molen AJ, Cowan NG, Mueller-Lisse UG et al (2008) CT urography: definition, indications and techniques. A guideline for clinical practice. Eur Radiol 18:4–17
- Vickram R, Sandler CM, Ng CS (2009) Imaging and staging of transitional cell carcinoma: part 2, upper urinary tract. AJR Am J Roentgenol 192:1488–1493
- Vikram R, Sandler CM, Ng CS (2009) Imaging and staging of transitional cell carcinoma: part 1, lower urinary tract. AJR Am J Roentgenol 192(6):1481–1487
- Vrtiska TJ, Takayashu N, Fletcher JG, Hartman RP, Yu L, Kawashima A (2010) Genitourinary applications of dualenergy CT. AJR Am J Roentgenol 194:1434–1442
- Wang J, Wang H, Tang G, Hou Z, Wang G (2009) Transitional cell carcinoma of upper urinary tract vs. benign lesions: distinctive MSCT features. Abdom Imaging 34:94–106
- Wong-You-Cheong JJ, Woodward PJ, Manning MA, Sesterhenn IA (2006) Neoplasms of the urinary bladder: radiologicpathologic correlation. Radiographics 26:553–580
- Yu J-S, Kim KW, Lee H-J, Lee Y-J, Yoon Ch-S, Kim M-J (2001) Urachal remnant diseases: spectrum of CT and US findings. Radiographics 21:451–461
- Zhang J, Gerst S, Lefkowitz RA, Bach A (2007) Imaging of bladder cancer. Radiol Clin North Am 45(1):183–205

JOAN C. VILANOVA, ROBERTO GARCÍA-FIGUEIRAS, MARIA BOADA, AND JOAQUIM BARCELÓ

#### Contents

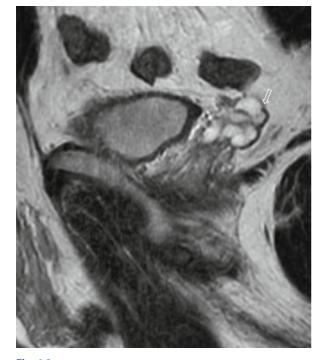
Case 1	Vesiculitis	68
Case 2	Utricle Cyst	70
Case 3	Seminal Vesicle Cyst with Renal Agenesis	72
Case 4	Chronic Prostatitis	74
Case 5	Benign Prostatic Hypertrophy	76
Case 6	Seminal Vesicles Infiltration	78
Case 7	Central Gland Prostate Cancer.	80
Case 8	Bilateral Peripheral Prostate Cancer	82
Case 9	Local Recurrence After Radical Prostatectomy	84
Case 10	Local Recurrence After Brachytherapy	88







Fig. 4.2



```
Fig. 4.4
```

A 59-year-old male presented with repeated hemospermia for several months, without a history of vague pelvic pain. A digital rectal examination determined a normal size of the prostate.

Patients with seminal vesiculitis typically present with vague pain in the lower abdomen,

#### perineum, scrotum, inguina, or lower back. The presence of hemospermia is more uncommon, although not exceptional. Due to the multiplicity of symptoms and low morbidity, the diagnosis of seminal vesiculitis has been frequently difficult. Imaging techniques, such as vesiculography, CT, transrectal ultrasonography, and MRI have allowed the depiction of a possible chronic infection of the seminal vesicle (SV). However, the limitations of vesiculography, CT, and transrectal ultrasonography are well recognized. The use of MRI may be superior to the use of the above-mentioned imaging techniques. First,

the depiction of a possible chronic infection of the seminal vesicle (SV). However, the limitations of vesiculography, CT, and transrectal ultrasonography are well recognized. The use of MRI may be superior to the use of the above-mentioned imaging techniques. First, MRI does not have the potential side effects of radiation exposure or allergic response to iodinate contrast medium, and MRI can provide more information regarding tissue characteristics. For example, fluid content, high protein content, or hemorrhage within the cystic lesions can be easily determined by using various pulse sequences. MR imaging may demonstrate diffuse SV wall thickening. Diffuse enhancement of the wall and septa of the SV can be seen at CT or MR imaging. Although diffuse wall thickening and enhancement are considered imaging findings of vesiculitis, no reports have described the diagnostic criterion for the wall thickening.

Axial T1-weighted MRI (Fig. 4.1) shows high signal intensity on the left seminal vesicle due to hemorrhage or proteinaceous fluid. T2-weighted MRI on the three planes (Figs. 4.2–4.4) (*open arrows*) shows higher signal intensity of the left seminal vesicle and wall thickening related to chronic seminal vesiculitis.

#### Comments

#### **Imaging Findings**

# Case 2 Utricle Cyst

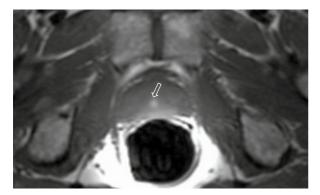
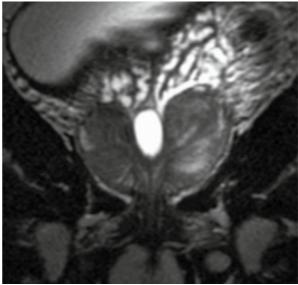
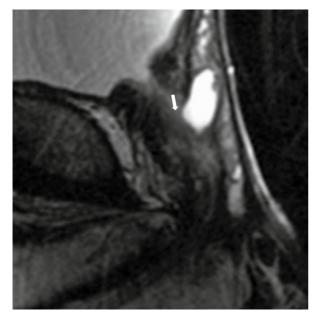
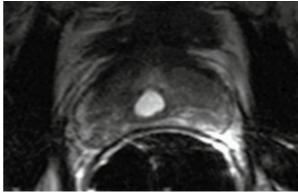


Fig. 4.5











#### A 54-year-old man presented with lower urinary tract symptoms and hematuria.

Prostatic cysts are the most commonly encountered congenital anomalies of the prostate. Prostatic cysts are characterized by their location in relation to the prostate, which may be midline (prostatic utricle and Mullerian duct cysts), paramedian (cysts of the ampulla of the vas deferens and ejaculatory duct), or lateral (seminal vesicle and prostatic cysts).

Utricular cysts arise from the dilatation of the prostatic utricle, originating from the verumontanum. They communicate with the prostatic urethra and contain white or straw-colored sperm-free fluid, which is of high signal on T2-weighted MR images. Utricular cysts are usually smaller than Mullerian duct cysts, showing a teardrop shaped, and do not extend above the base of the prostate. They usually manifest in the first two decades of life and are frequently associated with other genital anomalies including hypospadias, cryptorchidism, or ipsilateral renal agenesis.

Mullerian duct cysts are embryologic remnants of the Mullerian duct system. Unlike utricular cysts, Mullerian duct cysts do not communicate with the prostatic urethra. When large, Mullerian duct cysts can extend superolaterally above the prostate gland and may contain hemorrhage and debris. They are connected to the verumontanum by a stalk. Mullerian duct cysts are rarely associated with renal agenesis. These cysts are usually discovered in infertile males in the third or fourth decade of life because they are the most common cause of ejaculatory duct obstruction. Stones, which may cause hemorrhage into the cyst, are common and virtually diagnostic if found to lie in a retrovesical cavity that is not connected to the bladder.

Clinical symptoms in Mullerian and utricular cyst can range from voiding difficulty to infertility and often overlap between the two cyst types, although most patients are asymptomatic. The clinical features of utricular and Mullerian duct cysts include pelvic mass, obstructive and irritative urinary tract symptoms, hematuria, suprapubic or rectal pain, sexual dysfunction, and symptoms of ejaculatory duct obstruction, such as hematospermia. Urine may pool in utricle cysts since these cysts communicate with the urethra, occasionally resulting in the distinctive feature of postvoid dribbling.

Utricular and Mullerian duct cysts show generally high signal intensity on T2-weighted MR images secondary to their fluid contents. These cysts demonstrate variable signal intensity on T1-weighted MR images depending on the presence of infection or hemorrhage.

The indication for treatment of these cysts is based on symptoms and does not differ between cyst types. Generally small, asymptomatic, incidentally diagnosed cysts and welldrained cysts are best left alone with periodic follow-up.

Axial T1-weighted MRI (Fig. 4.5) shows a small high signal intensity cyst located in the midline. T2-weighted MRI on the three planes (Figs. 4.6–4.8) shows the cyst arising from the verumontanum and communicating with the urethra (*open arrow*)

#### **Comments**

#### **Imaging Findings**

#### Case 3 Case 3 Seminal Vesicle Cyst with Renal Agenesis

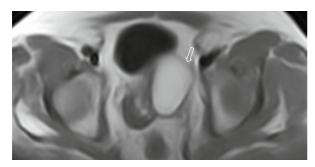


Fig. 4.9

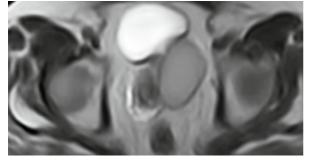


Fig. 4.10

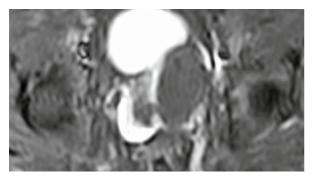
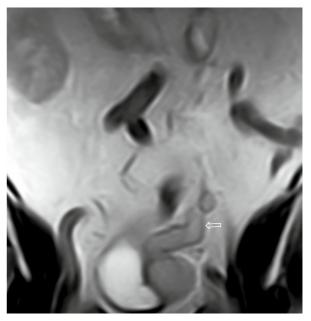


Fig. 4.11







A 43-year-old man was referred for further evaluation of a cystic lesion in the pelvis. He was completely asymptomatic, although he experienced gross hematuria several months before his visit.

# Seminal vesicle cysts may be congenital or acquired. Congenital seminal vesicle cysts can be classified as isolated cysts, cysts associated with upper urinary tract anomalies, and cysts associated with autosomal-dominant polycystic kidney disease. SVC are associated with ipsilateral renal agenesis or dysplasia in two-thirds of patients. Ectopic ureteral insertion into the seminal vesicle, ejaculatory duct, vas deferens (VD), prostatic urethra, or agenesis of the VD or a blind-ending ureteral bud remnant may be associated. The male reproductive and urinary systems are closely related embryologically and anatomically, explaining the coexistence of renal and reproductive duct anomalies. Symptoms mostly develop due to the irritation of adjacent organs by the enlarged and inflamed cyst. Bladder irritation causes urgency, frequency, dysuria, and hematuria. Cyst distention may cause perineal, suprapubic, flank, pelvic, and scrotal pain; hematospermia; postcoital pain or discomfort; as well as painful defecation. Occasionally, infertility may be the chief complaint.

Although congenital anomalies of the seminal vesicles are rare, they are likely to be increasingly encountered because of the continued growth in the use of ultrasound, CT, and MRI. In ultrasonography, SVC typically appear as paramedian cystic structures. Such cysts should be distinguished from Müllerian duct cysts, which are characterized by a midline location with normal seminal vesicles on either side. On MRI, SVC are of variable signal intensity on T1-weighted images, generally of fluid signal intensity on T2-weighted images, and are nonenhancing after intravenous gadolinium administration. High signal on T1-weighted intensity is thought to be due to hemorrhage or an increased concentration of proteinaceous fluid. MRI is a better technique for defining anatomic relationships. Differential diagnosis must be made from cystadenoma and papillary adenoma, both benign tumors of the seminal vesicle, which may mimic simple cystic enlargement. Other differential diagnoses include Müllerian duct cysts, diverticula of the ejaculatory ducts or ampulla of the vas DEFERENS, prostatic cysts, and malignant tumors of the vesicles, both primary (adenocarcinoma and sarcoma) and secondary, caused by spread from the bladder, prostate, rectum, and lymphomas. When the patient is symptomatic, surgical excision is the treatment of choice.

#### Comments

#### **Imaging Findings**

Axial T1-weighted MR image (Fig. 4.9) shows a round well-defined mass arising from the left side of the base of the prostate, causing impression to the bladder with high signal due to hemorrhage or proteinaceous fluid. Axial T2-weighted image (Fig. 4.10) shows intermediate signal of the cyst due to the related component of the fluid and the corresponding STIR sequence (Fig. 4.11) shows low signal due to suppression of the high T1 signal of the fluid. Coronal T2-weighted image (Fig. 4.12) shows the cyst connected to a blind-ending ureteral bud remnant due to ipsilateral renal agenesis (Figs. 4.12 and 4.13).

# Case 4 Chronic Prostatitis

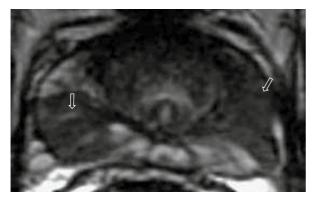


Fig. 4.14

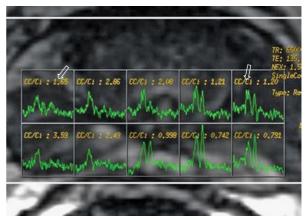
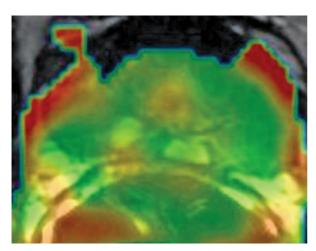


Fig. 4.15





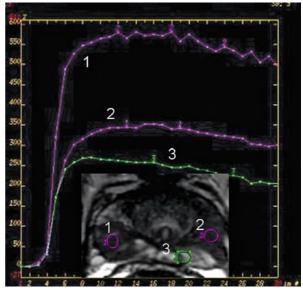


Fig. 4.17

A 45-year-old male with dysuria, malaise, and intermittent fever of unknown origin for several weeks has revealed a PSA level of 17 ng/mL. A repeated analytic examination showed similar PSA value.

#### Comments

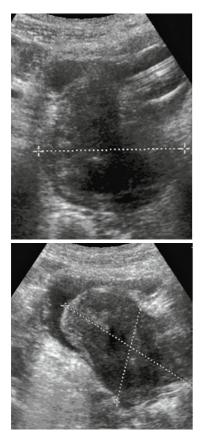
Chronic prostatitis is one of the diagnostic challenge on MRI imaging. Either conventional T2-weighted MRI, dynamic contrast enhancement, or MR spectroscopy might show similar findings as prostate cancer. On T2-weighted sequence prostatitis might show also low signal intensity within the normal high signal of the peripheral zone. Nevertheless usually prostatitis might show either diffuse low signal intensity or a patch pattern with regular margins which could differentiate the nodular irregular pattern of prostate cancer. There is much overlap with the metabolic ratio on spectroscopy with prostatitis and prostate cancer as both conditions might show elevated choline plus creatine/citrate (CC/Ci) ratio.

Histologically, chronic prostatitis is characterized by extracellular edema surrounding the involved prostatic cells with lymphocytes, plasma cells, macrophages, and neutrophils in the prostatic stroma. This abundance in cells as compared with normal prostatic tissue may lead to an ADC decrease because of decreased extracellular to intracellular fluid volume ratio, but probably not as low as prostate cancer. There are no available reports on DWI characteristics of chronic prostatitis, but probably as the present case, data of diffusion-weighted sequence with the ADC map might help to differentiate prostatitis and prostate cancer combining also the information of T2-weighted image. Either spectroscopy or dynamic contrast MR imaging might show similar findings in chronic inflammatory and neoplastic disease; for this reason DWI might improve the negative predictive value of functional MRI on patients with high level PSA due to either chronic prostatitis or benign prostatic hyperplasia.

#### **Imaging Findings**

Axial T2-weighted MRI (Fig. 4.14) shows bilateral low signal intensity focus, although with regular edges suspicious for malignancy. The corresponding three-dimensional 1H MR spectroscopic imaging data (Fig. 4.15) shows an elevated (choline plus creatine/citrate) CC/ Ci ratio from both sizes suspicious for cancer. The DWI on the ADC map does not show reduction of diffusion, without demonstrating low ADC values (Fig. 4.16), which would be represented by blue color. The dynamic contrast-enhanced MRI image (Fig. 4.17) shows bilateral high vascularization, especially on the right side suspicious for cancer. Histologic diagnosis was diffuse prostatitis.

## Case 5 Benign Prostatic Hypertrophy



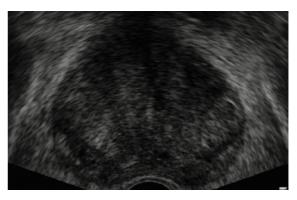
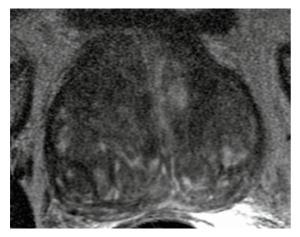
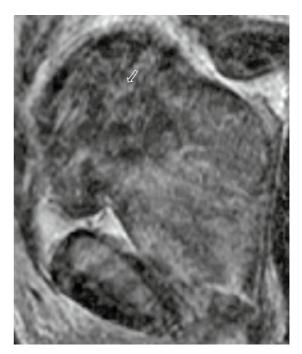


Fig. 4.19

Fig. 4.18







A 67-year-old male had a history of moderate lower urinary tract obstructive and irritative symptoms consisting of frequency, urgency, poor force and caliber of his urinary stream, and nocturia. The rectal exam revealed a markedly enlarged prostate gland, and a urinalysis revealed 5–7 white blood cells/high power field. The patient's prostate-specific antigen (PSA) was 6.5 ng/mL.

#### **Comments**

Benign prostatic hyperplasia (BPH), also known as benign prostatic hypertrophy or prostatic adenoma, is a histologic diagnosis characterized by proliferation of the cellular elements of the prostate, especially located in the transitional zone. BPH is considered a normal part of the aging process in men and is hormonally dependent on testosterone and dihydrotestosterone (DHT) production. An estimated 50% of men demonstrate histopathologic BPH by age 60 years, and 90% by age 85 years. The voiding dysfunction that results from prostate gland enlargement and bladder outlet obstruction is termed lower urinary tract symptoms or prostatism. BPH can be treated with medication, a minimally invasive procedure or, in extreme cases, surgery that removes the prostate. Although MR imaging provides excellent resolution of internal prostatic anatomy, information with respect to the ratio of glandular to stromal tissue in the prostate, and an accurate estimate of prostate volume, its use in patients with BPH is limited by its high cost and limited availability. In contrast, TRUS remains an important tool in the evaluation of patients with prostatic disease. Similar to MR imaging, TRUS provides excellent images of internal prostatic anatomy and an accurate estimate of prostate volume prior to treatment. In addition, this imaging modality is noninvasive, cost-efficient, easily adapted to office use, and able to provide guidance for transrectal prostate biopsy. Transabdominal ultrasound is used to assess prostate volume. For a symmetrical gland the following formula is commonly used to calculate the size: = weight =  $0.5 \times D1 \times D2 \times D3$ , where D1 is the transverse diameter, D2 the anteroposterior, and D3 the craniocaudal. BPH can show a wide and variable aspect on ultrasound. Typically the larger size of the transitional zone is less echogenic than the peripheral gland compressed. Hypertrophic transition zone can be homogeneous or heterogeneous. Echogenic foci can be observed with ultrasound, especially in the area of the surgical capsule, corresponding to calcifications.

BPH might raise the levels of prostate-specific antigen (PSA). For this reason currently it is a challenge to rule out prostate cancer on those patients with BPH, high PSA levels, and with several negative biopsies. Thus MRI could play a role to select patient candidates to biopsy and avoid unnecessary biopsies in patients where the high levels of PSA can be due to the BHP.

Transabdominal US (Fig. 4.18) showing the measurement of the size of the BPH. Axial view from transrectal ultrasound (Fig. 4.19) shows a large size from the prostate gland. Corresponding axial T2-weighted image (Fig. 4.20) shows the heterogeneity of the transitional zone with low signal and some high signal areas due to adenomatous tissue. Sagittal T2-weighted image (Fig. 4.21) demonstrates the large size of the anterior transitional zone, compressing the bladder.

#### **Imaging Findings**

### Case 6 Seminal Vesicles Infiltration

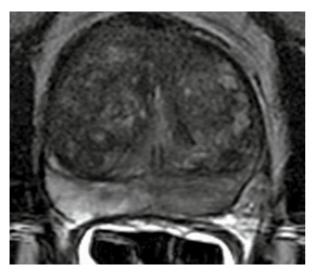


Fig. 4.22

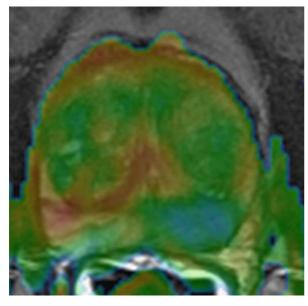


Fig. 4.24

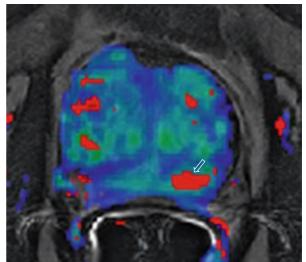


Fig. 4.23



Fig. 4.25

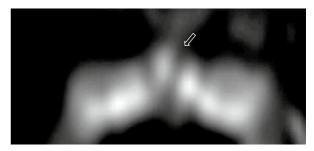


Fig. 4.26

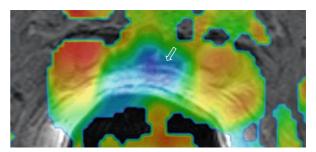


Fig. 4.27

A 67-year-old male without a previous biopsy presented with a PSA level of 6.7 ng/mL and free-to-total PSA ratio (%fPSA) of 8%. Previous PSA level one year before was 3.5 ng/mL. Digital rectal examination was unremarkable. The urologist requested an MRI previously to perform a biopsy.

#### Comments

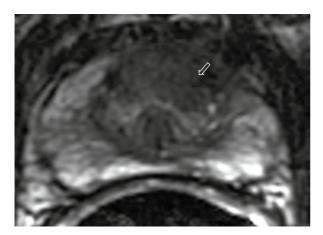
The methods most commonly used to detect prostate cancer (PC) are digital rectal examination (DRE) and serum prostate-specific antigen (PSA) levels. Both methods provide suboptimal accuracy for PC diagnosis. The specificity of PSA levels is poor for PSA level below 10 ng/mL. %fPSA could be a useful tool combined with imaging, as Vilanova et al. reported that MR and MR spectroscopy combined with free-to-total PSA ratio improves the predictive value for PC detection. Improved staging is crucial to determine risk and prognosis, especially when differentiating between organ-confined PC and extracapsular extension or seminal vesicle invasion (SVI). Clinical factors associated with an increased incidence of SVI include a high PSA level, a high Gleason grade, the presence of tumor at the base of the prostate gland, and lymph node metastasis. MRI is superior to DRE, transrectal ultrasound, and CT in predicting prostate-confined cancer.

Tumor in the SV appears as a low-signal area in the high-signal fluid on T2-weighted images and as a low-signal area on T1-weighted images. Other findings, such as loss of the normal architecture of the SV, asymmetry, loss of the fat plane between the base of the bladder and the inferior aspect of the SV, focal or diffuse wall thickening, obliteration of the angle between the prostate and the SV, or direct tumor extension from the base of the prostate into and around the SV, may represent SVI. The use of functional techniques, such as dynamic contrast-enhanced MRI (DCE-MRI) or MR spectroscopy, can improve tumor detection and staging. Concerning SVs, T2 images combined with DWI shows significantly higher accuracy than T2-weighted imaging alone in the detection of SVI. The ADC values of SVI are significantly lower than those of normal SVs and cases of SVI exhibit high signal intensity on DWI.

#### **Imaging Findings**

Axial T2-weighted fast spin echo (FSE) (Fig. 4.22) shows diffuse low signal in left peripheral gland. DCE-MR (Fig. 4.23, *open arrow*) demonstrates focal area of increased wash-out rate in the peripheral gland (*red area, open arrow*). Combined T2-weighted-FSE image plus parametric color map of ADC values (Fig. 4.24) demonstrates low ADC values (*blue color*) in the left peripheral gland. Axial T2-weighted fast spin echo (FSE) (Fig. 4.25), DWI (Fig. 4.26), and combined T2-weighted plus parametric map of ADC values (Fig. 4.27), at the level of SVs demonstrate low ADC values (*blue color*) in the seminal vesicles due to infiltration (*open arrows*).

# Case 7 Central Gland Prostate Cancer



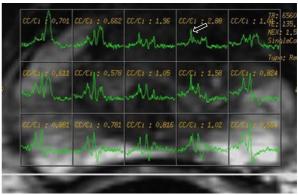
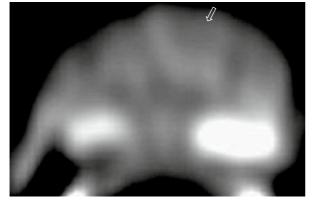
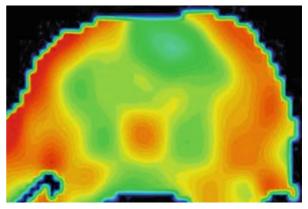


Fig. 4.29

Fig. 4.28









A 67-year-old male presented with previous four negative biopsies for prostate cancer. His PSA level shows progressive rising from 6.70 ng/mL and currently 16.57 ng/mL. Free-to-total PSA ratio: 14.40%

#### Prostate cancer occurs in the peripheral zone in 75-85% of cases; however, it has been shown that the transition zone, central gland, harbors cancer in up to 25% of radical prostatectomy specimens. Cancers located in the transition zone show some pathologic and clinical features that are different from the features shown by cancers located in the peripheral zone. It is important to accurately distinguish transition zone cancers with imaging to guide biopsy, plan disease-targeting therapies, and avoid positive anterior surgical margins at radical prostatectomy. Moreover, it is important to detect central gland prostate cancer in order to avoid repeated overlooked blinded biopsies. Biopsying the target lesion detected by MRI, especially using DWI, is more accurate than the current blind biopsy method, and the indication for biopsy could be more efficient than with current methods based on DRE and PSA values. Thus, performing prostate biopsy with MRI/DWI data available could improve the biopsy detection rate of prostate cancer. Despite the tendency of different ADC values in prostate cancer and noncancerous tissue, studies have also shown a significant overlap of the ADC values between prostate cancer and noncancerous tissue, which is attributed to the fact that the ADC varies widely in both prostate cancer and noncancerous tissue. This overlap of the ADC limits the accuracy of DWI in cancer detection. This overlap seems to be prominent between both prostate cancer and noncancerous transitional zone tissue because it has a lower ADC than peripheral zone tissue. Therefore, a higher diagnostic accuracy based on a region-of-interest analysis in previous studies might be exaggerated, and the actual diagnostic accuracy for cancer detection may not be as satisfactory as expected in clinical practice. Nevertheless, ADC values of prostate cancer seem to show lower values than central gland tissue. One of the advantages of MRI technique is the possibility to combine conventional T2-weighted sequence with functional techniques such as DWI, spectroscopy, or dynamic contrast enhancement sequence. The increase of diagnostic power for prostate cancer using combined functional MRI has been demonstrated.

#### Axial T2-weighted image reveals a low signal intensity nodular lesion in the central anterior **Imaging Findings** left gland (Fig. 4.28, *open arrow*). Combined spectroscopy curves show higher level of choline related to citrate corresponding to prostate cancer profile (Fig. 4.29, *open arrow*). Axial DWI at b = 1,000 s/mm<sup>2</sup> shows slightly higher signal intensity on the left side of the central gland which is not significant (Fig. 4.30, *open arrow*). The same image on ADC color parametric map shows the significantly low ADC value demonstrated as blue color (Fig. 4.31). It is necessary to perform the ADC map to display accurate data from the DWI sequence and minimize the T2 shine-through effect.

#### **Comments**

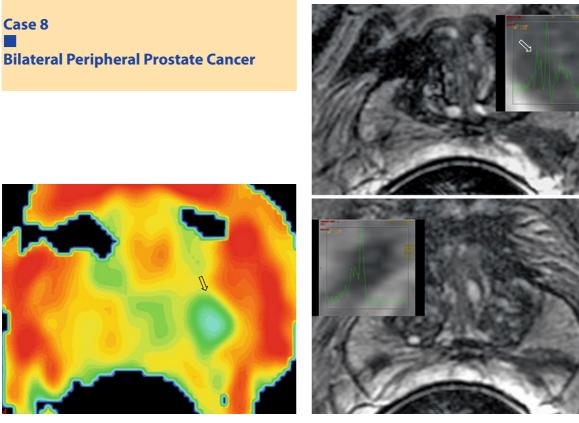
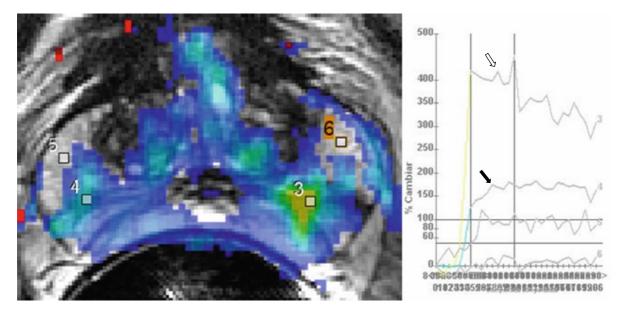


Fig. 4.33

Fig. 4.32



A 58-year-old male presents with a PSA level of 3.90 ng/mL and a free-to-total PSA ratio of 7%. Before a biopsy is performed the urologist requests an MRI study to rule out prostate cancer. Due to the MRI findings a targeted biopsy was performed with the final result of bilateral peripheral prostate cancer, Gleason 6 (3+3) on the right side and Gleason 7 (4+3) on the left side.

#### Comments

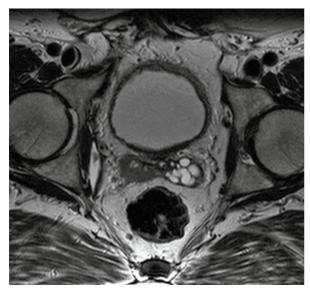
Tumor detection on standard T2-weighted MRI in the evaluation of prostate cancer is recognized as a focus of low signal intensity relative to the surrounding signal intensity of the peripheral zone. But the accuracy of T2-weighted MRI in the detection of prostate cancer is approximately 65–77% using a high-resolution endorectal technique as other benign conditions such as prostatitis or hyperplasia can show similar features.

Advanced functional imaging techniques, such as DWI, spectroscopy (MRSI), and dynamic contrast enhance technique (DCE) significantly increase the sensitivity of MRI in the detection and staging of prostate cancer. MRSI, DW-MRI, and DCE-MRI all deliver additional information to morphologic changes depicted on T2-weighted MR images. It is important to carefully tailor MRI examination protocols to individual patient clinical history; if applied to appropriately selected patients, each of the three techniques will help to better characterize, stage, and grade potential malignancy of the prostate. Although experience with DWI is still relatively limited, interest is growing in this technique as an adjunct to T2-weighted imaging. DWI might have potential for grading of prostate carcinoma. The histopathologic Gleason score remains one of the most important prognostic factors for progression-free and disease-specific survival in prostate cancer. Previous reports have found that higher Gleason grades were associated with lower tumormuscle signal intensity ratios on T2-weighted imaging. Hypothetically, DWI has far more potential than any other MR imaging sequence in grading of prostate carcinoma, because increased cellular density and loss of tubular structures implicate a higher Gleason score and also seriously hamper self-diffusion in the involved tissue leading to lower ADC levels on DWI.

#### **Imaging Findings**

Axial T2-weighted image (Fig. 4.32) shows bilateral low signal intensity in the peripheral gland, with higher size on the left side. MR spectroscopy curves reveal no significantly high level of choline on neither side, although slightly higher on the left side (*open arrow*) (Fig. 4.32). DWI on the parametric ADC color map (Fig. 4.33, *open arrow*) shows a significantly low value from the left side demonstrated as a blue color. The lesion from the right side does not show restricted diffusion on the ADC map (Fig. 4.33). The dynamic contrast-enhanced sequence reveals a significant wash-in with a wash-out on the left side (*open arrow*) (Fig. 4.34)





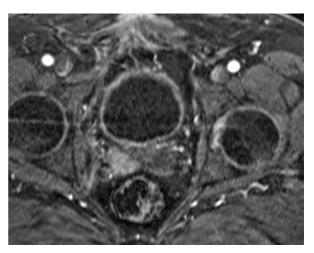


Fig. 4.36

Fig. 4.35



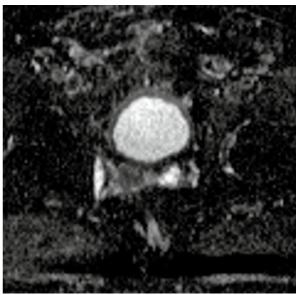




Fig. 4.38

A 68-year-old male presented with clinical history of radical prostatectomy 1 year ago for prostate cancer (pT2c, Gleason 6, PSA 6.45 ng/mL). Currently, the patient presents fast rising serum PSA level increasing from 2.36 to 2.60 ng/mL during the last 3 months.

# After definitive radical prostatectomy (RP), serum PSA should fall to undetectable levels (less than 0.1 ng/mL). A rise in serum PSA is usually the first indication of cancer recurrence. The incidence of biochemical failure (BF) following radical prostatectomy reported ranges from 15% to 53% and it often precedes detectable recurrence by years. The definition of BF varies in the literature from 0.2 to 0.5 ng/mL, but a PSA level of 0.2 ng/mL is considered indicative of BF. A PSA level of 0.4 ng/mL or greater is associated most strongly to PSA progression or disease progression. Clinically, we can consider four main categories of recurrence: PSA-only relapse, local recurrence in the prostatectomy bed, metastatic disease, and combined local and distance recurrence. Different nomograms based on the combination of pathologic stage and tumor grade at diagnosis, PSA doubling time, time interval between surgery and PSA relapse, and others help to distinguish among these four situations in order to decide patient's treatment.

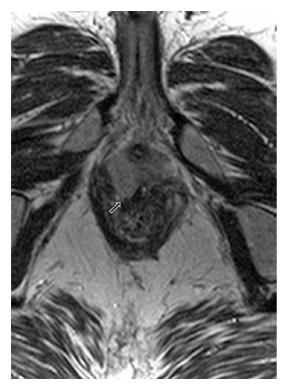
Local recurrence after RP is frequently not detectable by rectal examination. Accurate information on local patterns of failure has been frequently used to improve target volume definition for adjuvant radiotherapy. Magnetic resonance imaging (MRI) may be a basic tool in the evaluation of the postsurgical pelvis to define the site of local recurrence in the tumor bed region after surgery.

It must be addressed that it is not infrequent to observe small amounts of residual benign prostatic tissue responsible for persistent mild elevation of PSA levels. Tumoral relapse is more frequently demonstrated in the perianastomotic area (from the bladder neck to the penile bulb). At MRI, normal postsurgical perianastomotic fibrosis appears hypointense on T1-weighted and T2-weighted images and with small or no enhancement on dynamic contrast-enhanced (DCE) images. Incomplete resection of the seminal vesicles (SVs) after RP is not an infrequent finding and patients may fail within these retained remnants. The retained SVs are easily diagnosed when they keep their characteristic morphology and high signal intensity on T2-weighted images. They can also appear as distorted low signal intensity nodules or linear structures suggesting residual fibrotic SV tips. Recurrences present as lobulated masses with intermediate signal intensity on T2-weighted images and they enhance early on DCE-MRI and restricted diffusion. MRI can detect and localize local recurrences early in patients with low PSA levels and it might be used in the future to define and reduce the radiotherapy clinical target volume to the suspicious area.

The role of MR spectroscopy (MRSI) in patients with BF after prostatectomy remains controversial. MRSI is a demanding technique. It is limited by its poor spatial resolution and it shows high sensitivity to field inhomogeneities induced by surgical clips. Beside this, diagnostic criteria using MRSI are still unclear, since normal citrate is in theory undetectable after RP and thus the classic choline-to-citrate ratio might not be accurate.

The best treatment for local recurrence is salvage external beam radiotherapy. Its outcome is more favorable in patients at PSA levels <1–1.5 ng/mL. New therapeutic procedures such as high-intensity focused ultrasound or cryotherapy are actually under evaluation.

#### **Comments**



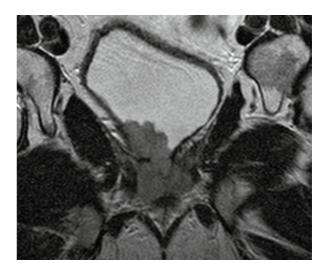
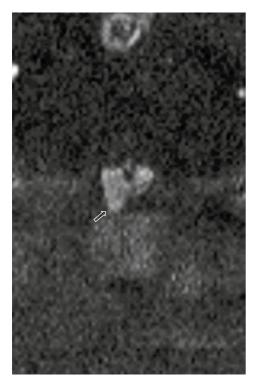


Fig. 4.40

Fig. 4.39



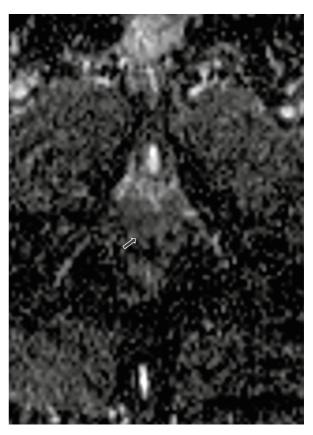


Fig. 4.42

#### **Imaging Findings**

Axial T2-weighted FSE (Fig. 4.35), DCE (Fig. 4.36), and DW (*b*-value = 800) (Fig. 4.37) MR images and ADC map (Fig. 4.38) demonstrate retained seminal vesicles. Tumoral invasion can be clearly depicted on the right side with low signal on T2-weighted imaging, early enhancement on DCE-MRI, high signal on DWI, and low ADC values.

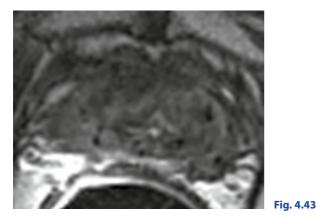
Axial (Fig. 4.39) and coronal T2-weighted FSE images (Fig. 4.40) in a different case of recurrence postprostatectomy shows a tumoral mass with intermediate signal situated posterolateral to the perianastomotic area and invading the bladder. DW (b-value = 1,000) (Fig. 4.41) and ADC map (Fig. 4.42) images show high signal intensity, restricted diffusion on the high b-value imaging, and a low ADC value (*open arrows*).

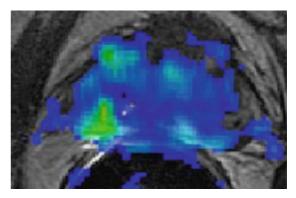
### Case 10 Local Recurrence After Brachytherapy

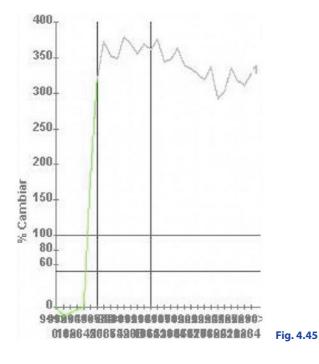
**Comments** 

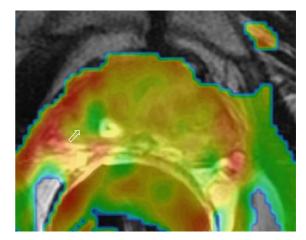
A 60-year-old male with clinical history of prostate cancer (pT2N0. Gleason 3+3 and PSA 5.5 ng/mL) was treated with brachytherapy 4 years ago. Two years later, PSA value was 0.6 ng/mL. Actually, the patient presents high serum PSA level: 4 ng/mL.

In recent years, there have been significant improvements in the management of localized prostate cancer but the optimal treatment remains undefined. Brachytherapy (BT) is an effective option for prostate cancer treatment in selected patients. The indications for prostate BT are very similar to those for any form of radical treatment for prostate cancer; it is a treatment for organ-confined, early stage disease. Prostate BT delivers a high dose of radiation to a very small target volume and hence there is very little unnecessary irradiation of adjacent bowel and bladder. After BT, serum PSA levels decrease slowly with a nadir observed at 2–4 years, but a temporary increase of PSA level followed by a further decrease











can occur. This temporary increase is named PSA bounce. Follow-up after BT is performed clinically, and imaging has a limited role for direct patient management. Unfortunately, there is no consensus definition of BF following BT. ASTRO criteria and Phoenix definition has been used. Based upon sensitivity and specificity profiles as well as regression analysis, a serum PSA level of the nadir + two appears to be the best value for defining a BF.

Imaging usually has a limited role for detecting local recurrence after BT. In practice, exclusion of metastatic relapse with CT scanning and bone scanning will be used as indirect evidence of local failure in patients with BF. Local recurrence after BT is difficult to detect. MRI of the post-treatment gland can be difficult to evaluate. Areas of low signal may represent recurrent/residual disease, or merely be part of the spectrum of therapy change. Additionally, brachytherapy seeds result in metallic susceptibility artifacts, which obscure fine detail and can impair interpretation of certain MRI sequences, such as diffusion imaging or MR spectroscopy (MRSI), within the prostate. At MRI, "normal" post-BT prostate shows diffuse low signal intensity on T1-weighted and T2-weighted images and with little or no enhancement on dynamic contrast-enhanced (DCE) images. MRSI shows a metabolic atrophy. Recurrences may be depicted on DCE-MRI due to their early enhancement, but interpreting post-BT DCE images is difficult, because the decrease of prostate vascularization is not homogeneous. Beside this, there is a short experience using MRSI in patients with BF after BT and its role is not clear. Increased metabolic activity within the implanted prostate may indicate local recurrence but this is still an area of research.

DWI has its limitations. False-positive results can occur in the setting of hemorrhage, infection, or artifact from implanted metal. But, DWI may be a powerful adjunct to the detection of residual or recurrent prostate carcinoma. Highly cellular tumor tissue will demonstrate significantly restricted diffusion, compared with nonspecific hypointense areas on T2-weighted imaging and it will exhibit high signal intensity restricted diffusion on the high *b*-value imaging and a low ADC value. Occasionally, discordant results between techniques are found; for example, DCE-MRI might not depict suspicious areas but DWI could be indicative for active tumor. This may occur because of intrinsic tumor biology (with high cellularity but low perfusion) and it illustrates the importance of using a multiparametric MRI approach to assess the pelvis when a recurrent prostate cancer is suspected.

Salvage treatment options are limited in recurrence. New therapeutic procedures such as high-intensity focused ultrasound (HIFU) or cryotherapy are currently under evaluation. MRI may detect and localize local recurrences early and it might be used in the future to define HIFU or high-dose-rate BT target areas.

Axial T2-weighted fast spin echo (FSE) image (Fig. 4.43) shows a diffuse low signal intensity secondary to brachytherapy. Some brachytherapy seeds can be depicted. The recurrent cancer is not visible on this sequence.

Parametric map from DCE-MRI (Fig. 4.44) shows increased wash-in rate in the right peripheral gland (green area) corresponding to the recurrent cancer. Qualitative analysis of this area (Fig. 4.45) demonstrates a type III curve that shows a wash-in/wash-out pattern.

Combined image of T2-weighted-FSE image and parametric map of ADC values (Fig. 4.46) clearly depicts an area with low ADC value (green) at the same level of anomalous dynamic pattern on DCE-MRI (*open arrow*).

#### **Imaging Findings**

#### **Further Reading**

#### Books

- Futterer JJ, Barentsz JO, Debruyne FMJ (2011) Imaging of the prostate. Springer, Heidelberg
- Hricak H, Scardino PT (2008) Prostate cancer. Cambridge University Press, Cambridge
- Husband JE, Sohaib SA (2004) Prostate cancer. In: Husband JE, Reznek RH (eds) Imaging in oncology, 2nd edn. Taylor & Francis, London, pp 375–400
- Ramchandani P (2008) Prostate imaging, an issue of radiologic clinics. Saunders, Philadelphia
- Scardino PT (2006) Dr. Peter Scardino's prostate book. Penguin Group, New York

#### Web Links

http://www.auanet.org

http://www.uroweb.org/ http://www.nccn.org/professionals/physician\_gls/f\_guidelines.asp http://www.cancerstaging.org/ http://www.esur.org/

#### Articles

- Akin O, Sala E, Moskowitz CS, Kuroiwa K, Ishill NM, Pucar D et al (2006) Transition zone prostate cancers: features, detection, localization, and staging at endorectal MR imaging. Radiology 239:784–792
- Bonekamp D, Jacobs MA, El-Khouli R, Stoianovici D, Macura KJ (2011) Advancements in MR imaging of the prostate: from diagnosis to interventions. Radiographics 31:677–703
- Coakley FV, Chen I, Qayyum A, Westphalen AC, Carroll PR, Hricak H et al (2007) Validity of prostate-specific antigen as a tumour marker in men with prostate cancer managed by watchful-waiting: correlation with findings at serial endorectal magnetic resonance imaging and spectroscopic imaging. BJU Int 99:41–45
- Engelbrecht MR, Huisman HJ, Laheij RJ, Jager GJ, van Leenders GJ, Hulsbergen-Van De Kaa CA et al (2003) Discrimination of prostate cancer from normal peripheral zone and central gland tissue by using dynamic contrast-enhanced MR imaging. Radiology 229:248–254
- Engelbrecht MR, Jager GJ, Laheij RJ, Verbeek AL, van Lier HJ, Barentsz JO (2002) Local staging of prostate cancer using magnetic resonance imaging: a meta-analysis. Eur Radiol 12:2294–2302
- Futterer JJ, Heijmink SW, Scheenen TW, Veltman J, Huisman HJ, Vos P et al (2006) Prostate cancer localization with dynamic contrast-enhanced MR imaging and proton MR spectroscopic imaging. Radiology 241:449–458
- Hricak H, Choyke PL, Eberhardt SC, Leibel SA, Scardino PT (2007) Imaging prostate cancer: a multidisciplinary perspective. Radiology 243:28–53
- Kaji Y, Kurhanewicz J, Hricak H, Sokolov DL, Huang LR, Nelson SJ et al (1998) Localizing prostate cancer in the presence of

postbiopsy changes on MR images: role of proton MR spectroscopic imaging. Radiology 206:785-790

- Kurhanewicz J, Vigneron DB (2008) Advances in MR spectroscopy of the prostate. Magn Reson Imaging Clin N Am 16:697-710
- Prando A (2007) The utility of magnetic resonance imaging and spectroscopy for predicting insignificant prostate cancer: an initial analysis. Int Braz J Urol 33:577–578
- Qayyum A, Coakley FV, Lu Y, Olpin JD, Wu L, Yeh BM et al (2004) Organ-confined prostate cancer: effect of prior transrectal biopsy on endorectal MRI and MR spectroscopic imaging. AJR Am J Roentgenol 183:1079–1083
- Ravizzini G, Turkbey B, Kurdziel K, Choyke PL (2009) New horizons in prostate cancer imaging. Eur J Radiol 70:212–226
- Ren J, Huan Y, Wang H, Ge Y, Chang Y, Yin H et al (2009) Seminal vesicle invasion in prostate cancer: prediction with combined T2-weighted and diffusion-weighted MR imaging. Eur Radiol 19:2481–2486
- Sala E, Akin O, Moskowitz CS, Eisenberg HF, Kuroiwa K, Ishill NM et al (2006) Endorectal MR imaging in the evaluation of seminal vesicle invasion: diagnostic accuracy and multivariate feature analysis. Radiology 238:929–937
- Sciarra A, Panebianco V, Salciccia S, Osimani M, Lisi D, Ciccariello M et al (2008) Role of dynamic contrast-enhanced magnetic resonance (MR) imaging and proton MR spectroscopic imaging in the detection of local recurrence after radical prostatectomy for prostate cancer. Eur Urol 54:589–600
- Shukla-DaveA,HricakH,EberhardtSC,OlgacS,Muruganandham M, Scardino PT et al (2004) Chronic prostatitis: MR imaging and 1H MR spectroscopic imaging findings – initial observations. Radiology 231:717–724
- Somford DM, Futterer JJ, Hambrock T, Barentsz JO (2008) Diffusion and perfusion MR imaging of the prostate. Magn Reson Imaging Clin N Am 16:685–695, ix
- Tabatabaei S, Saylor PJ, Coen J, Dahl DM (2011) Prostate cancer imaging: what surgeons, radiation oncologists, and medical oncologists want to know. AJR Am J Roentgenol 196: 1263–1266
- van As NJ, de Souza NM, Riches SF, Morgan VA, Sohaib SA, Dearnaley DP et al (2009) A study of diffusion-weighted magnetic resonance imaging in men with untreated localised prostate cancer on active surveillance. Eur Urol 56(6): 981–987
- Vilanova JC, Barcelo-Vidal C, Comet J, Boada M, Barcelo J, Ferrer J et al (2011) Usefulness of prebiopsy multifunctional and morphologic MRI combined with free-to-total prostate-specific antigen ratio in the detection of prostate cancer. AJR Am J Roentgenol 196:W715–W722
- Vilanova JC, Comet J, Barcelo-Vidal C, Barcelo J, Lopez-Bonet E, Maroto A et al (2009) Peripheral zone prostate cancer in patients with elevated PSA levels and low free-to-total PSA ratio: detection with MR imaging and MR spectroscopy. Radiology 253:135–143
- Vilanova JC, Comet J, Capdevila A, Barcelo J, Dolz JL, Huguet M et al (2001) The value of endorectal MR imaging to predict positive biopsies in clinically intermediate-risk prostate cancer patients. Eur Radiol 11:229–235
- Wefer AE, Hricak H, Vigneron DB, Coakley FV, Lu Y, Wefer J et al (2000) Sextant localization of prostate cancer: comparison of

sextant biopsy, magnetic resonance imaging and magnetic resonance spectroscopic imaging with step section histology. J Urol 164:400–404

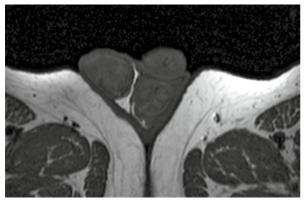
- Wu JN, Dall'Era MA (2010) Active surveillance for localized prostate cancer – current practices and recommendations. ScientificWorldJournal 10:2352–2361
- Zakian KL, Eberhardt S, Hricak H, Shukla-Dave A, Kleinman S, Muruganandham M et al (2003) Transition zone prostate cancer: metabolic characteristics at 1H MR spectroscopic imaging – initial results. Radiology 229:241–247

# Scrotum

#### Contents

Case 1	Testicular Adrenal Rest Tissues	94
Case 2	Giant Intratesticular Cyst	96
Case 3	Scrotal Trauma: Testicular Rupture	98
Case 4	Segmental Testicular Infarction	100
Case 5	Spermatic Cord Torsion	102
Case 6	Torsion of the Appendix Testis	104
Case 7	Cystic Transformation of the Rete Testis	106
Case 8	Fibrous Pseudotumor of the Testis	108
Case 9	Seminoma	110
Case 10	Leydig Cell Tumor of the Testis	112

# Case 1 Testicular Adrenal Rest Tissues



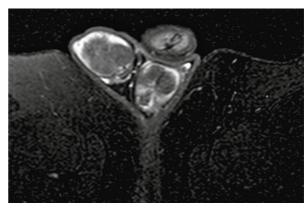


Fig. 5.1

Fig. 5.2



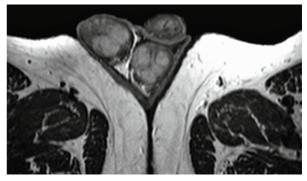




Fig. 5.4

A 25-year-old patient presented with congenital adrenal hyperplasia and enlargement of the testicles.

# Adrenal rests is a rare cause of testicular masses, which can be seen in about 29% of patients with congenital adrenal hyperplasia (CAH) and rarely in those with Cushing syndrome. CAH is an autosomal recessive disease characterized by a deficiency of adrenocortical enzymes, particularly 21-hydroxylase. An increase in adrenocorticotropic hormone (ACTH) levels causes hyperplasia of adrenal remnants in the testes in patients with CAH and results in the development of intratesticular masses. They are discovered clinically or on systematic sonography, generally in the young adult.

The sonographic appearance is variable. In the literature, some authors describe the adrenal rests as predominantly hypoechoic masses and others as heterogeneously hyperechoic masses with posterior acoustic shadowing depending on the degree of fibrosis. Intratesticular masses are typically bilateral, located in the region of the mediastinum testis in 86% of cases and show no distortion of the testicular contour.

At MR Imaging adrenal rests have been reported to have low signal intensity on both T1- and T2-weighted images with a diffuse enhancement pattern after gadolinium administration.

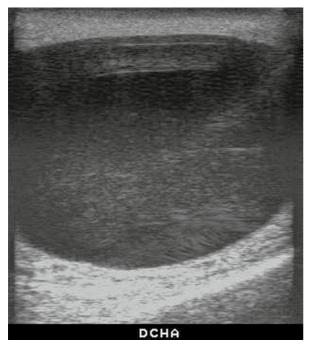
The most important factor is to recognize these lesions as benign to avoid unnecessary orchiectomy. Bilateral, synchronous testicular tumors are extremely rare (about 1%) and are the main differential consideration in bilateral testicular masses. These masses typically regress or stabilize with glucocorticoid replacement therapy. Once a testicular mass is diagnosed with congenital adrenal hyperplasia, it must be followed up. If the size of testicular lesion remains stable or decreases during hormonal therapy, further evaluation such as biopsy or testicular venous sampling is unnecessary.

#### **Imaging Findings**

Axial T1-weighted MR image (Fig. 5.1) of the testes shows no discernible abnormality. These masses are isointense compared with surrounding normal testicular tissue. Axial and coronal fat-suppressed T2-weighted images (Figs. 5.2 and 5.3) show multiple lobulated intratesticular masses in both testes that are hypointense compared with normal testicular parenchyma. After gadolinium administration (Fig. 5.4) these masses present a diffuse enhancement.

#### Comments

# Case 2 Giant Intratesticular Cyst



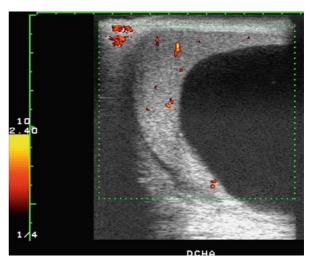


Fig. 5.6

Fig. 5.5









A 68-year-old male underwent US examination for increased size and vague symptoms in the right testis. There was no previous history of fever or trauma. On physical examination, the right testis was increased in size but no clear palpable mass or inflammatory signs were described. Analytical results were normal.

#### Comments

**Imaging Findings** 

Simple cysts are detected incidentally and occur in men of 40 years of age and older. Their size is variable and can range from 2 mm to several centimeters, as this case. The cysts are usually solitary and occur anywhere in the testis but are often near the mediastinum testis and are associated with extratesticular spermatoceles. Simple testicular cysts are usually not palpable and, even when large, are not firm. At US, simple cysts have an imperceptible wall, an anechoic center, and through transmission. Intratesticular cysts, once thought to be a rarity, are now being reported with an increasing prevalence as a result of the wider use of scrotal ultrasound scanning. It has been suggested that testicular cysts arise from remnants of Mullerian or Wolffian ducts, since such cysts have been reported in children. Other possible etiologies include trauma and inflammation, which can cause occlusion of the spermatic ducts with subsequent ectasia and cystic alterations in the rete testis; however, the exact etiology of the cysts remains unclear.

The management of intratesticular cysts remains unclear. Treatment has included enucleation and even radical orchiectomy over fear of the possibility of an associated malignancy. A more conservative approach with serial ultrasound scanning has been advocated if a clear distinction can be made between neoplastic and non-neoplastic testicular cysts. However, in view of the benign nature of such cysts, even repeated ultrasound scanning may not be necessary and may be considered overtreatment.

#### Longitudinal US examination (Fig. 5.5) shows a $6.5 \times 5$ cm simple cyst in a middle location of the otherwise normal right testis. The cyst was well circumscribed, anechoic with smooth wall and posterior acoustic enhancement. Color Doppler US examination demonstrated normal vascularization in the testicular parenchyma. No flow was observed into or in the cyst wall (Fig. 5.6). T2-weighted MR imaging (Fig. 5.7) shows a giant cyst into the right testicular parenchyma leading to an increase in the size of the testis. The cyst has the characteristic high signal intensity. On surgery, the intratesticular cyst is surrounded by the normal testicular parenchyma with a clear fluid content (epithelial cyst). Total cyst was removed preserving the rest of testis (Fig. 5.8).

# Case 3 Scrotal Trauma: Testicular Rupture

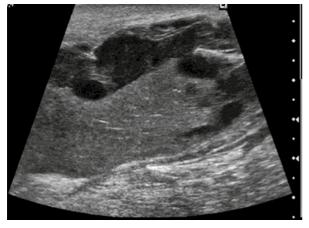


Fig. 5.9

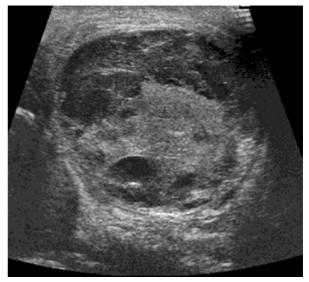


Fig. 5.10









A 20-year-old patient attended the emergency department for scrotal pain 2 days after a motorcycle trauma.

# Scrotal trauma (ST) accounts for less than 1% of all trauma-related injuries, because of the anatomic location and mobility of the scrotum. Blunt injury is the most common mechanism, followed by penetrating injury from gunshot or other assault, and iatrogenic. The main mechanism of injury in blunt trauma is crushing of the testis against the symphysis publis or between the thighs. Its peak of incidence is in the age range of 10–30 years.

US is the modality of choice for the initial evaluation of patients with acute scrotal pain after trauma and US findings are crucial in clinical decision making. US findings may vary from a small hematocele requiring conservative management to a testicular rupture demanding surgical intervention.

The testes are evaluated in longitudinal and transverse planes. The size and echogenicity of each testis and epididymis should be compared with the contralateral side.

Characteristic findings of testicular rupture on US are: disruption of tunica albuginea, contour abnormality of the testis, heterogeneous echoestructure of the testicular parenchyma, and absence or decreased vascularity.

Usually, the tunica albuginea is not normally visible at US unless there is fluid surrounding the testis. In such cases, the tunica can be seen as an echogenic line surrounding the testis. Discontinuity of the echogenic tunica albuginea is indicative of testicular rupture and requires emergent surgery. Management of testicular trauma depends on testicular integrity and perfusion. Early intervention is very important in testicular rupture in order to improve testicular salvage rates. The surgical approach varies with the type of trauma.

#### **Imaging Findings**

Longitudinal (Fig. 5.9) and axial (Fig. 5.10) US of the left testis shows a heterogeneous echotexture with internal cystic areas that represent hematomas and an abnormal contour of the parenchyma with extrusion of the testicular contents through the tunica albuginea. Coronal fat-suppressed GE T1 (Fig. 5.11) shows multiple hyperintensity due to methemoglobin on left testis that continues to inguinal canal. Coronal T2-weighted MR image demonstrates (Fig. 5.12) a normal signal on the right testis and a hyperintense (contrary to tumors) heterogeneous mass that arises from the left testicle involving the spermatic cord, and extends into the superficial inguinal ring (arrow).

#### Comments

# Case 4 Segmental Testicular Infarction



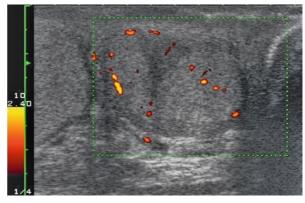


Fig. 5.14

Fig. 5.13









A 32-year-old boy presented to our hospital with acute onset of severe left scrotal pain for 24 h. He was previously healthy without any personal or familial history, and had no prior trauma to the scrotum. He underwent urological evaluation, and his physical examination demonstrated minimal tenderness in the left testis. There was no palpable intratesticular mass. Analytical results were normal and included serum tumor markers.

### Comments

Segmental testicular infarction is an infrequent testicular disorder usually diagnosed after orchiectomy. Several etiologies have been pointed, such as acute epididymitis, hematologic disorders such as sickle cell disease or polycythemia, and vaculitis. This disorder affects patients between the second and the fourth decades, although it occasionally has been reported in neonates.

US with color Doppler is the first imaging method of choice for diagnosis. Usually, US shows a triangular area without flow, being normal the rest of testicular parenchyma. However, in some patients this entity cannot be easily distinguished from a necrotic tumor, particularly when the segmental infarction has a round morphology. The diagnosis may be aided by MRI, as one of the most relevant findings is the presence of an enhanced rim surrounding the infarction. Other common findings are the characteristic wedge shape and the association with hemorrhagic foci. Fernández-Pérez et al. have described a slight retraction of the tunica albuginea in the area containing the lesion, during the evolution of segmental testicular infarction, indicating a loss of volume due to hyalinization and fibrosis occurring in the infarcted tissue. In addition to the radiologic findings, negative testicular tumor markers provide further reassurance. In a small percentage of cases, diagnosis may still be doubtful and a definite exclusion of testicular tumor may be difficult. In these situations, exploratory surgery with possible total or partial orchiectomy can be required.

# **Imaging Findings**

Scrotal ultrasound on transverse plane (Fig. 5.13) shows a well-circumscribed margin lesion (arrow), hypoechogenic and with wedge shape in the left testicle. Color Doppler US demonstrates as this lesion is hypovascular (Fig. 5.14). A coronal T2-weighted image on MRI (Fig. 5.15) shows a low signal intensity lesion in the left testis with triangular morphology. The rest of the testicular parenchyma is preserved. There is no hydrocele or other inflammatory findings in the testicular scrotum. Coronal T1-weighted (Fig. 5.16, arrow) MRI image after contrast administration allows the diagnosis of this lesion as hypovascular due to absence of enhancement within the lesion and also through the extension of the affected testicular parenchyma.

Case 5

**Spermatic Cord Torsion** 

A 17-year-old male was attended in the emergency room for acute testicular pain. The symptoms begun 10 h before and the patient did not mention previous trauma or fever. Physical examination showed a slightly ascended testicle compared to contralateral. Analytical results were irrelevant.

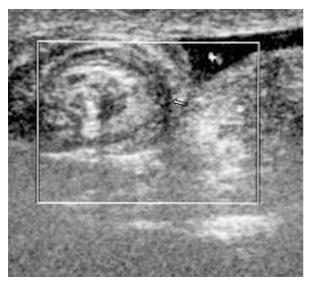


Fig. 5.17

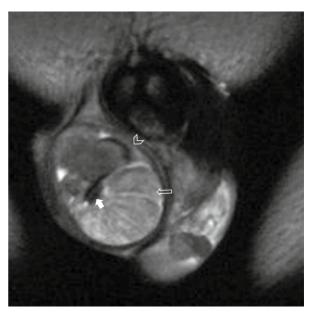


Fig. 5.18

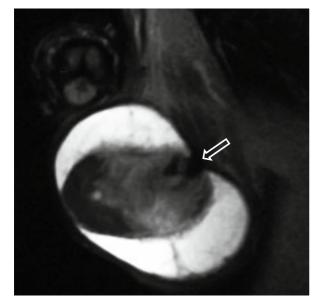
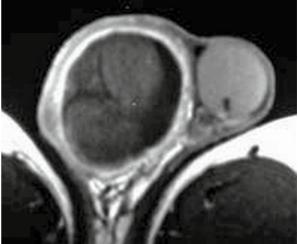


Fig. 5.19





# Comments

Testicular torsion is due to a rotation of the testis on the longitudinal axis of the spermatic cord. Taking into account the site of torsion spermatic cord, torsion can be classified into three groups: supravaginal, intravaginal, mesorchial torsion. The most frequent is the intravaginal torsion where the twist is located into the tunica vaginalis. Intravaginal torsion, caused by this congenital malformation of the processus vaginalis, accounts for 90% of cases. In this malformation, the tunica vaginalis covers not only the testicle and the epididymis but also the spermatic cord. This creates a "bell-clapper deformity" that allows the testis to rotate freely within the tunica vaginalis. Torsion is most frequent among adolescents with about 65% of cases presenting between 12 and 18 years of age. It occurs in about 1 in 160 males or 1 in 4,000 males per year before 25 years of age.

Torsion usually occurs in the absence of any precipitating event; only 4–8% of cases are a result of trauma. Other factors predisposing patients to testicular torsion include an increase in testicular volume (often associated with puberty), testicular tumor, testicles with horizon-tal lie, a history of cryptorchidism, and a spermatic cord with a long intrascrotal portion.

Torsion initially obstructs venous return. Subsequent equalization of venous and arterial pressures compromises arterial flow, resulting in testicular ischemia. The degree of ischemia depends on the duration of torsion and the degree of rotation of the spermatic cord. Ischemia can occur as soon as 4 h after torsion and is almost certain after 24 h. In one study, investigators quoted a testicular salvage rate of 90% if detorsion occurred less than 6 h from the onset of symptoms; this rate fell to 50% after 12 h and to less than 10% after 24 h. Rotation can range from 180° to more than 720°. Greater degrees of rotation lead to a more rapid onset of ischemia, but the degree of rotation rarely can be determined without surgical intervention.

Testicular torsion is characterized by excruciating one-sided testicular pain, with sudden swelling. Since the cord structures twist (like the strings of a puppet), the testicle elevates as well. Patients may have nausea and vomiting. Patients may also have abdominal pain. There may be a history of previous testicular pain. Fever may also accompany the testicular pain.

# **Imaging Findings**

Scrotal ultrasound on longitudinal view (Fig. 5.17) shows the "torsion knot" with typical whirlpool pattern (open arrow) which is highly specific findings of torsion of the spermatic cord. This pattern is detected as a lobulated mass in the supratesticular space with concentric layers because of coiling of the cord vessels.

Coronal T2-weighted images (Fig. 5.18) show the findings 10 h after initiation of symptoms. The testis has a heterogeneous sign with a striated pattern due to an edema and hemorrhagic changes in the testicular parenchyma (open arrow). Torsion Knot is seen between epididymis and testis (arrow). The epididymis is enlarged with low signal (arrowhead). Also the tunica vaginalis is thickened.

Sagittal T2-weighted image with fat saturation (Fig. 5.19) shows the late stage of this spermatic cord torsion where the testis has a low signal because of necrosis, fibrosis, and hemosiderin deposition following hemorrhagic infarction. The epididymis is markedly thickened with hemorrhage. Note the "torsion knot" (open arrow) representing the point of twist. Associated hematocele is also seen.

Axial T1-weighted MR image after contrast administration (Fig. 5.20) shows the absence of contrast enhancement in the torsed testis. A rim enhancement in the tunica vaginalis can be observed.





Fig. 5.21



Fig. 5.22





Fig. 5.23

Fig. 5.24

A 10-year-old boy was attended for acute onset of pain in the right testis. There was no history of fever, dysuria, or trauma. On physical examination, point tenderness was found superior to the right testicle with a bluish skin discoloration.

Torsion of the appendix testis is a twisting of a vestigial appendage that is located along the testicle. A testicular appendage is a vestigial remnant of the müllerian duct. At approximately 8 weeks of fetal development, the müllerian ducts remain in a craniocaudal direction and becomes the appendix testis, also known as the hydatid of Morgagni.

The testicular appendage is a polypoid structure, which measures 1–3 mm in length and is located on the anterior–superior aspect of each testicle at or near the groove formed by the head of epididymis and the testis. It is unknown which is the etiology for torsion of the appendix testis. Several causes have been proposed, including enlargement of the appendix testis at puberty, increased vascularity of the appendix testis, violent cremasteric reflexes, and trauma.

During an acute episode of torsion of the appendix testis, it can increase its size to over 1 cm because of edema, vascular congestion, hemorrhage, and infarction. Following torsion, the appendix testis may: detorse and return to its normal structure, undergo varying degrees of atrophy, fibrosis, inflammation, and calcification with or without undergoing detachment. Whenever the testis is detached it might become transformed into a calcified intrascrotal body; however, little evidence supports the suggestion that scrotal calculi can form because of calcification of the necrotic appendix.

Torsion of the testicular appendage was first described in 1922 by Colt et al. It is more common in the adolescence, although it has been described from 1 to 18 years, with the highest frequency occurring in boys between the ages of 10 and 13 years.

The patient's history is important in distinguishing torsion of the testicular appendages from testicular torsion and other causes of acute scrotum. Pain is usually acute, but pain may develop over time. Typically, it has a more gradual onset than testicular torsion and is located in the superior pole of the testicle. This is a key distinguishing factor from testicular torsion. A focal point of pain on the testicle is uncommon in complete testicular torsion. Systemic and urinary symptoms are absent. The presence of a nodule at the superior aspect of the testicle, with characteristic blue-dot appearance, is pathognomonic for this condition, but a blue-dot sign is present in only 21% of cases.

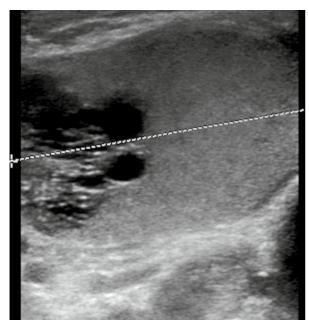
The treatment of choice is conservative. Pain usually resolves within 1 week and nonsteroidal anti-inflammatory drugs are administrated to reduce the pain and inflammation. In exceptional cases, uncontrolled pain can be relieved by surgical excision of the appendix.

Longitudinal US examination (Fig. 5.21) shows marked variation in appearance and size of normal testicular appendages which is variably hypoechoic centrally with a thick or thin echogenic periphery. The degree of echogenicity did not correlate with any temporal delay between symptoms and diagnosis. Transverse US (Fig. 5.22) shows partially enlarged appendages between the epididymis head and testicular parenchyma (*open arrow*). Axial T2-weighted (Fig. 5.23) MR image shows a small nodule between the left epididymis head and testis with low signal intensity (*open arrow*). Coronal T1-weighted MRI after contrast administration shows higher enhancement in the periphery of the appendages than in the center (Fig. 5.24, *open arrow*).

### **Comments**

# **Imaging Findings**

# Case 7 Cystic Transformation of the Rete Testis



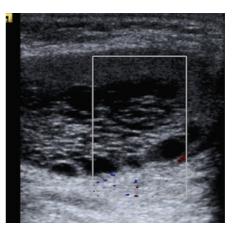


Fig. 5.26

Fig. 5.25

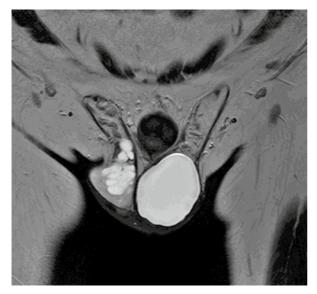






Fig. 5.28

A 46-year-old man had a low sperm count. In the course of the infertility evaluation an ultrasound was performed that showed bilateral tubular ectasia of the rete testis.

Benign intratesticular lesions are rare, but recognition is important to avoid unnecessary surgical intervention. Sonography is frequently the initial imaging technique for the evaluation of many scrotal diseases. In the normal testis, the seminiferous tubules merge at the apex of each lobule and connect with the tubuli recti. The tubuli recti then enter the mediastinum testis, forming irregular anastomosing spaces known as the rete testis. Several efferent ductules arise from the rete testis to form the head of epididymis.

Cystic transformation of the rete testis, also known as tubular ectasia, results from partial or complete obstruction in the epididymis or efferent ductules, which cause ectasia in the more proximal ductal system and, eventually, cystic transformation. Usually, the process occurs in men older than 55 years, and its involvement is frequently bilateral and asymmetric.

The keys to the diagnosis of this condition are; their location, always adjacent to the mediastinum testis and, their sonographic appearance as multiple anechoic spaces with no evidence of flow at Doppler US, without a focal solid component and the presence of epididymal cysts (spermatoceles). Spermatoceles have a high association with tubular ectasia of rete testis and can sometimes be large at up to 15 cm.

At MR imaging the dilated rete testis will be hypointense on T1-weighted images and isointense or hyperintense on T2-weighted images. This MR imaging appearance is in marked contrast to that of testicular tumors, which are low signal intensity on T2-weighted images.

It is important to differentiate this benign entity from malignant tumors of the testis and thus avoid unnecessary orchiectomy. Cystic malignant tumors, most commonly teratomas, can be distinguished sonographically by the presence of multiple cystic areas, often surrounded by a soft tissue rind. They are almost always unilateral and are not limited to the mediastinum. They can be further confirmed by measuring serum tumor markers.

# **Imaging Findings**

Longitudinal ultrasound scan of the left testis (Fig. 5.25) shows multiple avascular circular structures in the posterolateral region near the mediastinum testis, with no evidence flow at Doppler ultrasound (Fig. 5.26). Coronal T2-weighted MR image (Fig. 5.27) shows a cystic transformation of the right rete testis and a large epididymal cyst (spermatocele) in the left testis. Sagittal T2-weighted MR image of the left testis (Fig. 5.28) reveals the lesion as a high signal intensity with associated ipsilateral spermatocele.

### **Comments**

# Case 8 Fibrous Pseudotumor of the Testis

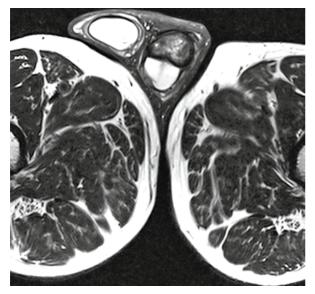


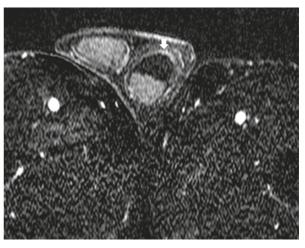
Fig. 5.29



Fig. 5.30









A 62-year-old man presented with a 2-year history of an irregular, non-tender, asymptomatic mass located in the left hemiscrotum. US and MR images confirmed a paratesticular mass.

# Fibrous pseudotumor of the testis is not a neoplasm but rather a benign fibroinflammatory reaction that results in the formation of one or more nodules, diffuse thickening, or a plaque-like process of the testicular capsule. A fibrous tumor is a painless tumor of the tunica that clinically mimics testicular and paratesticular neoplasms. Almost 75% of these pseudotumors arise from the tunica vaginalis, and the remainder arises from the epididymis, spermatic cord, or tunica albuginea.

Although fibrous pseudotumors are rare, they are the second most common mass involving paratesticular tissue behind adenomatoid tumors. Peak incidence is in the third decade, but these lesions have been observed over a wide age range (7–95 years). Many patients present after detecting a small circumscribed firm mass in the scrotum. Patients commonly relate a history of hydrocele, trauma, or infection. Hydrocele represents the most frequently associated finding with the lesion and has been found in nearly 50% of cases of fibrous pseudotumor. Physical examination often reveals single or multiple smooth circumscribed nodules, rare thickening of the scrotal surface, and occasional satellite lesions within the adnexa.

The sonographic appearance is nonspecific and calcification is common, possibly secondary to the inflammatory process. At MR Imaging, owing to the presence of fibrosis, the lesion has low signal intensity on both T1-and T2-weighted images with variable enhancement.

The lesions present macroscopically as multiple nodules of varying sizes ranging from 0.5 to 8 cm, associated with fibrosis of the testicular tunics. At histologic analysis, the masses are typically composed of hyalinized collagen and granulation tissue, and they may be extensively calcified.

The diagnosis of these lesions is difficult, but recognition of the benign nature of this entity should allow for a more conservative scrotal evaluation rather than orchiectomy.

# **Imaging Findings**

T2-weighted MR image shows a single round, paratesticular mass markedly hypointense on axial (Fig. 5.29) and sagittal plane (Fig. 5.30) with a pedunculated attachment to the tunica vaginalis (open arrow). Minimal hydrocele is present. Unenhanced axial T1-weighted fat-suppressed image (Fig. 5.31) and dynamic-enhanced following the administration of gadolinium chelate contrast agent (Fig. 5.32) demonstrate no appreciable enhancement of the mass (arrows).

### **Comments**





Fig. 5.33

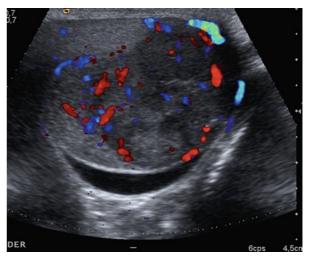


Fig. 5.34



Fig. 5.35



Fig. 5.36

A 27-year-old man presented with a right testicular mass and pain. The patient underwent sonography and MRI of the scrotum, which confirmed the mass.

# Testicular cancer is the most common neoplasm in boys and young adults, and represents 1% of all malignancies in men. One of the primary indications for scrotal Imaging is to evaluate for the presence of intratesticular tumor in the setting of scrotal enlargement or a probable abnormality at physical examination. The presence of a solitary intratesticular solid mass is highly suspicious for malignancy. Germ cell tumors constitute 95% of all testicular tumors and seminoma is the most common histological subtype which accounts for 35–50%. Compared to the nonseminomatous tumors, seminoma occurs in a somewhat older population, with a mean age of approximately 40 years. An estimated 5–25% of men with testicular seminomas have elevated levels of $\beta$ -hCG, which is produced by syncytiotrophoblastic giant cells. However, the elevated level of $\beta$ -hCG is not typically high enough to cause clinical symptoms, such as gynecomastia.

At the time of the diagnosis, approximately 75% of patients present with disease limited to the testis, 20% have retroperitoneal adenopathy, and 5% have extranodal metastases. However, the prognosis is favorable, resulting in a 5-year survival rate of 95%, due to their sensitivity to radiation and chemotherapy.

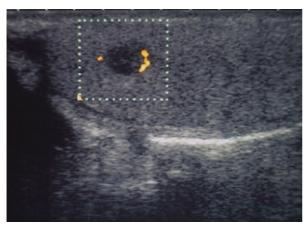
Imaging findings of seminomas reflect the uniform cellular configuration of these tumors. US typically demonstrate a rounded, well-circumscribed, hypoechoic, and homogeneous mass that does not contain significant cystic or calcific foci. Seminomas range in size from a small well-defined lesion to large masses that totally replace the testicle. They may be lobulated or multinodular; however, these nodules are most commonly in continuity with one another. Bilateral tumors are also rare, occurring in 2% of patients, and are almost always asynchronous. At MR imaging, seminomas are usually homogeneously hypointense and relatively isointense to the normal testicular parenchyma on T1-weighted images and hypointense on T2-weighted images. Band-like structures of low signal intensity on T2-weighted images may be detected within these tumors, corresponding to the fibrovascular septa. After gadolinium administration there is a heterogeneous enhancement of the mass. However, fibrovascular septa often show a greater enhancement than the tumoral tissue. The tumor is less aggressive than other testicular neoplasms and is therefore usually confined to the tunica albuginea.

# **Imaging Findings**

Longitudinal ultrasound of the right testis shows a rounded hypoechoic mass (Fig. 5.33). On color Doppler imaging, the mass shows increased vascularity and feeding vessels (Fig. 5.34). Small right hydrocele is also seen. Coronal T2-weighted image shows multinodular intratesticular mass lesions (Fig. 5.35). This tumor is homogeneous and hypointense on T2 compared with normal testicular parenchyma. Multiple septa (arrows) are detected within the lesion, both on T2-weighted and contrast-enhanced T1-weighted images (Fig. 5.36). These are typical findings for seminoma.

### **Comments**

# Case 10 Leydig Cell Tumor of the Testis



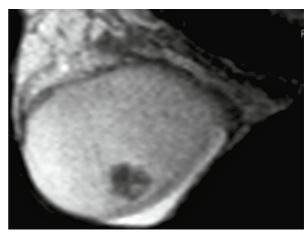
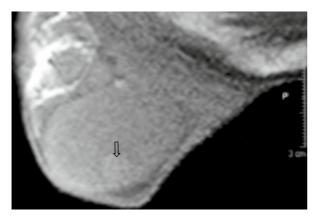
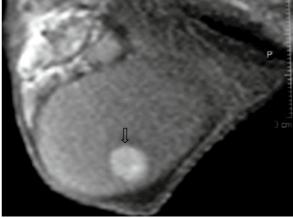


Fig. 5.37

Fig. 5.38









A 21-year-old man with gynecomastia was referred for US examination. He had never had pain or swelling on the scrotum and physical exploration was irrelevant. Laboratory results including tumoral markers were normal.

# Leydig cell tumors (LCTs) are rare testicular tumors of the male gonadal interstitium. They are frequently hormonally active, leading to feminizing or virilizing syndromes. They are the most common sex cord-stromal tumors and comprise 1–3% of all testicular neoplasms. These tumors are most common in prepubertal boys aged 5–10 years and in adults aged 30–60 years. LCTs are usually benign, but malignant variants also occur.

Adults usually complain of testicular swelling, but in many cases gynecomastia causes the patient to seek medical attention. In several adult patients with gynecomastia an impalpable tumor is detected by US. Other symptoms are decrease in libido or potency. In children, symptoms of isosexual pseudoprecocity can be noted. In these cases, they have small tumors more frequently, thus requiring devoted studies for its detection. Approximately 10% of patients are asymptomatic and tumors are discovered on physical examination. Rare cases have been described associated with cryptorchidism and Klinelfelter's syndrome.

The mechanism of Leydig cell oncogenesis is still poorly understood. The disruption of the hypothalamic-pituitary testicular axis leading to excessive stimulation of Leydig cells by excess luteinizing hormone is thought to play an important role in the pathogenesis. However, structural changes of the luteinizing hormone receptors and G proteins in Leydig cells have been postulated to induce tumorigenesis. Although these tumors usually secrete testosterone, the production of estrogen, progesterone, and corticosteroids have also been described. Estrogen excess and feminizing syndromes may occur from the peripheral aromatization of testosterone or from the direct production of estradiol by the tumor itself.

It should be emphasized that when patients present with either feminizing or virilizing symptoms, clinicians should consider LCT in the differential diagnosis and examination of the testis is warranted. Clinicians should be aware that a LCT cannot be excluded if a mass is not palpable, as the tumor can be clinically occult. In these setting, a testicular ultrasonography should be performed. Laboratory studies in LCTs are nonspecific and US examination must be performed to exclude the possibility of LCTS. LCTs were once managed primarily with radical orchiectomy. However, the experience with conservative approaches has been growing, and enucleation has been used increasingly in both the adult and pediatric populations.

# **Imaging Findings**

Longitudinal US with color Doppler examination (Fig. 5.37) shows a small intratesticular solid lesion in the upper pole of the right testis. Vascularization of the lesion is increased compared to the adjacent testicular parenchyma. Sagittal T2-weighted MR image (Fig. 5.38) shows a well-defined low signal intensity lesion. High signal intensity foci secondary to central scars and a high signal intensity capsule are also present. On precontrast sagittal T1-weighted image (Fig. 5.39); the lesion is not practically visualized (open arrow). Marked enhancement on postcontrast sagittal T1-weighted images (Fig. 5.40) is a very reliable sign to differentiate these LCTs from other solid testicular tumors.

### **Comments**

# **Further Reading**

# Books

Bluth EI, Benson CB, Ralls CW, Siegel MJ (2007) Ultrasonography in urology: a practical approach to clinical problems. Thieme, Stuttgart

- Kim B, Hricak H, Hamm B (1995) Imaging of the scrotum: textbook and atlas. Lippincott Williams & Wilkins, Philadelphia
- Olivetti L, Grazioli L (2009) Imaging of urogenital diseases: a color atlas. Springer, Heidelberg
- Ulbright TM, Amin MB, Young RH (1999) Atlas of tumor pathology. Tumors of the testis, adnexa, spermatic cord and scrotum. Armed Forces Institute of Pathology, Washington, DC
- Zagoria RJ (2006) Genitourinary radiology: the requisites. Mosby, Philadelphia

# Web Links

http://www.ultrasound-images.com/

http://www.sonoguide.com

http://www.med.uottawa.ca/radiolog/assets/documents/gi\_gu\_ imaging/lectures/scrotal\_us\_with\_audio/scrotal\_us\_with\_ audio.html

http://www.mypacs.net/repos/mpv3\_repo/cgi/case-manager.pl

http://www.med-ed.virginia.edu/courses/rad/testicularUS/ index.htm

# Articles

- Ahmed HU, Arya M, Muneer A, Mushtaq I, Sebire NJ (2010) Testicular and paratesticular tumours in the prepubertal population. Lancet Oncol 11(5):476-483
- Avila NA, Premkumar A, Merke DP (1999) Testicular adrenal rest tissue in congenital adrenal hyperplasia: comparison of MR imaging and sonographic findings. AJR Am J Roentgenol 172(4):1003–1006
- Baldisserotto M, de Souza JC, Pertence AP, Dora MD (2005) Color Doppler sonography of normal and torsed testicular appendages in children. AJR Am J Roentgenol 184(4): 1287–1292
- Bhatt S, Jafri SZ, Wasserman N, Dogra VS (2011) Imaging of non-neoplastic intratesticular masses. Diagn Interv Radiol 17(1):52-63
- Bhatt S, Dogra VS (2008) Role of US in testicular and scrotal trauma. Radiographics 28(6):1617-1629
- Barwick TD, Malhotra A, Webb JA, Savage MO, Reznek RH (2005) Embryology of the adrenal glands and its relevance to diagnostic imaging. Clin Radiol 60(9):953–959
- Bilagi P, Sriprasad S, Clarke JL, Sellars ME, Muir GH, Sidhu PS (2007) Clinical and ultrasound features of segmental testicular infarction: six-year experience from a single centre. Eur Radiol 17(11):2810–2818
- Cassidy FH, Ishioka KM, McMahon CJ, Chu P, Sakamoto K, Lee KS, Aganovic L (2010) MR imaging of scrotal tumors and pseudotumors. Radiographics 30(3):665–683

- Cokkinos DD, Antypa E, Tserotas P, Kratimenou E, Kyratzi E, Deligiannis I, Kachrimanis G, Piperopoulos PN (2011) Emergency ultrasound of the scrotum: a review of the commonest pathologic conditions. Curr Probl Diagn Radiol 40(1):1-14
- Dudea SM, Ciurea A, Chiorean A, Botar-Jid C (2010) Doppler applications in testicular and scrotal disease. Med Ultrason 12(1):43-51
- Dogra V, Bhatt S (2004) Acute painful scrotum. Radiol Clin North Am 42(2):349–363
- Dogra VS, Gottlieb RH, Rubens DJ, Liao L (2001) Benign intratesticular cystic lesions: US features. Radiographics 21 Spec No:S273–S281
- Enríquez G, Aso C (2008) Sonographic appearance of the epididymis in pediatric testicular torsion. AJR Am J Roentgenol 190(1):W74
- Fernández-Pérez GC, Tardáguila FM, Velasco M, Rivas C, Dos Santos J, Cambronero J, Trinidad C, San Miguel P (2005) Radiologic findings of segmental testicular infarction. AJR Am J Roentgenol 184(5):1587–1593
- Gotto GT, Chang SD, Nigro MK (2010) MRI in the diagnosis of incomplete testicular torsion. Br J Radiol 83(989):e 105–e 107
- Kim W, Rosen MA, Langer JE, Banner MP, Siegelman ES, Ramchandani P (2007) US-MR imaging correlation in pathologic conditions of the scrotum. Radiographics 27(5): 1239–1253
- Lin EP, Bhatt S, Rubens DJ, Dogra VS (2007) Testicular torsion: twists and turns. Semin Ultrasound CT MR 28(4):317–328
- Maizlin ZV, Belenky A, Kunichezky M, Sandbank J, Strauss S (2004) Leydig cell tumors of the testis: gray scale and color Doppler sonographic appearance. J Ultrasound Med 23(7):959–964
- Bertolotto M, Derchi LE, Sidhu PS, Serafini G, Valentino M, Grenier N, Cova MA (2011) Acute segmental testicular infarction at contrast-enhanced ultrasound: early features and changes during follow-up. AJR Am J Roentgenol 196(4):834–841
- Parker PM, Pugliese JM, Allen RC Jr (2006) Benign fibrous pseudotumor of tunica vaginalis testis. Urology 68(2):427. e17-427.e19, Review
- Rubenstein RA, Dogra VS, Seftel AD, Resnick MI (2004) Benign intrascrotal lesions. J Urol 171(5):1765–1772, Review
- Tsili AC, Argyropoulou MI, Giannakis D, Sofikitis N, Tsampoulas K (2010) MRI in the characterization and local staging of testicular neoplasms. AJR Am J Roentgenol 194(3):682–689
- Watanabe Y, Nagayama M, Okumura A, Amoh Y, Suga T, Terai A, Dodo Y (2007) MR imaging of testicular torsion: features of testicular hemorrhagic necrosis and clinical outcomes. J Magn Reson Imaging 26(1):100–108
- Woodward PJ, Schwab CM, Sesterhenn IA (2003) From the archives of the AFIP: extratesticular scrotal masses: radiologic-pathologic correlation. Radiographics 23(1):215–240, Review
- Woodward PJ, Sohaey R, O'Donoghue MJ, Green DE (2002) From the archives of the AFIP: tumors and tumorlike lesions of the testis: radiologic-pathologic correlation. Radiographics 22(1):189–216

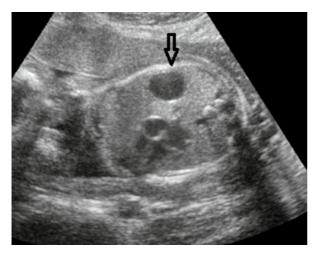
# **Obstetrics**

Marcelo Potolicchio, Antonio Luna, and Joan C. Vilanova

# Contents

Case 1	Pulmonary Cystic Adenomatosis	116
Case 2	Arthrogryposis	120
Case 3	Harelip	122
Case 4	Fetal Myelomeningocele	124
Case 5	Fetal Renal Polycystosis	126
Case 6	Down Syndrome	128
Case 7	Edward's Syndrome	130
Case 8	Fallot's Tetralogy	134
Case 9	Congenital Spondyloepimetaphyseal Dysplasia (SEDC), Strudwick Type	136
	Su uuwick Type	130
Case 10	Fetal Lissencephaly	138

# Case 1 Pulmonary Cystic Adenomatosis



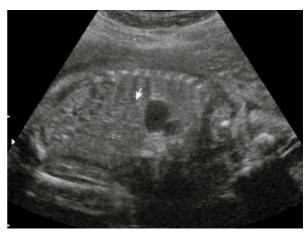


Fig. 6.2

Fig. 6.1

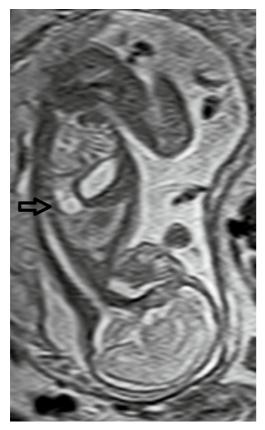
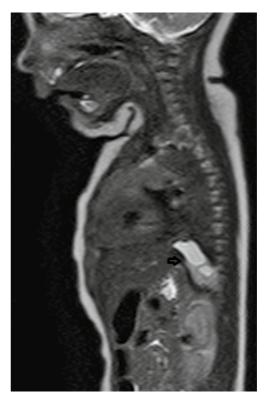


Fig. 6.3



An expectant woman in the 24th gestational week was referred for further evaluation of two pulmonary cystic masses detected on routine US examination.

# Comments

Congenital cystic adenomatoid malformation (CCAM) is a benign hamartomatous or dysplastic tumor characterized by the overgrowth of the terminal bronchioles and the decreased number of alveoli. It has an incidence of one in 5,000 live births. It represents about 25% of all congenital pulmonary lesions, and represents more than 75% of all the pulmonary lesions detected in fetuses. The cause is not known although genetic interaction has been suggested.

It is characterized by a multicystic mass containing primitive pulmonary tissue and anomalous bronchial and bronchiolar structures inside the lung, unilateral and lobular being more common. Usually, CCAM communicates with the tracheobronchial tree and is vascularized by a branch of the pulmonary artery, which reflects its origin as an aberration of the pulmonary development.

A more recent classification describes five subtypes of CCAM: Type 0: it shows acinar dysplasia or agenesis without pulmonary tissue. Type 1: There is a large or predominant cyst (macrocystic) of 3–10 cm, which compresses the normal parenchyma. Type 2: It is characterized by a mixture of solid tissue and small cysts (<2 cm). Type 3: It is a solid adenomatoid malformation with minor cystic components, and Type 4: It is formed by a large peripheral cyst of distal acinar origin covered by alveolar type cells. It is not readily distinguishable either clinically or radiologically from type 1.

The risk of chromosomal anomalies associated with CCAM might be slightly increasing in the general population, although the exact risk is not known. A chromosomal study and a detailed examination of the fetal anatomy should be considered after a diagnosis of CCAM has been performed

Differential diagnosis includes:

- Cystic mass: Diaphragmatic hernia, teratoma, neuroenteric cyst, esophageal duplication, Hybrid CCMM or, less probably, pulmonary sequestration.
- Solid mass: Pulmonary sequestration; other less frequent possibilities are congenital lobar emphysema, bronchial atresia, or bronchogenic cyst.

CCAM appears as a solid or cystic lesion in the lung. It can be classified as microcystic or macrocystic. The macrocystic lesion contains one or multiple cysts with a diameter >5 cm. and has a very favorable prognosis.

On ultrasound microcystic lesions appear as a solid echogenic mass, based on innumerable acoustic interphases. It can produce a mass effect, compressing the esophagus and leading to reduced fetal swallowing with subsequent polyhydramnios. The large lesions are associated with displacement of the mediastinum and flattening of the diaphragm. Color Doppler US may be used to evaluate the presence of a pulmonary arterial supply, to differentiate from pulmonary sequestration, which is supplied by a systemic artery. The size of the mass, and not the size of the cysts inside the mass, is the most important factor influencing the prognosis. Displacement of the mediastinum is considered to be serious whether the heart is displaced against the contralateral side of the ribcage.





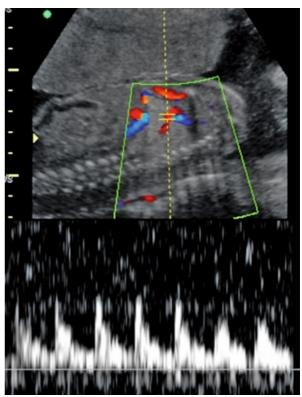


Fig. 6.6

On MRI microcystic lesions are homogenous and hyperintense on T2-weighted images compared to the lungs. The changes in the thoracic position of the pulmonary lobes, mediastinum and cardiac structure must be identified. The volume of the lesion can be measured more easily and reliably than using ultrasound.

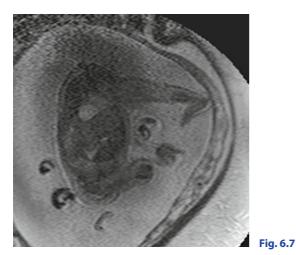
# Transverse ultrasound view shows the four heart chambers and the presence of a cystic lesion in the right lung (Fig. 6.1). Longitudinal US view demonstrates two supradiaphragmic cystic lesions in the right lung (Fig. 6.2).

MRI of the same fetus showing the supradiaphragmic cystic lesion (Fig. 6.3)

MRI of newborn confirming prenatal findings of cystic adenomatoid malformation (Fig. 6.4). US Imaging from pulmonary sequestration showing lobular triangular-shaped echogenic mass in the thorax with systemic blood supply (Figs. 6.5 and 6.6).

# **Imaging Findings**

Case 2 Arthrogryposis





An ultrasound at 34 week gestation showed a fetus with polyhydramnios, mild micrognathia, agenesis of the corpus callosum, microcephaly, flexion contracture of upper limbs and extension of lower limbs, rocker bottom feet, and cysts in the pelvic region.



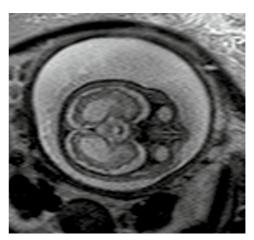
Fig. 6.8







Fig. 6.9



# Comments

Arthrogryposis multiplex congenita (cerebro-oculo-facio-skeletal syndrome) is a highly heterogeneous process with multiple fixed contractures, which can affect nearly all the joints. The major cause of arthrogryposis is fetal akinesia due to fetal abnormalities (e.g., neurogenic, muscle, or connective tissue abnormalities) or maternal disorders (e.g., infection, drugs, trauma, other maternal illnesses). Generalized fetal akinesia can also lead to polyhydramnios, pulmonary hypoplasia, micrognathia, ocular hypertelorism, and short umbilical cord. During early embryogenesis, joint development is almost always normal. Motion is essential for the normal development of joints; lack of fetal movement causes extra connective tissue to develop around the joint. In the majority of cases the disorders are usually symmetrical and affect all four extremities, although they may affect only the lower or the upper extremities.

The heterogeneous processes associated with arthrogryposis have given rise to confused terminology in the medical literature. Arthrogryposis generally leads also to other deformities, due to the absence or reduction of movement.

Symptoms for arthrogryposis vary from child to child but the most common characteristics are: Fetal akinesia/hypokinesia with skeletal deformation, thin muscles and the hips may be dislocated.

The processes which can be classified as arthrogryposis are: Pena Shokeir syndrome, lethal multiple pterygium syndrome, arthrogryposis multiplex congenita, Neu-Laxova syndrome and congenital muscular dystrophies or myopathies, Gaucher's disease type 2, Alpers' disease, trisomies 18 and 13 or Neurogenic arthrogryposis or cerebro-oculo-facioskeletal syndrome.

The most important ultrasound findings include the absence of fetal movement during the real-time exploration and serious flexion deformities with fixed limbs, arms flexed and hyperextension of the knees. The abnormal position of the extremities with restriction of movement is the key diagnostic feature, usually visible in the second or third trimester. Polyhydramnios, intrauterine growth retardation and pulmonary hypoplasia may develop. Low ear implantation, scalp edema, thoracic deformities, camptodactyly and micrognathia may be found. Cystic hygrosis and hydrops are relatively frequent findings during the first and second trimester associated with arthrogryposis multiplex congenita.

The prognosis is generally poor, especially for those cases diagnosed prenatally.

The ocular anomalies detectable by ultrasound on the cerebro-oculo-facio-skeletal syndrome are: microcephaly, micrognathia, cataracts, microphthalmia, agenesis of the corpus callosum, contracture of all the limbs and rocker bottom feet.

Fetal MRI showing a rocker bottom foot associated with amyoplasia (Fig. 6.7). 3D US Artrogriposis (cerebro-oculo-facio-skeletal syndrome) Extension contracture of both knees and flexion contracture of both elbows (Figs. 6.8 and 6.9).

3D US demonstrating low ear implantation and scalp edema (Fig. 6.10).

Fetal MRI shows cerebral disorders with microcephaly, atrophy of the cerebellum and brainstem and agenesis of the corpus callosum (Figs. 6.11 and 6.12).

# **Imaging Findings**







Fig. 6.14

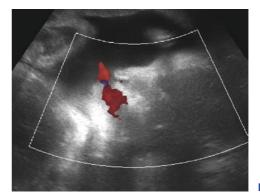
Fig. 6.13



Fig. 6.15



Fig. 6.16



A 36-year-old woman, who was 19 weeks pregnant, presented for a prenatal ultrasound.

Cleft lip (harelip) with or without a cleft palate is the most common facial malformation, occurring in approximately 1 in 700–1,000 live births. Approximately 80% of infants with cleft lip will also have a cleft palate. Male children are affected more often. In many neonates cleft lip and/or palate is an isolated anomaly, but in 29% there may be an underlying disorder. More than 200 recognized syndromes may include a facial cleft. The condition results during the fourth to sixth week of gestation from a failure of fusion of one or both of the medial nasal prominences.

Several classification systems exist. The Nyberg 1995 antenatal ultrasound classification system is one that correlates well with the severity of the defect and outcome:

Type I: Cleft lip (a linear defect which extends from one side of the lip towards the nostril) Type II: Unilateral cleft lip and palate (this can extend from alveolar edge and the hard palate, reaching the floor of the nasal cavity or even the floor of the eye socket).

Type III: Bilateral cleft lip and palate, frequently with premaxillary protrusion.

Type IV: Midline cleft lip and palate, ample midline separation with hypoplastic hemiface and absence of primary palate.

Type V: Amniotic bands and slash-type defects.

Identification of a facial cleft on prenatal imaging should alert the ultrasonographer to evaluate for other anomalies.

The malformation is usually paramedian and might be bilateral or unilateral. In the great majority of cases typical facial clefts have a multifactorial etiology. A median cleft lip is a much rarer abnormality and can be associated with holoprosencephaly and other intracranial anomalies.

At US, the defect is recognized as a gap in the upper lip seen on coronal views of the nose and lips. On sagittal views of the face, one may miss the defect if the view is obtained in the midline or if it is focused on the normal side of a fetus with a unilateral cleft lip and palate.

It is possible to see the magnitude of the process and discover whether the lesion is limited to the anterior edge of the palate or extends towards the posterior or secondary to the palate. In the axial and coronal projections of typical cases of bilateral cleft lip and palate (type III) a protrusion in the central part of the palate and lip (called premaxillary pseudomass) can be observed.

Color Doppler during swallowing is a useful tool for evaluating the defect. MRI can also be used in selected cases as it is helpful to evaluate the extension of the affected palate.

The prognosis of facial clefts mainly depends on the presence and type of the associated anomaly. Slight clefts, such as linear indentations of the lips or a submucous cleft of the soft palate, at times do not require surgery. The greatest defects cause aesthetic, swallowing, vocalization and respiratory problems.

Anterior coronal 2D ultrasound shows the medial lip defect type IV (Fig. 6.13).

3D US demonstrates the midline cleft lip and palate (type IV) with depressed nose (Fig. 6.14). Fetal MRI shows medial cleft compromising the lip and palate in coronal and sagittal plane, and clearly appreciating the extension of the defect to the entire secondary palate (Figs. 6.15 and 6.16). Color Doppler US in the longitudinal plane at swallowing shows the defect of the palate communication with the nasal cavity (Fig. 6.17).

### Comments

# **Imaging Findings**

# Case 4 Fetal Myelomeningocele





Fig. 6.19







Fig. 6.18

A fetus of 23 weeks of gestation presented a cerebral disorder in the posterior fossa and a cystic mass in the lumbosacral region on the prenatal ultrasound.

The term spina bifida refers to the incomplete closure of the bony elements (spinal laminae and apophyses) of the posterior part of the spine. This disorder is divided into open and closed.

Open spina bifida (85% of dorsal defects) predominates at birth and is a full-thickness skin defect, where the underlying soft tissues and vertebral arches are left exposed. The defect may be covered by a fine meningeal membrane, an extension of the dura mater and the arachnoid without neural tissue through the posterior spina bifida (meningocele). If there is neural tissue inside the sac the lesion is defined as myelomeningocele.

Closed spina bifida (15%) may be asymptomatic and can be an incidental finding. It is characterised by a vertebral schisis covered by skin. The skin is usually pigmented, depressed (dimple) or composed of areas of hypertrichosis. It is associated with a normal intracranial anatomy and a normal alpha fetoprotein.

Open spina bifida is always associated with cranial alterations, the most common is type II Arnold-Chiari malformation.

It is characterized by the displacement of the cerebellar tonsils, part of the cerebellum, the fourth ventricle, the annular protuberance and the medulla oblongata through the foramen magnum towards the spinal canal. In 95% of the cases it is accompanied by myelomeningocele and hydrocephalus.

The displacement of the cerebellum deforms the lateral lobes which lose their rounded form and the vermis notch, thus appearing more continuous (the banana sign).

Imaging findings include:

- Lemon-shaped cranium (deformity of the frontal bone)
- Dilation of the cerebral ventricles (70% in the second trimester)
- Obliteration of the cisterna magna
- Distortion of the cerebellum (banana sign)
- Separated lateral processes (fusiform thickening of the spinal canal) with the neural canal exposed in the posterior zone.
- Open spina bifida: Absence of the posterior line and the soft tissues. Appearance from a flat, non protruding defect to a dorsal sac with a cystic or solid lesion
- Displacement of the posterior elements.

The main differential diagnosis is cystic sacrococcygeal teratoma in cases where there is a cystic dorsal sac (the diagnostic key is the presence of cranial malformations associated with spina bifida).

Associated anomalies for myelomeningocele include alterations of the corpus callosum, or foot deformities (clubfeet or rocker bottom feet).

US examination shows a defect of the spinal canal and the presence of a dorsal sac with cystic appearance. The vertex of the lesion extends slightly above the iliac crest (L5-S1) (Figs. 6.18 and 6.19). Transversal plane on US at the level of the cerebellum shows the banana sign due to compression of the cerebellar hemispheres. Cisterna magna not visualized (Fig. 6.20). The lemon sign due to concave frontal bones (Fig. 6.21).

### **Comments**

# **Imaging Findings**

# Case 5 Fetal Renal Polycystosis

**Comments** 

A 30-year-old woman at 21 weeks gestation presented a fetal US examination with bilaterally symmetrical hyperechogenic kidneys.

Cystic renal disease comprises a heterogeneous group of inherited, developmental and acquired disorders. Potter's classification, although incomplete and without general acceptance, covers all the most important pathologies. Many other uncommon syndromes are associated with cystic renal disease, which should be known whenever hyperechogenic and multicystic kidneys are identified.



Fig. 6.22









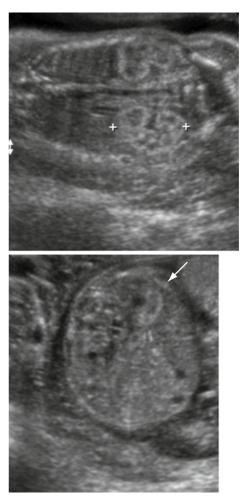


Fig. 6.23

Potter type I:	Autosomal recessive polycystic kidney disease (infants)
Potter type II:	Multicystic renal dysplasia
Potter type III:	Autosomal dominant polycystic kidney disease (adults)
Potter type IV:	Obstructive cystic dysplasia.

Autosomal dominant polycystic kidney disease (adults) has an incidence of 1/1,000 live births and is the most frequent hereditary cystic kidney disease. It is a systemic disorder characterised by the formation of cysts in the organs with ductules, especially the kidney and the liver, and occasionally might be present in the pancreas, spleen and central nervous system.

Ultrasound image is similar to that of autosomal recessive polycystic renal disease, presenting dilated, hyperechogenic, enlarged and symmetrical kidneys. The bladder is generally present and the amount of amniotic fluid is normal. Corticomedullary differentiation may be indistinguishable and some authors have described the presence of macroscopic cysts inside hyperechogenic kidneys. Renal hyperechogenicity is defined through comparison with the adjacent liver and spleen. It is difficult to evaluate during the first and second trimesters because, at the end of the second trimester the kidney is hyperechoic or isoechoic with respect to the liver. It is easy to determine from week 27 when the renal cortex should be hypoechogenic with respect to the liver. Increased cortical echogenicity may be due to the presence of multiple microcysts. The cysts only appear in later stages of adulthood although, exceptionally, cysts may be found during intrauterine life.

Associated anomalies are hepatic, splenic and pancreatic cysts but they are only present in adulthood. Non-cystic abnormalities include cardiopathies (mitral valve prolapse), skeletal anomalies, pyloric stenosis and intracranial aneurysms.

A prenatal genetic diagnosis can be performed by a chorion biopsy. The process is frequently asymptomatic and usually presents itself during the fifth decade of life.

It is difficult to determine the prognosis of cases diagnosed in utero. If there are affected siblings, later pregnancies will have a similar prognosis. The chance of acquiring a dominant disease is higher than the chance of acquiring a recessive disease.

The presence of at least two cysts in each kidney by age 30 in a patient with a family history of the disease can confirm the diagnosis of autosomal dominant PKD. If there is any question about the diagnosis, a family history of autosomal dominant PKD and cysts found in other organs make the diagnosis more likely.

# **Imaging Findings**

US imaging from a fetus at 27 weeks shows symmetric hyperechogenic enlargement of both kidneys, and pyelocalyceal ectasia in a patient being monitored from week 20. After week 27 the renal cortex should be hypoechogenic related to the liver (Fig. 6.22). Expectant mother at 21 weeks whose fetal morphological study revealed the presence of hyperechogenic, symmetrical kidneys with mild pyelocalyceal ectasia (Fig. 6.23). US shows a hyperechogenic fetal kidney compared to the liver or spleen at 27 weeks (Fig. 6.24). US demonstrates hyperechogenic kidney with no corticomedullary differentiation in trisomy 13 (Fig. 6.25).



Fig. 6.30

A 42-year-old woman, who was 22 weeks pregnant, presented for a prenatal ultrasound. Down syndrome is the most frequent autosomal trisomy in live births. The relevance of trisomy Comments 21 lies in the fact that it is the most frequent isolated genetic cause of mental retardation. Ultrasound Markers Cardiac malformations Cystic hygroma (31%) Ventriculomegaly/hydrocephalus: Ventriculomegaly is suspected when the atrial diameter exceeds 1 mm, although the separation of the choroid plexuses (more than 3 mm) depending on the medial ventricular wall may be visible proof of early dilation. Esophageal atresia Duodenal atresia (33%) Omphalocele Other Common Signs of Trisomy 21 Shortened limbs: The Femur/Foot Length Ratio is almost constant from week 14 to week 40 of gestation, with a median value of  $0.99 \pm 0.06$  standard deviation. A ratio below 0.87 is considered abnormal. Renal pyelectasis Nuchal thickening: Benacerraf et al. suggest that a threshold of 6 mm or more after week 15 indicates a high risk of trisomy 21. Currently, it is described that the excess of skin from a fetus with Down syndrome can be visualized by ultrasound as an increased Nuchal Translucency (NT) between weeks 11 and 14 of gestation (minimum fetal craniocaudal length 45 mm and a maximum of 84 mm). Intrahepatic calcification Brachycephaly Hyperechogenic bowel • Sandal gap (larger than normal gap between the big and second toes) • Widened pelvis • Absence or hypoplasia of the nasal bone. Unique umbilical artery: Non-specific data more frequently observed in healthy fetuses. Relation to Down (5%). • Clinodactyly (hypoplastic middle phalanx of the little finger) Small ears Hydropesia • Lack of fusion of the Amnion and Chorion during week 14. • Intracardiac echogenic focus (IEF). In low-risk populations when the focus appears in isolation and no other alterations are identified it is considered to be a "normal variant" and other tests are not usually recommended. US examination shows shortening of the femur in relation to the foot in a patient carrying a **Imaging Findings** fetus with trisomy 21 at 22 weeks of gestation. The Femur/Foot Length Ratio of 0.84 is considered abnormal (Figs. 6.26 and 6.27). US view demonstrates a unique umbilical artery (Fig. 6.28). US examination demonstrates an intracardiac hyperechogenic focus in trisomy 21 (Fig. 6.29). US in the axial and longitudinal plane depicts nuchal thickening in a fetus with trisomy 21 at 21 weeks (Figs. 6.30 and 6.31). The sandal gap sign is shown in the US image (Fig. 6.32).







Fig. 6.34









An ultrasound examination at 14 week gestation showed a cystic hygroma in the cervical region.

Edward's syndrome or Trisomy 18 has an estimated prevalence of 1/6,000–1/13,000 of live births. It occurs in all races and geographic areas.

It is characterised by low weight at birth, short stature, mental and psychomotor development retardation (delay in the acquisition of abilities which require the coordination of muscular and mental activity) and hypertonia (abnormally high muscle tone). It is accompanied by various visceral abnormalities.

There is a death rate of 90% during the first year of life. The 10% who survive suffer from severe mental retardation and disabilities. Medium- and long-term physical and mental development varies greatly among the survivors. The few patients who achieve long-term survival have marked psychomotor limitations.

Ultrasound Markers *Structural anomalies*:

- Cardiac malformations: defect of the auriculo-ventricular septum, patent ductus arteriosus, aortic coarctation, Fallot's tetralogy and double outlet right ventricle.
- Cystic hygroma: abnormal cystic masses of lymphatic origin which usually appear in the posterolateral area of the neck. They are often associated with fetal aneuploidy (18, 21 and Turner's syndrome). The frequency varies depending on the gestational age, the aspect, the presence of hydrops and other abnormalities. More than 60% of fetuses with cystic hygroma have chromosomopathies.
- Diaphragmatic hernia: It indicates a high risk of chromosomopathy, 18 being the most frequent.
- Hydrocephalus and spina bifida.
- Cerebellar dysgenesis: Associated with an enlarged cisterna magna. Generally diagnosed during the third trimester and associated with polyhydramnios.
- Micrognathia:
- Omphalocele: A central defect in the abdominal wall with herniation of the intraabdominal structures at the base of the umbilical cord.
- Clenched Wrist/Hands: The most characteristic finding is the fixed flexion of the hands, often with the fingers intertwined.
- Radial aplasia: This is a relatively common finding in trisomy 18; in fact, when radial aplasia is detected, the first consideration should be trisomy 18.
- Clubfeet (32%): Have been associated with several chromosomopathies, especially 18 and 13. Some authors recommend karyotype analysis in the presence of an isolated clubfoot since some mild associations may not be appreciated at the beginning of the second trimester.
- Rocker bottom feet (28%): similar to the base of a rocking chair instead of having the medial arch of the normal foot.
- Shortening of the limbs
- Arthrogryposis: Flexion deformities or movement disorders

# **Comments**

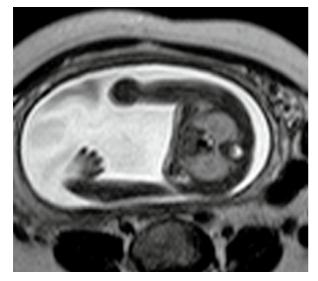
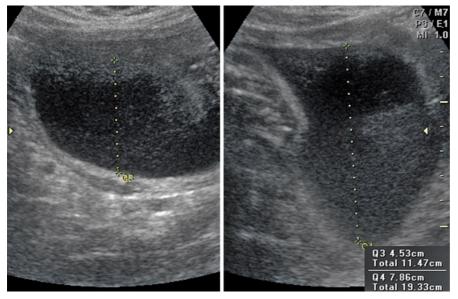


Fig. 6.37



Fig. 6.38





# Minor characteristics:

- Central nervous system: Agenesis of the corpus callosum, ventriculomegaly, dilation of the cisterna magna, Dandy Walker malformation, holoprosencephaly.
- Esophageal atresia (with or without traqueo-esophageal fistula)
- Craniofacial: Strawberry-shaped skull, hare lip, (the medial cleft being the most frequent), small ears with low implantation.
- Genitourinary: hydronephrosis, horseshoe kidney, bladder outlet obstruction, genital anomalies.

# Aneuploidy markers

- Choroid plexus cyst: found in 50% of fetuses with trisomy 18 and 1% in normal fetuses. A variant often seen during the second trimester. They are transitory and have no known effect on fetal development. When the karyotype is normal there is no known association. Observed choroid plexus cysts in 50% of the fetuses with trisomy 18 and in 1% of fetuses with a normal karyotype. The detection of choroid plexus cysts as an isolated finding after a detailed ultrasound analysis should not alter the obstetric treatment, assuming that the patient is considered low risk for aneuploidy.
- Strawberry-shaped skull: Brachycephaly is a common characteristic of trisomy 18. It is a non-specific finding more frequently observed in normal fetuses, the same as choroid plexus cysts, but an association between the two indicates a high risk of trisomy 18.
- Nuchal thickening of more than 6 mm in the second trimester.
- Unique umbilical artery: trisomy 18 is the aneuploidy most frequently associated with unique umbilical artery (10–50%)
- Shortening of the limbs
- Other findings:
- Intrauterine growth retardation
- Abnormalities of the amniotic liquid
- Umbilical cord cysts
- Non-immune hydrops: Ascites, pleural and pericardial effusion, polyhydramnios, thickening of the placenta and cutaneous edema are identified. 13% of fetuses with trisomy 18 have hydropesia/pleural effusion. The physiopathology implies congestive heart failure and lymphatic dysplasia.

# **Imaging Findings**

US examination in the axial and longitudinal plane at 14 weeks gestation shows a cystic hygroma in the cervical region of a fetus with trisomy 18 (Figs. 6.33 and 6.34). 2D, 3D ultrasound and MRI shows radial aplasia. The hand turns inwards and the forearm appears shortened (Figs. 6.35–6.38). US shows polyhydramnios in a fetus with trisomy 18 (Fig. 6.39).

Case 8 Fallot's Tetralogy



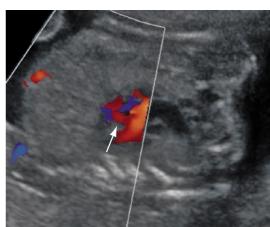
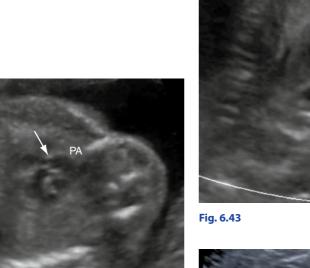


Fig. 6.41

Fig. 6.40









A routine ultrasound at 20 weeks of gestation showed a cardiac malformation

Fallot's tetralogy (FT) is the association of:

- 1. Subaortic interventricular septal defect.
- 2. Overriding aorta. It is usually accompanied by an increase in the caliber of the ascending aorta (the first sign for an experienced observer).
- 3. Infundibular pulmonary stenosis
- 4. Hypertrophy of the right ventricle, which only manifests itself after birth.

FT is the most frequent cyanotic heart defect, accounting for 7% of structural heart defects. The main pulmonary artery is small, and characterised by a superior and anterior deviation of the entrance or the infundibular septum with respect to the rest of the interventricular septum, giving rise to interventricular communication with a deficient alignment together with pulmonary and subpulmonary stenosis. The ascending aorta is dilated.

Chamber views, as interventricular communication involves the septal exit area, but this may not be appreciated unless the defect extends towards the septal entrance area or the tetralogy is associated with AV communication;

In three vessel views the alignment is abnormal. Instead of the vena cava, aorta and pulmonary artery being in a straight line there is an anterior and right displacement of the ascending aorta, with or without posterior displacement of the main pulmonary artery, but without altering the left to right order, which is maintained.

The obstructive lesion of the right ventricular infundibulum is characteristically observed. In 20% of cases no continuity is observed between the right ventricle outflow tract and the pulmonary trunk, a condition known as pulmonary atresia with ventricular septal defect, and the pulmonary circulation is maintained by the reverse flow in the ductus arteriosus (fetuses with duct-dependent circulation) or by collaterals which connect the systemic circulation to the pulmonary artery.

Various syndromes related to the chromosome 22q11 deletion are often associated with Fallot's tetralogy: pulmonary atresia, absence of pulmonary valve, atrioventricular defects, interruption of the aortic arch and aortic arch anomalies, hypoplasia or aplasia of the thymus.

An incorrect orientation of the transducer may show an aortic septal discontinuity reminiscent of aortic straddling and simulate the pathology. It should, therefore, be explored.

There is a good prognosis for isolated intrauterine Fallot's Tetralogy but worse for chromosomal or extracardial associations.

Surgery series show an operative mortality of 2%. The long-term prognosis is good.

Axial US view shows straddled aorta with the subaortic interventricular defect of a fetus with Fallot's tetralogy (Fig. 6.40, *arrow*). US Color Doppler mapping showing interventricular communication (Fig. 6.41, *arrow*). Cross section US showing infundibular pulmonary stenosis (Fig. 6.42). Axial US view demonstrates subaortic interventricular communication (Fig. 6.43, *arrow*). US examination shows Incorrect orientation of the transducer demonstrating an aortic septal discontinuity in relation to a reminiscent artifact of an inexistent straddling (Fig. 6.44, *arrow*).

### Comments

# Associated Anomalies

# **Imaging Findings**

## Case 9

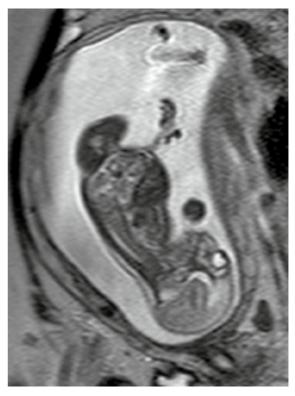
#### Congenital Spondyloepimetaphyseal Dysplasia (SEDC), Strudwick Type



Fig. 6.46



Fig. 6.48





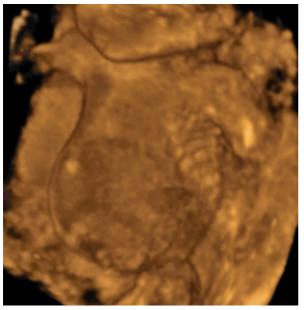


Fig. 6.45



Fig. 6.47

A 29-year-old woman at 20 weeks gestation presented a fetal US examination showing shortening of the trunk and neck and a curvature of the long bones.

#### **Comments**

Spondyloepimetaphyseal dysplasia, Strudwick type is an inherited disorder of bone growth that results in dwarfism, characteristic skeletal abnormalities, and problems with vision. The signs and symptoms of this condition at birth are very similar to those of spondyloepiphyseal dysplasia congenita. Spondyloepiphyseal dysplasia (SED) is a descriptive term for a group of disorders with primary involvement of the vertebrae and epiphyseal centers resulting in a short-trunk disproportionate dwarfism. Two major types of SED are recognized, namely, SED congenita and SED tarda. It is an autosomal dominant syndrome which is believed to be the result of alterations in type II collagen due to the presence of an abnormal COL2A1 gene. Strudwick type is a subtype of collagenopathy, types II and XI. Other syndromes which could be related are spondyloepimetaphyseal dysplasia, Kniest syndrome, achondrogenesis type II and Stickler syndrome.

The neck and spine are short, with platyspondyly and reduced intervertebral distance which produces kyphoscoliosis and lordosis. There is an absence of ossification of the pubis, calcaneous or astragalus. The long bones are short, with delayed mineralization of the epiphysis and curvature of the long bones which may be bowed. Often, a valgus alignment of the knees may develop, associated with overgrowth of the medial femoral condyle. Genu varum may also occur, though it is rare. Clubfeet may be present in some patients.

Increased incidence of lumbar lordosis and associated hip flexion contractures are observed even in the newborn period. The abdomen is protuberant. Thoracic scoliosis or kyphosis may become evident in adolescence. Single and double curve patterns have been noted. Thoracic kyphosis may be severe, measuring up to 130°. Kyphosis or kyphoscoliosis can be rigid and severe.

Associated ocular anomalies include myopia with retinal detachment (>50%) and cataracts. Other ocular manifestations include buphthalmos, secondary glaucoma, and strabismus; however, the corneas are clear.

Other associated conditions include deafness and abdominal or inguinal hernia. A rare form of SED congenita is associated with nephrotic syndrome.

It is compatible with life although affected adults are short in stature.

# US 3D volumetric and 2D image in the sagittal plane showing a globular abdomen and a small thorax with no pulmonary hypoplasia, related to shortening of the trunk (Figs. 6.45 and 6.46). US shows short, curved long bones characteristic of this syndrome (Fig. 6.47). 2D ultrasound in the sagittal plane showing a short neck and spine with platyspondyly and reduced intervertebral distance (Fig. 6.48). MRI in the sagittal plane shows the same findings as described on Fig. 6.48 (Fig. 6.49).



Fig. 6.50



5.76cm al 16.15cm

Routi





Fig. 6.52

A 36-year-old woman was submitted to a routine 28 week fetal ultrasound showing isolated ventriculomegaly of the posterior horns and polyhidramnios. The analysis of the fetal amniotic fluid did not reveal any chromosomopathy.

#### Comments

The term lissencephaly means "smooth brain". It corresponds to a severe malformation of the cerebral cortex, secondary to an impaired neuronal migration between the third and fourth months of gestation. The most common findings are either the absence (agyria) or the paucity (pachigyria) of cerebral convolutions, although other cranial and extracranial features may be present depending on the manifestations of associated syndrome. Lissencephaly is classified into two groups: Type I or classic lissencephaly, where neurons fail to reach the cortical plate, shows different degrees of agyria, pachigyria and/or subcortical band heterotopia. It is most commonly associated to Miller-Dieker or Norman-Roberts syndrome. Type II, or cobblestone complex, where neurons move into the subpial space. It is observed in some forms of congenital muscular dystrophy associated with cortical maldevelopment.

Prenatal diagnosis with ultrasound is difficult. Depending on the series, there are cases diagnosed between 23 and 31 weeks of gestation, as earlier. Cases associated to Miller-Dieker (type I lissencephaly) or Walker-Warburg (type II lissencephaly) syndromes are easier to diagnose due to associated intracranial malformations. Fetal MR allows detection and confirms the abnormal cortical development and associated abnormalities. MR also increases the conspicuousity of less severe forms of cortical dysplasia, which may not become evident in ultrasound until late in pregnancy or might never be detected. A variable rate of lissencephaly cases has an underlying genetic malformation. If a mutation is present, early prenatal diagnosis can be achieved with a DNA analysis and MR and genetic study of the mother is advised.

Obstetric ultrasound has become a routine tool performed in almost every pregnant woman. It is a safe and accurate marker of the gestation, allowing the detection of many fetal malformations or other types of complications. Fetal MR is a recent application of MR, due to the lack of use of ionizing radiation. It is most commonly used after the detection of a genetic, analytical or ultrasound abnormality, to establish or confirm a suspected diagnosis.

#### **Imaging Findings**

US axial images demonstrate isolated ventriculomegaly of posterior horns and polyhidramnios. Previous fetal ultrasound at 12 and 20 weeks were normal (Figs. 6.50 and 6.51). Fetal MRI performed at 31st week of gestation reveals: hypoplasia of corpus callosum, dilatation of posterior horns, delayed cerebral sulci development (corresponding to 26th week of gestation), agyria (absence of sulci and convolutions) (Fig. 6.52). MRI after birth confirmed the prenatal diagnosis of lissencephaly type I (Fig. 6.53).

#### **Further Reading**

#### Books

- Benacerraf BR (2008) Ultrasound of fetal syndromes. Churchill Livingstone, New York
- Callen P (2007) Ultrasonography in obstetric and gynecology. Saunders Company, Philadelphia
- Nyberg DA (2002) Diagnostic imaging of fetal anomalies. Lippincott Williams & Wilkins, Philadelphia
- Rumack CM, Wilson SR, Charboneau JW, Levine D (2011) Diagnostic ultrasound. Mosby, St Louis
- Woodward PL, Kennedy A, Sohaey R, Oh KY, Puchalski MD, Byrne JL (2008) EXPERTdd: obstetrics. Lippincott Williams & Wilkins, Philadelphia

#### Web Links

http://www.isuog.org http://www.sru.org http://www.ajog.org http://www.studiolift.com/fetal/site/ http://www.fetalsono.com/

#### Articles

- Benacerraf BR, Benson CB, Abuhamad AZ, Copel JA, Abramowicz JS, Devore GR et al (2005) Three-and 4-dimensional ultrasound in obstetrics and gynecology: proceedings of the American Institute of Ultrasound in Medicine Consensus Conference. J Ultrasound Med 24(12):1587–1597
- Cannie M, Jani J, Dymarkowski S, Deprest J (2006) Fetal magnetic resonance imaging: luxury or necessity? Ultrasound Obstet Gynecol 27(5):471–476
- Cesko I, Hajdú J, Marton T, Tóth-Pál E, Papp C, Papp Z (1998) Fetal atrioventricular septal defect associated with Patau and Edwards syndromes, as well as trisomy 22. Orv Hetil 139(18):1087–1089
- Chelli D, Dimassi K, Bouaziz M, Masmoudi A, Ben Jemaa N et al (2008) Prenatal ultrasound aspects of arthrogryposis multiplex congenita. Tunis Med 86(4):328–334
- Cho HJ, Won HS, Ju DH, Roh HJ, Lee PR, Kim A (2010) Evaluation of the usefulness of the fetal femur length with respect to gestational age to detect Down syndrome in Korean subjects. Prenat Diagn 30(8):734–738
- Dane B, Dane C, Aksoy F, Cetin A, Yayla M (2009) Arthrogryposis multiplex congenita: analysis of twelve cases. Clin Exp Obstet Gynecol 36(4):259–262
- Egan JF, Malakh L, Turner GW, Markenson G, Wax JR, Benn PA (2001) Role of ultrasound for Down syndrome screening in advanced maternal age. Am J Obstet Gynecol 185(5): 1028–1031
- Emmanuelli V, Lahoche-Manucci A, Holder-Espinasse M, Devisme L, Vaast P, Dieux-Coeslier A et al. (2010) Prenatal diagnosis of hyperechogenic kidneys: A study of 17 cases. J Gynecol Obstet Biol Reprod (Paris) 39(8):637–46

- Frates MC, Kumar AJ, Benson CB, Ward VL, Tempany CM (2004) Fetal anomalies: comparison of MR imaging and US for diagnosis. Radiology 232(2):398–404
- García-López MA, Bermúdez-Rojas Mde L, Oaxaca-Escobar C (2010) Prenatal diagnosis of cleft palate by 3D ultrasound. Ginecol Obstet Mex 78(11):626–632
- Kalish RB, Thaler HT, Chasen ST, Gupta M, Berman SJ, Rosenwaks Z, Chervenak FA (2004) First- and second-trimester ultrasound assessment of gestational age. Am J Obstet Gynecol 191(3):975–978
- Li H, Liu T, Liu C, Shang T (2007) Prenatal diagnosis and clinical prognosis of fetal hyperechogenic kidneys. Zhonghua Fu Chan Ke Za Zhi 42(4):236–238
- Martínez JM, Gómez O, Bennasar M, Olivella A, Crispi F, Puerto B, Gratacós E (2010) The 'question mark' sign as a new ultrasound marker of tetralogy of Fallot in the fetus. Ultrasound Obstet Gynecol 36(5):556–560
- Van den Hof MC, Wilson RD (2005) Fetal soft markers in obstetric ultrasound. J Obstet Gynaecol Can 27(6):592–636
- Nemec SF, Höftberger R, Nemec U, Bettelheim D, Brugger PC, Kasprian G et al (2011) Fetal akinesia and associated abnormalities on prenatal MRI. Prenat Diagn 31(5):484–490
- Nicolaides KH, Bindra R, Turan OM, Chefetz I, Sammar M, Meiri H et al (2006) A novel approach to first-trimester screening for early pre-eclampsia combining serum PP-13 and Doppler ultrasound. Ultrasound Obstet Gynecol 27(1):13–17
- Nicolaides KH (2011) Screening for fetal aneuploidies at 11 to 13 weeks. Prenat Diagn 31(1):7–15
- Paladini D, Sglavo G, Greco E, Nappi C (2008) Cardiac screening by STIC: can sonologists performing the 20-week anomaly scan pick up outflow tract abnormalities by scrolling the A-plane of STIC volumes? Ultrasound Obstet Gynecol 32(7):865–870
- Peisner D (2010) Importance of minor markers on the secondtrimester sonogram. J Ultrasound Med 29(9):1383
- Pereira S, Ganapathy R, Syngelaki A, Maiz N, Nicolaides KH (2011) Contribution of fetal tricuspid regurgitation in firsttrimester screening for major cardiac defects. Obstet Gynecol 117(6):1384–1391
- Emmanuelli V, Lahoche-Manucci A, Holder-Espinasse M, Devisme L, Vaast P, Dieux-Coeslier A, Dehennault M, Petit S, Besson R, Houfflin-Debarge V (2010) Prenatal diagnosis of hyperechogenic kidneys: a study of 17 cases. J Gynecol Obstet Biol Reprod (Paris) 39(8):637–646, Epub 2010 Sep 15
- Quarello E, Salomon LJ (2011) Quality control of first trimester US for Down syndrome screening: more questions than answers. Gynecol Obstet Fertil 39(6):335–338
- Sepulveda W, Wong AE, Fauchon DE (2011) Fetal spinal anomalies in a first-trimester sonographic screening program for aneuploidy. Prenat Diagn 31(1):107–114. doi:10.1002/pd.2608
- Sohan K, Freer M, Mercer N, Soothill P, Kyle P (2001) Prenatal detection of facial clefts. Fetal Diagn Ther 16(4):196–199
- Sonek J, Nicolaides K (2010) Additional first-trimester ultrasound markers. Clin Lab Med 30(3):573–592
- Yagel S, Cohen SM, Shapiro I, Valsky DV (2007) 3D and 4D ultrasound in fetal cardiac scanning: a new look at the fetal heart. Ultrasound Obstet Gynecol 29(1):81–95

## Uterus

Teodoro Martín Noguerol, Antonio Luna, and Joan C. Vilanova

#### Contents

Case 1	Bicornuate uterus	142
Case 2	Rokitanski Syndrome	144
Case 3	Uterine Leiomyomas	146
Case 4	Endometrial Polyp	148
Case 5	Adenomyosis	150
Case 6	Endometrial Cancer	152
Case 7	Recurrent Endometrial Cancer	154
Case 8	Imaging Follow-Up of Embolized Uterine Fibroid	156
Case 9	Hydatiform Mole	158
Case 10	Uterine Sarcoma	160

## Case 1 Bicornuate uterus

#### Comments

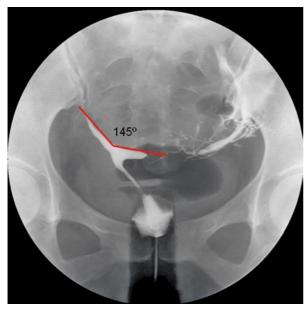


Fig. 7.1



Fig. 7.3

A 34-year-old woman had a history of repeated abortions. On transvaginal ultrasound, a double uterine cavity was identified. MR was performed for further assessment.

Müllerian anomalies are a group of malformations that usually result from a stop in development, an abnormal formation, or incomplete fusion of the mesonephric ducts. Their possible outcomes are uterine agenesis or dysgenesis, vaginal and cervical abnormalities or



Fig. 7.2





uterine malformations. These entities were classified by the American Fertility Society in 1988. They can be associated with other genital malformations, urological, rectal, or skeletal dysplasia. Exceptionally, it may be an acquired alteration. Its prevalence in fertile women is about 1%. The most common presentation is primary infertility or repeated abortions.

Three imaging techniques are traditionally used to study Müllerian abnormalities: transvaginal sonography, hysterosalpingography (HSG), and pelvic MRI. The first two are often used as screening tools, but they have some limitations to assess the outer contour of the uterus or to exclude other associated anomalies. HSG can only display the endometrial cavity. Today MRI is the imaging technique of choice, as it allows both adequate assessment of Müllerian anomalies and an accurate preoperative diagnosis. MRI study of uterine Müllerian anomalies usually includes T2-weighted acquisitions in the three planes or a 3D acquisition with isotropic voxel, which allows performing multiplanar reconstructions.

One of the most common anomalies is the existence of a uterine septum. Uterine septum is secondary to the absence of resorption of the medial segments of the paramesonephric ducts after their fusion, and it is formed by fibrous tissue. It is associated with a high rate of abortions, probably due to lack of blood flow at the septum. It may be partial or complete, and even, it may extend up to the cervix and vagina. The outer contour of uterine fundus is normal, smooth, and convex. The definitive diagnosis can be made by MRI or hysteroscopy:

Its main differential diagnosis is a bicornuate uterus, which is caused by an incomplete fusion of paramesonephric ducts, resulting in two endometrial cavities communicating with a single cervix. The degree of fusion can be variable. Externally, bicornuate uterus has an indentation of the contour of the uterine fundus, with a separation of the two horns and a bilobulated morphology.

HSG shows the uterine cervix with a single or two divergent uterine horns. The differential diagnosis must be made with a septated uterus based on the intercornual angle: if it is greater than 105°, it is considered diagnostic of a bicornuate uterus, and if less than 75°, it may correspond to a uterine septum. Definitive diagnosis is usually made either by MRI, which allows visualizing the external contour and nature of uterine septum (fibrous tissue or myometrium), or by hysteroscopy, which allows direct visualization.

The differentiation between these two diseases is important because treatment is different: a hysteroscopy-guided metroplastia is performed for a uterine septum, while a bicornuate uterus needs an open surgery in order to be corrected.

*Hysterosalpingogram.* Uterus is displaced to the right. Two divergent uterine horns are displayed, that have an intercornual angle greater than 105°. The left tube is permeable, while the right one is not well opacified (Fig. 7.1). Coronal multiplanar reconstruction T2-weighted image. Similar findings as on hysterosalpingography are shown, consistent with bicornuate uterus. Note the presence of a large subserosal fibroid at the uterine fundus (*arrow*) (Fig. 7.2) Pelvic sagittal T2-weighted image. Large subserosal fibroid is seen with hyperintense areas inside it, probable due to hyaline degeneration. Small amount of free fluid is identified on the Douglas pouch (Fig. 7.3). Pelvic postcontrast fat suppression fast gradient echo image. Heterogeneous enhancement of the fibroid is visualized. Note the presence of a small well-defined cystic lesion at the left adnexa (Fig. 7.4)

## Case 2 Rokitanski Syndrome











Fig. 7.6



Fig. 7.8

A 16-year-old girl was referred for study of primary amenorrhea.

The Mayer-Rokitansky-Küster-Hauser (MRKH) syndrome is characterized by a congenital aplasia of the uterus and the upper two-third of the vagina. These women have otherwise normal development of secondary sexual characteristics and normal external genitalia, with normal ovarian function, and karyotype 46 XX without visible chromosomal anomalies. It affects at least 1 of every 4,500 women. MRKH can be isolated (type I), but is more frequently associated with renal or vertebral anomalies, or auditory and cardiac defects (type II or association MRKH MURCS – Mullerian, renal, cancer, somites anomalies). Symptoms depend on the presence of rudimentary structures, but generally the first sign of MRKH is a syndrome of primary amenorrhea, being its second most common cause in young women after gonadal dysgenesis. It may be also manifested by recurrent abdominal pain or hematometra.

MRI is the most appropriate imaging test, which reveals an absent or very small uterus, cervix, or vagina, depending on the affected segment. The uterine remnants are usually better displayed in sagittal projections. In fact, up to 10% of cases may have a structure that shows a rudimentary Müllerian myometrium, with low signal on T2-weighted sequences, or it is possible to even identify a functional endometrium.

Sagittal fat suppression T2-weighted sequence depicts that uterus, cervix, or proximal vagina are not seen (Fig. 7.5). Axial T2-weighted sequences. There is no evidence of Müllerian rests between rectum and bladder. In a lower level, a rudimentary distal third of vagina is displayed (Figs. 7.6 and 7.7). Coronal T2-weighted sequence. Both adnexa are adequately seen with small peripheral follicular cysts (Fig. 7.8).

#### Comments





Fig. 7.9



Fig. 7.10

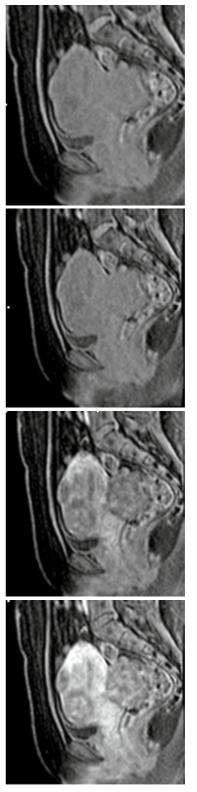


Fig. 7.11

A 39-year-old woman had a history of infertility. She was referred to our imaging department to perform HSG and pelvic MRI studies.

Leiomyoma, also known as myoma or fibroid tumor is the most common uterine mass with a prevalence between 30% and 40% of women on reproductive age.

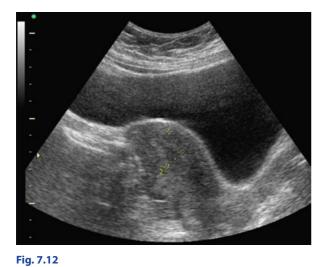
Fibroids are tumors derived from myometrial smooth muscle cells with a support of connective tissue. They are influenced by hormonal changes, growing in size with estrogens and decreasing with progesterone. A small percentage of them are symptomatic, which depends on its location: submucosal, intramural, or subserosal. Submucosal fibroids may clinically present as metrorrhagia or infertility. Intramural or subserosal could manifest as palpable abdominal mass if they reach a certain size, or as acute pelvic pain in the case of torsion, when they are pedunculated. Natural evolution of fibroids may be hyaline degeneration, fat necrosis or less often malignant transformation. Ultrasound (especially the transvaginal approach) has a detection rate of fibroids superior to 90%, and constitutes a first-line imaging test for diagnosis. The classic ultrasound appearance is a hypoechoic mass that deformates or increases the uterine contour. When there is doubt about the diagnosis, location, or number, the imaging technique of choice is pelvic MRI with gadolinium. On MRI, fibroids appear as well-defined lesions with low signal on both T1-weighted and T2-weighted sequences. They usually show a pseudocapsule that surrounds them with a thin hyperintense ring on T2-weighted sequences. After administration of gadolinium, fibroids shows lower enhancement than the myometrium. When there are degenerative changes, fibroids signal becomes heterogeneous, with high intensity on T2-weighted sequences and areas of absent enhancement. When bleeding or red degeneration occur, hyperintense foci appear on T1-weighted sequences. Fibroids can calcify in up to 5% of cases, which would result in low signal foci on MRI.

#### **Imaging Findings**

The Hysterosalpingogram shows a small filling defect within the endometrial cavity at the level of the uterine corpus. An abnormal uterine contour is also identified on both uterine edges (Fig. 7.9). The sagittal TSE T2-weighted sequence shows submucosal and intramural fibroids, as well as a large posterior subserosal one (Fig. 7.10). A postcontrast sagittal dynamic fat suppression fast gradient echo T1-weighted image demonstrates a progressive enhancement of the normal myometrium compared with hypoenhancement of the multiple fibroids (Fig. 7.11)

#### Comments

## Case 4 Endometrial Polyp



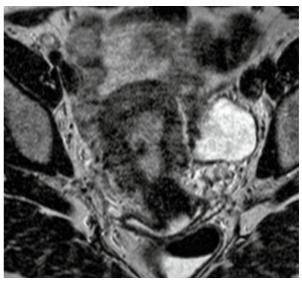


Fig. 7.13









A 47-year-old woman was referred due to hypermenorrhea and pelvic pain. US and MRI were requested for further assessment.

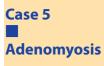
#### Comments

Endometrial polyps are very frequent, up to 10%, especially in perimenopausal women. It is believed to be related to glandular proliferation in response to estrogenic stimuli. Histologically they are composed by dilated endometrial glands within a vascular stroma. Clinically, they are associated with menstrual abnormalities and dysmenorrhea, although they may twist or even become malignant (less than 1% of cases).

The diagnostic approach may be performed by conventional imaging techniques such as hysterosalpingogram or ultrasound (including sonohysterography), and using MRI as a second-line test in doubtful cases. In hysterosalpingography, polyps are often displayed as pedunculated or sessile not mobile filling defects. In occasion, due to their small size, polyps may go unnoticed if the contrast is instilled quickly. On ultrasound, these lesions appear isoechoic with the endometrium, with the endometrial-myometrial line preserved and a visible stalk. On MRI, polyps are usually identified as isointense or slightly hypointense structures within the endometrium. Sometimes, polyps can become heterogeneous with small cysts within them, when they are larger. The differential diagnosis includes endometrial carcinoma, which does not enhance very intensely with gadolinium, as polyps do. However, it is not always possible to distinguish these two entities based on imaging findings, which could even coexist. Another differential diagnosis is submucosal fibroids, which tend to be more hypointense on T2-weighted sequences than polyps.

#### **Imaging Findings**

Pelvic ultrasound shows thickening of endometrial line with a heterogeneous, predominantly hypoechoic content (Fig. 7.12). High-resolution axial and coronal TSE T2-weighted MRI shows a hypointense nodule attached by a thin pedicle to the right wall of endometrium (Figs. 7.13 and 7.14). Postcontrast fat suppression fast gradient echo T1-weighted image demonstrates homogeneous enhancement of both endometrial line and polyp (Fig. 7.15).







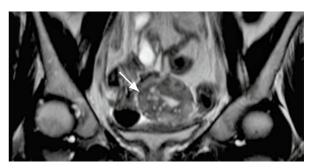


Fig. 7.17

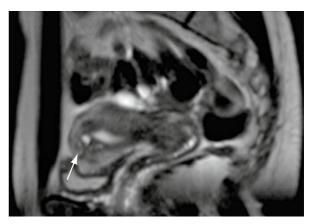
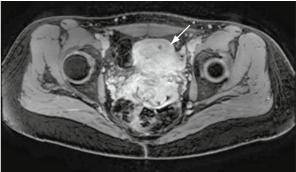


Fig. 7.18









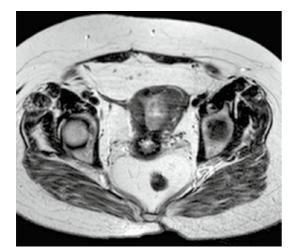
A 36-year-old woman was referred for infertility problems.

Adenomyosis is a disorder characterized by the existence of ectopic endometrial tissue within the myometrium. It typically appears in multiparous females among 30-55 years old. Clinical manifestations of this entity are metrorrhagia, abdominal pain, and even palpable mass because of the increased uterine volume by reactive hyperplasia of smooth muscle cells of the myometrium. The classic radiological appearance of adenomyosis on ultrasound is the presence of heterogeneous areas with low echogenicity within the myometrium. The presence of small dilated cystic glands within the heterotopic endometrial tissue may occur in up to 50% of patients. The ectopic tissue can be arranged in lines and causing the appearance of striations parallel to the endometrial lining causing a pseudowidening and poor demarcation of this line. Hysterosalpingography usually shows diverticula within the endometrium contour due to the introduction of contrast media within the subendometrial glands. T2-weighted sequences are the most useful MRI sequences for the study of adenomiosis, showing a thickening of the endomyometrial transitional zone, greater than 12 mm. Multiple hyperintense foci in the myometrium can be displayed on T2-weighted images representing small endometrial cysts or small hemorrhages, which will appear also as hyperintense areas on T1-weighted sequences. An overall increase in uterine volume is common. The differential diagnosis includes leiomyomas and focal adenosis, which is more elliptical, less well defined, and it does not show a clear mass effect.

Hysterosalpingography identifies bilateral pseudodiverticular lesions on both uterine horns, with an irregular uterine contour due to filling of subendometrial ectopic glands (Fig. 7.16). Coronal and sagittal T2-weighted images show ill-defined thickening of the transitional zone, with decreased signal intensity and small cystic lesion within it, consistent with adenomyosis (Figs. 7.17 and 7.18). Axial fat suppression T2-weighted image demonstrates similar findings as on Figs. 7.17 and 7.18. Note also the presence of small hyperintensity foci communicating with the endometrial cavity (Fig. 7.19) The postcontrast fat suppression fast gradient echo T1-weighted image displays small hypointense foci at the transitional zone at the level of the left uterine horn. The rest of the myometrium shows homogeneous enhancement (Fig. 7.20)

#### Comments





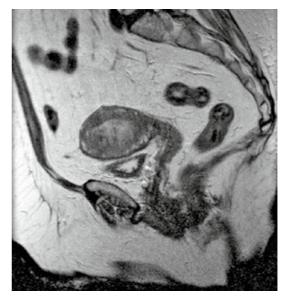


Fig. 7.22

Fig. 7.21





Fig. 7.24

Fig. 7.23

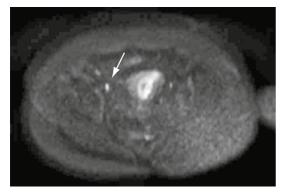
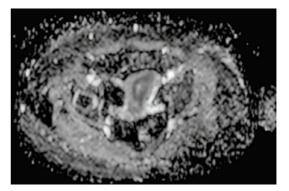


Fig. 7.25





A 76-year-old woman was referred for endometrial cancer staging.

Endometrial carcinoma is the most common gynecologic malignancy in developed countries. This cancer mainly appears in postmenopausal women. Signs and symptoms of presentation, mainly bleeding, help early diagnosis in more than 80% of cases, which show an initial FIGO stage I, without extrauterine extension. The FIGO classification is the most common staging tool. The invasion of the cervix, stage II, occurs in up to 10% of cases. Involvement of pelvic structures (stage III and IV) is less common. The lymphatic spread usually correlates with the degree of myometrial invasion, and the presence of pelvic or retroperitoneal lymph nodes is not rare. Distant metastases are more common to the lungs. Adenocarcinomas account for 80–90% of all endometrial carcinomas.

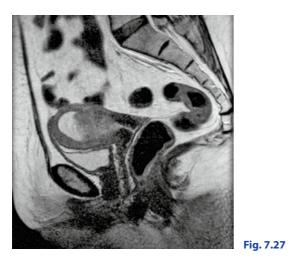
Both ultrasound and MRI are the most common techniques for the study of endometrial carcinoma. Ultrasonography is an acceptable first-line modality to assess postmenopausal bleeding. An endometrial thickness of 5 mm has a sensitivity of over 95% for endometrial cancer detection. A thickened endometrium is usually identified, with irregular or poorly defined small cystic lesions within it. Moreover, MRI is the technique of choice for presurgical staging especially in cases with difficulty in the biopsy or in which there are doubts among cervical or uterine origin of the primary tumor. MRI has shown its superiority over other techniques (US and CT) in tumor staging of endometrial cancer. There are three items to be investigated; myometrial involvement, cervical stroma integrity, and the presence of locoregional lymph nodes. T2-weighted sequences and dynamic contrast T1 are commonly used for tumor staging. After gadolinium administration, endometrial cancer usually enhances less than neighboring myometrium, but enough to distinguish it from hematometra. Disruption of the junctional zone by a hyperintense lesion is indicative of myometrial invasion. Disruption of the hypointense cervical stroma on T2-weighted sequences with endocervical canal widening is highly suspicious of cervical invasion. MRI also enables to rule out invasion of adjacent pelvic structures and to exclude the presence of lymph nodes. Diffusion-weighted sequence is a promising tool to increase the sensitivity and specificity for tumor and lymph node characterization.

Axial and sagittal T2-weighted images confirm a diffuse endometrial thickening at the left uterine horn. It affects the entire myometrial thickness without deforming the external uterine contour. It extends through the cervical canal but the stromal ring is preserved. These findings are consistent with stage IIA (Figs. 7.21 and 7.22).

Pre- and postcontrast fat suppression fast gradient echo T1-weighted image. Note the hypovascular appearance of the mass compared to the surrounding myometrium (Figs. 7.23 and 7.24). EPI DWI with a b value of 1,000 s/mm<sup>2</sup> and corresponding ADC map show markedly restriction of the free water diffusion within the endometrial lesion and a small right iliac lymph node with restricted diffusion corresponding to a metastatic lymph node (Figs. 7.25 and 7.26).

#### Comments

Case 7 Recurrent Endometrial Cancer





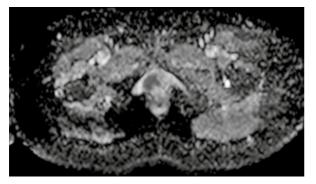


Fig. 7.32

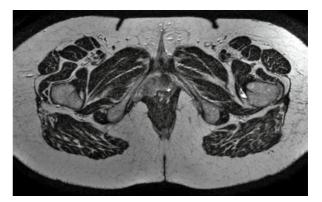


Fig. 7.28

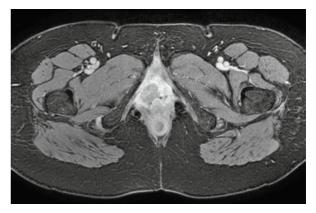
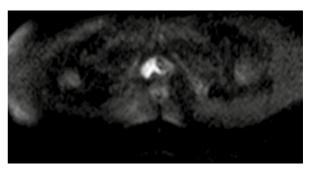
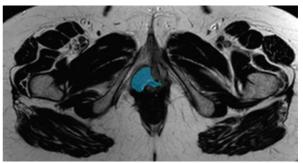


Fig. 7.30









A 65-year-old woman diagnosed of endometrial adenocarcinoma 3 years ago was treated with hysterectomy. She is referred to our department to perform an MRI follow-up (stage IB G2).

The survival and recurrence rates of endometrial carcinoma are closely related to its preoperative staging. The overall survival rate for this disease is about 77%. For stage I disease, survival is 86% at 5 years, and in stage IV cases is 16%. This survival rate is mainly due to the high percentage of patients diagnosed with stage I, which stands at 73%. Although a recurrent endometrial carcinoma may be occasionally diagnosed even after 10 years of the initial treatment, it will normally appear in the first 5 years after treatment.

The vagina is the sole site of recurrence in 30–50% of patients with endometrial carcinoma recurrence; the remaining patients develop pelvic or paraaortic lymph node metastasis or systemic spread manifesting as hepatic, pulmonary, or osseous metastasis or even peritoneal carcinomatosis.

There are three mechanisms which can explain the vaginal recurrence in endometrial carcinoma; implantation or seeding of the cancer cells in the vaginal vault at the time of surgery, lymphatic spread, and venous spread.

The degree of dedifferentiation and depth of endometrial muscle invasion also increase the risk for the development of vaginal recurrence.

On pelvic MRI, vaginal vault recurrence is characterized by loss of the low-signalintensity linear configuration of the vaginal vault and visualization of an associated softtissue mass of heterogeneous signal intensity on T2-weighted images, similar to that of the primary tumor. Sometimes, it is difficult to distinguish these findings from postirradiation changes. Dynamic contrast-enhanced MRI has been shown to be helpful in improving the specificity and accuracy of tumor recurrence detection, as it demonstrates maximum enhancement between 45 and 90 s after contrast administration. However, early irradiation changes and the presence of infection could simulate recurrence and continue to pose a diagnostic dilemma, because both entities may show enhancement. Serial imaging, imaging-guided biopsy, or PET may be required to further clarify this situation. Diffusionweighted MRI imaging is a new tool useful in this distinction, due to its ability to detect areas of high cellularity related to tumor recurrence.

Sagittal T2-weighted MRI shows large endometrial mass that invades more than 50% of the myometrium. It also infiltrates the cervix but without disruption of the cervical stroma (Fig. 7.27). Axial and sagittal T2-weighted MRI images for follow-up after surgery. A slight hyperintense mass located in the right lateral side of the lower third of vagina is identified (Figs. 7.28 and 7.29). Postcontrast fat suppression fast gradient echo T1-weighted image shows moderate peripheral enhancement of the mass. Note the invasion of the right puborectal muscle (Fig. 7.30). EPI DWI with a b value of 1,000 mm/s<sup>2</sup>, ADC map and fusion image of the T2-weighted and DWI images. The mass shows a markedly restricted diffusion (ADC value of  $0.7 \times 10^{-3}$  s/mm<sup>2</sup>), better displayed on the fusion image, consistent with recurrence of endometrial adenocarcinoma (Figs. 7.31–7.33).

#### **Comments**

Case 8 Imaging Follow-Up of Embolized Uterine Fibroid

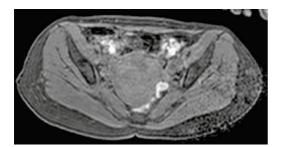


#### Fig. 7.34

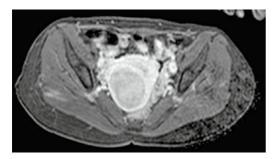


#### Fig. 7.35



Fig. 7.36



Fig. 7.37

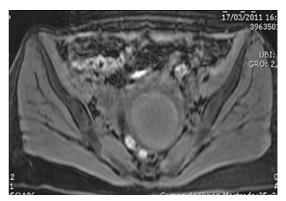


Fig. 7.38





A 28-year-old female with previous history of a large symptomatic fibroid and pregnancy desires was referred for embolization.

Uterine fibroids are the most common solid tumors of the female genital tract. They are benign and more than 50% of the affected women have no symptoms; for this reason they usually do not need treatment. When there are symptoms, hysterectomy has been, and remains as the only definitive solution adopted in many of these patients. In 1995, Ravina and colleagues proposed the uterine artery embolization (UAE) as an alternative treatment to surgery in women with symptomatic fibroids, a technique that has been proven as effective and safe, with lower incidence of major complications, than hysterectomy.

Women candidates to UAE have to satisfy the following criteria: symptomatic fibroids (meno-metrorrhagia or painful fibroids), women of reproductive age with uterine fibroids that prevent from pregnancy (fibroid as cause of primary infertility or repeated abortions). The type and location of fibroid is not a main contraindication for UAE.

Pretreatment evaluation of a patient with leiomyomas must include pelvic MRI to determine size, location, and contrast enhancement of uterine fibroids, as well as, alternative or unsuspected coexistent pelvic abnormalities. At least, a pre-embolization MRI study requires a T2-weighted sequence in the three planes and a dynamic postcontrast sequence. A timing bolus is recommended to obtain an adequate arterial phase during the dynamic acquisition, which will allow angiographic reconstruction of the uterine artery. MRI should be able to exclude the presence of vascular anomalies, and to determine the size, number, and location of fibroids, and intralesional characteristics such as bleeding or necrosis. These data are of great importance, as they may determine the outcome of embolization. The less necrosis exists, the greater fibroid volume reduction after embolization will become.

Follow-up 1 and 6 months after embolization by MRI is recommended, performing the same protocol as to evaluate the characteristics of the fibroids and to confirm the response to treatment. Hemorrhagic changes and lack of enhancement are sings of successful embolization.

#### **Imaging Findings**

Pre- and postcontrast fat suppression fast gradient echo T1-weighted image performed pre-embolization. Large slightly hypoenhancing intramural fibroid is seen at the posterior aspect of the uterus (Figs. 7.34 and 7.35). Pelvic angiogram before embolization shows both feeding uterine arteries and an ill-defined enhancement of the uterine fibroid (Fig. 7.36). Pelvic angiogram after embolization of both uterine arteries with microspheres depicts that there is no evidence of flow, either on the uterine vessels or within the uterine fibroid (Fig. 7.37). Pre and postcontrast fat suppression fast gradient echo T1-weighted image 1 month after UAE showing complete absence of enhancement within the fibroid, consistent with adequate embolization. Note the normal enhancement of the rest of the myometrium (Case courtesy of Dr. F. Garrido, Hospital Clínico, Granada, Spain) (Figs. 7.38 and 7.39).

#### **Comments**

Case 9 Hydatiform Mole

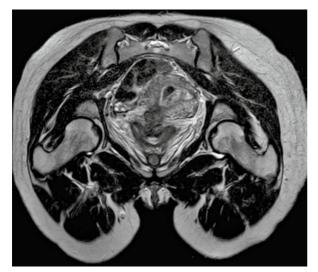


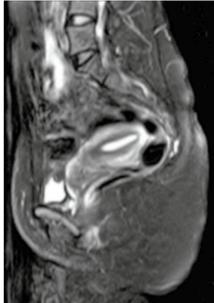
Fig. 7.40



Fig. 7.42









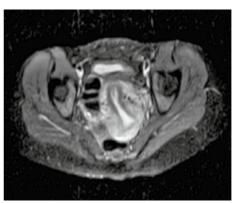


Fig. 7.44

A 34-year-old woman with recurrent gestational trophoblastic disease was referred to our department to perform follow-up imaging, after being treated by two curettages.

#### Comments

Gestational trophoblastic disease (GTD) is a set of benign and malignant diseases, resulting from an abnormal proliferation of trophoblast from the human placenta (hyperplasia) and the paternal genome, with an occasional maternal contribution.

From a clinical standpoint, GTD includes malignant entities such as choriocarcinoma and placental site tumor, and others. The main clinical risk is bleeding, especially for some complete moles (invasive), or the rare trophoblastic hyperplasia, sometimes complicated with partial moles. Others types are benign as most of partial and complete moles. Genital bleeding is the most common symptom in patients with complete mole, due to the separation of the molar tissue from the uterine wall. In general, the clinical features include symptoms and signs of a threatened abortion, and in some cases, the diagnosis is only performed after the histological examination of the abortion material.

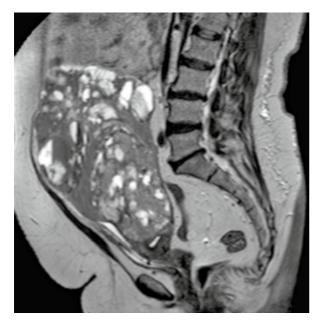
Since the beta HCG is used as a method of diagnosis and management of this disease, the use of imaging tests are limited to study the extension of the lesion. Transvaginal ultrasound is the first-choice technique for diagnosis and staging, but also to rule out the existence of the fetus or yolk sac. CT examination has proven to be useful in metastatic disease, especially for thoracic involvement. Pelvic MRI is very useful to assess the degree of myometrial invasion in patients with invasive mole or choriocarcinoma. Choriocarcinoma is usually seen as an intrauterine mass with heterogeneous high signal intensity on T2-weighted images. After gadolinium injection, the mass enhances markedly, consistent with the rich vascularity of the tumor, and even signal voids can be identified. Myometrial invasion is visible as high-signal-intensity foci within the myometrium, which demonstrate enhancement on postcontrast images. An enhancing parametrial soft tissue mass is characteristic of local spread.

Invasive mole is the less aggressive of the two forms of persistent gestational trophoblastic disease, seen in about 10% of cases after complete hydatidiform mole treatment (and less frequently in patients with partial hydatidiform mole). Patients usually present persistent bleeding and elevations in the serum of beta-HCG level.

Coronal and sagittal T2-weighted image shows a heterogeneous fundal uterine mass with hypointense areas which may correspond to foci of hemorrhage due to curettage. Note also the presence of an adnexal cyst (Figs. 7.40 and 7.41). Sagittal postcontrast fat suppression T1-weighted image demonstrates heterogeneous enhancement and miometrial extension (partially invaded) of the lesion (Fig. 7.42)

Sagittal and transverse fat suppression T2-weighted images of a pelvic MRI follow-up, performed after a third curettage, shows complete remission of the disease without evidence of either residual mass or myometrial invasion (Figs. 7.43 and 7.44).

Case 10 Uterine Sarcoma



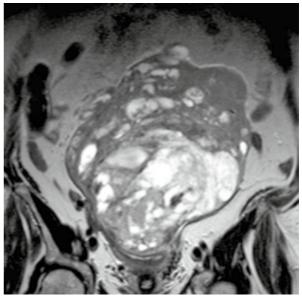


Fig. 7.46

Fig. 7.45

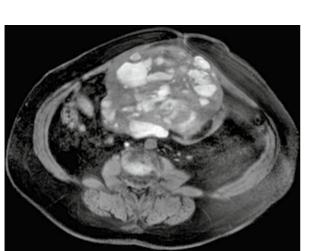
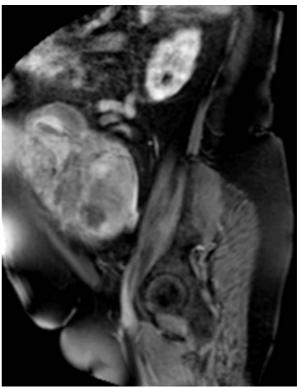


Fig. 7.47





A 56-year-old woman was referred for MRI evaluation of a large heterogeneous cysticsolid pelvic mass seen on a previous pelvic ultrasound.

Uterine sarcoma is a rare malignant tumor with poor prognosis, usually coursing with extraordinary aggressiveness. Its incidence is estimated to be 1.7/100,000 women over 20 years, their frequency ranges from 1% to 6% of malignant tumors of the uterus, and together accounts for 1–2% of malignant tumors of the female genital tract. The most common histologic variants are mixed Müllerian tumors (the most common type), leiomyosarcoma, endometrial stromal sarcoma, and rhabdosarcoma. The clinical course of sarcomas is quite unspecific. The most common symptoms are changes in the cadence and intensity of menstruation in premenopausal women and postmenopausal metrorrhagia, with a rapid increase in uterine size.

In many cases the diagnosis is made by endovaginal pelvic ultrasound in patients with bleeding. In other cases, the diagnosis is performed on the MRI examination in patients with known fibroids, where it shows areas of degeneration. Although most of the leiomyosarcomas arise de novo from the myometrium, malignant transformation of leiomyomas can occur too.

Uterine sarcomas are frequently large tumors at the time of the diagnosis, making it difficult to determine the primary origin of the mass. On MRI, these lesions usually show low or intermediate signal intensity on T1-weighted sequences, with small areas of high signal intensity on T1-weighted due to microhemorrhage. They also show areas with lack of enhancement after gadolinium injection. They appear as heterogeneous masses with high signal on T2-weighted images in more than 50% of the tumor volume. The differential diagnosis includes benign leiomiomas. Uterine sarcomas usually are larger and ill defined. They also show hypoenhancing areas with focal necrosis and intratumoral hemorrhage. These findings, along with the existence of local invasion and metastatic disease with peritoneal dissemination at the time of diagnosis, usually favor the diagnosis of uterine sarcoma. MRI has shown its accuracy to provide an adequate preoperative assessment of uterine size and the degree of involvement.

Treatment of uterine sarcoma is total hysterectomy with bilateral oophorectomy. The usefulness of pelvic and/or retroperitoneal lymphadenectomy, radiotherapy, and adjuvant chemotherapy for the treatment of lymph node metastasis is still under discussion.

Sagittal and coronal T2-weighted image shows a large lobulated mass dependent on the uterine fundus without a well-defined capsule. Note the presence of multiple cysts with fluid-fluid levels inside (Figs. 7.45 and 7.46). Precontrast fat suppression fast gradient echo T1-weighted image identifies a large hemorrhagic component within the mass (Fig. 7.47). Postcontrast fat suppression fast gradient echo T1-weighted image demonstrates several hypoenhancing intratumoral areas of focal necrosis and hemorrhage (Fig. 7.48).

#### Comments

#### **Further Reading**

#### Books

Fleischer AC, Javitt MC, Jeffrey RB, Jones HW (1997) Clinical gynecologic imaging. Lippincott Williams & Wilkins, Philadelphia

- Hamm B, Forstner R (2007) MRI and CT of the female pelvis. Springer, Berlin
- Maulik D, Zalud I (2005) Doppler ultrasound in obstetrics and gynecology, 2nd rev. and enl. ed. Springer, Berlin

Rumack CM, Wilson S, Charboneau JW, Johnson JA (2005) Diagnostic ultrasound. Mosby, St Louis

Semelka RC (2006) Abdominal-pelvic MRI, 2nd edn. Wiley-Liss, New York

#### Web Links

http://www.obgyn.net/ultrasound/Default.asp

http://www.dukehealth.org/services/radiology/care-guides/ uterine-fibroid-embolization-ufe/

http://uterinearteryembolization.org/

http://www.medscape.com/viewarticle/722721

http://www.cancer.gov/cancertopics/wyntk/uterus/page1

#### Articles

- Bell DJ, Pannu HK (2011) Radiological assessment of gynecologic malignancies. Obstet Gynecol Clin North Am 45(1), vii
- Bilhim T, Pisco JM, Duarte M, Oliveira AG (2011) Polyvinyl alcohol particle size for uterine artery embolization: a prospective randomized study of initial use of 350–500 μm particles versus initial use of 500–700 μm particles. J Vasc Interv Radiol 22(1):21–27
- Cao K, Gao M, Sun YS, Li YL, Sun Y, Gao YN, et al (2011) Apparent diffusion coefficient of diffusion weighted MRI in endometrial carcinoma-Relationship with local invasiveness. Eur J Radiol May 16 [Epub ahead of print]
- Chassang M, Novellas S, Baudin G, Delotte J, Mialon O, Bongain A et al (2011) Contribution of new MRI sequences in the exploration of the pelvic gynaecological disease. J Gynecol Obstet Biol Reprod (Paris) 40(5):399–406
- Emoto M, Sadamori R, Hachisuga T, Kawarabayashi T, Miyamoto S (2011) Clinical usefulness of contrast-enhanced color Doppler ultrasonography in invasive and noninvasive gestational trophoblastic diseases: a preliminary study. J Reprod Med 56(5–6):224–234
- Fan TY, Zhang L, Chen W, Liu Y, He M, Huang X, et al (2011) Feasibility of MRI-guided high intensity focused ultrasound treatment for adenomyosis. Eur J Radiol Jun 28 [Epub ahead of print]
- Fennessy FM, Kong CY, Tempany CM, Swan JS (2011) Qualityof-life assessment of fibroid treatment options and outcomes. Radiology 259(3):785–792
- Genever AV, Abdi S (2011) Can MRI predict the diagnosis of endometrial carcinosarcoma? Clin Radiol 66(7):621-624
- Hecht EM, Do RK, Kang SK, Bennett GL, Babb JS, Clark TW (2011) Diffusion-weighted imaging for prediction of volumetric response of leiomyomas following uterine artery

embolization: a preliminary study. J Magn Reson Imaging 33(3):641-646

- Kamimori T, Sakamoto K, Fujiwara K, Umayahara K, Sugiyama Y, Utsugi K, Takeshima N, Tanaka H, Gomi N, Takizawa K (2011) Parametrial involvement in FIGO stage IB1 cervical carcinoma diagnostic impact of tumor diameter in preoperative magnetic resonance imaging. Int J Gynecol Cancer 21(2):349–354
- Kido A, Ascher SM, Kishimoto K, Hahn W, Jha RC, Togashi K et al (2011) Comparison of uterine peristalsis before and after uterine artery embolization at 3-T MRI. AJR Am J Roentgenol 196(6):1431–1435
- Kim HS, Baik JH, Pham LD, Jacobs MA (2011a) MR-guided highintensity focused ultrasound treatment for symptomatic uterine leiomyomata long-term outcomes. Acad Radiol 18(8):970–976
- Kim YS, Lim HK, Kim JH, Rhim H, Park BK, Keserci B, et al (2011) Dynamic contrast-enhanced magnetic resonance imaging predicts immediate therapeutic response of magnetic resonance-guided high-intensity focused ultrasound ablation of symptomatic uterine fibroids. Invest Radiol [Epub ahead of print]
- Lee EJ, Kim SH, Kim YH (2011) Uterine cavernous haemangioma in a post-menopausal woman: CT and MRI findings mimicking uterine myoma with degeneration. Br J Radiol 84(1000):e68-e71
- Levy A, Medjhoul A, Caramella C, Zareski E, Berges O, Chargari C et al (2011) Interest of diffusion-weighted echo-planar MR imaging and apparent diffusion coefficient mapping in gynecological malignancies: a review. J Magn Reson Imaging 33(5):1020–1027
- Marcal L, Nothaft MA, Coelho F, Volpato R, Iyer R (2011) Mullerian duct anomalies: MR imaging. Abdom Imaging [Epub ahead of print]
- Mori K, Saida T, Shibuya Y, Takahashi N, Shiigai M, Osada K, et al (2011) Unenhanced MR angiography of uterine and ovarian arteries after uterine artery embolization: differences between patients with incomplete and complete fibroid infarction. Cardiovasc Intervent Radiol [Epub ahead of print]
- Novellas S, Chassang M, Delotte J, Toullalan O, Chevallier A, Bouaziz J et al (2011) MRI characteristics of the uterine junctional zone: from normal to the diagnosis of adenomyosis. AJR Am J Roentgenol 196(5):1206–1213
- Ruuskanen AJ, Hippeläinen MI, Sipola P, Manninen HI (2011) Association between magnetic resonance imaging findings of uterine leiomyomas and symptoms demanding treatment. Eur J Radiol [Epub ahead of print]
- Smeets AJ, Nijenhuis RJ, Boekkooi PF, Vervest HA, van Rooij WJ, Lohle PN (2011) Long-term follow-up of uterine artery embolization for symptomatic adenomyosis. Cardiovasc Intervent Radiol [Epub ahead of print]
- Takatsu A, Shiozawa T, Miyamoto T, Kurosawa K, Kashima H, Yamada T, et al (2011) Preoperative differential diagnosis of minimal deviation adenocarcinoma and lobular endocervical glandular hyperplasia of the uterine cervix: a multicenter study of clinicopathology and magnetic resonance imaging findings. Int J Gynecol Cancer [Epub ahead of print]
- Takeuchi M, Matsuzaki K (2011) Adenomyosis: usual and unusual imaging manifestations, pitfalls, and problem-solving MR imaging techniques. Radiographics 31(1):99–115

- Vargas HA, Akin O, Zheng J, Moskowitz C, Soslow R, Abu-Rustum N et al (2011) The value of MR imaging when the site of uterine cancer origin is uncertain. Radiology 258(3):785–792
- Vivier PH, Liard A, Beurdeley M, Brasseur-Daudruy M, Cellier C, Le Dosseur P, et al (2011) Uterus didelphys, hemihydrocolpos and empty ipsilateral lumbar fossa in a newborn girl: invo-

luted dysplastic kidney rather than renal agenesis. Pediatr Radiol [Epub ahead of print]

Yazdi AT, De Smet K, Ernst C, Desprechins B, de Mey J (2011) Uterus didelphys with obstructed hemivagina and renal agenesis: MRI findings. JBR-BTR 94(1):16–18

## **Cervix and Vagina**

#### MARIANO VOLPACCHIO, JOAN C. VILANOVA, AND ANTONIO LUNA

#### Contents

Case 1	Incidental Cervical Cancer	166
Case 2	MR Staging of Cervical Cancer	168
Case 3	Bicornuate Bicollis Uterus	170
Case 4	Nabothian Cysts	172
Case 5	Adenoma Malignum	174
Case 6	Bartholin Gland Cyst	176
Case 7	Endometriosis	178
Case 8	Vaginal Prolapse	180
Case 9	Vaginal Cancer	182
Case 10	Vesicovaginal Fistula	184

#### Case 1 L Incidental Cervical Cancer



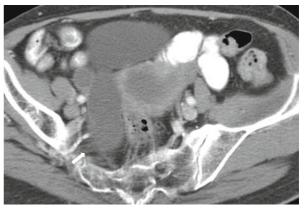
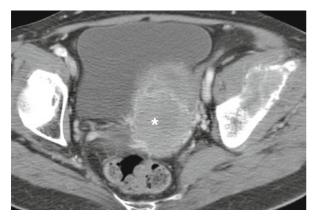
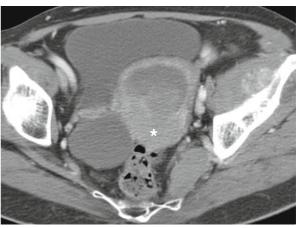


Fig. 8.1

Fig. 8.2









A 70-year-old woman with left iliac pain was admitted for a pelvic CT.

About 90% of cervical carcinomas are squamous cell carcinoma, 5–10% are adenocarcinoma, and others are rare histologic subtypes. Prevalence of invasive squamous cell carcinoma has been decreasing because of cytologic screening (Papanicolaou smear). Most cervical squamous cell carcinomas grow at the squamocolumnar junction. In younger women, the tumor tends to grow outward (exophytic growth pattern). In elderly patients, cervical cancer tends to grow inward along the cervical canal (endophytic growth pattern). Occasionally, as in this case, cervical cancer may present in an advanced stage, and it is diagnosed incidentally by imaging.

Accurate staging and assessment of prognostic factors are crucial for determining the optimal treatment modality in cervical cancer. Therapy decisions are based on integrated data from physical examination and imaging studies, essentially computed tomography (CT) and magnetic resonance (MR) imaging. These modalities provide anatomic information for accurate evaluation of primary tumor size, depth of stromal invasion, and pelvic side wall involvement, although MR is superior to CT in local staging of cervical cancer. Computed tomography is also indicated in diagnosing hydronephrosis associated with cancer invasion, lymph node metastases, or distant metastases.

CT and MRI cannot evaluate properly nodal spread due to an inherent inability to depict small-volume disease in nonenlarged lymph nodes. Positron emission tomography (PET) with 2-[fluorine-18] fluoro-2-deoxy-D-glucose (FDG) provides both qualitative and quantitative metabolic information for diagnosis and disease management. Primary tumor can spread by direct extension or via the regional lymphatic vessels. FDG PET with concurrent abdominopelvic CT is considered highly appropriate in assessing nodal disease on stage II or higher, and in patients with suspected tumor recurrence. FDG PET or PET/CT has proved to be more accurate than high-resolution CT alone, particularly in determining locoregional lymph node involvement and extrapelvic disease extension.

A novel functional MRI approach using diffusion-weighted imaging has recently revealed potential for accurate detection and characterization of nodal metastasis of cervical cancer. Paraaortic lymph node metastasis, which is an important determinant of progression-free survival, is observed in approximately one-third of patients with locally advanced cervical cancer (FIGO stage IIB–IVA). Distant metastasis can be observed even in patients with small-volume tumors.

#### **Imaging Findings**

Figures 8.1–8.4: Axial CT images with oral and IV contrast at different consecutive levels. Show a moderate right hydronephrosis (*white arrows*). Figure 8.2 identifies an endometrial cavity dilatation. An obstructive heterogeneous cervical mass with irregular borders is demonstrated in Figs. 8.3 and 8.4 (*asterisks*) causing right ureteral entrapment. A left iliac bone metastases is seen in Fig. 8.4.

#### **Comments**

## Case 2 MR Staging of Cervical Cancer



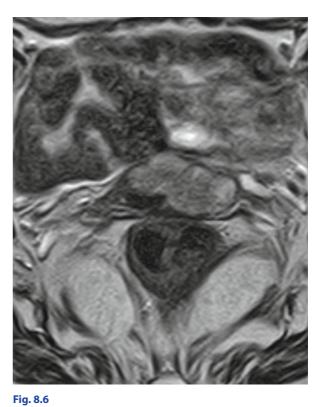


Fig. 8.5

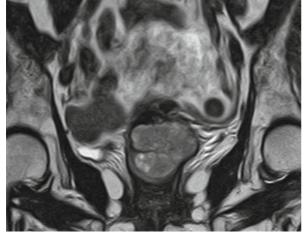


Fig. 8.7



A 60-year-old woman with a previous diagnosis of squamous cell carcinoma was submitted for staging on MRI.

#### Comments

MR imaging can provide highly accurate information on the local extent of pelvic tumors. MR imaging has better soft-tissue contrast resolution and multiplanar capability than CT. It has 50–75% sensitivity for estimation of the degree of parametrial invasion, while CT has 43–55%. MR imaging performs better than CT in the detection of bladder and rectal invasion (sensitivity: 75% and specificity: 90%, versus 75% for both values for CT). Cervical cancer appears hyperintense on T2-weighted images. Sagittal T1-weighted and T2-weighted images and oblique axial T2-weighted images obtained perpendicular to the uterine axis are used for staging.

Staging of cervical carcinoma with MR imaging is based on the International Federation of Gynecology and Obstetrics (FIGO) classification system.

STAGE IA: microinvasive tumor (cannot be demonstrated at MR imaging)

*STAGE IB*: confined to cervix (tumor is completely surrounded by hypointense cervical stroma on axial T2-weighted images)

*STAGE IIA*: invades upper two-thirds of the vagina (segmental disruption of the hypointense vaginal wall on T2-weighted images)

STAGE *IIB*: parametrial invasion (triangular protrusion of the tumor through the disrupted hypointense ring of cervical stroma)

STAGE IIIA: vaginal involvement reaches the lower third of the vaginal canal

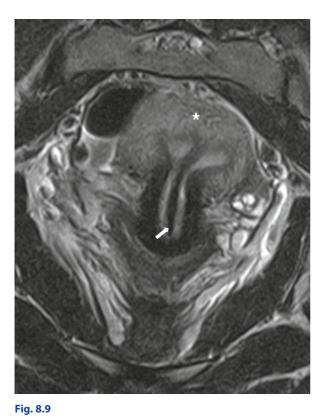
*STAGE IIIB*: extension to the pelvic wall or hydronephrosis (obliterates the entire cardinal ligament and extends to the pelvic muscles)

*STAGE IVA*: the tumor invades the vesical or rectal mucosa (disruption of the hypointense vesical or rectal wall or a segmental thickened rectal wall)

STAGE IVB: distant metastases, paraaortic or inguinal lymph node metastases

Sagittal T2-weighted image (Fig. 8.5) shows a cervical mass (*asterisk*) with segmental disruption of the hypointense vaginal wall, including the lower third of the vaginal canal (*arrow*). Axial T2-weighted image (Fig. 8.6) demonstrates lack of rectal mucosa invasion. Coronal T2-weighted (Fig. 8.7) and axial fat-suppression T1-weighted images after contrast administration (Fig. 8.8) does not demonstrate parametrial invasion.

## Case 3 Bicornuate Bicollis Uterus



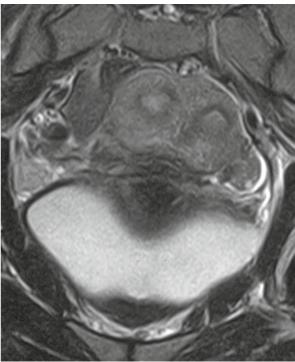


Fig. 8.10

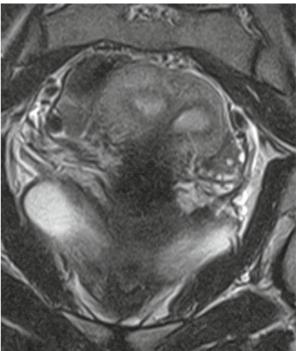


Fig. 8.11

A 30-year-old woman with a previous history of infertility was referred to the radiology department for further assessment.

#### Approximately 1% of all women and 3% of women with recurrent pregnancy losses have an uterovaginal anomaly. As many as 25% of women with müllerian duct anomalies have reproductive problems, including increased risk for spontaneous abortion, prematurity, and intrauterine growth retardation. A correct classification of congenital abnormalities of the female reproductive system is important in the treatment of infertility. Imaging is essential in their classification. Histerosalpingography, ultrasound, and MRI are used on the imaging workup, but the most common technique used to establish or confirm the type of congenital anomaly is MRI.

MR is able to rule out involvement of the cervix and vagina. MR sequences that may be used for diagnosis of uterovaginal anomalies are: coronal T1-weighted sequence for the kidneys and pelvis, sagittal T2-weighted fast-spin-echo sequence, axial T1-weighted spin-echo sequence, and oblique long-axis T2-weighted FSE sequence.

Bicornuate bicollis uterus is a variant of bicornuate uterus in which the anomaly is combined with a muscular uterine septum that extends to the external os. MR imaging may help differentiate a septated from a bicornuate uterus, by depicting a normal convex, flat, or minimally concave external fundal contour with a septate uterus. MR imaging can demonstrate the composition and extent of the septum.

On MR, the normal vagina is normally seen as a tube of intermediate signal intensity between the bladder base and urethra anteriorly and the anal canal posteriorly. The direction and extent of a vaginal septum should be assessed. A vaginal septum could be in a high, middle, or low position. It is more common in the upper vagina, and it is not uncommon that it causes obstruction and a blood-filled vagina (hematocolpos).

## Figures 8.9–8.11: Oblique coronal T2-weighted MR images show a concave external uterine fundal contour (*asterisk*) and a low-signal-intensity fibrous septum (*arrow*) that extends to the external cervical os. Incomplete septal resorption after müllerian duct fusion results in a bicornuate bicollis uterus.

#### Comments

Case 4 Nabothian Cysts

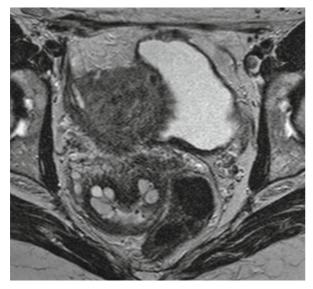


Fig. 8.12

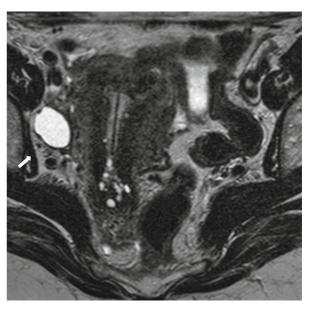


Fig. 8.13

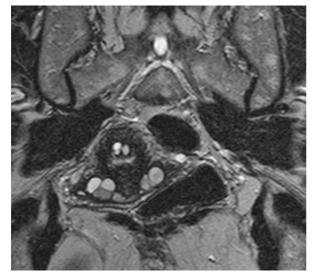
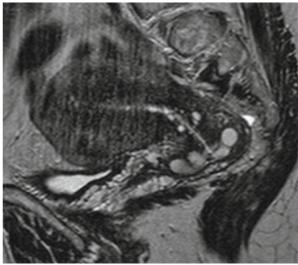


Fig. 8.14





A 52-year-old woman with conglomerated cervical cysts detected on ultrasound was referred for an MRI examination.

#### Comments

Nabothian cysts are retention cysts of the uterine cervix. Nabothian cysts are a common incidental finding that is usually located in the uterine cervix. At this level, endocervical glands are present and they occasionally extend deep into the cervical stroma. They result from healing process of chronic cervicitis. During chronic inflammation, the squamous epithelium proliferates, covering the columnar epithelium of the endocervical glands. After that, the mucus secreted by the columnar epithelium (now covered by the squamous epithelium) cannot be evacuated and forms a retention cyst. They might reach large size ( $\geq$ 4 cm). These cysts can be easily diagnosed clinically by visual inspection. Large cysts located deeper in the cervical stroma can cause unexplained enlargement of the cervix. Tunnel cluster, a special type of nabothian cyst, is characterized by complex multicystic dilatation of the endocervical glands.

Nabothian cysts appear as a single cystic or multiple cystic lesion in the fibrous cervical stroma, contiguous and round, with regular boundaries on imaging techniques. Multiple nabothian cysts show posterior acoustic enhancement on ultrasound and appear as low-attenuated cysts in the cervix on CT. The cysts show intermediate or slightly high signal intensity on T1-weighted images and have high signal intensity on T2-weighted images. A solid component surrounding or separating multiple cysts is considered a clue in distinguishing adenoma malignum from benign lesions such as nabothian cysts.

# Axial T2-weighted (Fig. 8.12), long axis T2-weighted (Fig. 8.13), coronal T2-weighted (Fig. 8.14), and sagittal T2-weighted (Fig. 8.15) MR images show multiple small cysts in the deep stroma of the cervix. A small cystic image is depicted in the right adnexa (Fig. 8.13).



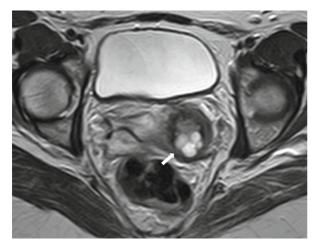


Fig. 8.16

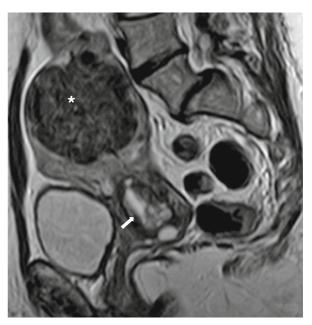


Fig. 8.17

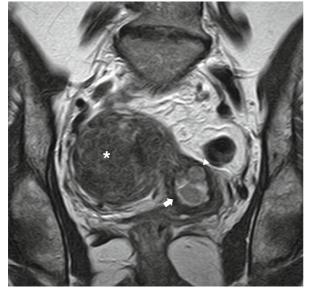


Fig. 8.18

A 56-year-old woman complained of vaginal discharge. An MRI examination was performed for further assessment.

Minimal-deviation adenocarcinoma, also known as adenoma malignum, is a rare variant of well-differentiated mucinous adenocarcinoma of the uterine cervix, which is characterized by multilocular cystic lesions extending from the endocervical glands to the deep cervical stroma. Its prevalence is about 3% of all cervical adenocarcinomas. To make a correct diagnosis, it is necessary to find a characteristic pathological feature such as multiple irregular lobulations of distorted glands demonstrating a "hair-pin" shape. The most common initial symptom is a watery discharge that is often associated with Peutz-Jeghers syndrome and mucinous tumors of the ovary. The prognosis of adenoma malignum is known to be poor because of early dissemination into the peritoneal cavity and early distant metastasis. It disseminates into the peritoneal cavity even during the early stage of the disease and responds poorly to radiation or chemotherapy.

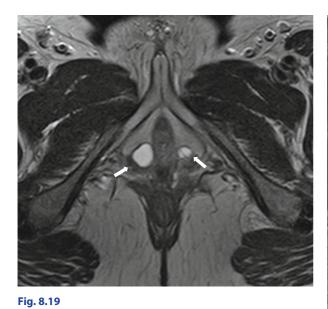
A multicystic lesion with some solid components in the deep cervical stroma on imaging has been reported to be evidence of adenoma malignum. Pathologic analysis shows conjugation of small cystic spaces lined predominantly by mucin-containing columnar epithelial cells with cystic spaces filled with mucin. Most of the glands have cellular atypia and structural dysplasia. The differential diagnosis includes deep nabothian cysts, florid endocervical hyperplasia, and well-differentiated adenocarcinoma. The possibility of differentiating these lesions from adenoma malignum with MR imaging is controversial. It has been reported that a multicystic lesion with some solid components in the deep cervical stroma is evidence of adenoma malignum at MR imaging, although some benign cystic lesions that affect the cervix also appear multicystic with solid features. There have been many reports investigating pseudoneoplastic glandular lesions, which are benign lesions that are often confused with adenoma malignum, either histologically or radiographically. These include papillary endocervicitis, tunnel cluster, deep endocervical glands, deep nabothian cysts, microglandular hyperplasia, mesonephric hyperplasia, diffuse laminar endocervical glandular hyperplasia, glandular hyperplasia not otherwise specified, metaplasias, endometriosis, Atrias-Stella reaction, changes secondary to extravasation of mucin, and infectious and reactive atypias. The MR findings of pseudoneoplastic glandular lesions have been shown identical to those of adenoma malignum.

#### Imaging Findings

Axial and sagittal T2-weighted MR images (Figs. 8.16 and 8.17) show a high-signal-intensity multilocular cystic lesion (*arrows*) within the posterior aspect of an enlarged uterine cervix. Coronal T1-weighted MR image (Fig. 8.18) demonstrates high signal of the cystic lesions due to proteinaceous content (*arrowheads*). A large hypointense uterine myoma is also noticed (*asterisks*).

#### Comments

## Case 6 Bartholin Gland Cyst



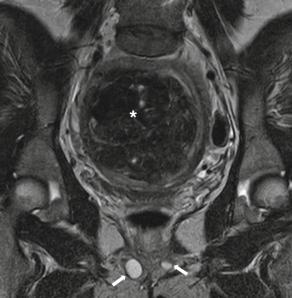
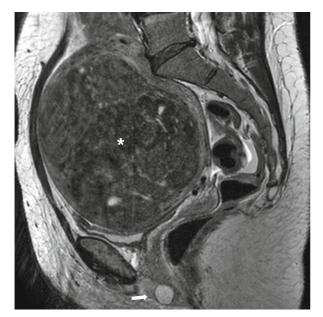


Fig. 8.20





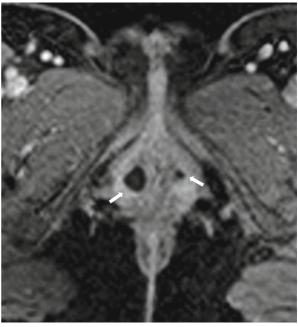


Fig. 8.22

#### A 38-year-old woman with dyspareunia is submitted to perform a pelvic MRI examination.

Bartholin gland cyst formation is caused by chronic inflammation or infection of the underlying glands, resulting in ductal obstruction from purulent material or mucus. Bartholin glands are small glands located on the posterolateral vagina. They are derived from the urogenital sinus and are lined with transitional or columnar epithelium. Most of these lesions are asymptomatic. They may be complicated with infection, hemorrhage, and rupture. Treatment options for symptomatic cysts include administration of silver nitrate, surgical excision, and marsupialization.

Bartholin gland cysts are located in the posterolateral inferior third of the vagina medial to the labia minora and at or below the level of the pubic symphysis. The cysts are usually unilocular, with a size ranging from 1 to 4 cm. They are hyperintense on T2-weighted images and have variable signal on T1-weighted images depending on their proteinaceous or mucinous content.

Their main differential diagnosis is Gartner cysts. The classic location of this vaginal cyst is along the anterolateral vagina above the level of the most inferior aspect of the pubic symphysis. The cyst is usually solitary and less than 2 cm, and may contain septa. They appear hyperintense on T2-weighted and hypointense on T1-WI on MR imaging if the contents are primarily simple fluid; and hyperintense on T1-WI and hypointense on T2-WI if the contents are hemorrhagic or proteinaceous.

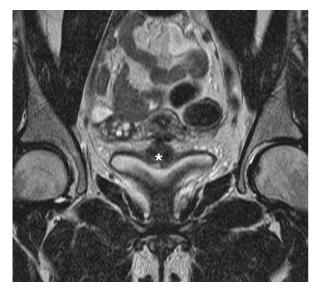
Other differential diagnoses are:

- Urethral diverticula: communication with urethra, wrap around the urethra in a horseshoe configuration
- Skene duct cyst: located just lateral to the external urethral meatus
- Müllerian cyst
- Epidermal inclusion cyst
- Perineal-vulvovaginal endometriomas

Axial (Fig. 8.19), coronal (Fig. 8.20), and sagittal (Fig. 8.21) T2-weighted MR images demonstrate two hyperintense cysts (*arrows*) located on the posterolateral vaginal wall, without urethral communication. Axial T1-weighted image after contrast administration (Fig. 8.22) does not show enhancement, demonstrating low signal intensity. A large leiomyoma is also noted (Fig. 8.20, *asterisks*).

#### **Comments**





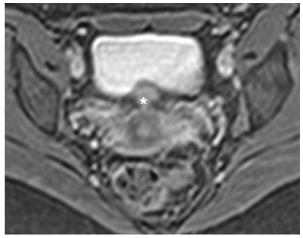


Fig. 8.24

Fig. 8.23



Fig. 8.25





#### A 32-year-old woman with chronic pelvic pain was referred to an MRI examination.

Endometriosis is defined as the presence of functional endometrial glands and stroma outside the uterine cavity. Deep pelvic endometriosis is defined as subperitoneal invasion by endometriotic lesions exceeding 5 mm in depth. It can affect fibromuscular pelvic structures, such as the rectovaginal septum and uterosacral ligaments, as well as the vagina (15% of the cases), alimentary tract, and urinary tract. Deep pelvic endometriosis is frequently associated with dysmenorrhea, dyspareunia, pelvic pain, urinary tract symptoms, and infertility. As the standard treatment for deep endometriosis is complete surgical excision of the endometriotic lesions, presurgical diagnosis and accurate knowledge of the precise location of the lesions are essential prerequisites for successful outcomes.

Transvaginal ultrasonography is usually the first imaging technique used to diagnose endometriosis. It is the method of choice for differentiating endometriomas from other ovarian cysts.

MRI is highly accurate in the diagnosis of infiltrating extraperitoneal endometriosis; it allows the identification of lesions that are hidden by adhesions and also detects subperitoneal lesion extension. MR imaging allows a complete survey of the anterior and posterior compartments of the pelvis.

Involvement of anatomic structures such as the vaginal or rectal wall should be suspected when these structures have a hypointense thickened or nodular appearance on T2-weighted images.

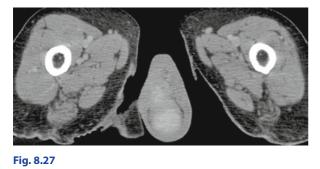
Hyperintense foci may be observed with T2-weighted sequences, findings that correspond to dilated ectopic endometrial glands. These foci may have high or low signal intensity, depending on the presence or absence of bloody content, on fat-suppressed T1-weighted MR images.

#### **Imaging Findings**

Coronal T2-weighted (Fig. 8.23), axial fat-suppressed T1-weighted after contrast administration (Fig. 8.24), axial T1-weighted (Fig. 8.25), and sagittal T2-weighted (Fig. 8.26) MR images show irregular thickening of the upper and posterior aspect of the bladder wall (*arrow*). A nodular lesion, predominantly hypointense on T2-weighted sequences and of intermediate signal on T1-weighted image, obliterates the vesicouterine recesses and contacts with the anterior vaginal wall (*asterisk*). This finding indicates endometriotic involvement of the vesicovaginal septum and the vesicouterine pouch.

#### **Comments**





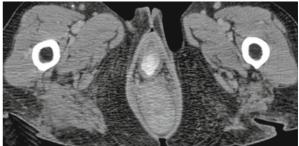


Fig. 8.28

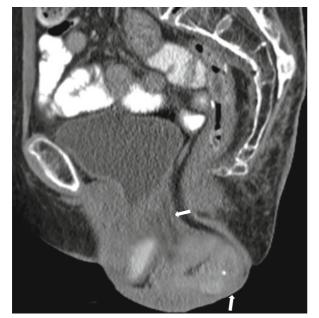


Fig. 8.29



Fig. 8.30

A 88-year-old woman with known prolapsed vaginal vault by physical examination was referred for a CT exam.

Vault prolapse consists of descent and eversion of the vaginal vault. In cases of complete eversion, a bulging "mass" can be seen outside the external genitalia. The outer wall of this "mass" is the mucosa of the vagina, and the contents are the prolapsed pelvic organs. Patients with vaginal eversion have difficulty walking or sitting, as well as, pelvic pressure and protrusion of tissue through the vagina. Patients may also have urinary or rectal dysfunction secondary to additional coexisting pelvic floor defects.

The uterosacral ligaments suspend the cervix and upper vagina from the presacral fascia. This attachment pulls these structures superiorly and posteriorly over the levator plate toward the sacrum. This mechanism is protective because the vagina moves into the hollow of the sacrum and forms a horizontal supporting shelf when abdominal pressure increases. The pubocervical fascia attaches the lateral vagina to the pelvic sidewall at the arcus tendineus fascia pelvis. The inferior lateral wall is attached to the pubococcygeal muscle by the connective tissue fibers of Luschka. Posteriorly, the rectovaginal fascia attaches the vagina to the perineal body inferiorly and blends with the uterosacral ligaments superiorly. Diagnosis is made at physical examination with visual assessment of vault prolapse and mucosal eversion. When the uterus is present, prolapse of the cervix relative to the hymen is noted.

Straining displaces the vagina inferiorly, and the distal portion may be displaced anteriorly. The vagina may appear shortened due to partial eversion of the vault. Vaginal vault descent causes a traction effect on the cul-de-sac, displacing it inferiorly. This phenomenon results in an increase in the potential space of the cul-de-sac so that small bowel loops can be seen low in the pelvis. If cervix and uterus are present, rotational descent of these structures can occur. Complete prolapse of the uterus is called uterine procidentia. Criteria used to define cervical and vaginal vault prolapse include (a) cervix or vaginal vault below the pubococcygeal line and (b) cervix or vault less than 1 cm above the pubococcygeal line.

Figures 8.27 and 8.28: Axial CT images with oral and urinary contrast obtained with the patient at rest show extrapelvic prolapse of the bladder and uterus. Sagittal MPR reconstruction demonstrates uterine descent and rotation (*arrows*), called procidentia (Fig. 8.29). Coronal MPR reconstruction shows the prolapsed bladder with an elongated appearance (*asterisk*) (Fig. 8.30).

#### Comments

Case 9 D Vaginal Cancer

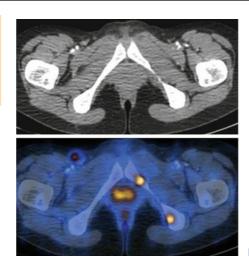


Fig. 8.31

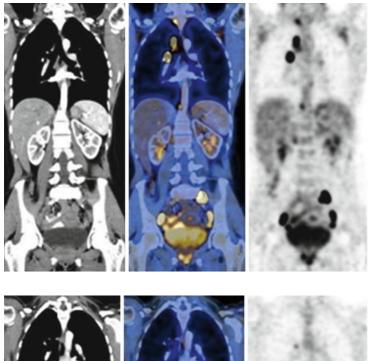


Fig. 8.32

Fig. 8.33

A 63-year-old woman was referred for a PET-CT for local and distance staging from a vaginal carcinoma.

#### Comments

Primary vaginal carcinoma is rare, accounting for only 1–2% of gynecologic malignancies and ranking fifth in frequency behind carcinoma of the ovary, uterus, cervix, and vulva. Squamous cell carcinoma makes up about 85% of primary vaginal malignancies, occurring predominantly in postmenopausal women (peak age 60 years).

Primary vaginal carcinoma occurs most commonly in the upper third and posterior wall of the vaginal. It tends to spread early, by direct invasion of the bladder and urethra anteriorly and the rectum posteriorly. One-third of patients have pelvic or groin lymph node involvement at diagnosis owing to early spread through the blood and lymphatic system.

Malignant involvement of the vagina occurs more commonly from metastatic spread, and except for isolated reports of metastases from extragenital cancers, the most common cause of metastatic disease is direct local invasion from malignancies of the female urogenital tract.

Pelvic computed tomography (CT) scan is generally performed to evaluate pelvic lymph nodes, as well as extension of local disease. Magnetic resonance imaging (MRI) has emerged as a potentially important modality in the evaluation of vaginal cancers. An additional role of MRI is to differentiate tumor from fibrotic tissue in patients with suspected recurrent vaginal carcinoma. Positron emission tomography (PET) is evolving as a modality of potential use in the evaluation of vaginal cancer to detect with higher accuracy than CT scan the extension of the primary tumor as well as abnormal lymph nodes. In current practice, therapeutic planning radiotherapy for disease volume assessment is performed using guidance by CT, MRI, and/or PET-CT.

Although MRI provides greater resolution to assess the local extension of tumor, FDG-PET detects the primary tumor, abnormal lymph nodes, and distal staging more accurately than CT. PET-CT is also useful to assess response to treatment.

Figure 8.31: Axial FDG PET/CT shows a focal area of uptake in the distal third of the vagina. Bone involvement is evident. Figure 8.32: Coronal FDG PET/CT demonstrates multiple mediastinal and pelvic lymph node metastases. Figure 8.33: Coronal FDG PET/C performed after 3 months of chemotherapy at a similar level as Fig. 8.32 shows a good response to treatment.



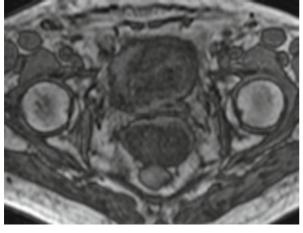


Fig. 8.34

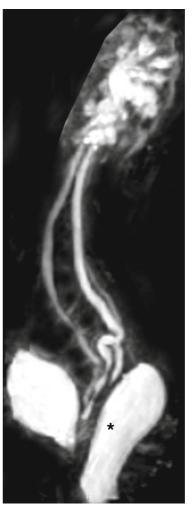
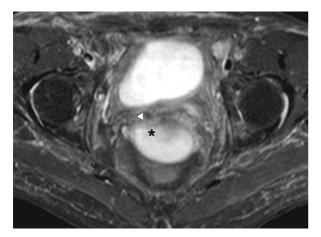
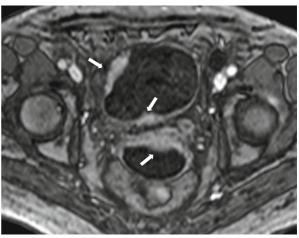


Fig. 8.35









A 50-year-old woman with vaginal leakage of urine after radiation therapy due to bladder cancer was referred for an MRI examination for further assessment.

# Vesicovaginal fistulas usually occur as a complication of childbirth or gynecologic procedures. Hysterectomy is a common culprit for bladder injury and subsequent fistula formation. The remainder causes are irradiation, trauma, and fulguration. In patients with a malignancy, fistulas may occur as a result of a primary or recurrent tumor or as a consequence of surgery or radiation therapy. Vesicovaginal and enterovaginal fistulas are the most common types seen in association with gynecologic malignancies. Neoplasms of the bladder and cervix, especially with ischemic endarteritis obliterans from irradiation, may lead to a vesicovaginal fistula.

Vaginography in conjunction with physical examination have traditionally been used for diagnosis, with sensitivities of 40–100%.

When a low vesicouterine fistula is present, CT after IV contrast injection is a good method to show the fistula, but a high pressure in the bladder may be necessary.

When a high vesicouterine fistula is suspected, it is best shown on hysterography.

Simple vesicovaginal fistulas usually have a diameter of less than 0.5 cm, are unique, and occur in nonirradiated tissue.

Complex vesicovaginal fistulas typically are larger, include multiple tracts, and occur in previously irradiated tissue.

MRI is probably the best imaging technique for identification of fistulas involving the vagina, and to depict their anatomical extent. Sagittal plane is preferred to detect vaginal fistulas. It affords optimal depiction of disruption from the muscularis of the posterior bladder wall in a vesicovaginal fistula and discontinuity of the posterior vaginal or anterior rectal wall in a rectovaginal fistula. On T2-weighted images, the fistula is typically seen as a high-signal-intensity, fluid-filled communication. Short inversion time inversion-recovery (STIR) images may provide even more elegant depiction of a fistulous tract than conventional T2-weighted images. An air-filled tract produces low signal intensity on MR images, regardless of the pulse sequence used.

#### **Imaging Findings**

Axial T1-weighted image (Fig. 8.34), MR Urography (Fig. 8.35), fat suppression T2-weighted (Fig. 8.36) and axial T1-weighted images after contrast administration (Fig. 8.37) show focal enhancing areas of due to vaginal and vesical parietal thickening (*arrows*). Edema of the bladder and vagina is indicative of a nonspecific mucosal reaction to impaired perfusion. Figure 8.36 shows disruption of the posterior bladder wall in a vesicovaginal fistula (*arrowhead*). The vagina is distended with fluid within (*asterisk*).

#### **Comments**

#### **Further Reading**

#### Books

- Dähnert W (2007) Radiology review manual. Lippincott Williams & Wilkins, Philadelphia
- Fleischer AC, Javitt MC, Jeffrey RB, Jones HW (1997) Clinical gynecologic imaging. Lippincott Williams & Wilkins, Philadelphia
- Ros PR, Mortele KJ, Lee S, Pelsser V (2006) CT and MRI of the abdomen and pelvis: a teaching file. Lippincott Williams & Wilkins, Philadelphia
- Rumack CM, Wilson S, Charboneau JW, Johnson JA (2005) Diagnostic ultrasound. Mosby, St Louis

Semelka RC (2010) Abdomino pelvic MRI. Wiley, New York

#### Web Links

http://www.med.nyu.edu/mri/women/

- http://www.molecularimaging.com.sg/cercival\_cancer\_02.asp http://www.auntminnie.com/
- http://www.radiologyteacher.com

http://www.eurorad.org/

#### Articles

- Blask AR, Sanders RC, Rock JA (1991) Obstructed uterovaginal anomalies: demonstration with sonography. II. Teenagers. Radiology 179:84–88
- Cannistra SA, Niloff JM (1996) Cancer of the uterine cervix (review). N Engl J Med 334:1030–1038
- Carrington BM, Hricak H (1991) In: Hricak H, Carrington BM (eds) MRI of the pelvis: a text atlas. Conn: Appleton & Lange, Norwalk, pp 93–184
- Coutinho A Jr, Bittencourt LK, Pires CE, Junqueira F, Lima CM, Coutinho E, Domingues MA, Domingues RC, Marchiori E (2011) MR imaging in deep pelvic endometriosis: a pictorial essay. Radiographics 31(2):549–567
- Danforth DN, Scott JR (1986) Obstetrics and gynecology. Lippincott, Philadelphia
- Hawnaur J (2004) Uterine and cervical tumours. In: Husband JE, Reznek RH (eds) Imaging in oncology, 2nd edn. Taylor & Francis, London, pp 467–496
- Healy JC (2008) Female reproductive system. In: Standring S (ed) Gray's anatomy: the anatomical basis of clinical practice, 40th edn. Churchill Livingstone Elsevier, London, pp 1289–1290
- Son H, Kositwattanarerk A, Hayes MP, Chuang L, Rahaman J, Heiba S, Machac J, Zakashansky K, Kostakoglu L (2010) PET/ CT evaluation of cervical cancer: spectrum of disease. Radiographics 30:1251–1268. doi:10.1148/rg.305105703
- Hricak H, Kim B (1993) Contrast-enhanced MR imaging of the female pelvis. J Magn Reson Imaging 3:297–306

- Imaoka I, Wada A, Matsuo M, Yoshida M, Kitagaki H, Sugimura K (2003) MR imaging of disorders associated with female infertility: use in diagnosis, treatment, and management. Radiographics 23:1401-1421. doi:10.1148/rg.236025115
- Parikh JH, Barton DP, Ind TE, Sohaib SA (2008) MR imaging features of vaginal malignancies. Radiographics 28:49–63. doi:10.1148/rg.281075065
- Bis KG, Vrachliotis TG, Agrawal R, Shetty AN, Maximovich A, Hricak H (1997) Pelvic endometriosis: MR imaging spectrum with laparoscopic correlation and diagnostic pitfalls. Radiographics 17:639–655
- Kinkel K, Ariche M, Tardivon AA et al (1997) Differentiation between recurrent tumor and benign conditions after treatment of gynecologic pelvic carcinoma: value of dynamic contrast-enhanced subtraction MR imaging. Radiology 204:55–63
- Boyadzhyan L, Raman SS, Raz S (2008) Role of static and dynamic MR imaging in surgical pelvic floor dysfunction. Radiographics 28:949–967. doi:10.1148/rg.284075139
- Milestone BN, Schnall MD, Lenkinski RE, Kressel HY (1991) Cervical carcinoma: MR imaging with an endorectal surface coil. Radiology 180:91–95
- Moulopoulos LA, Varma DG, Charnsangavej C, Wallace S (1993) Magnetic resonance imaging and computed tomography appearance of asymptomatic paravaginal cysts. Clin Imaging 17:126–132
- Okamoto Y, Tanaka YO, Nishida M, Tsunoda H, Yoshikawa H, Itai Y (2003) MR imaging of the uterine cervix: imaging-pathologic correlation. Radiographics 23:425–445. doi:10.1148/ rg.232025065
- Sam JW, Jacobs JE, Birnbaum BA (2002) Spectrum of CT findings in acute pyogenic pelvic inflammatory disease. Radiographics 22:1327–1334
- Schmidt WA (1995) Pathology of the vagina. In: Fox H, Wells M (eds) Haines and Taylor obstetrical and gynecological pathology, 4th edn. Churchill-Livingstone, Edinburgh, pp 176–180
- Scoutt LM, McCauley TR, Flynn SD, Luthringer DJ, McCarthy SM (1993) Zonal anatomy of the cervix: correlation of MR imaging and histologic examination of hysterectomy specimens. Radiology 186:159–162
- Semelka RC, Hricak H, Kim B et al (1997) Pelvic fistula: appearances on MR images. Abdom Imaging 22:91–95
- Siddall KA, Rubens DJ (2005) Multidetector CT of the female pelvis. Radiol Clin North Am 43:1097–1118
- Siegelman ES, Banner MP, Ramchandani P, Schnall MD (1997a) Multicoil MR imaging of symptomatic female urethral and periurethral disease. Radiographics 17:349–365
- Siegelman ES, Outwater EK, Banner MP, Ramchandi P, Anderson TL, Schnall MD (1997b) High resolution MR imaging of the vagina. Radiographics 17:1183–1203
- Yitta S, Hecht EM, Slywotzky CM, Bennett GL (2009) Added value of multiplanar reformation in the multidetector CT evaluation of the female pelvis: a pictorial review. Radiographics 29:1987–2003

Guadalupe Garrido, Ignacio Alvarez Rey, and Joan C. Vilanova

#### Contents

Case 1	Borderline Mucinous Ovarian Tumor	188
Case 2	Ovarian Torsion	190
Case 3	Ovarian Mature Cystic Teratoma	192
Case 4	Pelvic Congestion Syndrome	194
Case 5	Pelvic Inflammatory Disease and Fitz-Hugh-Curtis Syndrome	196
Case 6	Bilateral Hydrosalpinx	198
Case 7	Virchow's Node as First Manifestation of Bilateral Ovarian Serous Carcinoma	200
Case 8	Ovarian Endometriosis and Hematosalpinx	202
Case 9	Hemorrhagic Corpus Luteum Cyst	204
Case 10	Fallopian Tube Metastases in Endometrial Carcinoma	206

## Case 1 Borderline Mucinous Ovarian Tumor





Fig. 9.2

Fig. 9.1









A 30-year-old woman presented with a 1-year history of low abdominal pain. A palpable low abdominal mass was noted. Pregnancy was ruled out, and an abdominal plain film and ultrasound study were performed. US detected a multiloculated cystic mass, and on this basis, contrast-enhanced abdominopelvic CT was carried out.

# Mucinous ovarian tumor is a subtype of epithelial ovarian neoplasm. Epithelial ovarian neoplasms are classified as benign, borderline (low malignant potential), or malignant, according to their histologic characteristics and biologic behavior.

Epithelial neoplasms are typically cystic, and may be unilocular or multilocular with varying proportions of solid components. In general, the cell type cannot be established on imaging findings, but they are extremely useful to determine the likelihood of a mass being benign or malignant.

Mucinous borderline ovarian tumors are usually very large, around twice the size of serous borderline ovarian tumors, and on US, CT, and MRI, commonly manifest as multilocular cystic masses with numerous septa.

US is the imaging modality of choice in the initial evaluation of a suspected adnexal mass. Transabdominal US, endovaginal US, or both should be performed. A number of morphologic features have being described as suggestive of malignant tumor. These include thick, irregular walls and septa, papillary projections, and solid, moderately echogenic loculi.

CT scanning better delineates the extent of the mass, shows enhancing and nonenhancing internal structures, and can depict hemorrhagic areas without contrast medium administration. Enlarged lymph nodes and peritoneal implants can also be well assessed with this technique.

On T1- and T2-weighted images, MRI study shows variable signal intensity within the loculi of the mass, depending on the proteinaceous or mucinous content, and hemorrhage. The signal intensity of mucin on T1-weighted images varies according to its degree of hydration, with higher signal intensity as hydration decreases.

The differential diagnosis should include other epithelial ovarian tumors, hemorrhagic ovarian cyst, endometrioma, ectopic pregnancy, teratoma, tubo-ovarian abscess, pelvic hematoma, and peritoneal inclusion cyst.

# Plain abdominal radiograph (Fig. 9.1) shows a mass effect in the pelvis extending to midabdomen with upward displacement of the bowel loops (*open arrows*).

Transabdominal US (Fig. 9.2) shows a well-defined multilocular cystic mass with moderately echogenic content in some loculi.

Transabdominal US focused on the right side of the mass (Fig. 9.3) shows greater multiplicity of the loculi with a honeycomb appearance, irregular thickened septa, and a solid component (*arrow*).

Contrast-enhanced CT scan (Fig. 9.4) demonstrates a huge multilocular cystic mass with enhancement of the thickened septa and of the solid component.

#### Comments





Fig. 9.5

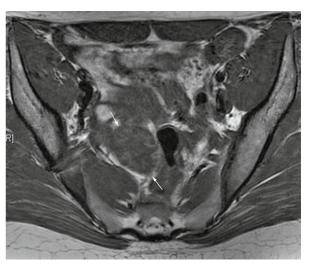


Fig. 9.6

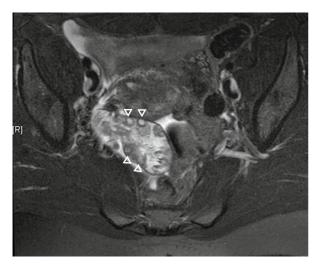


Fig. 9.7





A 19-year-old woman came to the emergency room with acute onset of lower abdominal pain and nausea. She related a history of similar episodes that had been self-limited. Abdominal ultrasound and a pelvic MRI study were performed.

#### Comments

Ovarian torsion accounts for approximately 3% of acute gynecological surgical emergencies. It can occur at any age, but most patients are younger than 20 years. Ovarian torsion consists of twisting of the vascular pedicle of the ovary, leading to ischemia and ultimately, infarction. An early diagnosis and early surgery are important to achieve a better outcome and prognosis.

Ultrasound is the diagnostic imaging modality of choice, with CT and MRI being rarely used. In girls who are not sexually active, transabdominal imaging is carried out, using the distended bladder as a window. In sexually active females, transvaginal imaging is usually performed.

A unilateral, enlarged, hypoechoic ovary with 8–12-mm peripheral follicles is a sensitive, specific ultrasound finding. Associated free pelvic fluid may be seen. Color Doppler study can be helpful if there is an absence of arterial or venous flow, or a twisted vascular pedicle. Nonetheless, normal Doppler flow does not exclude ovarian torsion because the ovary has a dual blood supply from the ovarian and uterine arteries, and because torsion may be incomplete or intermittent.

When CT or MRI are performed to evaluate the lower abdomen, some findings may be suggestive of ovarian torsion: an enlarged, displaced ovary, congested vessels and lack of ovarian enhancement, obliteration of the normal fat planes around the ovary, deviation of the uterus to the affected side, and ascites. On unenhanced CT scans, high attenuation values suggest hemorrhagic infarction of the torsed ovary. MRI shows acute or subacute hemorrhage within the ovary.

The differential diagnosis should include complicated ovarian cysts or tumors, ovarian hyperstimulation syndrome, pelvic inflammatory disease, and endometriosis.

Ultrasound image (Fig. 9.5) demonstrates a significantly enlarged, diffusely hypoechoic, right ovary with multiple small peripheral follicles measuring less than 1 cm in diameter (*open arrows*).

Axial T1-weighted MR image (Fig. 9.6) shows an enlarged, low signal intensity, right ovary (*arrows*).

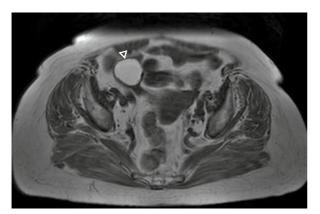
Axial fat-suppressed (Fig. 9.7) and sagittal (Fig. 9.8) T2-weighted MR images show an enlarged right ovary displaying heterogeneous high signal intensity, with multiple small cystic structures in its periphery (*open arrowheads*), consistent with right ovarian torsion. There is associated free fluid in the pelvis (*arrowhead*).



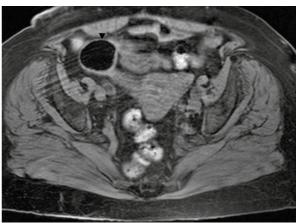




Fig. 9.10









A 24-year-old woman presented with a history of intermittent vague lower abdominal pain of 3 years' duration, with no other specific symptoms. On clinical examination of the abdomen, no tenderness or pain was noted. Blood test results were normal. The patient underwent abdominal US and CT examinations, and pelvic MRI.

#### Comments

Ovarian teratomas are the most common germ cell neoplasm. Teratomas are tumors comprising more than a single cell type, derived from more than one germ cell. Ovarian teratomas include mature cystic teratomas (dermoid cysts), immature teratomas, and monodermal teratomas (e.g., struma ovarii, carcinoid tumors, neural tumors). Mature cystic teratoma, the most common type, usually contains mature tissues of ectodermal, mesodermal, and endodermal origin. The median age at presentation is 30 years. Most women with mature teratomas are asymptomatic.

Most mature cystic teratomas can be diagnosed on US study. The ultrasonographic appearance varies from a cystic lesion with a mural nodule (Rokitansky nodule), the "tip of the iceberg" appearance caused by high echogenicity secondary to the mixture of sebum and hair, associated with a massive acoustic shadow that obscures the posterior wall of the mass, to solid mass appearances. Calcification may not be easily detected on US.

CT and MRI are more sensitive for fat detection than US. On CT, fat attenuation within a cyst, with or without a mural calcification, is diagnostic of mature cystic teratoma.

On MRI, the fatty component of mature cystic teratoma usually displays a very high signal intensity on T1-weighted images, and a high-to-intermediate signal intensity on T2-weighted images, although this appearance can vary somewhat depending on the fluid and fat content.

Other adnexal lesions such as endometriomas and functional hemorrhagic cysts can also show high signal intensity on T1-weighted images. Use of a fat-suppression sequence allows differentiation of hemorrhagic lesions from lipid-containing lesions. Identification of a chemical shift artifact may also be helpful in establishing the diagnosis of mature cystic teratoma.

Owing to their fat content, mature teratomas should also be differentiated from malignant immature teratomas, which are largely solid in nature and contain small foci of fat and coarse calcifications. Other conditions to be differentiated from mature cystic teratomas include malignant ovarian neoplasms, tubo-ovarian abscesses, pedunculated uterine cysts, fibroids, hydrosalpinx, ectopic pregnancies, and peritoneal cysts.

Complications of an ovarian teratoma include torsion, rupture with subsequent peritonitis, and malignant degeneration.

Transabdominal US image at the level of the pelvis (Fig. 9.9) shows a diffusely echogenic mass with some sound attenuation (*open arrows*), in the right ovary.

Contrast-enhanced CT scan (Fig. 9.10) demonstrates a well-defined right ovarian mass with internal fat attenuation (*arrow*), consistent with a mature cystic teratoma.

On the T1-weighted MR image (Fig. 9.11) the mass displays high signal intensity (*open arrowhead*).

Fat-suppressed T1-weighted MR image (Fig. 9.12) demonstrates a signal loss within the mass (*arrowhead*) secondary to the large amount of fat in the lesion.

### Case 4 Pelvic Congestion Syndrome



Fig. 9.13

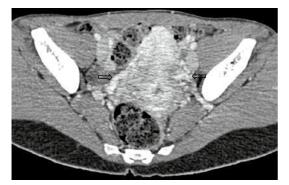


Fig. 9.15



Fig. 9.16

A 37-year-old woman presented with a 1-year history of chronic pelvic pain and heaviness. Initial radiologic investigations included transabdominal US and contrastenhanced abdominal CT. The main finding was a left ovarian varicocele, and the patient was referred for selective left gonadal vein venography and embolization.

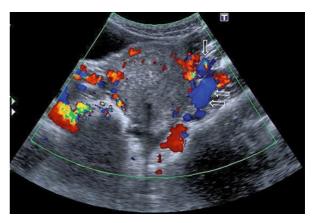
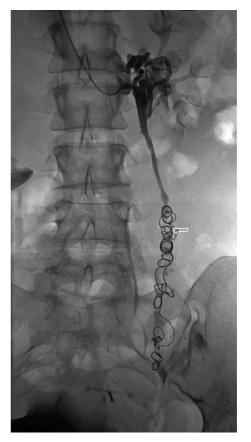


Fig. 9.14





#### Comments

Pelvic congestion syndrome (PCS), a common cause of chronic pelvic pain, often results from dilated and congested veins around the ovaries produced by retrograde blood flow in the gonadal veins. Ovarian varices occur in approximately 10% of women, and up to 60% of those with varices experience PCS.

Although the imaging technique of choice for PCS is selective ovarian venography, patients with a medical history consistent with PCS should first undergo transabdominal or transvaginal US to exclude other pelvic abnormalities and investigate dilated uterine and ovarian vein structures related to pelvic varices.

Color Doppler ultrasound study with spectral Doppler analysis usually demonstrates multiple tortuous pelvic veins with a diameter greater than 5 mm, slow blood flow (3 cm/s), and a dilated arcuate vein in the myometrium communicating bilateral pelvic varicose veins. Other findings include a dilated ovarian vein (commonly the left ovarian vein) with flow reversal, polycystic changes in the ovary, and a variable duplex waveform in the varicoceles during Valsalva maneuvers.

CT and MRI examinations in PCS usually demonstrate dilated, tortuous veins around the ovaries and uterus, with possible extension of varices into the broad ligament, pelvic sidewall, and paravaginal venous plexus. Contrast-enhanced CT in the arterial phase may show simultaneous opacification of a dilated ovarian vein and the renal veins, thus indicating retrograde venous flow.

On MRI, pelvic varices show flow-void artifact on T1-weighted images, and high signal intensity on gradient-echo images. On T2-weighted images, varices may display low-to-high or mixed signal intensity because of their relatively slow flow.

Retrograde ovarian venography usually shows an incompetent, dilated ovarian vein with a diameter greater than 10 mm. Other criteria in favor of PCS include congestion of the uterine or ovarian plexus, filling of the pelvic veins across the midline, and vulvovaginal or thigh varicosities. Endovascular ovarian vein embolization is an alternative to surgery that has shown good response rates in most cases.

Transabdominal US image (Fig. 9.13) shows multiple dilated tubular structures around the uterus and left ovary (*open arrows*).

Color Doppler US image (Fig. 9.14) depicts a venous blood Doppler signal within these structures, demonstrating an ovarian varicocele (*open arrows*).

Contrast-enhanced CT image (Fig. 9.15) shows multiple, tortuous, enhancing vessels around the uterus and ovaries that are more abundant on the left side (*open arrows*).

Selective left ovarian venogram (Fig. 9.16) shows rapid filling of the dilated ovarian venous plexus (*open arrow*) and filling of the pelvic veins across a dilated arcuate vein in the myometrium (*arrow*) and throughout the pelvic sidewall plexus (*open arrowhead*).

Left renal vein injection during Valsalva maneuver following embolization with coils (*arrow*) (Fig. 9.17) shows complete absence of reflux into the distal gonadal vein.

Case 5 Pelvic Inflammatory Disease and Fitz-Hugh-Curtis Syndrome A 29-year-old woman came to the ER with low, rightsided abdominal pain and mild fever (38°C). Laboratory testing demonstrated leukocytosis. The patient reported that she had undergone IUD insertion 2 weeks previously. Transabdominal ultrasonography and abdominopelvic CT were performed.



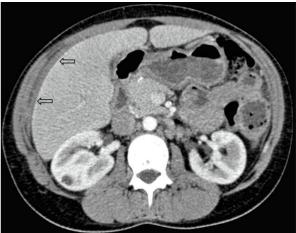


Fig. 9.19

Fig. 9.18









#### Comments

Pelvic inflammatory disease (PID) is the inflammation and infection of the upper genital tract in women, caused by ascending spread of microorganisms from the vagina or cervix to the endometrium, fallopian tubes, and contiguous structures. Neisseria gonorrhoeae and Chlamydia trachomatis are the primary causes of PID, although the condition may be polymicrobial in up to 30–40% of cases. Right upper quadrant pain and perihepatitis can occur in the setting of a PID, leading to the so-called Fitz-Hugh-Curtis syndrome (FHCS), which results from intraperitoneal spread of infection from the pelvic cavity.

Imaging findings vary with the disease stage. Ultrasound is the first imaging technique performed when PID is suspected. Thickened fluid-filled fallopian tubes, an enlarged ovary with hyperechoic surrounding fat, or an adnexal mass with heterogeneous echogenicity are some of the findings. In more severe cases, tubo-ovarian abscesses may be seen, appearing as a cystic mass, often with septations, debris, and irregular walls.

CT is performed when US findings are equivocal or to identify associated complications. A small amount of fluid in the cul-de-sac, obscuration of the normal pelvic floor fascial planes, thickening of the uterosacral ligaments, cervicitis, oophoritis, salpingitis, and accumulation of simple fluid in the endometrial canal and fallopian tubes may be found in early PID. With progression to tubo-ovarian abscess, CT findings include a thick-walled, complex adnexal mass with low-attenuation center, septations, and often, an associated serpiginous structure corresponding to a dilated, pus-filled fallopian tube. Air within the mass is the most specific sign of an abscess, but is unusual in tubo-ovarian abscess. Reactive inflammation of adjacent structures is common and can appear as bowel ileus, hydroureter and hydronephrosis, right upper quadrant inflammation (FHCS), or peritonitis. At dynamic CT, FHCS manifests as intense capsular enhancement along the anterior surface of the liver, secondary to inflammation of the peritoneal covering of the liver.

Another noninvasive imaging option is MRI, which demonstrates tubal enlargement as tortuous folding of fluid-filled structures on T2-weighted images.

A differential diagnosis from adnexal neoplasm is necessary in almost all cases. Differentiation from acute appendicitis, hemorrhagic corpus luteum, ectopic pregnancy, endometriosis, and paraovarian cyst should also be established.

Pelvic US image (Fig. 9.18) shows a thickened fluid-filled right fallopian tube with solidappearing internal echoes consistent with pyosalpinx (*open arrows*). Hyperechoic surrounding fat is observed, due to edema (*arrow*).

Abdominal US image (Fig. 9.19) demonstrates perihepatic free fluid adjacent to the left hepatic lobe (*open arrow*).

Contrast-enhanced CT (Fig. 9.20) shows an enlarged tubular structure with enhancing walls and central low density, consistent with right tubo-ovarian abscess (*open arrow*). Surrounding pelvic inflammatory changes and associated pouch of Douglas abscess (*arrow*) are demonstrated. The IUD is noted in the uterine fundus (*open arrowhead*).

Contrast-enhanced CT scan (Fig. 9.21) demonstrates mild hepatic capsular enhancement (*open arrows*) and free perihepatic fluid.

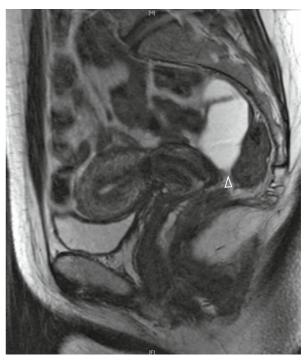
Case 6 Bilateral Hydrosalpinx







Fig. 9.23





A 26-year-old woman presented with pain in her right lower quadrant for approximately 10 days. Laboratory tests only revealed microcytic anemia. An abdominopelvic CT was requested. Based on the findings, a hysterosalpingography and a pelvic MRI were realized.

#### Comments

A hydrosalpinx is a distally blocked fallopian tube filled with serous or clear fluid. The blocked tube may become substantially distended giving the tube a characteristic sausage-like or retort-like shape. The condition is often bilateral and the affected tubes may reach several centimeters in diameter.

The major cause for distal tubal occlusion is pelvic inflammatory disease (PID).

Some patients have lower, often recurring, abdominal pain or pelvic pain, while others may be asymptomatic. The blocked tubes cause infertility.

At ultrasonography, hydrosalpinx appear as tortuous, tube-like structures, with thin walls and no internal echoes, because of the fluid-filled elongated and distended tubes.

Hysterosalpingogram (HSG) shows the retort-like shape of the distended tubes and the absence of spillage of the dye into the peritoneum. However, if there is a tubal occlusion at the utero-tubal junction, hydrosalpinx may be undetected. When hydrosalpinx is detected in a HSG, it is prudent to administer antibiotics to reduce the risk of reactivation of an inflammatory process.

At CT, bilateral hydrosalpinx appears as paired tubular juxtauterine fluid-density structures.

On magnetic resonance (MR) images, hydrosalpinx appears as a fluid-filled C- or S-shaped tubular structure that arises from the upper lateral margin of the uterus. The signal intensity of the tubal fluid varies with the cause of the obstruction. On T1-weighted MR images, the signal intensity of the content of a dilated fallopian tube is usually that of simple fluid, but the tubal content may have high signal intensity if it is hemorrhagic or proteinaceous. On T2-weighted MR images, the cystic nature of the lesion displays high signal intensity with incomplete internal septa, which are usually low signal intensity.

Differential diagnosis of hydrosalpinx includes cystic ovarian masses, loculated peritoneal fluid, peritoneal cysts, and tubo-ovarian abscesses.

#### **Imaging Findings**

Axial contrast-enhanced CT image (Fig. 9.22) shows simple folded fluid-attenuation tubular structures in the bilateral adnexa (*open arrows*) with no adjacent inflammatory stranding or free fluid. Hysterosalpingogram (Fig. 9.23) shows dilatation of both fallopian tubes (*arrows*) with absence of contrast material outflow, findings indicative of tubal occlusion. Sagittal T2-weighted MR image (Fig. 9.24) shows a tortuous tubular structure with high signal intensity, corresponding to the dilated right fallopian tube (*open arrowhead*).

Case 7 Virchow's Node as First Manifestation of Bilateral Ovarian Serous Carcinoma A 41-year-old woman presented with a lump in her left supraclavicular fossa with no other symptoms. An ultrasound was performed, demonstrating an enlarged ovoid and hypoechoic lymph-node without fatty hilum. A biopsy was performed with the resulting pathological diagnosis of infiltration by adenocarcinoma. 18-FDG PET-CT was performed and showed high rate of metabolism in the left supraclavicular lymph node, multiple enlarged lymph node with high rate of metabolism in the retroperitoneal space, and bilateral ovarian enlargement with multiple lumps with high-rate metabolism. Under suspicion of bilateral ovarian cancer, pelvic MRI was performed.

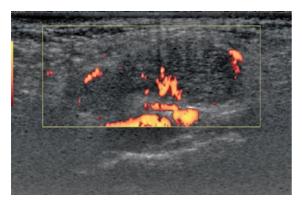


Fig. 9.25



Fig. 9.26

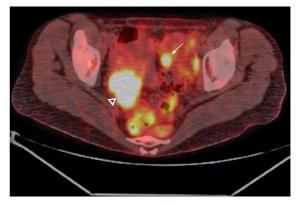


Fig. 9.27

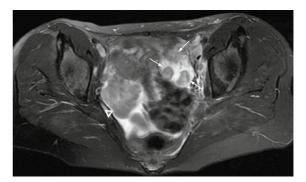


Fig. 9.28

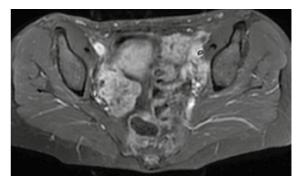


Fig. 9.29

#### Comments

Virchow's node is a lymph node in the left supraclavicular fossa. It takes its supply from lymph vessels in the abdominal cavity. The finding of an enlarged, hard node (also referred to as Troisier's sign) has long been regarded as strongly indicative of the presence of cancer in the abdomen (stomach, gallbladder, pancreas, kidneys, ovaries, testicles, or prostate) that has spread through the lymph vessels.

Serous cystadenocarcinoma comprises 60–80% of all ovarian carcinomas. More than half of these tumors are bilateral (50–70%). Their size is smaller than that of the mucinous cysts. The borders are irregular with a loss of capsular definition. The tumor may be accompanied by bilateral ovarian enlargement. Multilocular cysts contain chambers of varying size with septated, internal papillary projections. The malignant tumors are thick walled and multilocular with multiple papilla. Calcifications may be present. Solid elements or bilateral tumors suggest malignancy. Ascites forms secondary to peritoneal surface implantation. The tumor may spread to the lymph nodes, i.e. periaortic, mediastinal, supraclavicular.

In many instances, epithelial tumors tend to be cystic and solid at gross morphologic examination, and their cell types cannot be differentiated on the basis of their appearance at MR imaging, CT, or ultrasonography (US).

In a ovarian mass, the US, CT, and MRI features suggestive of malignancy include a lesion diameter greater than 4 cm; papillary projections (which are often seen on contrast material–enhanced images or demonstrated with Doppler-color or power-doppler); walls and septa more than 3 mm thick; a large soft-tissue component with necrosis; a lobulated solid mass; and the presence of tumor vessels on contrast-enhanced images or demonstrated with Doppler-color or power-doppler. None of these features are specific enough to indicate the diagnosis preoperatively. However, in general, the likelihood of malignancy increases with increasing solid-tissue elements and thicker septa. Ancillary findings of pelvic organ invasion, implants (peritoneal, omental, mesenteric), ascites, and enlarged lymph nodes increase the diagnostic confidence for malignancy.

Power-doppler ultrasound image of the supraclavicular area (Fig. 9.25) shows an enlarged ovoid and hypoechoic lymph-node without fatty hilum. Coronal view of the 18-FDG PET-CT (Fig. 9.26) shows high rate of metabolism (increased FDG uptake) in the left supraclavicular lymph node (*open arrow*) and in multiple enlarged lymph node located in the retroperitoneal space (*arrows*). Axial view of the 18-FDG PET-CT (Fig. 9.27) shows an enlarged right ovary with high rate metabolism (*open arrow*), and focus of high rate metabolism in the left ovary (*arrow*). Axial T2-weighted MR image (Fig. 9.28) shows an enlarged right ovary with solid component (*open arrow*) and an enlarged left ovary with cystic component and intracystic papillary projections (*arrows*). Axial gadolinium-enhanced fat-suppressed T1-weighted MR image (Fig. 9.29) shows marked enhancement of the right ovary and of the papillary projections in the left ovary.

#### Case 8 **Ovarian Endometriosis and Hematosalpinx**

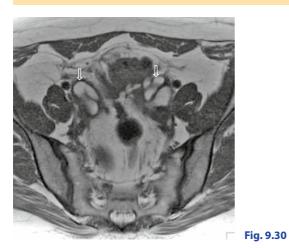
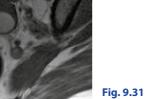


Fig. 9.33





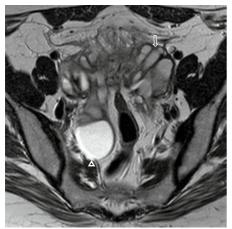


Fig. 9.32

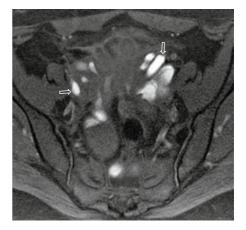


Fig. 9.34

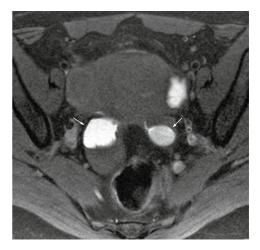


Fig. 9.35

A 47-year-old woman presented with lower abdominal pain that began 1 day before her menstrual period started and continued through it ended. She had a previous history of infertility. A pelvic MRI was performed.

Endometriosis is the presence of functional endometrial glands and stroma outside the uterine cavity. Symptoms associated with endometriosis include infertility and pelvic pain. Endrometriosis can vary from microscopic foci to large, grossly visible endometriotic cysts (endometriomas).

The most common site of involvement is the ovary, but all pelvic organs can virtually be affected.

Endometriotic cysts (endometriomas) are usually the result of repeated cyclic hemorrhage within a deep implant. Although cyst contents can be watery, they are more typically composed of thick, dark, degenerated blood products. This appearance has been called "chocolate cyst."

Endometriosis can cause peritubal adhesions, and can produce an obstruction and bleeding into the fallopian tubes leading to hematosalpinx.

The classic features of uniform low-level echogenicity or a ground-glass appearance is a result of repeated episodes of cyclic bleeding. Hematosalpinx usually appears as a tortuous, tube-like structure, with fine internal echoes.

MRI using T1-weighted, T2-weighted, and T1-weighted fat-suppressed sequences have always to be performed. Administration of gadolinium-based contrast material is not particularly useful in the evaluation of endometriomas.

MR imaging findings are adnexal cysts of high signal intensity on both T1- and T2-weighted MR images, or of high signal intensity on T1-weighted MR images and low signal intensity on T2-weighted MR images (shading).

Other lesions that may appear with high signal intensity on T1-weighted MR images include dermoids, mucinous cystic neoplasms, and hemorrhagic masses. Dermoids can be recognized by the presence of chemical shift artifact and signal drop-out on the fat-suppression images. Mucinous lesions can have increased signal intensity on T1-weighted images, but the signal is considerably less intense than that of fat or blood. The most problematic lesions to differentiate are hemorrhagic corpus luteum cysts, whose MR imaging appearance may be similar to that of endometriomas. Hemorrhagic cysts are usually unilocular, opposed to endometriomas, which are frequently multilocular and bilateral. In addition, hemorrhagic cysts do not exhibit shading on T2-weighted MR images and resolve with time.

Hematosalpinx appears high signal intensity on T1-weighted MR images.

Axial T1-weighted (Figs. 9.30 and 9.31) and T2-weighted (Figs. 9.32 and 9.33) MR images show multiple bilateral ovarian endometriomas and bilateral hematosalpinx (*open arrows*). Most of the ovarian lesions are hyperintense on T1-weighted MR images (*arrows*); however, two lesions in the right ovary (*open arrowheads*) have low signal intensity on T1-weighted image and high signal intensity on T2-weighted image, in relation with simple cysts.

Axial T1-weighted fat-suppressed images (Figs. 9.34 and 9.35) show bilateral hematosalpinx (*open arrows*) and bilateral ovarian endometriomas (*arrows*).

#### **Comments**





Fig. 9.36



Fig. 9.37

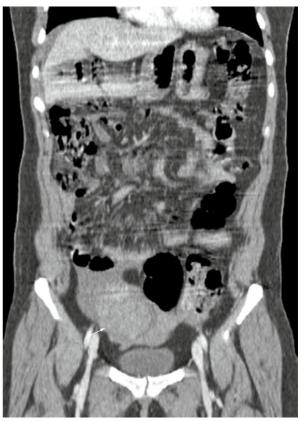


Fig. 9.38

A 33-year-old woman presented to the ER with acute pain in the hypogastric area of 6 h of duration. At physical examination a painful mass was palpated in her right lower quadrant. Laboratory tests were unremarkable. Abdominal US and abdominal contrast-enhanced CT were performed.

Hemorrhagic ovarian cysts are likely caused by bleeding into a corpus luteum.

#### Comments

The distinction between a hemorrhagic corpus luteum and a corpus luteum cyst is largely arbitrary, with some authors using a size of 2 cm as the threshold.

At US, a hemorrhagic corpus luteum cyst is a cyst that typically contains spiderweb-like material. Bizarre blood clots may also be seen. Even an experienced ultrasound examiner may confuse such clots with papillary projections or solid components. This explains why there is a risk of misclassifying hemorrhagic corpus luteum cysts as malignant tumors. While a clot may occasionally simulate a solid nodule, it is usually recognizable by its concave outer margin, and Doppler ultrasound examination may help to discriminate between a clot (no detectable Doppler signal) and a solid component (detectable Doppler signal). Blood clot can sometimes be recognized on gray-scale US scan by its jelly-like movement when pressure is applied with the transducer. If imaged acutely, before fibrin strands or a retracting clot develops, a hemorrhagic cyst can be partly or completely filled with heterogeneous echoes that may simulate a solid mass. One should consider this possibility in a young woman with an ovarian mass that contains a seemingly solid heterogeneous component that lacks internal flow at Doppler US. When in doubt, follow-up ultrasound after 6–12 weeks may be performed. However, some hemorrhagic cysts may take up to 4 months to regress.

At CT, hemorrhagic luteal cyst attenuation is high because of the intracystic presence of blood products. When rupture occurs, CT depicts fluid surrounding the adnexa.

MR imaging findings suggestive of hemorrhagic corpus luteum cyst include a unilateral, unifocal ovarian lesion displaying high signal intensity on T1- and T2-weighted images. The reason for the relatively high signal intensity on T2-weighted images within the hemorrhagic corpus luteum cyst (as opposed to the low signal intensity on T2-weighted images within endometriomas) presumably relates to the lower proteinaceous and iron content of the former, which results in minimal T2 shortening. Usually, the degree of T1 shortening is greater for endometriomas than for hemorrhagic corpus luteum cysts. Unlike endometrial cysts, corpus luteum cysts contain a layer of luteinized cells that lines the cyst wall and that may appear thickened on MRI studies.

The differential diagnosis is extensive and should also include ectopic pregnancy, adnexal torsion, neoplasm, and pelvic inflammatory disease.

Abdominal US (Fig. 9.36) shows a 6 cm well-defined right adnexal solid mass (*open arrow*), with heterogeneous echotexture, and without vascularization. Axial (Fig. 9.37) and coronal (Fig. 9.38)-enhanced abdominal CT images show a predominantly isodense well-defined mass (*arrows*), with free intraperitoneal fluid in the right lower quadrant and in the perihepatic space.

Case 10 Fallopian Tube Metastases in Endometrial Carcinoma



Fig. 9.39

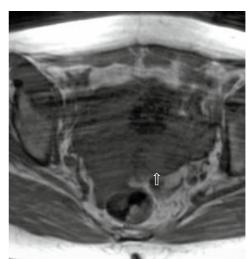


Fig. 9.40





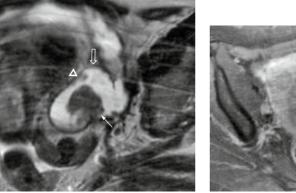


Fig. 9.41

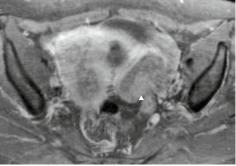


Fig. 9.43

An asymptomatic 72-year-old woman underwent her annual gynecological revision, where a 5 cm left adnexal mass and a 2 cm endometrial thickening with vascularized polypoid formations were ultrasonographically depicted. An endometrial biopsy was performed and the pathological diagnosis was a papillary serous carcinoma. Subsequently a pelvic MRI was performed, demonstrating a left hydrosalpinx with mural nodules.

Fallopian tube cancer is an extremely rare gynecological malignancy. Secondary cancers due to metastasis from the ovaries, endometrium, gastrointestinal tract, or breast are more common.

Initial symptoms are usually secondary to the primary tumor, but the effects on the Fallopian tubes could determine the clinical presentation with pain, genital bleeding, or a palpable pelvic mass.

The appearance of metastases in the Fallopian tubes depends on whether the solid tumor or the hydrosalpinx is the dominant component. If hydrosalpinx is the dominant component, it usually appears as a fluid-filled tubular adnexal structure that contains nodular or papillary solid components. If solid component is dominant, it appears as a sausage-shaped adnexal mass.

At US, the fluid within the distended tube may appear anechoic or with low-level internal echoes. The solid component appears as papillary projections or intraluminal masses. The presence of a vascular solid component at Doppler US helps differentiating tumor from blood clot or debris.

At CT, tubal metastases appear as masses with attenuation values similar to that of other pelvic soft tissues. Enhancement after contrast material administration occurs, in a lower grade than that of the myometrium.

At MR imaging, solid tumor implants are usually homogeneously or heterogeneously isointense on T2-weighted images, hypointense on T1-weighted images, and demonstrate enhancement after the administration of gadolinium-based contrast material. Associated hydrosalpinx may appear as simple serous fluid, with high signal intensity on T2-weighted images and low signal intensity on T1-weighted images. Signal intensity on T1-weighted images may be higher if hemorrhagic fluid is present.

Imaging findings are almost identical to those described in primary Fallopian tube carcinoma, which is considered the least common of all gynecologic malignancies.

Sagittal T2-weighted MR image (Fig. 9.39) shows a hypointense mass within the endometrial cavity.

Axial T1-weighted (Fig. 9.40), axial (Fig. 9.41) and coronal (Fig. 9.42) T2-weighted MR images show a left-sided hydrosalpinx (*open arrows*) with a low-signal intensity soft-tissue mural nodule (*arrow*), and small implants along the Fallopian tube (*open arrowheads*). Axial gadolinium-enhanced fat-suppressed MR image (Fig. 9.43) shows enhancement of the mural nodule (*arrowhead*).

#### **Comments**

#### **Further Reading**

#### Books

- Callen PW (2000) Ultrasonography in obstetrics and gynecology. Saunders, Philadelphia
- Dähnert W (2007) Radiology review manual. Lippincott Williams & Wilkins, Philadelphia
- Friedman A, Radecki PD (1989) Clinical pelvic imaging: CT, ultrasound, and MRI. Mosby, St. Louis
- Hamm B, Forstner R, Baert AL (2010) MRI and CT of the female pelvis (medical radiology/diagnostic imaging). Springer, Berlin/Heidelberg
- Ros PR, Mortele KJ, Lee S, Pelsser V (2006) CT and MRI of the abdomen and pelvis: a teaching file. Lippincott Williams & Wilkins, Philadelphia

#### Web Links

http://www.eurorad.org// http://3s.acr.org/CIP/ http://rad.usuhs.edy/medpix/ http://www.radiologyteacher.com// http://www.auntminnie.com//

#### Articles

- Benjaminov O, Atri M (2004) Sonography of abnormal fallopian tube. AJR Am J Roentgenol 183:737–742
- Bent CL, Sahdev A, Rockall AG et al (2009) MRI appearances of borderline ovarian tumours. Clin Radiol 64:430–438
- Brown DL, Doubilet PM, Miller FH et al (1998) Benign and malignant ovarian masses: selection of the most discriminating gray-scale and Doppler sonographic features. Radiology 208:103–110
- Chang HC, Bhatt S, Dogra VS (2008) Pearls and pitfalls in diagnosis of ovarian torsion. Radiographics 28:1355–1368
- Iyer VR, Lee SI (2010) MRI, CT, and PET/CT for ovarian cancer detection and adnexal lesion characterization. AJR Am J Roentgenol 194:311–321
- Jeong YY, Outwater EK, Kang HK (2000) Imaging evaluation of ovarian masses. Radiographics 20:1445–1470
- Jung SE, Lee JM, Rha SE et al (2002) CT and MR imaging of ovarian tumors with emphasis on differential diagnosis. Radiographics 22:1305–1325
- Kadar N, Taylor KJW, Rosenfield AT, Romero R (1983) Combined use of serum HCG and sonography in the diagnosis of ectopic pregnancy. AJR Am J Roentgenol 141:609–615

- Kim JY, Kim Y, Jeong WK, Song S-Y, Cho OK (2009a) Perihepatitis with pelvic inflammatory disease (PID) on MDCT: characteristic findings and relevance to PID. Abdom Imaging 34:737–742
- Kim KA, Park CM, Lee JH et al (2004) Benign ovarian tumors with solid and cystic components that mimic malignancy. AJR Am J Roentgenol 182:1259–1265
- Kim MY, Rha SE, Oh SN et al (2009b) MR imaging findings of hydrosalpinx: a comprehensive review. Radiographics 29:495–507
- Krysiewicz S (1992) Infertility in women: diagnostic evaluation with hysterosalpingography and other imaging techniques. AJR Am J Roentgenol 159:253–261
- Kuligowska E, Deeds L, Lu K (2005) Pelvic pain: overlooked and underdiagnosed gynecologic conditions. Radiographics 25:3–20
- Levine D (2007) Ectopic pregnancy. Radiology 245:385-397
- Mikami M, Tei C, Kurahashi T et al (2003) Preoperative diagnosis of fallopian tube cancer by imaging. Abdom Imaging 28:743-747
- Moyle JW, Rochester D, Sider L, Shrock K, Krause P (1983) Sonography of ovarian tumors: predictability of tumor type. AJR Am J Roentgenol 141:985–991
- Lalwani N, Shanbhoguel AKP, Vikram R et al (2010) Current update on borderline ovarian neoplasms. AJR Am J Roentgenol 194:330–336
- Outwater EK, Siegelman ES, Hunt JL (2001) Ovarian teratomas: tumor types and imaging characteristics. Radiographics 21:475-490
- Slanetz PJ, Whitman GJ, Halpern EF et al (1997) Imaging of fallopian tube tumors. AJR Am J Roentgenol 169:1321–1324
- Sutton CL, McKinney CD, Jones JE, Gay SB (1992) Ovarian masses revisited: radiologic and pathologic correlation. Radiographics 12:853–877
- Takeuchi M, Matsuzaki K, Uehara H, Nishitani H (2006) Malignant transformation of pelvic endometriosis: MR imaging findings and pathologic correlation. Radiographics 26:407–417
- Tamai K, Koyama T, Saga T et al (2006) MR features of physiologic and benign conditions of the ovary. Eur Radiol 16:2700-2711
- Tanaka YO, Yoshizako T, Nishida M, Yamaguchi M, Sugimura K, Itai Y (2000) Ovarian carcinoma in patients with endometriosis: MR imaging findings. AJR Am J Roentgenol 175:1423–1430
- Venbrux AC, Chung AH, Kim HS et al (2002) Pelvic congestion syndrome: impact of ovarian and internal iliac vein embolotherapy on menstrual cycle and chronic pelvic pain. J Vasc Interv Radiol 13:171–178
- Woodward PJ, Sohaey R, Mezzetti TP Jr (2001) Endometriosis: radiologic-pathologic correlation. Radiographics 21:193–216

# Retroperitoneum

## Roberto García Figueiras, María Pérez Alarcón, and Iria Couto Rodríguez

# Contents

Case 1	Retroperitoneal Hemorrhage	210
Case 2	Iliopsoas Abscess.	212
Case 3	Retroperitoneal Fibrosis	214
Case 4	Erdheim-Chester Disease	216
Case 5	Liposarcoma	218
Case 6	Leiomyosarcoma	220
Case 7	Ganglioneuroma	222
Case 8	Paraganglioma	224
Case 9	Lymphoma	226
Case 10	Retroperitoneal Soft Tissue Metastases	228

# Case 1 Retroperitoneal Hemorrhage

A 62-year-old man was admitted for investigation of a cerebral aneurysm. Cerebral angiography was performed. The procedure was undertaken by means of a right femoral artery approach. Two hours later the patient presented abdominal pain and a marked hypotension.

Comments

Retroperitoneal hematoma (RH) is a rare clinical entity with variable etiology. Hemorrhage confined within the retroperitoneum may be spontaneous or



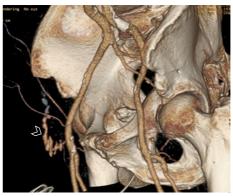


Fig. 10.3







Fig. 10.4

secondary to trauma and medical procedures. Presentation of this clinical entity may vary greatly depending on the degree and duration of the bleeding.

Spontaneous retroperitoneal bleeding can present in the absence of specific underlying pathology or trauma. It is most commonly seen in association with patients with anticoagulation therapy, bleeding abnormalities, and hemodialysis. Although the term spontaneous implies the lack of observable injury, many authors have suspected that unrecognized minor trauma, vomiting, or coughing may initiate bleeding. Wunderlich syndrome is a spontaneous nontraumatic bleeding confined to the subcapsular and/or perinephric space. Several causes have been reported, including benign and malignant renal neoplasms, vascular disease, nephritis, infections, undiagnosed hematological disorders, and anatomical lesions.

RH is a cause of death following blunt trauma, and a large percentage of deaths after trauma occur within the first 12 h from uncontrolled bleeding. Primary problems that must be addressed include the possibility of major associated intra-abdominal injury. In this setting, CT has been proven to be an excellent imaging modality for evaluation of hemodynamically stable patients with blunt abdominal trauma. The rapid diagnostic capability afforded by CT has contributed to a decrease in morbidity and mortality from traumatic abdominal injuries.

Beside this, RH is increasing in incidence mainly due to complications related to interventional procedures. Many different causes of RH secondary to medical procedures have been described in the literature: cardiac catheterization, coil embolization of cerebral aneurysm, extracorporeal shock wave lithotripsy, etc.

CT scan is the best imaging method to establish the diagnosis and the management of RH. On CT scans, fresh hemorrhage is seen as a discrete mass of high attenuation. A fluid-fluid level may be present owing to the hematocrit effect. Chronic hematomas may be hard to distinguish from abscesses and tumors. Contrast-enhanced CT is a basic tool for depicting active bleeding. Detection of active hemorrhage on CT is an important prognostic factor necessitating immediate surgery or interventional angiographic therapy. Active bleeding is depicted on CT scans as a focal or diffuse high-attenuation collection of contrast material surrounded by hematoma or damaged parenchyma or as a jet of extravasated contrast material.

There is a not established role for MR imaging in acute RH. The appearance of hemorrhage depends on the age of the hematoma.

Although patient management will need to be individualized for every case because it depends on the hemodynamic situation and etiologic diagnosis, endovascular treatment involving selective intra-arterial embolization or the deployment of stent-grafts over the punctured vessel is the treatment of choice in many patients.

Contrast-enhanced arterial phase axial CT image (Fig. 10.1) depicts a jet of extravasated contrast material (*open arrow*) in the right femoral artery and extraperitoneal hematoma.

Contrast-enhanced arterial phase coronal reformatted CT image (Fig. 10.2) shows better the retroperitoneal collection (*arrow*) and the jet of active bleeding.

Volume rendering reformatted image (Fig. 10.3) demonstrates the jet of extravasated contrast material in the femoral artery (*open arrowhead*).

Unenhanced coronal reformatted CT image (Fig. 10.4) in a patient treated with extracorporeal shock wave lithotripsy shows perirenal and retroperitoneal hemorrhage (*arrowhead*).

# Case 2 Liopsoas Abscess

A 57-year-old man with a history of chronic liver disease was admitted to hospital with 7-day history of right upper quadrant pain radiating toward the right leg. Patient also complained of fever and decreased appetite. On general examination he was pale and temperature was  $38.5^{\circ}$ C. Laboratory investigation revealed leucocytosis of  $16.3 \times 10^{9}$ /l.

### Comments

Psoas abscess is a rare clinical entity. The incidence is not known but it has probably increased in recent years. Iliopsoas abscesses may be classified as primary or secondary, depending on the presence or absence of underlying disease. Primary psoas abscess has a better prognosis with a lower mortality. The causes of psoas abscess have also changed in the last decades. At the beginning of the twentieth





Fig. 10.5

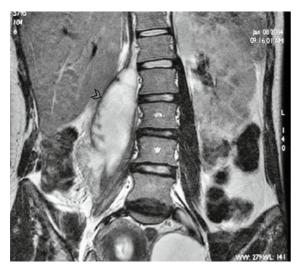


Fig. 10.6





century psoas abscess was mainly caused by tuberculosis of the spine (Pott's disease). Actually, primary iliopsoas abscesses secondary to hematogenous spread from an occult source, are more common, especially in immunocompromised and older patients. Secondary abscesses occur because of direct extension from bowel, kidney, or spine infections. Crohn's disease is the commonest cause of secondary iliopsoas abscess. The most common causative organisms are *Staphylococcus aureus* and mixed gram-negative organisms, though tuberculosis is on the increase again because of immigration and HIV infections in risk groups. It is difficult to determine the likely pathogen from the images, but the degree of soft tissue involvement and size of the abscess may suggest a particular organism, with gram-negative bacteria tending to be responsible for more extensive change.

Iliopsoas abscess may be life threatening owing to their insidious nature. The clinical presentation is often indolent and nonspecific. The classical clinical triad consisting of fever, back pain, and limp is present in only 30% of the patients.

Abdominal plain film provides limited information for detecting psoas infection. It may demonstrate mass effect, abnormal psoas contour, soft tissue gas, or bony destruction of the spine. CT is the best imaging technique for evaluation of iliopsoas disease. CT outlines the extent of disease and may identify the primary source of pathology.

Ultrasound is an operator-dependent imaging technique. Ultrasound is diagnostic in approximately 60% of the cases.

CT images of psoas abscess may manifest as enlargement of the iliopsoas muscle or may show characteristic features of a low attenuation mass with rim enhancement after the intravenous administration of contrast material. Imaging features of tuberculous psoas abscess differ from those of pyogenic infections, and include thickening or calcification of the abscess rim, multiple abscess cavities, and minimal new bone formation.

Abscesses show low signal intensity at T1-weighted MR imaging and high signal intensity at T2-weighted MR imaging. Imaging characteristics of spinal disease are more clearly seen on MRI, permitting a more complete definition of vertebral involvement with soft tissue extension, which may narrow the possible causative organisms. Gadolinium enhancement demonstrates the typical rim enhancement pattern.

Ultrasound or CT may guide diagnostic needle aspiration or drainage insertion and aids follow-up. Image-guided percutaneous drainage currently is the treatment of choice for iliopsoas abscess.

#### **Imaging Findings**

Transverse contrast-enhanced CT scan (Fig. 10.5) shows a hypodense lesion with enhancing rim in the right psoas muscle (*open arrow*). Microbiology reported *S. aureus* as causative organism. Coronal reformatted contrast-enhanced CT image (Fig. 10.6) in the same patient clearly demonstrates the craniocaudal extension of the rim enhanced fluid collection in the right psoas muscle (*arrow*).

Coronal T2-weighted TSE image (Fig. 10.7) in a different case evidences a high signal intensity collection into the right psoas muscle (*open arrowhead*).

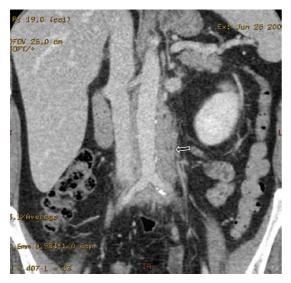
In a different patient, axial T1-weighted TSE image (Fig. 10.8) demonstrates tuberculosis of the spine (Pott disease) extending from the vertebral bodies into the psoas muscle (*arrowhead*).

# Case 3 Retroperitoneal Fibrosis

Comments

A 54-year-old woman presented with right renal colic.

Retroperitoneal fibrosis (RF) is a rare disease with an estimated incidence of 1/200,000 population. RF is a complex clinical entity characterized by a fibro-inflammatory reaction around the abdominal aorta and iliac arteries extended into the retroperitoneum. RF, Riedel's thyroiditis, mediastinal fibrosis, sclerosing cholangitis, and inflammatory pseudotumors are considered in the group of inflammatory fibrosclerosing disorders. Etiology, clinical presentation, and radiological appearance in many cases are variable. About two-thirds of cases are idiopathic, also known as "Ormond's syndrome." The characteristic perivascular distribution of the idiopathic form supports the theory that the disease is an immune-mediated response to severe atherosclerosis, but evidence



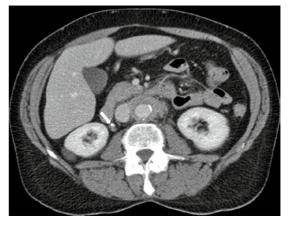


Fig. 10.10

Fig. 10.9



Fig. 10.11



suggests that idiopathic retroperitoneal fibrosis may be part of a systemic fibrosing disease. The remaining 30% are associated with drugs (ergot-derivative drugs), infection, trauma, retroperitoneal, or hemorrhage. Primary and metastatic tumors, including lymphoma and carcinoma of the breast, stomach, colon, prostate, lung, kidney, and uterine cervix, may cause a severe desmoplastic reaction caused by retroperitoneal tumor infiltration.

The signs and symptoms of RF are vague and nonspecific, and therefore the diagnosis relies heavily on radiologic findings.

RF extends along the aorta through a plaque-like infiltrative soft tissue process. The fibrous tissue is usually confined to the central and paravertebral aspect of the retroperitoneum. It usually begins at the level of the aortic bifurcation and spreads cephalad. The fibrosis tends to envelop the aorta and IVC, often entraps the ureter's RF, and is typically localized to the infrarenal aorta and the common iliac arteries. Although this is the most common presentation of RF, in 40% of patients it presents in atypical sites (involving single organs or other anatomical areas) and up to 15% of the patients have additional fibrotic processes outside the retroperitoneum.

On ultrasound exam, RF appears as a hypoechoic area that encases the aorta and inferior vena cava between the renal hila and sacral promontory and may cause hydronephrosis. CT is the method of choice to delineate the extent of the disease. On noncontrast CT scans, RF presents as a periaortic, plaque-like, soft tissue lesion that is usually isodense or slightly hyperdense with muscles. The mass tends not to displace the aorta anteriorly. After intravenous administration of contrast medium, the mass shows variable enhancement depending on the stage of the fibrotic process. However, patients with surgically proven retroperitoneal fibrosis may have no corresponding abnormality on CT.

RF has signal characteristics similar to those of other fibrotic processes, with diffusely low signal intensity on T1-weighted imaging. The T2-weighted MR signal intensity and dynamic enhancement characteristics depend on the stage of the disease. Whereas areas of fibrosis show low T2 signal intensity and delayed contrast enhancement, areas affected by active inflammation may have areas of high signal intensity on T2-weighted images and early contrast enhancement, due to the presence of abundant fluid content and hypercellularity. The same findings are observed in malignant RPF.

Lymphoma and metastatic lymph nodes can mimic RF, but a particular characteristic of RF is the tendency to infiltrate and envelop surrounding structures without displacing them. Malignancies, such as lymphomas and sarcomas, typically cause anterior displacement of the aorta and peripheral nodularity.

Contrast-enhanced coronal reformatted CT image (Fig. 10.9) depicts the presence of lowattenuation mass anterior and lateral to aorta and iliac vessels (*open arrow*).

Contrast-enhanced axial CT images show a low-attenuation mass anterior and lateral to aorta and iliac vessels, without anterior displacement of either aorta or inferior vena cava. Note lithiasis in right urether (Fig. 10.10) (*arrow*). Plaque bifurcates and follows common iliac arteries (Fig. 10.11) (*open arrowhead*).

Sagittal turbo spin-echo MR urogram (Fig. 10.12) shows ureteropyelectasis (*arrowhead*) in a different patient with RF.







Fig. 10.15









A 58-year-old woman presented with cough and dyspnea. She was previously diagnosed with diabetes insipidus. A chest plain film and a thoraco-abdominal CT were performed.

Erdheim-Chester disease (ECD) or polyostotic sclerosing histiocytosis is a rare, non-Langerhans cell histiocytosis of unknown etiology. This entity can affect multiple organs and shows various clinical manifestations, depending on the organs involved, ranging from asymptomatic disease to respiratory distress and/or cardiac failure. The average age at presentation for ECD is 53 years with bone pain as the most frequent clinical sign. The etiology remains unclear and their diagnosis relies on the association of specific radiologic and histologic findings. This entity is characterized by tissue infiltration by foamy histiocytes (xanthogranulomatous) that stain positively for CD68.

Lesions may be skeletal and/or extraskeletal in location, and may include the hypothalamus-pituitary axis, lung, heart, retroperitoneum, skin, liver, kidneys, spleen, and orbit.

Bony involvement is an almost constant finding and consists of symmetric osteoesclerosis of the long tubular bones in the region of the metadiaphyses. The most common extraosseous clinical manifestations of ECD are diabetes insipidus and painless bilateral exophthalmus. However, ECD shows a tropism for connective, adipose, and perivascular tissue that results in characteristic radiographic findings. These findings include:

- Retroperitoneal involvement secondary to infiltration of the fat and surrounding structures by histiocytes and associated fibrosis visualized on CT as hypoattenuated and homogeneous soft tissue masses in the retroperitoneum. The perirenal infiltration may extend to the fat of the anterior or posterior pararenal spaces of both causing the "hairy kidney appearance."
- Periaortic fibrosis has been described and has been shown to involve the ascending aorta to the iliac junction creating the appearance of "coated aorta." CT shows circumferential and regular periaortic tissue with the same attenuation of muscle. Unlike other vascular diseases ECD affects only the adventitial and periadventitial space.
- Cardiac involvement that can be endocardial, myocardial, or pericardial.
- Pulmonary involvement with a typical pattern on CT, which shows interlobular septal and pleural thickening. Other findings include patchy centrilobular ground glass opacities. The most common pulmonary symptom is progressive dyspnea. The liver, pancreas, and mesentery are extremely rarely affected.

The differential diagnosis should be made with retroperitoneal fibrosis. The diagnostic clues are noninvolvement of the inferior vena cava and circumferential infiltration of the aorta contrary to the anterior and lateral infiltration, sparing the posterior aspect of retroperitoneal fibrosis.

Axial abdominal CT (Fig. 10.13) reveals bilateral and symmetric perirenal infiltration. Contrast-enhanced scans of the thorax (Figs. 10.14 and 10.15) demonstrate infiltration of aortic arch and mediastinal involvement sheathing the descending aorta. Bilateral pleural thickening and effusion are also present. Figure 10.16 shows diffuse bilateral smooth interlobular septa thickening.

#### Comments

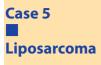




Fig. 10.17

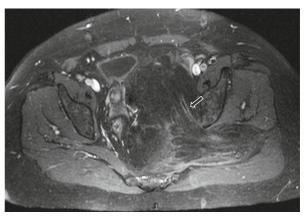


Fig. 10.18



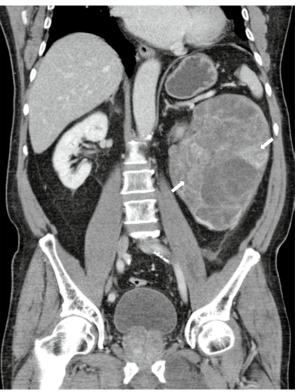


Fig. 10.20

A 71-year-old woman presented with a left lower quadrant abdominal mass.

Liposarcomas (LSs) are malignant tumors of mesenchymal origin that may arise in any fatcontaining region of the body. They typically occur in the fifth and sixth decades of life. LS is the most common retroperitoneal soft tissue tumors in adult patients and it represents 35% of all malignant primary neoplasms in the retroperitoneum. Histologically, LSs are classified in increasing order of malignancy as: (1) well-differentiated, (2) dedifferentiated, (3) myxoid, (4) round cell, and (5) pleomorphic LS. Well-differentiated LS is the most common subtype, while myxoid LS occurs typically within the extremity and only rarely is located in the retroperitoneum. CT and MR imaging appearances vary according to these histologic subtypes.

Well-differentiated LSs contain mature fatty elements with imaging characteristics that may be indistinguishable from those of normal fat or lipomas and they frequently may contain septa, as well as solid-appearing regions. These fibrous septa are thicker, more irregular, or more nodular than those seen in lipomas.

Dedifferentiated LS is defined as a neoplasm with a well-differentiated LS juxtaposed to pleomorphic sarcoma. Seventy five percent of all dedifferentiated LSs occur in the retroperitoneum. The tumor extent should be defined with caution as the fat components of the tumor could easily be mistaken for adjacent normal fat structures.

Myxoid LSs often have an inhomogeneous appearance and may mimic a cystic lesion on precontrast CT or MRI. They are readily differentiated after intravenous administration of contrast material. Slowly progressive enhancement is characteristic and reveals the solid nature of these tumors.

Round cell LSs represent the poorly differentiated form of myxoid liposarcoma with an aggressive clinical course and a tendency to metastasize. Pleomorphic and round cell LSs are heterogeneous, nonfatty tumors. Therefore, it is usually impossible to differentiate them from other sarcomas.

Most retroperitoneal LSs have grown to a very large size at the time of their initial detection, and they often involve critical structures. Surgery with tumor-free margins remains the cornerstone therapy for LSs and imaging techniques may help to precise delineation of tumor margins. Well-differentiated tumors do not metastasize, but tend to recur locally and may cause significant morbidity and mortality due to mass effect, compression, and/or encasement of vital structures. In contrast, pleomorphic LSs are highgrade aggressive neoplasms that frequently metastasize early. Approximately 80% of metastatic lesions from sarcomas involve the lungs.

### **Imaging Findings**

Comments

signal intensity of the fatty component of the tumor is suppressed (open arrow). Myxoid liposarcoma of the retroperitoneum in a 65-year-old man. Contrast-enhanced axial CT image shows a low-attenuation mass (25 HU) (Fig. 10.19) lateral to the left kidney. Contrast-enhanced coronal reformatted CT image (Fig. 10.20) acquired in a late phase depicts the presence of a slowly progressive enhancement of the tumor (arrows).

Well-differentiated liposarcoma of the pelvis in a 71-year-old woman. Axial T1-weighted

image (Fig. 10.17) demonstrates a fatty tumor with signal intensity equal to that of subcutaneous fat. Axial fat-suppressed T1-weighted image (Fig. 10.18) shows that the high

# Case 6 Leiomyosarcoma





Fig. 10.22

Fig. 10.21



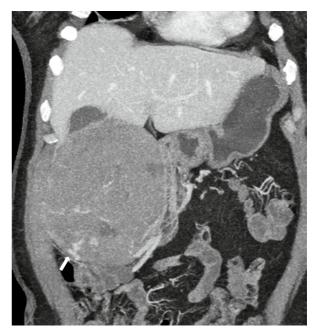


Fig. 10.24

A 62-year-old woman complained of diffuse abdominal pain accompanied by anorexia and weight loss. Physical exam revealed a large right upper quadrant mass.

## Leiomyosarcoma (LM) is a soft tissue sarcoma originated from smooth muscle cells, including the muscle layer of a blood vessel (the tunica media). LM principally affects patients in their fifth to seventh decades of life. Retroperitoneal LM is a rare entity, accounting for 5-15% of all retroperitoneal tumors. Retroperitoneal LM is the second most common primary retroperitoneal tumor in adults (30%) after liposarcoma (61%). Involvement of the retroperitoneum is more common in women than men. These tumors seldom present with symptoms until they progress into a huge mass. When the tumors are discovered at this later stage, there is a poor outlook for long-term survival. Retroperitoneal LM exhibits three major growth patterns: (a) completely extravascular (extraluminal) (62% of cases), (b) completely intravascular-intraluminal (5% of cases), and (c) a combination of both with extravascular tumor and tumor extending into the retropenitoneal veins and inferior vena cava (33% of cases). Tumor should be classified as a LM of the IVC if it has predominantly intraluminal growth or if a segment of the involved IVC needs to be resected with the extraluminal tumor. This intra- and extraluminal pattern of growth is very suggestive of LM because most other primary retroperitoneal tumors do not have this growth pattern.

Radiologic appearances of this tumor are not specific but both CT and MRI show a heterogeneous nonfatty soft tissue mass. The tumor is usually well circumscribed by a pseudocapsule that is formed when the tumor compresses adjacent structures, but tumor cells frequently invade beyond this pseudocapsule. LMs usually have central nonenhancing foci that suggest necrosis. Necrosis is more commonly seen in LMs than other sarcomas and LMs tend to develop massive cystic necrotic degeneration. LMs may appear to be hypervascularized with a peripheral enhanced mass and showing vascular structures penetrating the tumor, a finding that is best visualized in maximal intensity projection (MIP) technique.

Although imaging findings are not specific for LM, they may provide useful information for the localization, size, internal structure of the mass, local or distant extension, and invasion of the tumor which are beneficial to the differential diagnosis and patient management.

Plain abdominal film (Fig. 10.21) evidences increased density in the right upper quadrant (*open arrows*).

Contrast-enhanced axial and coronal reformatted CT images (Figs. 10.22 and 10.23) depict the presence of a solid nonfatty soft tissue mass with necrotic areas that shows vascular structures penetrating the tumor (*arrows*), a finding that is best visualized in maximal intensity projection (MIP) technique (Fig. 10.24).

#### **Comments**





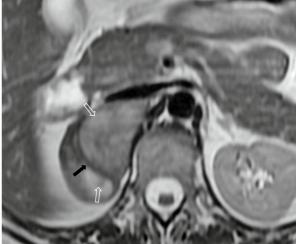


Fig. 10.26







Fig. 10.28

A primary, extra-adrenal retroperitoneal mass was found incidentally in a 33-year-old man while he was being studied for altered liver function tests.

### Comments

Ganglioneuromas are neurogenic tumors that arise from the autonomic ganglion cells of the peripheral nervous system, usually the sympathetic ganglion. Patients of all ages are affected, but predominantly children and young adults. Abdominal ganglioneuromas are most commonly located in the retroperitoneum, especially in the paraspinal areas and adrenal glands. These tumors are grossly well-circumscribed, solid, encapsulated masses that tend to partially or completely surround major blood vessels, with little or no compromise of the lumen. Tumors of the sympathetic ganglia tend to extend along the sympathetic chain and have an elongated shape. Ganglioneuromas show calcification in approximately 20% of cases (more frequently than nerve sheath tumors) and is usually punctuate. These tumors tend to present a whorled pattern that, at histopathologic analysis, corresponds to bundles of Schwann cells and collagen fibers within the mass. This pattern, that it is commonly seen in ganglioneuroma and neurofibroma, explains one of the MR imaging characteristics of this neoplasm, the presence of curvilinear bands of low signal intensity linear or curvilinear structures on T2-weighted images. Beside this, T2 signal intensity of ganglioneuromas depends on the varying degrees of myxoid stroma, cellular components, and collagen fibers in the tumor. A myxoid stroma is low on T1-weighted images and markedly high on T2-weighted images. Tumors with intermediate to high signal intensity on T2-weighted MR images consist of extensive cellular and fibrous components and only a small amount of myxoid stroma. Those with markedly high signal intensity on T2-weighted images consist of a large amount of myxoid stroma and relatively few cellular and fibrous components.

Ganglioneuromas usually demonstrate gradually increasing enhancement rather than early enhancement at contrast-enhanced dynamic MR imaging. These enhancement features are explained by the presence of an abundance of myxoid matrices in the tumors, resulting in delayed progressive accumulation of contrast material in the extracellular space that depends on the extent of the vascular network within the myxoid stroma. It has been reported that enhancement is delayed and mild (or absent) in benign masses and relatively early and pronounced in malignant masses.

Most neurogenic tumors in adults are benign. Benign and malignant neurogenic tumors are difficult to differentiate unless distant metastatic deposits are seen.

### **Imaging Findings**

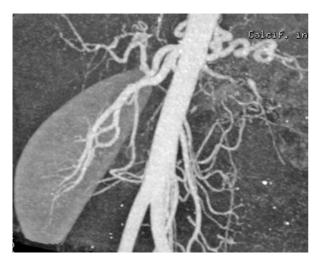
Axial T1-weighted MR image (Fig. 10.25) shows a homogeneous, low signal intensity tumor in the retroperitoneum lateral to the right kidney. Axial T2-weighted MR image (Fig. 10.26) shows areas within the markedly high signal intensity tumor (*open arrows*) and linear and curvilinear low signal intensity bands (*arrow*). Coronal T2-weighted MR image (Fig. 10.27) demonstrates that the mass is separated from the adrenal gland (*open arrowhead*). On an axial contrast-enhanced T1-weighted MR image (Fig. 10.28), the tumor evidences a discrete enhancement. Case 8 Paraganglioma Comments A 33-year-old man presented with a history of uncontrolled hypertension.

International nomenclature concerning pheochromocytoma have changed over the last few years. Actually, the term pheochromocytoma must be reserved for those paragangliomas located inside the adrenal glands, whereas sympathetic

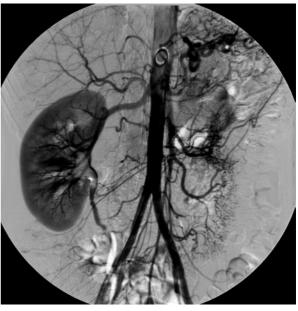




Fig. 10.30









paragangliomas outside the adrenals are referred to as extra-adrenal paragangliomas. This new classification reflects the distinctive biochemical and clinical properties of these tumors in different locations. Adrenal tumors are usually benign, secrete both epinephrine and norepinephrine in at least 50% of cases, are often related to a specific gene mutation if located bilaterally, and are frequently found as incidentalomas. In contrast, extra-adrenal tumors have a noradrenergic and/or dopaminergic phenotype, more often have an aggressive or metastatic nature, and are rarely associated with familial syndromes.

Pheochromocytoma has been called the 10% tumor because approximately 10% cases are bilateral, 10% are malignant, 10% occur in children, and 10% are extra-adrenal.

Biochemical diagnosis of pheochromocytoma (total urinary levels of catecholamines and their metabolites over 24 h or fractionated plasma-free metanephrines) must be established prior to undertaking imaging studies to avoid unnecessary exams. The role of imaging techniques in paragangliomas depends on clinical background. In patients with typical symptoms and signs, the important purpose of imaging examination is to localize the tumor and its extent preoperatively. For asymptomatic patients or incidentalomas, the role of imaging is to establish the diagnosis of paraganglioma based on imaging features.

Computed tomography is the initial imaging modality of choice for localization of paragangliomas. This technique shows high sensitivity (>90%) for localization of the tumor but low specificity. In contrast, metaiodobenzylguanidine (MIBG) scintigraphy demonstrates high sensitivity (85%) and specificity (>95%) for detection and localization of pheochromocytomas but we must have in mind that not all pheochromocytomas concentrate MIBG.

The sensitivity of MRI in detecting pheochromocytoma and extra-adrenal pheochromocytoma is 93.3–100% and the combination of MRI and MIBI has been reported as having a sensitivity and specificity of 100% in the detection of biochemically proven pheochromocytoma.

Most paragangliomas typically enhance avidly on enhanced CT or MR images, but enhancement can be heterogeneous due to regions of cystic changes. On MR imaging, paragangliomas usually have high signal intensity on T2-weighted MR images, but more than 30% have low signal intensity on these sequences. Imaging appearances of these tumors are varied and they may appear as fatty, cystic, hemorrhagic, or calcified masses.

Finally, <sup>18</sup>F-DOPA- Positron emission tomography (PET) with fluorine-18-labelled dihydroxyphenylalanine has emerged as an important tool in the diagnosis and staging of pheochromocytomas and extra-adrenal paraganglioma and preliminary data based on small case series have demonstrated sensitivity and specificity of 100%.

Ten percent of pheochromocytomas are malignant. Metastatic spread is the only reliable criterion for the diagnosis of malignant paraganglioma.

Contrast-enhanced axial image (Fig. 10.29) and oblique reformatted maximum intensity projection (MIP) (Fig. 10.30) CT image obtained in the arterial-phase depict the presence of a solid hypervascular retroperitoneal mass (*open arrow*) and a decreased enhancement in a small size left kidney (*arrow*).

Oblique reformatted MIP CT image (Fig. 10.31) and digital subtraction angiography (Fig. 10.32) image confirm the obstruction of the left renal artery.

A 68-year-old man was evaluated for fever, weight loss, and night sweats.

# Case 9 Lymphoma

Comments

Most patients with non-Hodgkin's lymphoma (NHL) compared with less than half of the patients with Hodgkin's lymphoma (HL) have abdominal involvement. Para-aortic lymphadenopathy is the most common finding. Although HL and NHL share similar radiologic features, there are some significant differences in their radiographic appearances. Extranodal disease is more common with NHL than with HL and is often intermediate to high-grade lymphoma. In NHL, involved lymph nodes tend to be larger as compared with HL and extranodal sites are also frequently involved. HL-isolated infradiaphragmatic lymphadenopathy occurs in less than 10% of patients at diagnosis. HL spreads in a contiguous fashion from one lymph node group to the adjacent lymph nodes.

Computed tomography (CT) is the most commonly used imaging modality for the detection, staging, and follow-up of lymphoma. In the retroperitoneum, lymphoma may present as



Fig. 10.33



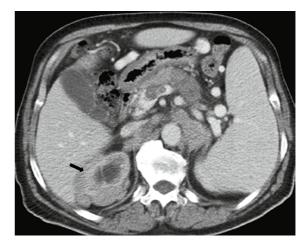


Fig. 10.34



Fig. 10.36

unifocal, multifocal masses; lymphadenopathy; or diffuse infiltration. In general, lymphoma causes a displacement of structures by the enlarged lymph nodes without invasion. This imaging feature may distinguish lymphomas from metastatic carcinomas. Lymphoma typically shows homogenous attenuation at unenhanced CT and has mild enhancement with contrast media. Calcification is rare without treatment.

Positron emission tomography (PET)/CT is superior to CT in detecting extranodal disease in the abdomen. The role for PET/CT in staging indolent histologies varies among histologies. Follicular lymphomas are routinely fluorodeoxyglucose (FDG) avid, whereas marginal zone lymphoma are less often avid, and T-cell NHL are markedly heterogeneous. CT remains the standard for low-grade and T-NHL. However, PET is currently not part of standard lymphoma staging primarily because of the generally small percentage of patients in whom PET alters management or outcome.

Sonography and magnetic resonance imaging do not have a key role for the evaluation of abdominal lymphoma. However new whole body MR diffusion imaging may open a future potential role of MR imaging in lymphoma.

CT scans obtained after treatment may demonstrate a residual tumor mass that is not metabolically active. FDG-PET is superior to CT in differentiation of viable tumor, necrosis, and fibrosis. PET/CT provides its greatest clinical benefit in the post-treatment evaluation of Hodgkin's lymphoma and diffuse large B-cell lymphoma.

Imaging for surveillance is performed after treatment with the goal of early detection of recurrence. However, several studies have shown that it is the patient or the physician who first suspects relapse more than 80% of the time. Beside this, the likelihood of tumor relapse became insignificant after 12 months for HL and after 18 months for diffuse large B-cell lymphoma, although there was a continuous risk of relapse with follicular lymphoma.

Differential diagnosis for retroperitoneal lymphoma may include diverse entities such as metastatic disease (in which the nodal enlargement is not usually as pronounced as that seen in patients with lymphoma), infection (tuberculosis, atypical mycobacterial infection, and Whipple disease), inflammatory conditions, or lymphoproliferative disorders (such as Castleman's disease). Metastatic deposits to the retroperitoneal lymph nodes frequently result from tumors of the kidney, colon, pancreas, lung, breast, testis, prostate, and cervix and melanoma. Differentiating metastatic lymphadenopathy from retroperitoneal lymphoma is a diagnostic challenge. The presence of lymph node necrosis is a feature that is more frequently associated to metastatic disease or tuberculosis than lymphoma.

Contrast-enhanced arterial phase axial CT image (Fig. 10.33) depicts extensive retroperitoneal lymphadenopathy encasing the renal vessels (*open arrow*). Contrast-enhanced venous phase axial image (Fig. 10.34) demonstrates extensive retroperitoneal lymphadenopathy, perirenal and renal infiltrative masses (*arrow*), pancreatic involvement, and splenomegaly with partial thrombosis of the mesenteric vein.

Plain abdominal film (Fig. 10.35) depicts multiple foci of calcification that corresponds to calcified mesenteric and retroperitoneal lymph nodes in a patient with tuberculosis.

CT exam (Fig. 10.36) in a patient with Whipple disease shows enlarged low-density mesenteric (*open arrowhead*) and retroperitoneal lymph nodes (due to high fat content) (*arrowhead*).

# Case 10 Retroperitoneal Soft Tissue Metastases

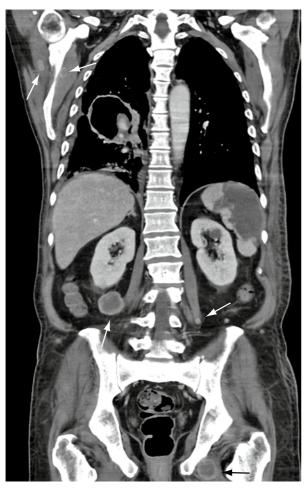




Fig. 10.38

A follow-up CT scan was requested for a 58-year-old man with a history of lung cancer stage IIIB treated with chemotherapy.

Retroperitoneal soft tissue (ST) metastases, defined as metastasis to skeletal muscle and subcutaneous tissues, are rarely reported in the literature. Autopsy series have reported ST metastatic disease in 0.75–9% of patients who died of carcinoma. Metastatic spread to the retroperitoneum most commonly involves the regional lymph nodes and radiologists must have in mind the specific metastatic pattern for every tumor, although in the case of ST metastases there is no correlation between the site of the metastases and the primary tumor.

Detection of ST metastasis may affect tumor staging and prognosis. ST metastases may present in patients with a history of malignancy or, in cases with no history of malignancy, if metastasis is the first presentation. Most metastases are caused by carcinomatous deposits, most common from the lung, kidney, and bowel carcinoma, while prostate, breast, and thyroid carcinoma only very rarely metastasise to the ST. Melanoma and lymphoma account for many cases of ST metastases and must be considered in the differential diagnosis. In this setting, the appearance of metastatic melanoma may be variable, but the presence of a mass with high signal on T1-weighted MRI due to melanin and/or hemorrhage may suggest the diagnosis. Despite clinical and imaging investigations, the primary sites remain unknown in a significant percentage of cases.

Metastatic tumors presenting as ST masses are relatively rare and can be the source of diagnostic confusion both clinically and pathologically. Retroperitoneal metastases are usually seen as late events and survival is generally poor, especially for primary carcinoma of the lung. The prognosis may be higher for renal carcinoma.

Radiological features are not specific and ST sarcoma represents a common clinical misdiagnosis, especially in those cases that present a solitary retroperitoneal metastatic deposit. <sup>18</sup>F-FDG PET/CT has a good sensitivity for skin and ST metastasis detection and in some cases, this feature might change tumor staging.

Percutaneous imaging-guided biopsy is reliable in confirming the diagnosis of malignancy and helpful in the detection of the possible origin of the primary tumor.

ST metastases should remain a differential diagnosis in any patient presenting with a suspicious soft tissue lump in the retroperitoneum.

Contrast-enhanced coronal reformatted CT image (Fig. 10.37) and contrast-enhanced axial CT images (Figs. 10.38) demonstrate the presence of a cavitated lung carcinoma and multiple metastatic deposits in soft tissue and muscles (*arrows*).

#### **Comments**

## **Further Reading**

### Books

- Casalino D, Miller F, Nikolaidis P, Hammond N (2010) Genitourinary imaging cases. McGraw-Hill Companies, Philadelphia
- Coakley FV (2010) Pearls and pitfalls in abdominal imaging: pseudotumors, variants and other difficult diagnoses. Cambridge University Press, Cambridge
- Feldberg MAM (2008) Computed tomography of the retroperitoneum. Springer, New York, LLC
- Joarder R (2011) Case studies in abdominal and pelvic imaging, 1st edn. Springer, New York, LLC
- Meyers MA (2010) Meyers' dynamic radiology of the abdomen: normal and pathologic anatomy, 6th edn. Springer, New York, LLC

### Web Links

http://www.medscape.org/radiology

http://www.med-ed.virginia.edu/courses/rad/CT%20 Abdominal%20Anatomy/CT%20Anatomy%20of%20the%20 Abdomen%20final.htm

http://www.mypacs.net/

http://rad.usuhs.edu/medpix/

http://www.wikiradiography.com/

## Articles

- Anis M, Irshad A (2008) Imaging of abdominal lymphoma. Radiol Clin North Am 46(2):265–285
- Blake MA, Kalra MK, Maher MM, Sahani DV, Sweeney AT, Mueller PR, Hahn PF, Boland GW (2004) Pheochromocytoma: an imaging chameleon. Radiographics 24(Suppl 1):S87–S99
- Cheson BD (2011) Role of functional imaging in the management of lymphoma. J Clin Oncol 29(14):1844–1854
- Craig WD, Fanburg-Smith JC, Henry LR, Guerrero R, Barton JH (2009) Fat-containing lesions of the retroperitoneum: radiologic-pathologic correlation. Radiographics 29(1):261–290
- Cronin CG, Lohan DG, Meehan CP, Delappe E, McLoughlin R, O'Sullivan GJ, McCarthy P (2008a) Anatomy, pathology, imaging and intervention of the iliopsoas muscle revisited. Emerg Radiol 15(5):295-310
- Cronin CG, Lohan DG, Blake MA, Roche C, McCarthy P, Murphy JM (2008b) Retroperitoneal fibrosis: a review of clinical features and imaging findings. AJR Am J Roentgenol 191(2):423–431
- Elsayes KM, Narra VR, Leyendecker JR et al (2005) MRI of adrenal and extraadrenal pheochromocytoma. AJR Am J Roentgenol 184:860–867
- Elsayes KM, Staveteig PT, Narra VR, Chen ZM, Moustafa YL, Brown J (2007) Retroperitoneal masses: magnetic resonance imaging findings with pathologic correlation. Curr Probl Diagn Radiol 36(3):97–106

- Kenn W, Stäbler A, Zachoval R, Zietz C, Raum W, Wittenberg G (1999) Erdheim-Chester disease: a case report and literature overview. Eur Radiol 9:153–158
- Kurugoglu S, Ogut G, Mihmanli I, Korman U, Durak H (2002) Abdominal leiomyosarcomas: radiologic appearances at various locations. Eur Radiol 12(12):2933–2942
- Muttarak M, Peh WC (2000) CT of unusual iliopsoas compartment lesions. Radiographics 20 Spec No:S53-S66
- Negus S, Sidhu PS (2000) MRI of retroperitoneal collections: a comparison with CT. Br J Radiol 73(872):907–912
- Nguyen NC, Chaar BT, Osman MM (2007) Prevalence and patterns of soft tissue metastasis: detection with true wholebody F-18 FDG PET/CT. BMC Med Imaging 7:8
- Nishimura H, Zhang Y, Ohkuma K, Uchida M, Hayabuchi N, Sun S (2001) MR imaging of soft-tissue masses of the extraperitoneal spaces. Radiographics 21(5):1141–1154
- Nishino M, Hayakawa K, Minami M, Yamamoto A, Ueda H, Takasu K (2003) Primary retroperitoneal neoplasms: CT and MR imaging findings with anatomic and pathologic diagnostic clues. Radiographics 23(1):45–57
- Pereira JM, Sirlin CB, Pinto PS, Casola G (2005) CT and MR imaging of extrahepatic fatty masses of the abdomen and pelvis: techniques, diagnosis, differential diagnosis, and pitfalls. Radiographics 25(1):69–85
- O'Sullivan PJ, Harris AC, Munk PL (2008) Radiological imaging features of non-uterine leiomyosarcoma. Br J Radiol 81(961): 73–81
- Qiao HS, Feng XL, Yong L, Yong Z, Lian ZJ, Ling LB (2007) The MRI of extraadrenal pheochromocytoma in the abdominal cavity. Eur J Radiol 62(3):335–341
- Rha SE, Byun JY, Jung SE, Chun HJ, Lee HG, Lee JM (2003) Neurogenic tumors in the abdomen: tumor types and imaging characteristics. Radiographics 23(1):29–43
- Sahdev A, Sohaib A, Monson JP, Grossman AB, Chew SL, Reznek RH (2005) CT and MR imaging of unusual locations of extraadrenal paragangliomas (pheochromocytomas). Eur Radiol 15(1):85–92
- Shin NY, Kim MJ, Chung JJ, Chung YE, Choi JY, Park YN (2010) The differential imaging features of fat-containing tumors in the peritoneal cavity and retroperitoneum: the radiologicpathologic correlation. Korean J Radiol 11(3):333–345
- Szklaruk J, Tamm EP, Choi H, Varavithya V (2003) MR imaging of common and uncommon large pelvic masses. Radiographics 23(2):403–424
- Torres GM, Cernigliaro JG, Abbitt PL, Mergo PJ, Hellein VF, Fernandez S, Ros PR (1995) Iliopsoas compartment: normal anatomy and pathologic processes. Radiographics 15(6): 1285–1297
- Vilanova JC, Woertler K, Narváez JA, Barceló J, Martínez SJ, Villalón M, Miró J (2007) Soft-tissue tumors update: MR imaging features according to the WHO classification. Eur Radiol 17(1):125–138
- Vivas I, Nicolás AI, Velázquez P, Elduayen B, Fernández-Villa T, Martínez-Cuesta A (2000) Retroperitoneal fibrosis: typical and atypical manifestations. Br J Radiol 73(866):214–222